論文 / 著書情報
Article / Book Information

題目(和文)	タイタン上の有機物の表面エネルギーと弾性に関する実験的研究
Title(English)	Experimental study on surface energy and elasticity of organic materials on Titan
著者(和文)	平井英人
Author(English)	Eito Hirai
出典(和文)	学位:博士(理学), 学位授与機関:東京科学大学, 報告番号:甲第221号, 授与年月日:2025年3月26日, 学位の種別:課程博士, 審査員:玄田 英典,中嶋 健,太田 健二,癸生川 陽子,関根 康人,筒井 智嗣
Citation(English)	Degree:Doctor (Science), Conferring organization: Institute of Science Tokyo, Report number:甲第221号, Conferred date:2025/3/26, Degree Type:Course doctor, Examiner:,,,,,
学位種別(和文)	博士論文
Type(English)	Doctoral Thesis

Doctoral Dissertation
博士論文

Experimental study on surface energy and elasticity of organic materials on Titan

（タイタン上の有機物の表面エネルギーと弾性に関する実験的研究）

A Dissertation Submitted for the Degree of Doctor of Philosophy
December 2024

令和 6 年 12 月博士（理学）申請

Department of Earth and Planetary Sciences,
School of Science
Institute of Science Tokyo

東京科学大学理学院地球惑星科学系
地球惑星科学コース

Eito Hirai
平井 英人

Abstract

Saturn's largest moon, Titan, has a dense reducing atmosphere, where organic aerosols are formed from methane (CH_4) and nitrogen (N_2) via photochemical reactions. These organic aerosols would deposit on the surface, where an active CH_4-based hydrological cycle exists. Thick organic sediments exist as dunes only at low latitude regions of Titan, but not in the middle latitude regions, although both low and middle latitude regions are generally arid. Given that no thick organic sediments exist on middle latitude regions where potentially H_2O ice crust exposed, organic aerosols at middle latitudes may have been transported spontaneously. Previous studies, however, have considered that saltation of organic aerosols would occur only by strong winds due to CH_4 storms at low latitudes but would not occur by seasonal wind at low and middle latitudes based on the high cohesiveness of Titan's organic aerosol analogs (Titan tholin) measured at room temperature. However, the cohesive force would be different at Titan's surface temperature (~93 K). In addition, various chemical process on the surface of Titan would result in the formation of organic materials with different chemical structures, which would show different cohesiveness. However, the temperature dependence and chemical structure dependence of cohesiveness, which depends on the surface energy and elasticity, of Titan's organic analog materials have been poorly understood.

The objectives of the present study are to investigate the temperature and chemical structure dependence of both surface energy (cohesion force) and elasticity (elastic wave velocities) of organic analog materials on Titan.

In Chapter 2, laboratory experiments generated three types of organic materials; the present study produced laboratory analogs of Titan's organic materials; 1) films and particles of Titan tholin, 2) films of altered tholin, and 3) films and solids of hydrothermal organics. Morphological observations were conducted using a field emission-scanning electron microscopy (FE-SEM) and an atomic force microscopy (AFM), while the chemical structures were investigated using a Fourier Transform Infrared (FT-IR) spectroscopy, elemental analysis, an ultraviolet/visible (UV/Vis) spectroscopy, and High-Performance Liquid Chromatography (HP-LC). Our results suggest that the organic films on the tip of the cantilever and Si wafer substrates have smooth surfaces at the nanometer scale. The chemical structure of film and particles of Titan tholin and film of hydrothermal organics would be N-bearing polycyclic aromatic compounds (N-PACs) connected with polymer-like chain structures. Altered tholin contains N-bearing heterocyclic aromatic structures with little aliphatic compounds. Solids of hydrothermal organics show the polyolefin with an abundance of C=O bonds in the structure.

In Chapter 3, the cohesion force and surface energy measurements of organic analog materials were performed using an atomic force microscope (AFM). Our results suggest that the

apparent surface energy of Titan tholin decreases as temperature decreases, following the Arrhenius equation with an activation energy E_{surf} = 1760 ± 190 J mol^{-1} and the surface energy of Titan tholin at absolute zero γ_0= 180 ± 20 mJ m^{-2}. The temperature dependence of the apparent surface energy would be derived from the decreasing of contact radius due to increasing of the elasticity and/or the reduction of the energy dissipation caused by a molecular stick-slip mechanism during separation with temperature drop, which results in the the observed temperature dependence of cohesion force. Our results also suggest that the surface energy of altered tholin and hydrothermal organics are 159 ± 39 mJ m^{-2} or 226 ± 77 mJ m^{-2}, and 57 ± 8 mJ m^{-2}, respectively. These values are higher than values obtained by contact angle measurements but are comparable to graphene measured by surface force balance (SFB) and lower than that of paraffin estimated from tensile strength measurement. The difference could arise from energy dissipation during separation, such as molecular stick-slip and mechanical adhesion effects, which are not considered in static contact angle measurements. Surface energy is influenced by factors, including elemental ratios such as C/H and C/N, the abundance of unsaturated bonds, and molecular size.

In Chapter 4, elastic wave velocities and elasticity measurements of organic analog materials were performed by synchrotron radiation X-ray experiments and ultrasonic wave experiments. Our results of ultrasonic wave experiments suggest that P-wave velocity (V_p) and S-wave velocity (V_s) of Titan tholin and hydrothermal organics at 300 K are 3260 ± 390 m/s and 1830 ± 60 m/s for Titan tholin and 2830 ± 60 m/s and 1740 ± 40 m/s for hydrothermal organics, respectively. The V_p values of the organic materials are consistent with the acoustic wave velocities estimated from phonon dispersion, which were determined through measurements of inelastic X-ray scattering (IXS) spectra at 300 K. Temperature dependence of the 2θ dependence of the intensity of elastic contribution $S(Q, 0)$ and the least square fitting results of phonon dispersion curve indicates that the overall lattice structure of Titan tholin does not change significantly between 300 K and 93 K. With assuming a constant density, temperature dependence of the longitudinal modulus of Titan tholin are estimated to be M_0 = 7.3 ± 1.2 GPa and E_a = -500 ± 230 J mol^{-1} for Arrhenius equation and in M_0 = 15 ± 2 GPa and T_m = 340 ± 110 K for linear relationship by least square fittings. Large errors indicate significant uncertainty in the temperature-dependent mechanism, requiring further analysis and alternative measurements. Our results of comparison of the Young's modulus of Titan tholin and hydrothermal organics with various organic materials as a function of their C/H ratio suggest that the elastic properties of organic materials could be determined by not only the elemental ratio but also elemental composition, functional groups, and the molecular configuration of aromatic and aliphatic structures. The comparison of phonon dispersion obtained from the IXS and ultrasonic methods for Titan tholin demonstrates that the ultrasonic measurements align with the phonon dispersion curve near the zero point, within the error. This suggests that the long-wavelength approximation

remains valid at the phonon scale of a few unit cells, indicating that the extrapolation of ultrasonic method results to the 0.1–10 Hz frequency range of the seismometer onboard NASA's *Dragonfly* mission is feasible. At Titan's surface temperature (~93 K), the elastic properties are estimated to be $K = 11 \pm 3.8$ GPa and $G = 6 \pm 2.0$ GPa for Titan tholin-like structure, and $K = 9.1 \pm 3.1$ GPa and $G = 6.9 \pm 2.4$ GPa for hydrothermal organic-like structure.

In Chapter 5, the saltation threshold wind speed u^* on Titan's surface temperature was estimated with the temperature dependence of the surface energy of Titan tholin (Chapter 3). Then, mass flux of sand transports from middle latitude regions toward lower latitude regions was compared with the deposition flux of organic aerosols. Our results suggest that the saltation threshold wind speed u^* would decrease by a factor ~3 than values previously expected, suggesting that saltation would occur by tidal wind at middle latitude regions in the summer. The mass flux of sand transportation would be larger than the deposition rate of organic aerosols. Sand transport from middle latitude regions toward low latitude regions by tidal wind in the summer would explain the absence of thick organic sediments exist on middle latitude regions where potentially H_2O ice crust exposed. To prove the hypothesis of transport of organic aerosols from middle latitude regions toward low latitude regions, the active seismic survey by NASA's *Dragonfly* will be useful. A sensitivity study of the detection limit of depths of organic sediments in shallow subsurface to the elasticity of organic materials (Chapter 4) was also performed using a rock physics model. Our results suggest that the detection limits of depths of P-wave and S-wave would be ~30 m at 10 Hz of frequency. P-wave and S-wave velocities of Titan's organic materials constrained in the present study are essential for estimating the thickness of organic sediments based on the travel time of reflected seismic echoes, which will be measured during the active seismic survey of NASA's *Dragonfly* mission.

In Chapter 6, the findings of the present study were synthesized. The fragmentation velocity of organic mantle grains (OMGs) was also calculated based on the temperature dependence of surface energy (Chapter 3) and elasticity (Chapter 4) of organic analog materials. The results indicate that the collisional growth of the OMGs would not proceed as efficiently as previously expected. Furthermore, our results of the temperature dependence of the surface energy indicate that the surface energy is not the factor controlling the haziness of the exoplanet atmosphere by effective wet/dry removal. This suggests that other factors are needed to explain the equilibrium temperature dependence of haziness in the atmospheres of exoplanets.

Acknowledgements

I would like to express my deepest appreciation to my supervisor, Prof. Y. Sekine, for his invaluable guidance, enduring encouragement, and unwavering support throughout my six-year graduate school journey. His insightful advice and critical reviews have greatly improved both this dissertation and my academic growth. His words and his professional attitude inspired me to overcome challenges.

I would also like to express my sincere appreciation to Prof. H. Genda, the chairperson of this thesis, for his kind support and valuable advice throughout my doctoral course. His guidance on research themes, seminars, presentations, and even humorous speeches was invaluable. Without his help, I could not have completed my PhD journey.

My heartfelt appreciation also goes to Assist. Prof. X. Yu for her invaluable support in helping me write this dissertation and for the many opportunities she provided. Her work deeply inspired me throughout my PhD journey. I learned not only academic skills from her but also the importance of sociality and collaboration.

I would like to thank Dr. S. Tsutsui, Prof. K. Nakajima, Assoc. Prof. K. Ohta, and Assoc. Prof. Y. Kebukawa for their critical reviews and helpful comments on this dissertation. I would like to gratefully acknowledge Dr. S. Tsutsui and Dr. Y. Higo for their invaluable assistance in conducting experiments and analyses on elastic wave velocity measurements. Without their collaboration and guidance, I would not have been able to write Chapter 4 of this thesis. I am deeply grateful to Dr. H. Ito, Mr. T. Saito, Prof. K. Nakajima, Dr. M. Ito, Prof. Y. Sugimoto, Assist. Prof. Y. Yasui, and Prof. M. Kasuya for their invaluable support in conducting experiments and analyses related to cohesion force and surface energy measurements. I would also like to express my gratitude to Prof. S. Okuzumi for his guidance in microphysical modeling, insightful suggestions and feedback on my PhD research, and warm encouragement throughout my doctoral journey. Their contributions and insights were essential for the completion of Chapter 3 of this thesis. I would also like to express my gratitude to Prof. T. Takeshi, Dr. T. Kawamura, Dr. K. Onodera, and Prof. S. Tanaka for their guidance, support, and valuable suggestions on seismic modeling in Chapter 5. I also appreciate Assoc. Prof. H. Hasegawa for his valuable review of my JSPS fellowship application and suggestion in selecting my PhD theme. I am also thankful to Dr. S. Hasegawa and Dr. Y. Yamamoto for their assistance in developing the experimental setup for ultrasonic measurements at cryogenic temperatures. I also appreciate Prof. H. Kagi and Prof. Y. Takahashi for their assistance in performing chemical analyses of organic materials. Without their help, I could not have published my research paper. I am also grateful to Assoc. Prof. Y. Li for helping me perform chemical analyses, including HP-

LC and FT-IR equipped with a microscope. I would like to thank Dr. T. Manjo, Dr. H. Fukui, and Dr. A. Baron for their support during experiments at SPring-8. Additionally, I thank Mr. S. Yoshii and Mr. H. Tomioka for their guidance on how to use metalworking machines.

I also appreciate the insightful suggestions provided by Prof. T. Kadono regarding sintering, which helped broaden my perspective. I would also like to express my gratitude to Dr. O. Nisizawa for his patient assistance, valuable suggestions, and insightful lectures on the mindset needed for constructing experimental methodologies. I am also grateful to Assoc. Prof. M. Kodama for his dedicated assistance in characterizing the shape of Titan tholin using X-ray CT and USAXS. I am indebted to Assoc. Prof. K. Ohta for his valuable comments and support in constructing the experimental setup for ultrasonic measurements under cryogenic conditions. I would also like to express my gratitude to Assoc. Prof. T. Kodama for his kind support and suggestions not only on general circulation modeling of Titan but also on private life. I also appreciate Assoc. Prof. S. Kaneko for helping me use the Raman spectrometer in OFC. My thanks also go to Dr. K. Ichiyanagi for providing access to the Au coater in SPring-8. I am grateful to Mr. K. Aoshima for his help and guidance in constructing experimental setups.

I would also like to thank Prof. K. Kiyoshi for his mentorship and guidance in pursuing my career. I am grateful to Assoc. Prof. Y. Furukawa and Prof. Y. Kimura for their unwavering advice on my academic career path. I deeply appreciate the support and suggestions provided by Dr. W. B. Brinckerhoff, Dr. M. G. Trainer, Dr. R. Lorenz, Dr. R. Hodyss, Dr. S. Vance, and Dr. M. Panning for their critical reviews of my research ideas.

I would like to thank Dr. S. Tan for his encouragement and suggestions throughout my doctoral course. I sincerely appreciate Assist. Prof. Y. Ito for his continuous support and encouragement. I am also thankful to Assistant Professor Y. Endo for his encouragement and assistance with the experiments. I am also grateful to Assist. Prof. K. Ohno for his constructive criticism and encouragement. I am also grateful to Assist. Prof. S. Kadoya for his encouragement during my studies. I am also grateful to Assoc. Prof. H. Kurokawa, Dr. K. Sugiura, and Dr. K. Hamano for their valuable comments during seminars at ELSI. My thanks also go to Prof. S. Sugita, Prof. S. Tachibana, Assoc. Prof. A. Takigawa, and Dr. H. Tabata for their insightful feedback during another seminar. I also thank to Assoc. Prof. T. Hatakeyama for their valuable advice. Additionally, I would like to thank Prof. K. Nishida for his comment in a seminar, and Dr. N. Zhang and Dr. N. Noda for their comments on my publication.

Throughout my doctoral course, I was greatly encouraged by the students and researchers at ELSI and outside ELSI. I would like to express my gratitude to the members of the Sekine Lab, including Mr. H. Shozaki, Mr. S. Nozaki, Ms. M. Koga, Mr. M. Craddock, Mr. Y. Mizukami, and Mr. W. Salgado, as well as former members Dr. M. Yoda, Ms. S. Imamura, Mr. M. Sugiuchi, Mr. K. Taniguchi, and Mr. Y. Sadakane, along with other members of the GS

seminar. I am also thankful to the PMCHEF group members for their encouragement and support during my time at UTSA, which motivated me to complete my PhD dissertation. I would like to express my sincere gratitude to Ms. Y. Ochiai for her invaluable assistance and encouragement. I would also like to express my appreciation to Mr. S. Nozaki for all his help in writing this thesis. I am also thankful to Mr. W. Amada for kindly bringing me donuts while writing this thesis. I also appreciate Mr. H. Shozaki, Dr. Y. Hirakawa, Dr. Y. Masuda, Dr. D. Boulesteix, Ms. L. Lopes and Dr. E. Czaplinski for their encouragement and assistance throughout my PhD. journey.

Finally, I would like to express my appreciation to my family and Ms. K. R. Kawase for their support and warm encouragement.

Contents

Nomenclature

Symbol	Meaning
2θ	Scattered angle
A_m	Molar surface area
a	The spacing of the lattice plane
A_s	The energy of the phonon at $Q = \pi/a$
$A(f)$	Amplitude of the reflected wave
$A_0(f)$	Amplitude of the initial, artificial seismic wave from the top of the layers of organic sediments
A_N	Empirical constant for spherical grains
b	Width of the cantilever
B_s	The half of the spacing of the lattice plane
c	Speed of light
C_B	Empirical factor of mass flux of steady-state saltation
C_r	Reflection coefficient
d	Particle diameter
d_s	Spacing of the diffraction planes
d_r	Reflection depth
D_{250}	Reference diameter of 250 μm
$\mathrm{d}E$	Energy bandwidth
$\mathrm{d}\Omega$	Solid angle
E	Energy of X-ray
E^{-Wd}	Deby-Waller factor to account for bond strength of each atom
E_{break}	Breakup energy to break the bond between two grains (so-called monomer)
E_{sil}	Breakup energy of silicates
E_{surf}	Activation energy of surface energy
E_1	Energy of incident X-ray beam
E_2	Energy of scattered beam
E_a	Activation energy of longitudinal modulus
E_{surf}	Activation energy of surface energy
e	Elementary charge
$\boldsymbol{e}_d(Q,j)$	Normalized phonon eigenvector in the phonon in the mode j with phonon wavevector Q for atom d
$\boldsymbol{e}_1$	Polarization of X-ray beam before scattering

$\boldsymbol{e}_2$	Polarization of X-ray beam after scattering
$\boldsymbol{f}$	Frequency of phonon
$f_{\mathrm{d}}(Q)$	Atomic form factor of the d^{th} atom at position $\boldsymbol{r}_{\mathrm{d}}$
f_{LF}	Ratio of the Lorentzian function and the Gaussian function of resolution function,
f_{r}	Resonant frequency of the cantilever in the air
F_{coh}	Cohesion force
F_D	Drag force by the shear wind
F_G	Gravity force
F_{Φ}	Cohesive force between particles
g	Gravitational constant
G	Shear modulus of zero porosity
G_{Dry}	Effective shear modulus
G_{HM}	Effective shear modulus at the critical porosity ϕ_{c}
G_{sat}	Shear modulus of organic sediments filled with fluid in the pore
h	Planck constant
$\hbar$	Dirac constant
$\hbar\vec{Q}$	Momentum transfer
$\hbar\omega$	Energy transfer
$I_0(Q)$	Intensity of the elastic contribution
$I_{\mathrm{j}}(Q)$	Constant value not related to phonon energy in the inelastic contribution of j^{th} phonon mode
k	Spring constant between atoms
k_{s}	Spring constant of the cantilever
k_1	Wavevector of the incident X-ray
k_2	Wavevector of the scattered beam
k_{B}	Boltzmann constant
K	Bulk modulus of zero porosity
K_0, K_1	Modified Bessel functions of the third kind
K_{Dry}	Effective bulk modulus
K_{f}	Bulk modulus of the fluid in the pore
K_{HM}	Effective bulk modulus at the critical porosity ϕ_{c}
K_{sat}	Bulk modulus of organic sediments filled with fluid in the pore
L	Length of the cantilever
m	Mass of each atom
m_{mon}	Mass of each monomer

M	Longitudinal modulus (elastic modulus)
M_0	Longitudinal modulus (elastic modulus) at absolute zero
M_d	Mass of the d-th atom at position r_d
n	Coordination number
n_i	Integral number
P	Effective pressure
P_atm	Titan's surface pressure
Q	Wave number (momentum) of phonon
$\boldsymbol{Q}$	Wavevector of phonon
Q_0	Attenuation coefficient
Q_f	Quality factor of the cantilever in the air
Q_a	Quality factor of the sediment
Q_mass	Mass flux of sand, steady-state saltation mass flux
r_e	Classical electron radius
R_mon	Radius of each monomer
R	Radius of the material
R^*	Reduced contact radius
R_gas	Gas constant
S	Entropy
$S(Q, 0)$	Dynamical structure factor at zero-energy transfer
$S(Q, \omega)$	Dynamical structure factor
$S(Q, \omega_{Q,\mathrm{j}})$	Contribution of inelastic scattering by phonon in $S(\boldsymbol{Q}, \omega)$
T	Temperature
t_p	Travel time of p-wave
T_g	Glass transition temperature
T_m	Melting point
t_s	Travel time of s-wave
u^*	Saltation threshold wind speed
u_max	The predicted maximum wind speeds
v	Seismic wave velocity
v_frag	Fragmentation threshold velocity
v_2	Bulk velocity of the H_2O ice crust, or organic sediments with CH_4 aquifer
V_p	P-wave velocity
V_s	S-wave velocity

W_{coh}	Work of cohesion
x	The thickness of the sample
Y	Young's modulus
Y_{or}	Young's modulus of organics
Y_{sil}	Young's modulus of silicates
β	Average cohesive force between grains
β_{Earth}	Average cohesive force between grains on Earth
β_{Titan}	Average cohesive force between grains on Titan
γ	Cohesion coefficient
$\gamma(0)$	Surface energy at temperature of absolute zero
$\Gamma(Re)$	Hydrodynamic function
$\gamma(T)$	Surface energy at temperature T
γ_1, γ_2	Surface energy of different materials
γ_{or}	Surface energy of organics
γ_{sil}	Surface energy of silicates
γ_0	Surface energy at absolute zero
γ_{Earth}	Cohesion coefficient on Earth
γ_s	Surface energy of materials
γ_{Titan}	Cohesion coefficient on Titan
Γ_i^{LF}	Full width at half maximum (FWHM) in the Lorentzian function
$\Gamma_i(Re)$	Imaginary part of the hydrodynamic function
ΔQ	Momentum resolution
ΔR_{or}	Ratio of thickness of organic mantle over R (radius of each monomer)
Δt	Travel time of wave
ΔU_{or}	Binding energy of organic mantle
$\Delta\omega$	Offset of the peaks from the zero-energy transfer
ζ_0	Interatomic distance
η	Dynamic viscosity of the air
λ_E	Elasticity parameter
λ	Wavelength of X-ray
λ_p	Wavelength of phonon
μ	Linear absorption coefficient
ν	Poisson's ratio
ν_{or}	Poisson's ratio of organics
ν_{sil}	Poisson's ratio of silicate

ρ	Density
ρ_{B}	Bulk density of regolith
ρ_{or}	Density of organic mantle
ρ_{sil}	Density of silicate
ρ_1	Bulk density of the organic sediments
ρ_2	Bulk density of the H_2O ice crust or organic sediments with CH_4 aquifer
ρ_{atm}	Air density on Earth
ρ_{f}	Air density on Titan
ρ_{p}	Density of the particle
σ_i^{GF}	FWHM in the Gaussian function
Φ	Porosity
Φ_{c}	Critical porosity
ω	Angular frequency (energy) of phonon
$\omega_{Q,j}$	Phonon energy of j^{th} phonon mode at momentum transfer Q
ω_j	Energy of j^{th} phonon mode

Chapter 1. General Introduction

1.1. Titan: Its climate and surface environments

Titan, Saturn's largest moon, possesses a dense, N_2-rich atmosphere with liquid CH_4-based hydrological cycles on the surface (e.g., Hörst, 2017 and references therein). In the upper atmosphere of Titan, complex organic aerosols are formed from N_2 and CH_4 via photochemical reaction induced by solar UV and charged particles from Saturn's magnetosphere (e.g., Sagan et al., 1992). These aerosols are considered to settle in the atmosphere and eventually deposit on the surface (e.g., Rannou et al., 2016). The organic aerosols deposited on the surface would cover the icy surface, interacting with wind, and potentially liquid CH_4 (Barnes, 2015; Hirai et al., 2023). Through these interactions, organic aerosols would be a constitute of surface geomorphologic features, such as organic-rich dunes in the low latitude regions (Lorenz et al., 2006; Radebaugh et al., 2008; Rodriguez et al., 2014) and evaporites on Titan (Barnes et al., 2011; MacKenzie et al., 2014; MacKenzie & Barnes, 2016).

One of the fundamental questions on Titan's surface is how long this atmosphere-surface system has been maintained against the efficient CH_4 consumption by the atmospheric chemistry (e.g., Sotin et al., 2012; Hayes et al., 2018; Nixon et al., 2018). The current CH_4 in the atmosphere-surface system will be photochemically consumed in ~10^7 years (e.g., Yung et al., 1984; Wilson and Atreya, 2004), which should induce an atmospheric collapse due to a decline in the greenhouse effects (Lorenz et al., 1997; Charnay et al., 2014). CH_4 may have been replenished from the interior through degassing (e.g., Tobie et al., 2006); however, the detailed quantity and timing of the degassing have been largely unknown. Since CH_4 and N_2 in the atmosphere would be irreversibly consumed as deposition of organics, including organic aerosols and C_2H_6, by atmospheric chemistry, knowledge of the fate and inventory of organic aerosols on the surface is a key to understanding the duration and evolution of the current atmosphere-surface system. For instance, such knowledge of the fate of organic aerosols includes the processes by which aerosols are transported, where they would accumulate, and what physical and chemical alterations they undergo after the deposition. Knowledge of the inventory of organic aerosols includes how thick organic aerosols deposit on the low, middle, and high latitudes of Titan.

In this chapter, we review the geological characteristics of Titan's surface based on Cassini's observations (Sec. 1.1.1) and climate patterns for different latitudes (Sec. 1.1.2) based on both observations and numerical climate modeling. Then, we discuss the discrepancy in the distribution of deposited organic aerosols and climate patterns on Titan (Sec. 1.2). Finally, the objectives of the present study and structure of this thesis are summarized (Sec. 1.3).

1.1.1. Geomorphic mapping and its characteristics

Titan's surface exhibits a variety of geological units, including dunes, plains, labyrinths, hummocky, craters, and lakes and seas (Lopes et al., 2019) (Fig. 1.1). The northern polar regions with latitudes 55–90° are characterized by the presence of large seas (10^3–10^4 km^2 in area) and small lakes (10^2–10^3 km^2 in area) composed mostly of liquid hydrocarbons (Stofan et al., 2007; Hayes et al., 2008; Hayes et al., 2011; Sotin et al., 2012; Hayes, 2016; Hayes et al., 2017; Birch et al., 2017; Hayes et al., 2018). The existence of liquid CH_4 is confirmed by radar-dark features, high emissivity and lacustrine morphologies based on K_u band (wavelength = 2.16 cm) Synthetic Aperture Radar (SAR) images. Morphologies of shorelines of large seas in the northern polar regions are characterized by drowned river valleys (Stofan et al., 2007) and abrupt termini of large river valleys (Aharonson et al., 2014), suggesting that the liquid level changes over a long-period CH_4 cycle (Hayes, 2016). Small lakes show unique morphology so-called sharp-edged depression (SEDs), which are characterized by relatively flat floors, steep walls, hundred-meter-scale of depth and rims, and absence of inflow and outflow channels. Based on altimetry observations, the liquid surface of each large sea shows a single equipotential surface (Hayes, 2016). The elevations of floors of empty lakes within the drainage basin tend to be higher than the liquid surface of lakes nearby and large seas (Hayes et al., 2017). The elevations of large seas are also the same within the observation resolution (Hayes, 2016). These observations infer the presence of local subsurface connectivity of lakes and seas, such as ground liquid CH_4 (Hayes, 2016; Hayes et al., 2017). Indeed, the distribution of clouds is well-explained with a general circulation model (GCM) assuming subsurface CH_4 table above 60° latitude (Turtle et al., 2018; Faulk et al., 2017). In the southern polar region, there is only one large lake (1.6×10^4 km^2 in area) (Hayes, et al., 2018), which is in contrast with the presence of multiple large seas and a number of small lakes in the northern pole region. This lake in the southern pole region is surrounded by dry broad depression of paleo basins, characterized by paleo shorelines, abandoned delta (Wall et al., 2010), and channels (Hayes, 2016), suggesting that the presence of more amounts of liquid in the past. Overall, the high latitude (60–90°) regions are geologically characterized as lakes, seas, and wetland of liquid CH_4 and other hydrocarbons.

Titan's middle latitude regions (30–60° in latitude) are mostly composed of three geological units; plains, hummocky terrains, and labyrinth terrains. Plains are mainly called as undifferentiated terrains of radar dark and uniform features without major topographical relief (Lopes et al., 2016). Hummocky terrains are characterized as radar-bright, mountain chains, and isolated terrains. Hummocky terrains are usually located at topographic high (Malaska et al., 2016). Labyrinth terrains are characterized as dissected, elevated terrains with high density of valleys (Malaska et al., 2020).

The surface materials of plains, hummocky terrains, and labyrinth terrains at middle latitudes have been also investigated with the Visual and Infrared Mapping Spectrometer (VIMS) (e.g., Solomonidou et al., 2018) and Radar radiometry (e.g., Janssen et al., 2016). Plains in higher latitude regions (30–50°N) at middle latitudes are suggested to be covered with a thin layer of organic materials on the H_2O ice crust based on the recent VIMS observation (Solomonidou et al., 2018); whereas, plains in relatively low-latitude regions at middle latitudes would be largely covered with organic materials based on high radar emissivity (Solomonidou et al., 2018; Malaska et al., 2016). This suggests that there are regional differences in the abundance of organic materials on plains of middle latitudes. Low radar emissivity feature of hummocky terrains suggests that these terrains are largely covered with H_2O ice of the icy crust with less organic materials on the surface (Janssen et al., 2016). The result of VIMS observation supports the conclusions of H_2O-rich surface of hummocky terrains (Barnes et al., 2007). VIMS observation suggests that the surface of labyrinth is also covered with H_2O ice (Solomonidou et al., 2018). Higher radar emissivity of labyrinth suggests the presence of organic materials on labyrinth (Lopes et al., 2016; Janssen et al., 2016; Malaska et al., 2020). To summarize, there are significant regional differences in an abundance of organic materials on the surface depending on the geological units and latitudes. At middle latitudes, H_2O ice together with organic materials is suggested to be exposed in labyrinth, hummocky terrains, and plains in higher latitude regions in the middle latitudes (Fig. 1.1). Plains in lower latitude regions in middle latitudes are considered to be covered with organic materials with less H_2O ice exposure, although the depth of organics is unclear.

In the low latitude regions (0–30° in latitudes), vast dune fields dominate the surface (Lorenz et al., 2006; Radebaugh et al., 2008; Rodriguez et al., 2014). The dunes are characterized as dark-brown spectra in atmospheric window wavelength regions at 5, 2, 1.6, and 1.3 -μm taken with Visual and Infrared Mapping Spectrometer (VIMS) (Barnes et al., 2007; Rodriguez et al., 2014; Soderblom et al., 2007). The spectral features of dark-brown show very weak absorption of 1.6 -μm and 2.0 -μm of H_2O-ice, suggesting that organic materials are the major constitutes of dunes (Soderblom et al., 2007). The Cassini spacecraft also performed active radar investigations for dunes during the flybys (Elachi et al., 2005). Radar dark features with low dielectric conductivity are attributed to weakly polarized structures of dune materials, which are consistent with organic materials rather than H_2O ice (Lorenz et al., 2006). Titan's equatorial dunes would reach heights of hundreds of meters and extend for several hundred kilometers (Lorenz et al., 2006). On the other hand, the interdune areas show the different IR spectra (dark-blue) and emissivity compared to dunes, suggesting that the interdune areas are sand-free areas (Bonnefoy et al., 2016). The dunes are oriented in an eastward, longitudinal direction (Lorenz & Radebaugh, 2009; Malaska et al., 2016). Longitudinal dunes are formed by winds from two different directions (i.e., winds from northwest and southwest) (Wasson and Hyde, 1983; Pye

and Tsoar, 1990; Lancaster, 1995). In addition to dunes, hummocky terrains exist in the low latitude regions. The largest hummocky terrain at low latitudes is called Xanadu. Similar to hummocky terrains at middle latitudes, hummocky terrains at low latitudes exhibit H_2O ice absorption features at 2.8 μm wavelength obtained by VIMS (Barnes et al., 2007). Based on these observations of dunes and hummocky, organic materials seem to be accumulated in the low latitude regions, forming thick aeolian sediments of dunes. Comparing the middle to the low latitudes of Titan, the surface organic materials would have been affected by winds at low latitudes.

1.1.2. Climate and wind patterns

As on Earth, Titan's obliquity (~26.7°) results in seasonal weather cycles. However, the weak Coriolis force due to Titan's slow rotation (~16 days) and Titan's low gravity leads to a single cell of Hadley circulation from pole to pole during summer/winter (Fig. 1.2) (e.g., Mitchell & Lora, 2016). At equinoxes, this Hadley circulation cell would be divided into two, in which air upwells at the equator and transports toward the poles (Fig. 1.2) (e.g., Mitchell & Lora, 2016). Along with this circulation, the intertropical convergence zone (ITCZ) on Titan migrates from one pole to the other pole throughout one Titan year (e.g., Mitchell and Lora, 2016; Hörst, 2017). During the summer of Titan, high insolation evaporates liquid CH_4 in the summer pole and upwells them into the atmosphere, leading to the formation of convective clouds and rains (Fig. 1.2) (Lora et al., 2015). In the winter pole, liquid CH_4 would become more thermodynamically stable due to colder temperatures (Aharonson et al., 2009; Lora et al., 2015). Both evaporation of liquid CH_4 and the atmospheric circulation would result in transport of liquid CH_4 to the winter pole. As a result, the climate of the polar regions is generally wet with evaporation and precipitation of liquid CH_4 (Aharonson et al., 2009; Lora et al., 2015). Owing to this climate, organic aerosols deposited at high latitudes would be transported by flow of liquid CH_4 and be altered with liquid CH_4 on the surface (Hirai et al., 2023).

In contrast to the high latitudes, Titan's middle to low latitude regions (0–60° in latitude) are considered to be generally arid in climate, because dried air generated at the colder polar regions is transported to these latitudes through pole-to-pole atmospheric circulation (Fig. 1.2) (Aharonson et al., 2009). In the middle to low latitudes, precipitation of CH_4 is expected to be available only at the equinoxes, when the ITCZ temporally passes these regions upon the division of one Hadley cell into two. In the low latitudes (0–30° in latitude), CH_4 storms would be grown due to interactions of multiple convective clouds (Fig. 1.2), which are formed by wind gust induced by other convective clouds and downdrafts (Charnay et al., 2015). Titan's linear dunes could be formed by CH_4 storm, whose wind directions are slightly converging to the equator (<12°N/S latitudes) and diverging from the equator (>12°N/S latitudes) (Charnay et al.,

2015). along with mean transport direction, called the resultant drift direction (RDD), in limited amount of sediment (Charnay et al., 2015).

Due to arid climates in the middle and low latitude regions, winds may play an important role in determining the distribution of deposited organic aerosols. The wind on the surface is, however, poorly constrained based on observations. Direct observations of wind on Titan have been conducted based on the measurements for doppler shifts in the emission of atmospheric components and tracking cloud movement (Folkner et al., 2006; Kostiuk et al., 2001; 2005; 2006; 2010; Luz et al., 2005; 2006; Moreno et al., 2005; Bouchez and Brown, 2005; Porco et al., 2005; Turtle et al., 2011); however, the wind on the surface has been poorly constrained. According to the lack of observations, wind speed and direction on the surface are theoretically investigated using general circulation models (GCMs) (Tokano, 2008; 2010; Charnay et al., 2015; Lebonnois et al., 2012; Lora et al., 2019). These models generally show that there are two types of seasonal winds in the summer, which are induced by differences in insolation and by mechanical forces from Saturn's tides, respectively. The direction of the seasonal wind induced by insolation flows from the winter pole to the summer pole (e.g., Tokano, 2010); whereas the tidal wind flows from the middle latitudes toward the equator (e.g., Tokano, 2002; 2008) (Fig. 1.2). The mean wind speeds near the surface predicted by GCMs are $(1–2) \times 10^{-2}$ m/s at the middle latitudes and $(2–3) \times 10^{-2}$ m/s at low latitudes (Tokano, 2008). Easterly strong wind with a speed of approximately 4×10^{-1} m/s near the surface can occur upon CH_4 storms at low latitudes during the equinox (Charnay et al., 2015; Tokano, 2010).

1.2. Discrepancy between geomorphic characteristics and climate

The geomorphologic characteristics of Titan (Sec. 1.1.1) (Fig. 1.1) are generally consistent with the climate pattern predicted by the general circulation models (Sec. 1.1.2) (Fig. 1.2). First, the existence of dunes at low latitudes with ± 30° indicates an arid climate (Mitchell and Lora, 2016; Lora et al., 2015; Lora and Ádámkovics, 2017). Formation of dunes requires that cohesion force of (organic) sands is sufficiently low to saltate by wind (Yu et al., 2017; Comola et al., 2022), which generally needs dry surface of (organic) sand grains. Second, the concentration of seas and lakes in the northern (and southern) polar regions shows good agreement with wet and humid climates in the high latitude regions (Mitchell and Lora, 2016; Lora et al., 2015; Lora and Ádámkovics, 2017).

However, there is also a discrepancy between the geomorphic characteristics and climate patterns on Titan; that is, the climate models predict that both middle and low latitude regions are arid; meanwhile, thick aeolian organic sediments (i.e., dunes) are present only at low latitudes.

At middle latitudes, the amounts of organic materials on the surface would vary depending on the locations and geological units. Previous work proposed that the difference in organic inventory between the middle and low latitudes could be explained by a combination of sintering and erosion of organic particles (Lapôtore et al., 2022). In this model, the balance between the size growth of organic sand due to sintering and the size reduction due to physical erosion (i.e., ablation) may lead to continuous sand transport in the low latitude regions. In contrast, in the mid latitude regions, high CH_4 humidity would trap particles and promote sintering, which results in the inhibition of transport. However, as mentioned above, the middle latitude regions expose H_2O ice on the surface together with organic materials (Solomonidou et al., 2018). No thick organic sediments have been found in the middle latitude regions (Solomonidou et al., 2018). These observations suggest that deposited organic aerosols at the middle latitudes may have been transported spontaneously, rather than trapping at the location where organic aerosols deposit at middle latitudes. In addition, the moisture of mid-latitude regions would not always be higher compared to low-latitude regions based on the results of GCMs (Mitchell and Lora, 2016; Lora and Ádámkovics, 2017). Thereby, these facts may call for any mechanisms that can transport deposited organic aerosols at middle latitude.

As discussed later in this section, previous experimental and theoretical studies suggested that the speed of seasonal surface winds on Titan might be insufficient to transport organic materials, except for low-latitude CH_4 storm at the equinox (Burr et al., 2015; Comola et al., 2022). Sand particles are floated in air by wind, which is called as saltation. Sand particles, including organic materials, can saltate when wind speed exceeds the saltation threshold velocity. This threshold velocity is derived from the force balance exerted on a grain (Fig. 1.3a), which occurs when the aerodynamic drag force exceeds a sum of gravitational and interparticle forces (Bagnold, 1941; Greeley and Iversen, 1985; Shao and Lu, 2000; Kok, 2012) (Fig. 1.3a). Based on this force balance, the following equation of the saltation threshold velocity, u_*, can be obtained (Shao and Lu, 2000; Comola et al., 2022),

$$u_* = \sqrt{A_N \left(\frac{\rho_p}{\rho_f} g d + \frac{\gamma}{\rho_f d} \right)}, \quad (1.1)$$

where A_N is an empirical constant (A_N = 0.0123 for spherical grains: Iversen & White, 1982), g is the gravitational constant (g = 1.35 m s^{-2} for Titan's surface), d is the particle diameter, ρ_f is the air density (ρ_f = 5.2 kg m^{-3} at Titan's surface), ρ_p is the density of the particle (ρ_p = 950 ± 450 kg m^{-3} assuming that organic sands on Titan are composed of organic aerosol analogs (Titan tholin) (Hörst and Tolbert, 2013; Imanaka et al., 2012; He et al., 2017)), and γ is a cohesion coefficient. Following the previous study (Comola et al., 2022), γ on Titan (γ_{Titan}) can be derived from the following equation,

$$\frac{\gamma_{\mathrm{Titan}}}{\beta_{\mathrm{Titan}}} = \frac{\gamma_{\mathrm{Earth}}}{\beta_{\mathrm{Earth}}}, \tag{1.2}$$

$$\gamma \propto \beta = F_{\phi}/d\,, \tag{1.3}$$

where β_{Earth} and β_{Titan} are the average cohesive force between grains on Earth and Titan, respectively, γ_{Earth} is a cohesion coefficient on Earth, and F_{Φ} is the cohesive force between particles. Here, the ratio of the cohesion coefficient γ to the average cohesive force β between grains is assumed to be equal on Earth and Titan because the proportionality constant between γ and β is unknown, as suggested by Comola et al. (2022). $\gamma_{\mathrm{Earth}} \approx 0.33 \pm 0.17$ mN m^{-1} and $\beta_{\mathrm{Earth}} \approx 1.2$ mN m^{-1} are estimated based on measurements of both threshold wind speed for quartz sand on Earth (Shao & Lu, 2000) and a study on adhesion of particles (Corn, 1961). $\beta_{\mathrm{Titan}} \approx 27 \pm 20$ mN m^{-1} is obtained based on cohesion force measurements of Titan tholin at room temperature, that is $F_{\phi} = 0.8 \pm 0.6$ μN for 30 μm-size organic particles (Yu et al., 2017). The cohesion coefficient of organic sand on Titan is estimated to be $\gamma_{\mathrm{Titan}} \approx 7.3 \pm 6.7$ mN m^{-1} with Eq. (1.2) and considering error propagation. Based on Eq. (1.1), the saltation threshold velocity, u_*, on Titan can be calculated (Fig. 1.3b). Comparing with the suggested mean wind velocity at low and middle latitudes ((1–3) × 10^{-2} m/s: see Sec. 1.1.2) (Tokano, 2008), organic sands on Titan may be difficult to saltate by seasonal winds induced by insolation and tidal force (Comola et al., 2022). On the other hand, CH_4 storms at low latitudes with wind velocity of ~ 4 × 10^{-1} m/s would saltate organic sands on Titan's surface (Charnay et al., 2015; Lucas et al., 2014; Tokano, 2010). However, these studies fail to account for the saltation of organic sands in the middle latitude regions, which is necessary to explain the absence of thick organic sediment layers in these areas. This limitation is primarily due to the predicted highly cohesive properties of organic materials (Yu et al., 2017), which inhibit saltation and sand transport under the current environmental conditions on Titan.

However, cohesive forces may exhibit temperature and compositional dependence, as cohesion is determined by the surface energy and the contact area between materials. Cohesion mechanisms can be broadly categorized as (1) mechanical interlocking due to surface roughness and irregularities, (2) molecular interactions such as dipole-dipole interactions or van der Waals forces, which are defined by the surface energy of the material, and (3) other mechanisms including diffusion or interdiffusion, electrostatic attraction, chemical bonding, and weak boundary layer effects (e.g., Baldan, 2012; Awaja et al., 2009). Elasticity, a fundamental material property that quantifies a material's resistance to deformation under applied stress, plays a critical role in determining the contact mechanics at the interface, thereby influencing both the effective contact area and the resultant cohesive forces.

Organic aerosols on Titan are believed to be complex, amorphous organic materials containing C, H, and N (e.g., McKay et al., 2001; Israël et al., 2005). Additionally, as discussed

later, different chemical processes on Titan's surface could produce amorphous organic materials with varying chemical compositions (see Chapter 2). Previous studies on the surface energy of amorphous carbon films and simulated organic aerosols in planetary atmospheres have shown surface energy values in the range of 10–100 mJ m^{-2} (e.g., Rahman et al., 2011; Yu et al., 2017; 2020; 2021; Li et al., 2022). However, the temperature dependence of the surface energy of these amorphous organic materials has never been investigated. Given that the surface energies of other materials tend to increase at lower temperatures, as observed in metals (McLean & Mykura, 1966; Zhang et al., 2019) and silicates (Lai et al., 2020), it is plausible that a similar trend might be observed for Titan's organic materials.

The elasticity of amorphous organic materials has been studied in analogous substances such as graphite and amorphous carbon films (Ferrari et al., 1999; Mason & Knibbs, 1967; Schultrich et al., 1996; Qasim et al., 2019; Lu & Komvopoulos, 1999). For instance, increased nitrogen or oxygen content reduces elasticity (Qasim et al., 2019; Lu & Komvopoulos, 1999), while higher densities or increased sp3-bond fractions enhance elasticity (Schultrich et al., 1996; Xu et al., 1997). These behaviors, however, result in elasticity values significantly higher (by two to three orders of magnitude) than those observed for Titan's tholin (Yu et al., 2018). Furthermore, the elasticity of amorphous organic materials is known to vary significantly above and below their glass transition temperature (e.g., Gilbert et al., 1986). Nevertheless, the temperature dependence of the elasticity of Titan tholin remains poorly understood.

Thus, the cohesive properties of Titan's surface organics under low-temperature conditions are still unclear. Understanding the cohesive forces of Titan's organic materials is essential for constraining surface processes such as organic sand transport on Titan. Therefore, it is crucial to investigate the temperature and compositional dependence of the physical properties of Titan's organic analog materials.

1.3. Objectives of this thesis

The objectives of the present study are to investigate the temperature and chemical structure dependence of both surface energy (cohesion force) and elasticity (Young's modulus and Poisson's ratio) of organic material analogs on Titan. The present study initially produces Titan's organic sand analogs and characterizes their chemical structure based on multiple chemical analyses (Chapter 2). Then, the present study investigates the cohesion force of organic materials at different temperatures using an atomic force microscope (AFM) to obtain the surface energy (Chapter 3). We also perform synchrotron radiation X-ray experiments and ultrasonic wave experiments to measure elastic wave velocities of the organic materials to determine the

elasticity (Chapter 4). Using the obtained cohesion force and surface energy, the present study discusses the saltation threshold velocity, u_*, of organic particles on Titan (Chapter 5). Then, we discuss the fate of deposited organic aerosols in the middle latitude regions on Titan and explain why thick organic sediments are absent in these regions (Chapter 5). Our results shown in Chapter 5 suggest that organic aerosols deposited at middle latitudes can saltate by seasonal winds and accumulate at low-latitude regions given the temperature dependence of surface energy. To prove our hypothesis, the on-site measurements of the thickness of organic sediments at Titan's low and middle latitudes by future missions are necessary. Our measurements of elastic wave velocities at low temperatures are essential not only to obtain elasticity of organic materials, but also to evaluate the ability of seismic measurements on Titan in future missions, including NASA's *Dragonfly* mission. In particular, at middle latitudes, there may be a significant regional difference in the amount of organic materials on the surface (labyrinth, hummocky, and plains: Sec. 1.1.1). The thickness of organic materials on plains at middle latitudes is largely unknown; however, revealing the inventory of organic materials on plains is essential to estimate the duration of current environments with a thick atmosphere and liquid CH_4 cycles. We also discuss the detection limit of depths of organic sediments in shallow subsurface with active seismic measurements assuming the seismometer of the Dragonfly Geophysics and Meteorology Package (DraGMet) (Chapter 5). Finally, we discuss the transport and accumulation of organic sands on Titan (Chapter 6). The cohesive properties of organic materials are also important for discussing the collisional growth of both dust particles in the protoplanetary disks and organic aerosols in reducing atmospheres of early Earth and exoplanets. We also discuss our future perspectives of this thesis (Chapter 6).

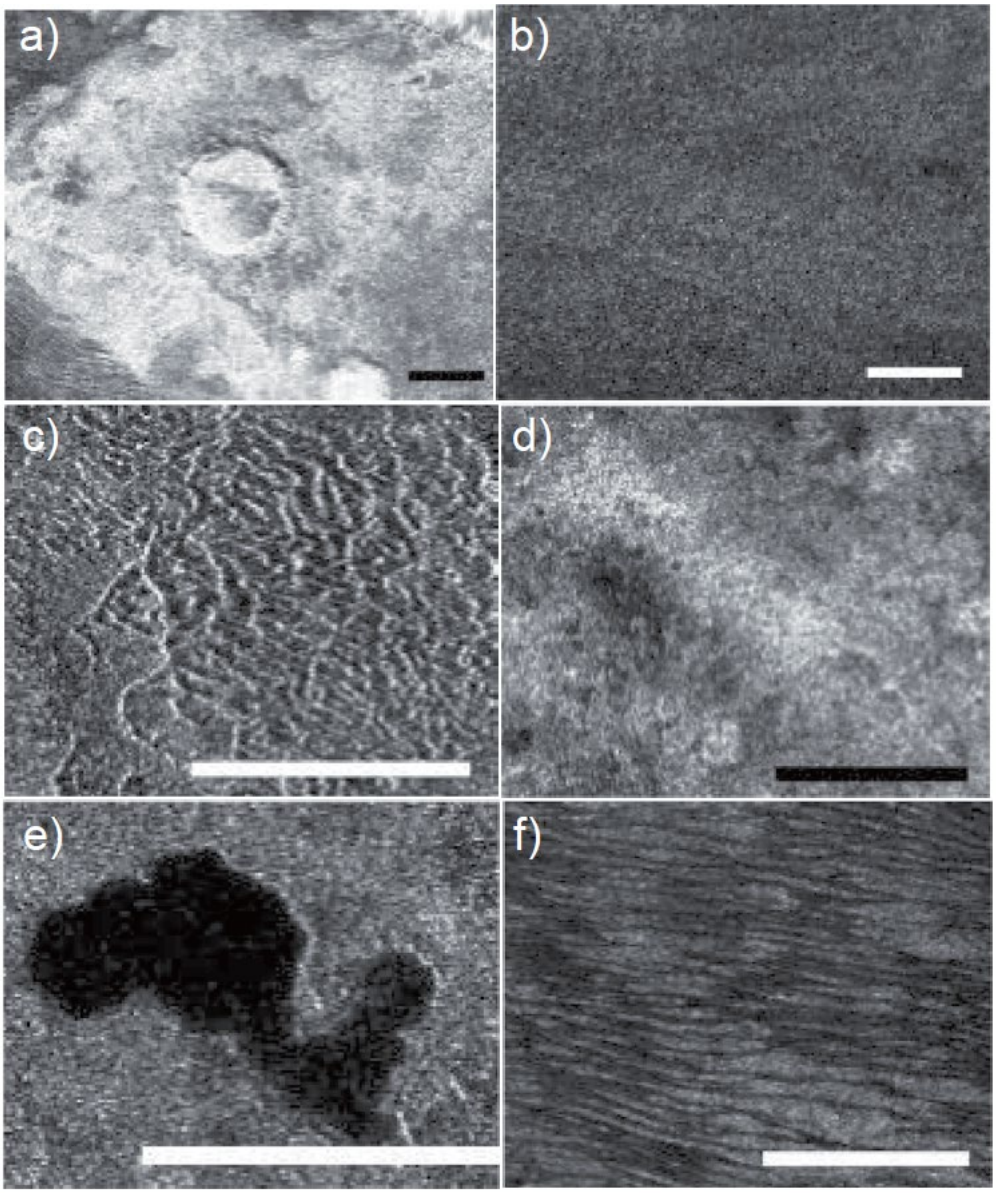

Figure 1.1 Typical SAR images of main geomorphological units on Titan including a) crater, b) plains, c) labyrinth, d) hummocky, e) lake, and f) dunes, shown in Fig.1 in Lopes et al. (2019). Each scale bar indicates 50 km.

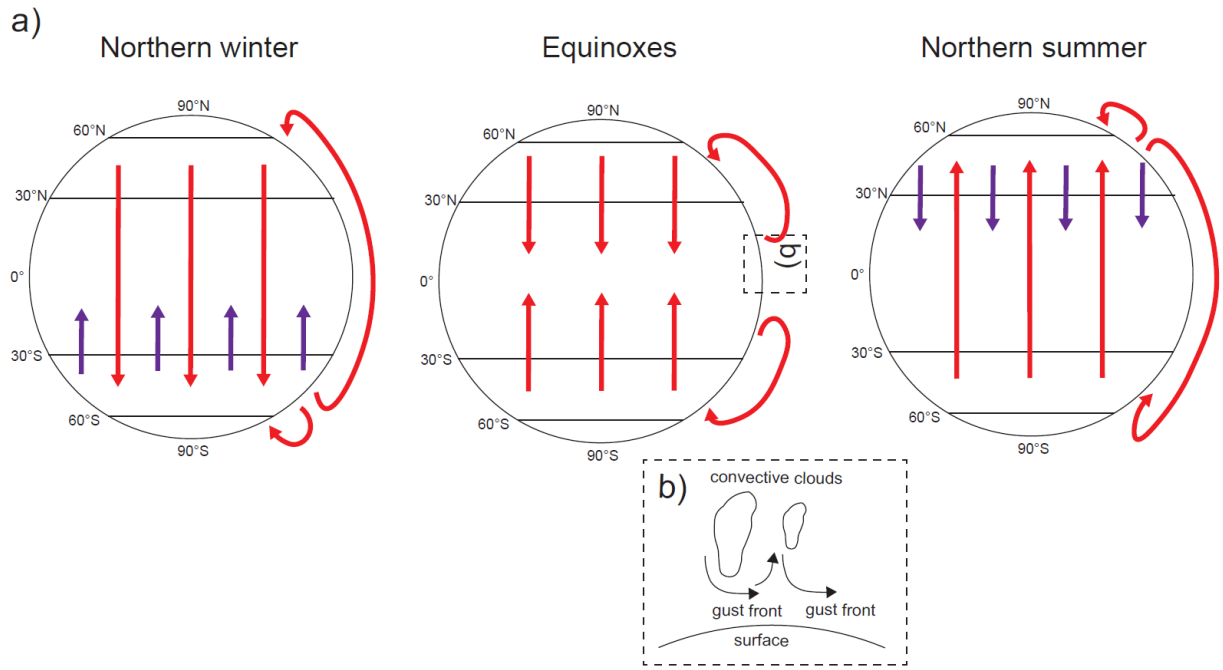

Figure 1.2 (a) Schematic illustrations of Titan's climates at northern winter, equinoxes and northern summer, respectively. Red arrows indicate the direction of Hadley circulation. Purple arrows indicate the direction of tidal wind in the summer at each hemisphere. (b) Schematic illustration of formation of gust wind at CH_4 storm during equinoxes as indicated by dashed box in (a). Gust wind formed with convective clouds induces formation of another convective clouds.

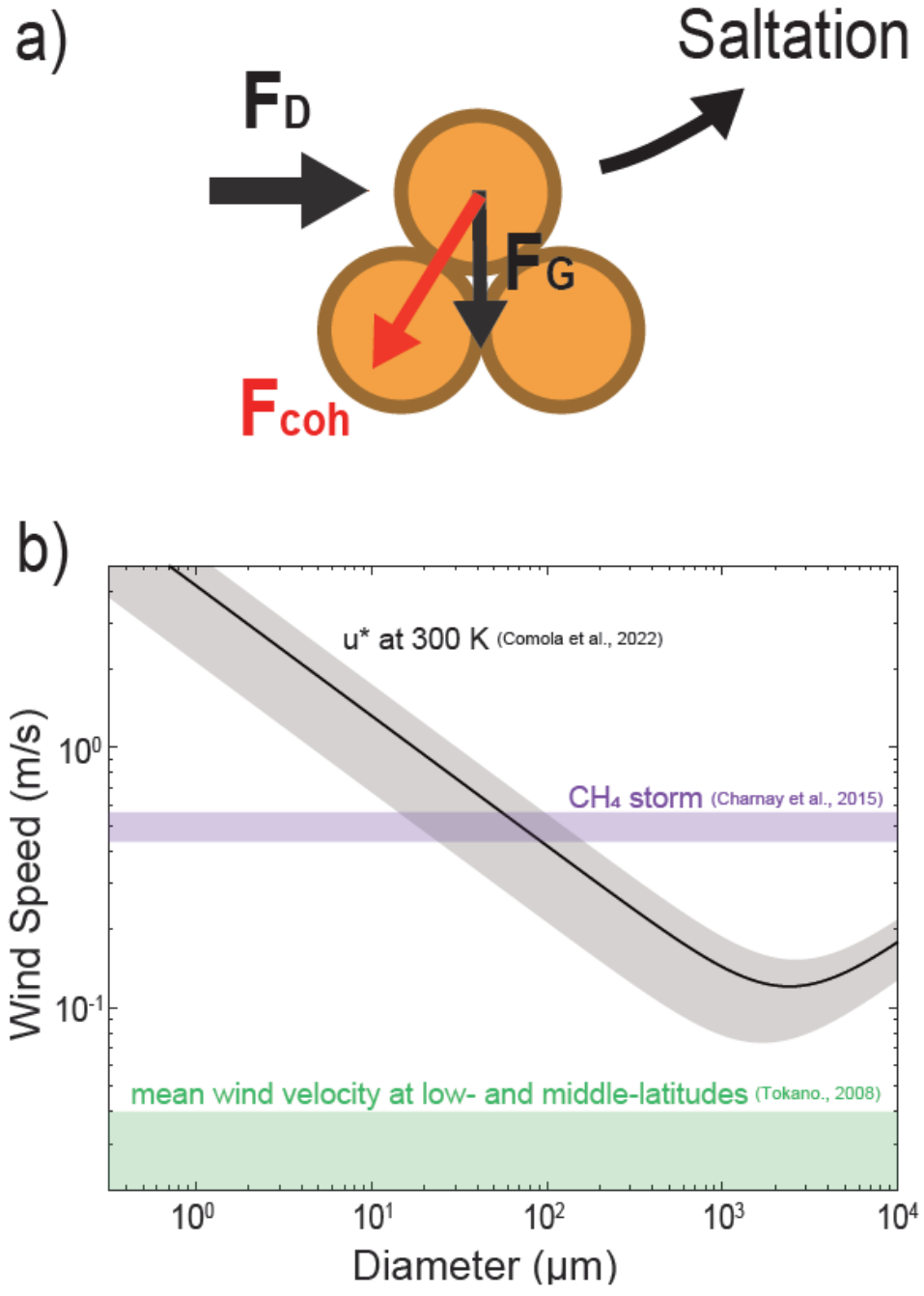

Figure 1.3. (a) Schematic diagram of the forces exerted on a sand particle resting on other particles. The black allow coincide with F_G indicates the gravity force. The red allow coincide with F_{coh} indicates the cohesive force. The black allow coincide with F_D indicates the drag force by the shear wind. (b) The u^* required to saltate the sticky organic particles on Titan (black curve with error). The green region indicates mean velocities on the surface of the equatorial region on Titan (Tokano, 2008). How u^* would be changed given the temperature and compositional dependence of cohesiveness is not understood.

Chapter 2. Characterization of laboratory analogs of Titan's organic materials used in the present study

2.1. Objectives of Chapter 2

The objective of this chapter is to describe the chemical structure and morphology of organic materials used in the present study.

One of organic materials on Titan is organic aerosols formed in Titan's atmosphere (Waite et al., 2007). After a fall in the atmosphere, these organic aerosols would deposit on the surface of Titan. Another is the evaporite appeared after evaporation of liquid CH_4 on Titan (Barnes et al., 2011; MacKenzie et al., 2014). Wet-and-dry cycles of liquid CH_4 on Titan may have altered deposited organic aerosols through dissolution of a soluble part and precipitated as evaporites (Hirai et al., 2023). Organic materials on Titan could also include complex organic matter formed through hydrothermal reactions induced by hypervelocity impacts (Artemieva and Lunine, 2003). Hypervelocity impacts on Titan could have induced melting of icy crust at the impact site, which can promote hydrothermal reactions near the surface. If the icy crust contains simple cometary organic molecules, such as NH_3 and HCHO, complex organic materials would be formed through the impact-induced hydrothermal reactions (Cody et al., 2011; Kebukawa et al., 2013).

The present study used three types of organic materials; 1) laboratory analogs of organic aerosols (Titan tholin: Khare et al., 1984; Imanaka et al., 2004; Sekine et al., 2008; Hirai et al., 2023), 2) laboratory analogs of evaporites formed by alteration of Titan tholin with liquid CH_4 (hereafter, we call this as altered tholin: Hirai et al., 2023), and 3) complex organic materials formed by hydrothermal reactions (hereafter, we call this as hydrothermal organics: Cody et al., 2011; Kebukawa et al., 2013; Sekine et al., 2017). In Sec. 2.2, we describe the methodology of formation of these organic materials, chemical analyses, and morphological observations. The results of chemical analyses and morphological observations are reported in Sec. 2.3. In Sec. 2.3., we also discuss the chemical structure of the organic analogs based on the comparison with other organic materials reported in previous studies.

2.2 Methods

This section describes the methodologies of formation of laboratory organic analogs (Sec. 2.2.1), the morphological observations (Sec. 2.2.2), and the chemical analyses (Sec. 2.2.3), respectively.

2.2.1. Sample preparation

2.2.1.1. Titan tholin formation

A variety of Titan tholin has been formed under different experimental conditions such as energy source (ultraviolet (UV) light, cold plasma, and discharge), temperature (room temperature to low temperatures), pressure (1 bar to 10 Pa), and composition of initial gas mixtures (N_2/CH_4 ratio) (e.g., Cable et al., 2012 and references therein). In the present study, Titan tholin was formed by cold plasma irradiation onto a gas mixture of N_2 and CH_4 (N_2/CH_4 = 90/10), following the experimental conditions developed by Khare et al. (1984). This was because the optical constant, IR spectra and pyrolysis products of Titan tholin formed by cold plasma irradiation are in general consistent with observations of Titan's aerosol by Voyager and Huygens probe (e.g., McKay et al., 1989; Israël et al., 2005; Coll et al., 2013). Cold plasma irradiation simulates bombardment of charged particles and UV irradiation, which are the energy source of photochemical reactions in Titan's atmosphere (e.g., Khare et al., 1984; Cable et al., 2012 and references therein).

Figure 2.1 shows a schematic illustration and picture of the reaction chamber for Titan tholin formation. A pre-mixed CH_4/N_2 gas mixture (10.1% (CH_4): 89.9% (N_2) by volume; Suzuki Shokan Inc.) was introduced into a quartz glass tube at a flow rate of 2.4 standard cm^3 min^{-1} (sccm) using a mass-flow controller (KOFLOC3200, Kofloc Inc.). Gas pressure inside the quartz tube was maintained at ~200 Pa, as measured using a transducer gauge (ConvecTorr gauge, Agilent Inc.). Cold plasma irradiation onto the introduced gas mixture was performed using a copper coil cooled with water circulation system (LTC-450α, AXEL Inc.) and equipped with matching networks, a 13.56 MHz RF power supply (Nihon Koshuha Inc.) at 80 W.

With the cold plasma irradiation onto N_2/CH_4 gas mixtures, Titan tholin was formed as both films and particles in our experiments (see Sec. 2.3.1 below). Films of Titan tholin were produced on the wall of the quartz tube, where cold plasma irradiation occurred. Similar films of Titan tholin were also reported previously (Imanaka et al., 2004; Sekine et al., 2008). Given the flat surface of films of Titan tholin (see Sec. 2.3.1 below), they were grown on the wall by heterogeneous additions of C/N-bearing radicals and molecules to the surface of Titan tholin (Sekine et al., 2008; Hong et al., 2018). Particles of Titan tholin were collected in a cold trap, allocated at the downstream of cold plasma irradiation. Similar particles of Titan tholin were

generated in cold plasma irradiations onto C_2H_2-containing gas mixtures (Clarke and Ferris, 1997). These particles would be generated by polymerization of gas molecules and growth by addition of radicals and molecules on the surface in the gas phase (Clarke and Ferris, 1997).

To estimate the surface energy and cohesion force of organic materials, we used films of Titan tholin for an atomic force microscope (AFM) analysis because AFM analysis required flat surface of sample (see Chapter 3 in detail). In AFM measurements, a cohesion force between a cantilever and materials was measured (e.g., Derjaguin et al., 1999; Johnson et al., 1971). To measure cohesion force between organic materials, we covered Si wafer substrates (Figure 2.4a; ~5 × ~5 mm; thickness 0.5 mm; SI-500443, Niraco Inc.) and cantilevers with Si tip (~10 nm tip diameter) (Figure 2.4b; SI-DF3-A, Seiko Instruments Inc.) with films of Titan tholin. To this end, Si wafer substrates and cantilevers were placed in the glass tube. A CaF_2 optical window (diameter 10 mm; thickness 0.5 mm; IR System Inc.) was also set on the quartz tube for IR transmittance analysis of the sample. After 100 mins of plasma irradiation, the Si wafer substrates, cantilevers, and CaF_2 window were coated with thin films of Titan tholin (see Sec. 2.3.1 below). The Si wafer substrate, cantilevers, and CaF_2 window were collected and stored in a desiccator until the analyses. After the AFM analysis, the surface of Si wafer substrates and cantilevers with Titan tholin were observed using a field emission-scanning electron microscope (FE-SEM) and AFM.

To measure the elastic wave velocities (Chapter 4), we used particles of Titan tholin because the elastic wave velocity measurements need a large amount of sample (~100 mg), and because particles of Titan tholin were generated in larger quantities than films. In the glass trap, Al foil tips (~5 × ~5 mm; thickness 0.5 mm; Niraco Inc.) were placed to effectively trap aerosol particles of Titan tholin flown with the reacted gas mixtures. After a total of 177 hours of irradiation, a total of ~170 mg of particles was collected. Titan tholin particles were stored into a glass vial in a desiccator.

2.2.1.2. Altered tholin formation

The chemical composition of organic evaporites on Titan has been poorly understood due to their limited spectral features, which are insufficient to identify the compounds that constitute the evaporites (MacKenzie et al., 2016). Theoretical studies on the chemical composition of Titan's lakes have predicted that simple hydrocarbons such as C_2H_2 and C_4H_{10} are responsible based on the ground-level atmospheric compounds and considering thermodynamic equilibria (Cordier et al., 2009; 2013; Glein & Shock, 2013; Tan et al., 2013). On the other hand, laboratory experiments have indicated that Titan's organic aerosols could be dissolved in non-polar solvent (Carrasco et al., 2009; He & Smith., 2014; Maillard et al., 2018) and even in cryogenic liquid CH_4 (Hirai et al. 2023). In the present study, Titan's evaporite analog materials

were produced by soaking Titan tholin into liquid CH_4, followed by the evaporation of the liquid CH_4 solution, representing one possible pathway for the formation of evaporites on Titan.

Figure 2.2 shows a schematic illustration and picture of the experiments that form altered tholin, which was developed in the previous work of the present study (Hirai et al., 2023). Si wafer substrates coated with films of Titan tholin were set on the dent of the cryo-chamber (Fig. 2.2b). Then, the cryo-chamber was evacuated to a pressure ~1 Pa with a rotary pump (GLD-051, ULVAC Inc.). After evacuation, the cryo-chamber was cooled to 110 K by immersing itself into a liquid N_2 bath. Subsequently, CH_4 gas (purity 99.999%; Suzuki Shokan Inc.) was into the cryo-chamber. The introduction of CH_4 results in a temperature decrease to ~90 K because the bellows between the bottom part of the cryochamber and the top part of the flange extended due to gas pressure, which thermally isolated from the bottom part from the top flange. Then, liquid CH_4 was produced at the bottom of the cryo-chamber (Fig. 2.2c). The temperature inside the chamber was controlled to 91–97 K during the experiments by adjusting the level of liquid N_2 in the cooling bath. Films of Titan tholin on Si wafer substrates were completely immersed into liquid CH_4 with approximately 10 mL of volume (Fig. 2.2c). After immersing into liquid CH_4 for 3 hours, the liquid CH_4 was slowly evaporated by evacuation of gaseous CH_4 of the cryo-chamber for 30 min by adjustment of a leak valve while avoiding boiling (Fig. 2.2d). The temperature was maintained at less than 100 K during the evacuation. After the evaporation, dissolved matter in the liquid CH_4 would deposit and coat on the surface of Titan tholin (Fig. 2.2e). After complete evaporation of liquid CH_4, the liquid N_2 bath was removed, which raised the interior temperature to room temperature (~300 K). With the same procedure of a wet-and-dry cycle of liquid CH_4, our previous study found a formation of evaporites on the surface of sample (Hirai et al., 2023). The collected sample on Si wafer substrates was stored in a desiccator for AFM measurements.

2.2.1.3. Hydrothermal organics formation

Formation of hydrothermal organics could occur in the melting of icy crust formed by hypervelocity impacts (Artemieva and Lunine, 2003) if NH_3 and HCHO exist in the icy crust on Titan. NH_3 could be supplied in icy crust and on the surface of Titan from subsurface ocean (Choukroun & Grasset, 2010) through cryovolcanic activity (Sotin et al., 2005; Lopes et al., 2007; Wall et al., 2009). Indeed, the presence of NH_3 on the surface of Titan has been inferred from Visual and Infrared Mapping Spectrometer (VIMS) observations (Nelson et al., 2009). On the other hand, the presence of HCHO has not been confirmed (Nixon et al., 2024), although HCHO could be supplied to icy crust on Titan by cometary impacts.

The methodology of synthesis of hydrothermal organics was based on the previous studies (Cody et al., 2011; Kebukawa et al., 2013; Sekine et al., 2017). A 2-ml starting solution with 1

mol.% CH_2O as paraformaldehyde, 1 mol.% NH_3, and 0.5 mol.% $C_2H_4O_2$ relative to H_2O was introduced into a Pyrex glass ampoule (Makuhari-Rikagaku Inc.) (Fig. 2.3b). The abundance of these non-H_2O volatiles in initial liquid was determined based on the composition of comets (Goesmann et al., 2015). The sealed ampoules were heated at 130–150 °C for 36–168 hours in an electric oven (Fig. 2.3a; DOV-300A, AS ONE Inc.). After heating, the solution color changed to a deep red brown color from transparent (Fig. 2.3c). The reacted samples were filtered using a 0.22 μm PTFE syringe filter (AS ONE Inc.). After filtering, the solid precipitates were washed with ultrapure water (MilliQ: Millipore) to rinse soluble organic materials on the surface. 20 μl of filtered liquid sample was dried on a cantilever, Si wafer substrates, and CaF_2 optical window in a draft chamber, leading to the formation of films of hydrothermal organics on their surfaces. IR transmittance of hydrothermal organics formed on a CaF_2 optical window was measured using a Fourier-transform infrared spectrometer (FT-IR). The cohesion force of hydrothermal organics on the cantilever and Si wafer substrate was measured using AFM. After the AFM analyses, the surface of the Si wafer substrate and the tip of the cantilever were observed using the FE-SEM.

To measure the elastic wave velocities (Chapter 4), we used the solid precipitates of hydrothermal organics because the elastic wave velocity measurements need a large amount of sample (~100 mg), as mentioned above. IR transmittance of solid precipitates of hydrothermal organics was also measured using FT-IR. The solid precipitates of hydrothermal organics were stored into a glass vial in a desiccator.

2.2.2. Morphological analysis for organic analogs

2.2.2.1. FE-SEM analysis

To observe the morphologies of films of Titan tholin, altered tholin, and hydrothermal organics, FE-SEM (LEO1550, ZEISS Inc.) was employed after the AFM measurement shown in Chapter 3. The samples were fixed on a sample holder of FE-SEM with carbon tape. The electron voltage of the observations was 3 keV or 20 keV. In order to estimate the surface energy of organic materials from the cohesion force, the contact radius between the tip and films of the samples on a Si wafer substrate was needed (see Chapter 3). The contact radius of the tip was obtained based on the images taken with the FE-SEM using the software of Image-J (Version 1.54k).

2.2.2.2. AFM analysis

To constrain the surface roughness of films of Titan tholin and altered tholin on Si wafer substrates, the substrates were analyzed using an AFM (Dimension Icon, Bruker Inc.) in the tapping mode. In this mode, the topography image of the sample was obtained by monitoring

changes of cantilever's oscillation amplitude. Cantilevers with Si tip (Figure 2.4c; AC200TS, Olympus Inc.) were used. The measurements were performed on the film of Titan tholin for a square area of 2×2 μm (512×512 points) and on the film of altered tholin for square area of 500×500 nm (512×512 points). The measurements were conducted in ambient conditions, i.e. 300 K and 1 bar atmosphere.

2.2.3. Chemical analysis for organic analogs

2.2.3.1. Infrared spectroscopy

Fourier-transform infrared spectrometer (FTIR; Frontier, PerkinElmer) was used to analyze the functional groups of film and particles of Titan tholin, and dried film and solid precipitates of hydrothermal organics. Transmittance spectra of the samples on CaF_2 windows were obtained at the wavenumbers of 4000–400 cm^{-1} with a resolution of 1 cm^{-1}. CaF_2 windows without samples were measured as background spectra to obtain the transmittance spectra. The IR transmittance spectra of particles of Titan tholin and solid precipitates of hydrothermal organics were measured with a diffuse-reflection method and mixing with KBr powder. Pellet of KBr powder without sample was measured as background spectra. To eliminate the effects of atmospheric H_2O and CO_2 during the measurements, pure nitrogen gas (G1 grade, N_2 > 99.99995%, Suzuki Shokan Inc.) was purged in the sample room of the FTIR throughout the measurements.

2.2.3.2. Elemental analyses

Elemental analysis was performed for Titan tholin particles and solid precipitates of hydrothermal organics. About 2 mg of the sample was set on a platinum boat and introduced into a CHN elementary analyzer (CHN Coder; JM10, J-Science Inc.). The relative amounts of C, H, and N were determined via combustion in the presence of O_2 (the Pregl-Dumas method) and subsequent measurements of collected CO_2, H_2O, and N_2. For the analysis of oxygen, precisely weighed samples in a gold capsule are subject to combustion to decompose, collected as CO gas, and detected using NDIR (Non-Dispersive Infrared) spectroscopy.

2.2.3.3. HP-LC measurements

High-Performance Liquid Chromatography (HPLC) was performed to analyze amine and amino acids in liquid sample of hydrothermal organics, following the experimental protocol described in Li et al. (2023). A Jasco HPLC system was composed of an autosampler (AS-4550, Jasco Inc.), a HPLC Pump (PU-4580, Jasco Inc.), a column oven (CO-4060, Jasco Inc.), a degassing unit (LV-4500, Jasco Inc.), a tertiary gradient unit (LG-1580-02, Jasco Inc.), and an interface box (LC-NetII/ADC, Jasco Inc.). The interface box was equipped with post-column

derivatization with opthalaldehyde and a fluorescence detector (FP-4025, Jasco Inc.) operated at 345 nm for excitation and 455 nm for emission. A cation-exchange column (AApak Na II-S2, Jasco Inc.) was used at 50 °C. Five citrate buffer solutions of different citrate concentrations and pH values were used as eluents in a stepwise manner.

The liquid sample of hydrothermal organics produced at 150℃ for 168 hours was diluted with ultrapure water (MilliQ: Millipore) by ten times to avoid the detection of excessive ions. Seventeen amino acids, i.e. histidine, aspartic acid, methylamine, ammonium chloride, ethylamine, L-alanine, γ-aminobutyric acid, β-alanine, glycine, DL-serine, glutamic acid, α-aminobutyric acid, L-histidine, phenylalanine, threonine, L-tryptophan and tyrosine, and ammonia water were used as standards. A solution before heating was also analyzed to measure the levels of amino acids and amines in the starting solutions.

2.2.3.4. UV-VIS spectroscopy

An ultraviolet-visible (or UV/Vis) spectrometer (LAMDA 650; PerkinElmer, Inc.) was performed to analyze liquid samples of hydrothermal organics produced at 150℃ for 168 hours. The liquid sample was diluted with ultrapure water by five times. Approximately 350 μl of liquid sample was filled in a quartz cuvette cell (45 × 12.5 mm, total thickness of 3.5 mm (sample thickness of 1 mm); B0631007, PerkinElmer Inc.). The wavelength range of the UV/Vis spectrometer was set to be 250−800 nm with a wavelength resolution of 1 nm.

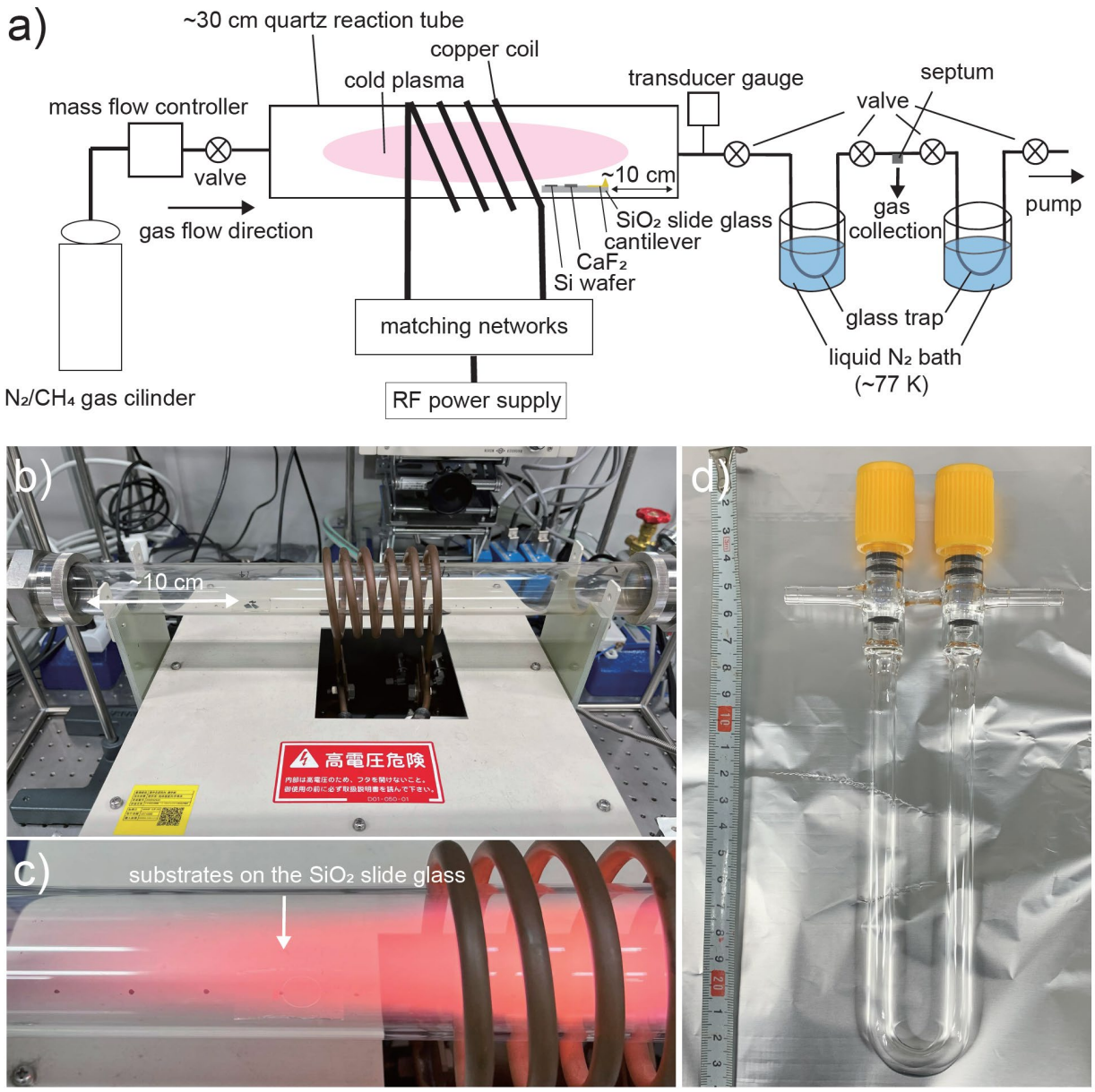

Figure 2.1 (a) Schematic illustration of Titan tholin production experiment with cold plasmas. A pre-mixed CH_4/N_2 gas mixture was introduced into a quartz glass tube at a constant flow rate using a mass-flow controller. Gas pressure inside the quartz tube was measured using a transducer gauge. Cold plasma irradiation onto the introduced gas mixture was performed by using a copper coil cooled with water circulation system and equipped with matching networks, a 13.56 MHz RF power supply. Si wafer substrates, cantilevers, and CaF_2 optical windows were set on the quartz tube during irradiation. (b) A picture of a quartz tube, copper coils, and matching box. (c) Cold plasma irradiation onto substrate on the SiO_2 slide glass. Redish pink glow is plasma formed in a N_2/CH_4 gas mixture. (d) Cold trap to collect particles of Titan tholin used in the present study.

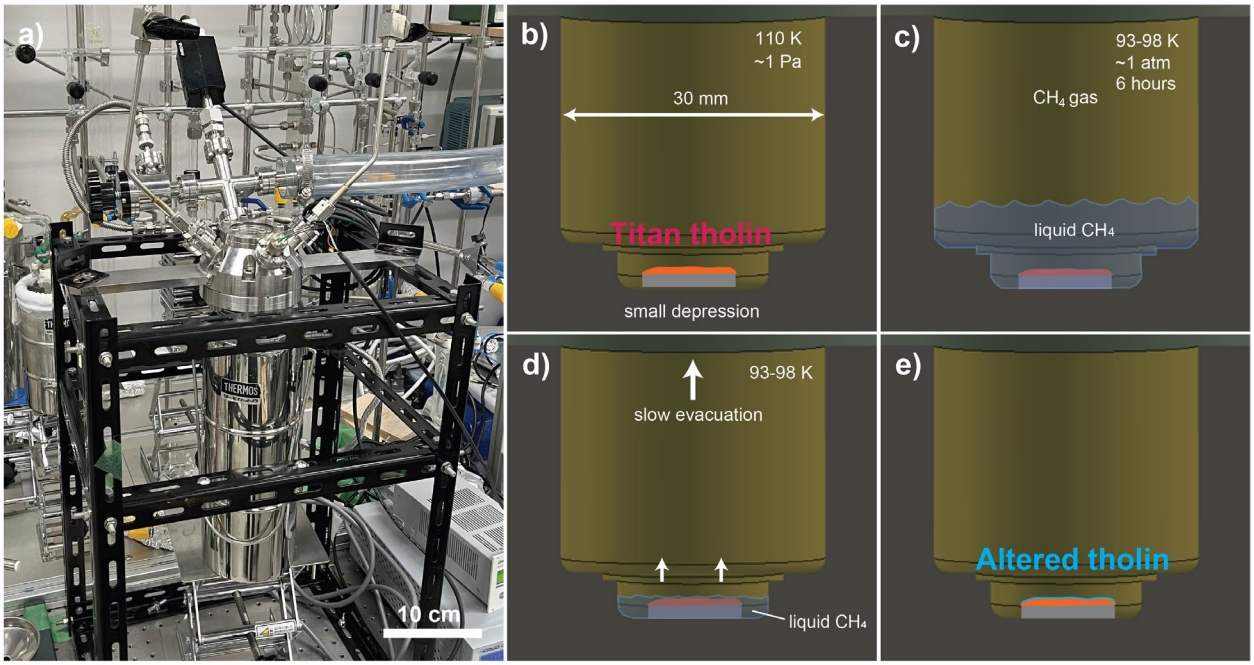

Figure 2.2 (a) A cryo-chamber for altered tholin film production developed in Hirai et al. (2023). (b-d) Schematic diagram of altered tholin production experiment. (b) Titan tholin on a Si wafer substrate was set on the dent of the chamber. After evacuation, the chamber was cooled to ~110 K by using liquid N_2 bath (~77 K). (c) Liquid CH_4 was generated after inlet CH_4 gas. The sample was immersed in liquid CH_4 for several hours. (d) After immersing, liquid CH_4 was slowly (~30 mins) evaporated by evacuating the gas phase CH_4. (e) After evaporation, the surface of Titan tholin was chemically altered, resulting in the formation of altered tholin.

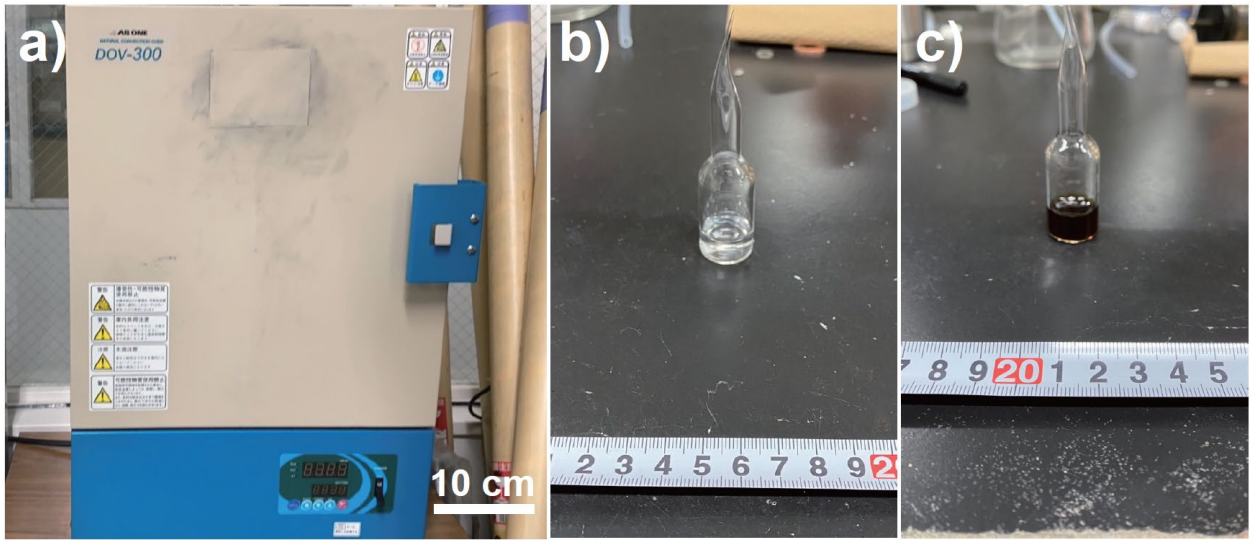

Figure 2.3 (a) An electric oven for the hydrothermal organics production experiments used in the present study. (b) An ammonia, formaldehyde, and glycolaldehyde solution in a glass vial before the experiment. (c) Same as (b) but after heating at 130℃ for 36 hours.

Figure 2.4 (a) Cantilevers (SI-DF3-A, Seiko Instruments Inc.), (b) Si wafer (SI-500443, Niraco Inc.), and (c) cantilevers (AC200TS, Olympus Inc.) used in the present study.

2.3 Results & Discussion

2.3.1. Morphologies of organic samples

Figure 2.5 shows the FE-SEM images of the tip of cantilever coated with and without film of Titan tholin. The FE-SEM image without organic sample was taken before measurement (Fig. 2.5a). Circular patterns were seen on the surface, which would be the surface texture of Au coated on the tip. The FE-SEM images with Titan tholins were taken after cohesion force measurements Run #2 in Chapter 3 as described below. The panel of b of Fig.2.5 shows a FE-SEM image with 20 keV electron acceleration. The panel c was the same as the panel b, but with 3 keV electron acceleration. The surface of the tips coated with film of Titan tholin were relatively smooth compared to tip without organic sample (panel of a in Fig. 2.5). The boundary between Titan tholin and the tip of the cantilever can be distinguished in the image with 20 keV because electrons accelerated with higher voltage could penetrate deeper depth of the organic layer. The thickness of film of Titan tholin on tip of the cantilever is estimated to be ~20 nm. The diameters of the tip coated with film of Titan tholin were measured to constrain the contact radius to estimate surface energy in Chapter 3 below.

Figure 2.5d shows the FE-SEM image of a tip of the cantilever without Titan tholin after cohesion force measurements with film of (altered) Titan tholin on Si wafer substrates at Run #3 in Chapter 3. Compared with the FE-SEM image before measurements, small materials were covered with the tip of the cantilever, suggesting that the samples on Si wafer substrate were peered and stuck on the tip during measurements. The small materials attached to the tip would be Titan tholin and/or altered tholin. The surface of the small materials on the tip appeared to be rough compared to film of Titan tholin shown in panels of b and d. The diameters of the tip stuck with the small materials were measured to constrain the contact radius to estimate surface energy in Chapter 3 below.

Figure 2.5e shows the FE-SEM image of the tip of cantilever coated with hydrothermal organics measured with 20 keV electron acceleration before measurement. The amoeboid patterns of relatively rough structure (roughness ~20 nm) were seen on the surface, suggesting that the film of hydrothermal organics was deposited on the tip of the cantilever. Figure 2.5f shows the tip of cantilever coated with hydrothermal organics after measurement of Run #4 in Chapter 3. A small grain (~200 nm) is attached to the top of the tip during measurements. We assumed that the small grain was the contact point during measurements. The diameters of the small grains were measured to constrain the contact radius to estimate surface energy in Chapter 3 below.

In the AFM measurements, a tip coated with organics was contacted and pushed to the surface of a sample coating a Si wafer substrate. In order to estimate the cohesion force, the

contact radius of the tip to the sample is required. However, organic materials on both tip and substrate may be deformed due to the force of pushing the tip onto the sample. We thereby estimated an upper limit of the contact radius from the maximum diameter of coated organic sample on the tip, because the original tip was made of silicon covered with gold and would not be easily deformed due to the contact in the AFM measurements. Figures 2.6–2.8 show the results of images to determine the maximum diameter of coated Titan tholin (Fig. 2.6), altered tholin (Fig. 2.7), and hydrothermal organics (Fig. 2.8) after the AFM measurements. The tips observed using FE-SEM before measurements were not used because the chemical composition of the organic films would be altered by irradiation of electron beam during FE-SEM measurements. Since the actual contact angle to the sample surface was unknown, the maximum diameters were measured nine times randomly in angle to calculate the average diameters and errors. The measured length of contact radius was chosen along with the boundary between the film of organics and Au-coated Si tip of the cantilever. The average diameters of tips were estimated to be 83 ± 5 nm for Titan tholin, 63 ± 15 nm for tip with the small materials potentially composed of Titan tholin or altered tholin, and 192 ± 25 nm for hydrothermal organics. These average diameters correspond to the maximum contact radius during cohesion force measurements.

Figure 2.9 shows the FE-SEM images of the surface of films of Titan tholin (Fig. 2.9a) and hydrothermal organics (Fig. 2.9b) deposited on Si wafer substrates. The surface roughness of the samples appeared to be less than the order of μm. Flat surface of films of Titan tholin was confirmed with AFM measurements. On the other hand, the surface of films of hydrothermal organics would be deduced to be ~20 nm, given the surface roughness of the tip of the cantilever coated with hydrothermal organics would be ~20 nm (Fig. 2.5e,f). Figure 2.10 shows the AFM images of the surface of film of Titan tholin (Fig. 2.10a) and film of altered tholin (Fig. 2.10b) on Si wafer substrates. In both figures, white areas show the higher topography regions, whereas the black areas show the depression of the structure. The surface roughness of film of Titan tholin is estimated to ~7 nm within an area of 2 μm × 2 μm. The surface roughness of film of altered tholin is estimated to as ~1 nm, suggesting that the surface of altered tholin was flattened due to dissolution and precipitation of dissolved species as evaporites. These results indicate that the surfaces of films of Titan tholin, altered tholin, and hydrothermal organics are flat in scale of ~10 nm or less, which are smaller than the diameter of the tip of the cantilever coated with organic materials.

2.3.2. Chemical structure of organic samples

Figure 2.11 shows the IR spectra of film and particles of Titan tholin, film of altered tholin, film of hydrothermal organics that were produced by evaporation of liquid sample, solid

of hydrothermal organics filtered from the liquid sample. These spectra were normalized at 1600 cm^{-1}.

Based on the IR spectra (Fig. 2.11), both film and particles of Titan tholin contain N-H bonds (3300 cm^{-1}), C-H bonds (2950 cm^{-1}), C≡N bonds (2200 cm^{-1}), conjugated C=C and/or C=N bonds (1620 cm^{-1}) and aromatic C=C and/or C=N bonds (1580 cm^{-1}) (e.g., Imanaka et al., 2004). Film of Titan tholin shows relatively strong absorption of aromatic C=C and/or C=N bonds (1580 cm^{-1}) and weak absorption of C≡N bonds (2200 cm^{-1}) compared to particles of Titan tholin. The absorption features of film of Titan tholin are consistent with the previous results of IR analysis of Titan tholin formed via cold plasma irradiation onto CH_4/N_2=10/90 gas mixture at ~150 Pa (Imanaka et al., 2004; Sekine et al., 2008). The results of the elemental analysis show that particles of Titan tholin have C/H = 0.7 and C/N = 2.1 (Table 2.2). C/N ratio of our particles of Titan tholin was comparable to Titan tholin formed by Imanaka et al. (2004) and less than Titan tholin formed by Sekine et al. (2008), whereas C/H ratio was comparable to the values in the previous studies (Imanaka et al., 2004; Sekine et al., 2008), although experimental apparatus for cold plasma irradiation used in the present study was the same apparatus used by Sekine et al. (2008). The difference in C/N ratios of Titan tholin between Sekine et al. (2008) and the present study would result from the difference of the formation processes; Titan tholin formed by Sekine et al. (2008) was produced in a quartz tube reaction chamber where catalysis and nucleation processes may occur on the wall of the chamber, whereas particles of Titan tholin formed in the present study were generated in levitation. Imanaka et al. (2004) performed UV/Vis spectroscopy, laser-desorption and laser-ionization mass spectrometry (μL^2MS), Raman analysis, and elemental analysis. Their results suggest that the chemical structure of Titan tholin formed at middle pressure contains N-bearing polycyclic aromatic compounds (N-PACs) connected with polymer-like chain structures terminated with -CH_3 and -C≡N (Figure 2.14). Given the results of the similarity of IR spectra, C/H ratio, and C/N ratio between particles of Titan tholin and Titan tholin formed in Imanaka et al. (2004), the chemical structure would be similar. Figure 2.14 shows the proposed chemical structure of film and particles of Titan tholin, based on the analysis performed by the present study and Imanaka et al. (2004). As described above in Sec. 2.2.1.1, we use film of Titan tholin for the AFM measurements (Chapter 3) and particles of Titan tholin for the elastic wave measurements (Chapter 4).

The IR spectrum of altered tholin shows the strong absorption at 1500–1400 cm^{-1} (Figure 2.11), which is derived from semi-circle stretching of aromatics, such as N-bearing hetero-aromatic rings (Larkin, 2017). The absorption at 1500–1400 cm^{-1} does not appear in the IR spectra of Titan tholin. Compared with Titan tholin, the C–H absorption at ~2,900 cm^{-1} is absent in altered tholin. These results show that altered tholin has a different chemical structure due to alteration by liquid CH_4. In particular, altered tholin seems to contain N-bearing heterocyclic

aromatics through selective dissolution of Titan tholin and precipitation upon drying. A possible dissolution mechanism of these N-bearing heterocyclic aromatics into liquid CH_4 would involve them being detached from Titan tholin through the dissolution of polymer-like potential chains of the original structure (Hirai et al., 2023). Figure 2.14 shows a potential chemical structure of altered tholin, suggested by Hirai et al. (2023). We use altered tholin for the AFM measurements (Chapter 3).

The IR spectra of solids of hydrothermal organics show that they contain the absorptions of N-H and/or O-H (2800–3600 cm^{-1}), C-H (2950 cm^{-1}), C=O (1650–1750 cm^{-1}), and small aromatic C=C and C=N (1580 cm^{-1}) (Figure 2.11). The IR spectra of film of hydrothermal organics are distinct from that of solid of hydrothermal organics (Figure 2.11). Film of hydrothermal organics contain relatively strong aromatic C=C and C=N (1580 cm^{-1}) and less C=O (1650–1750 cm^{-1}), compared with solid of hydrothermal organics (Figure 2.11). The IR spectra of film of hydrothermal organics are similar to those of Titan tholin, but the former does not contain strong C≡N bonds (Figure 2.11).

Our IR spectra of solid of hydrothermal organics are similar to those of organic solids formed via polymerization of formaldehyde or formaldehyde and ammonia shown in the previous studies (Cody et al., 2011; Kebukawa et al., 2013; Sekine et al., 2018). The results of elemental analysis show that C/N (= 5.3) and C/O (= 2) ratios of our hydrothermal organic solids are lower than those of the previous studies (C/N = 4.2–12.5 and C/O = 2.5–2.9) (Table 2.3; Kebukawa et al., 2013; Sekine et al., 2018), suggesting that our solids of hydrothermal organics contain more N and O. This could be derived from the higher NH_3 concentration of initial solution in the present study. Based on the NMR, XANES, and Raman analyses performed by the previous studies (Cody et al., 2011; Kebukawa et al., 2013), they suggest that the chemical structure of the hydrothermal organics is N incorporated polymers composed of poly-olefin with aromatic structure (Figure 2.14). Figure 2.14 shows a potential chemical structure of solids of hydrothermal organics. Compared with the previous studies (Kebukawa et al., 2013), our sample should contain more N and O; however, the chemical structure would be similar to them given the similarity in the IR spectra. We use solids of hydrothermal organics for the elastic wave measurements (Chapter 4).

The chemical structure of film of hydrothermal organics, which were generated by evaporation of filtered liquid sample after the reaction (Sec. 2.2.1.3), can be investigated not only with IR analysis but also with the analysis of liquid sample with HPLC. Figure 2.12 shows the results of HPLC analysis of the filtered liquid sample of hydrothermal organics, compared with the results of the initial solutions and standard materials. This figure shows that glycine, α-alanine, α-aminobutyric acid, β-alanine, methylamine, and ethylamine are formed due to the reaction. These amine compounds, amino acids, formaldehyde, and ammonia would form N-

bearing imidazole and pyrrole upon dehydration (Kebukawa et al., 2013). Figure 2.13 shows the UV/Vis spectra of the filtered liquid sample after the reaction. The continuous absorption peaks at wavelength of 260–270 nm and 300–330 nm suggest the presence of aromatics. These results are consistent with the strong absorptions due to aromatic C=C/C=N in IR spectra (Fig. 2.11). Given the possible presence of N-bearing aromatic compounds, a possible chemical structure of film of hydrothermal organics is shown in Figure 2.14. Considering the similarity in the IR spectra with Titan tholin, film of hydrothermal organics may have a similar chemical structure, N-bearing aromatics (e.g., pyrrole), but contain less C≡N at the termination of carbon chains due to the lack of the C≡N absorptions. We use film of hydrothermal organics for the AFM measurements.

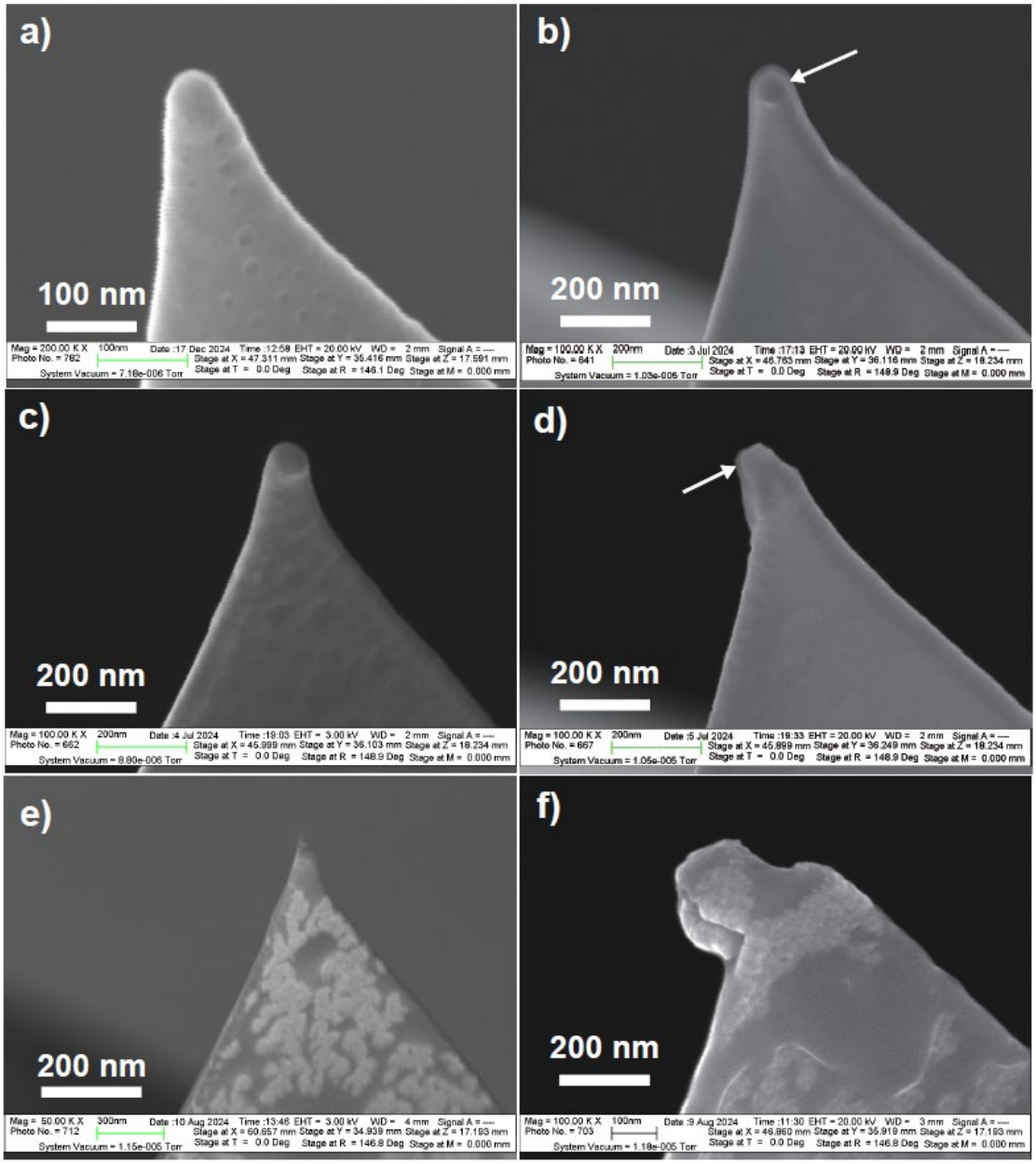

Figure 2.5 The FE-SEM images of cantilevers. (a) Tip of SI-DF3-A without organic sample. Circular patterns are seen on the surface. (b) Tip of SI-DF3-A coated with film of Titan tholin observed with 20 keV electron acceleration after Run #2 in Chapter 3. Thin film (~20 nm) of Titan tholin was indicated by white arrow. (c) Same as b but observed with 3 keV electron acceleration. The surface appears to be relatively smooth. (d) Tip of SI-DF3-A coated with small materials of Titan tholin or altered tholin observed with 20 keV electron acceleration after Run #3 in Chapter 3. (e) Tip of SI-DF3-A coated with film of hydrothermal organics before measurements observed at 20.00 keV. Amoeboid patterns are seen on the surface. (f) Same as e but after measurement of Run #4 in Chapter 3. A small grain (~200 nm) are attached to the top of the tip.

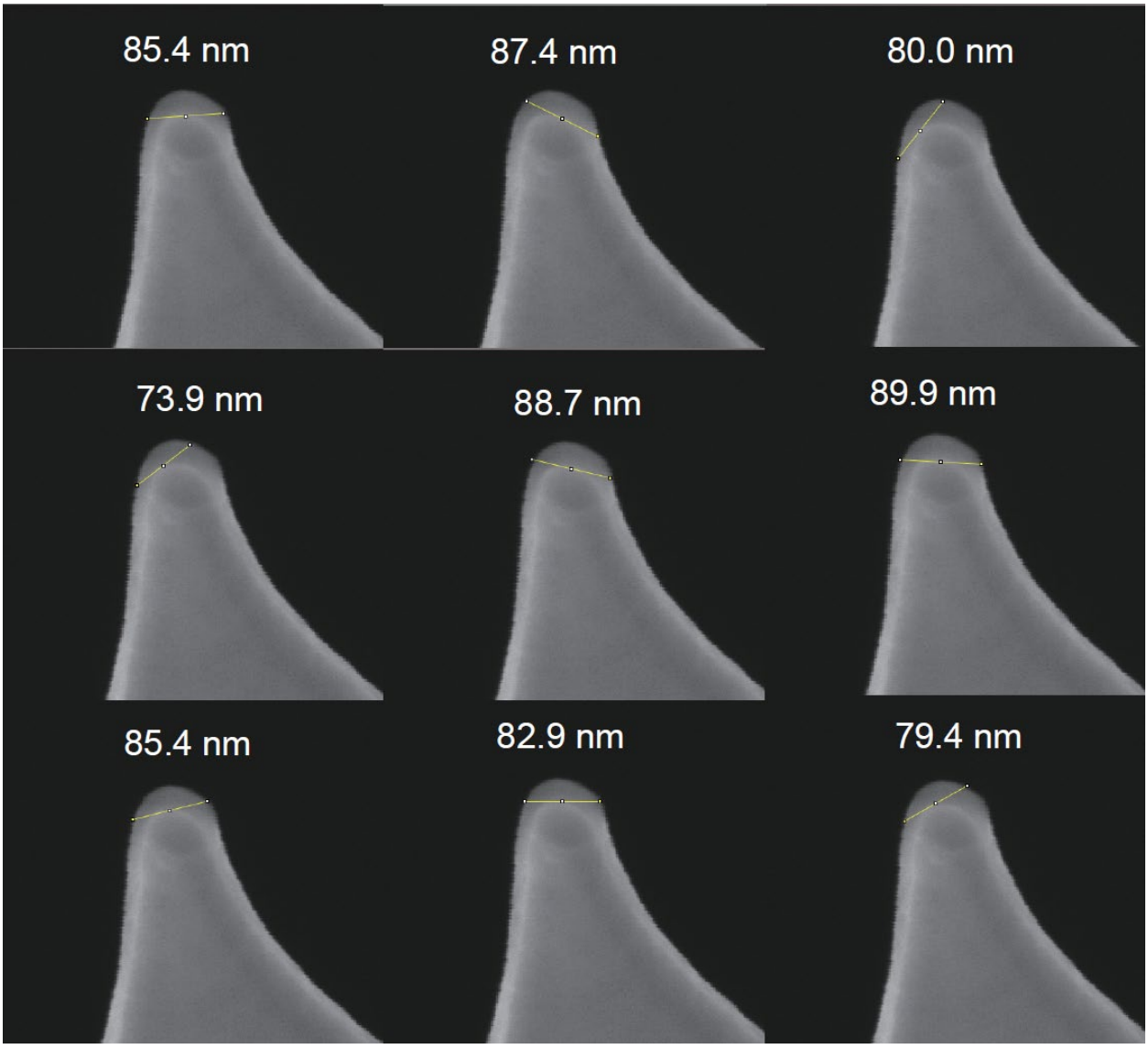

Figure 2.6 The FE-SEM images of Titan tholin cantilevers after AFM measurements in Chapter 3. The diameter of the tips is determined to be 83 ± 5 nm. Each yellow line indicates the measured length.

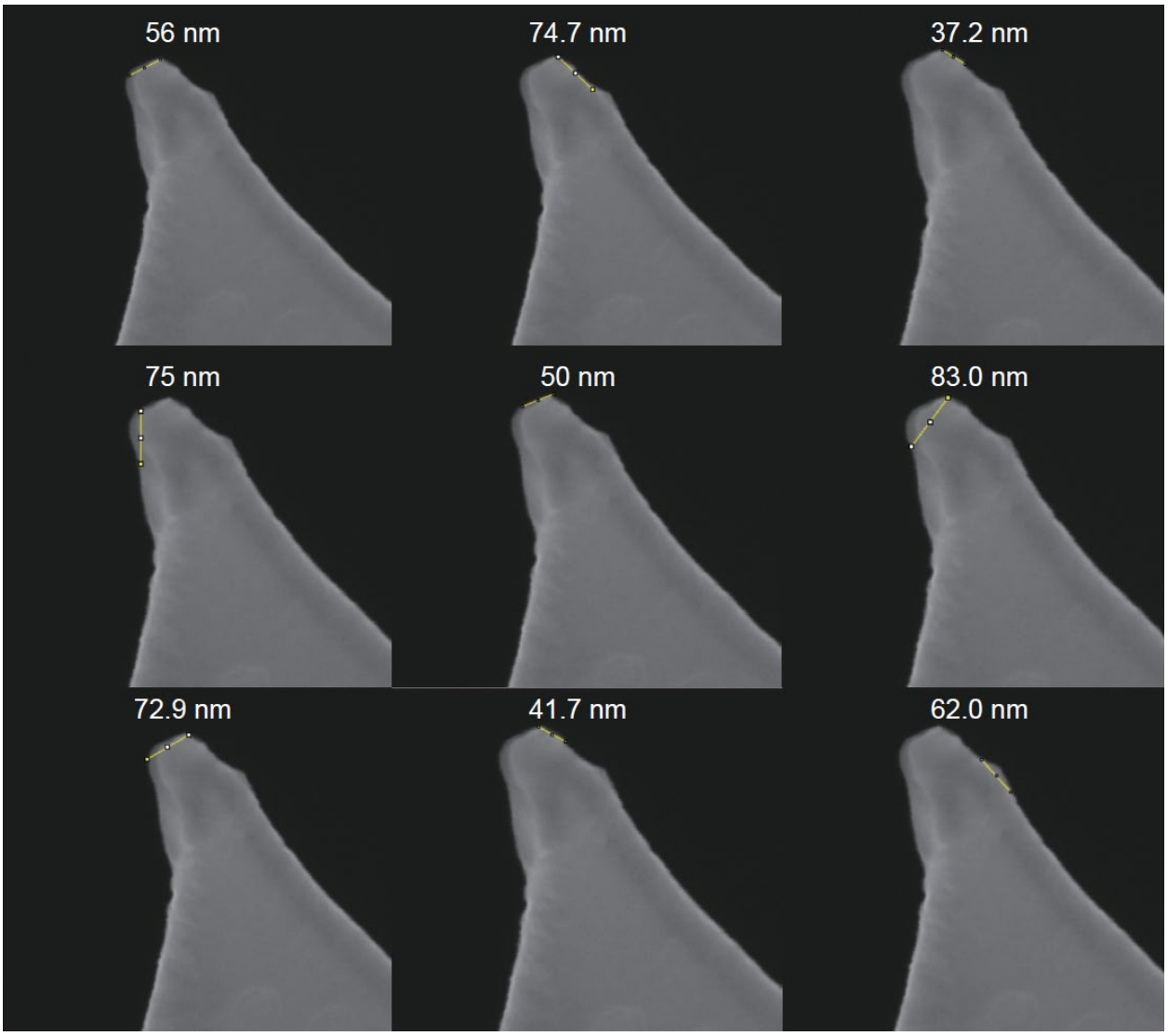

Figure 2.7 The FE-SEM images of Au-coated Si cantilevers with Titan tholin and/or altered tholin flake after AFM measurements in Chapter 3. The diameter of the tips is determined to be 63 ± 15 nm. Each yellow line indicates the measured length.

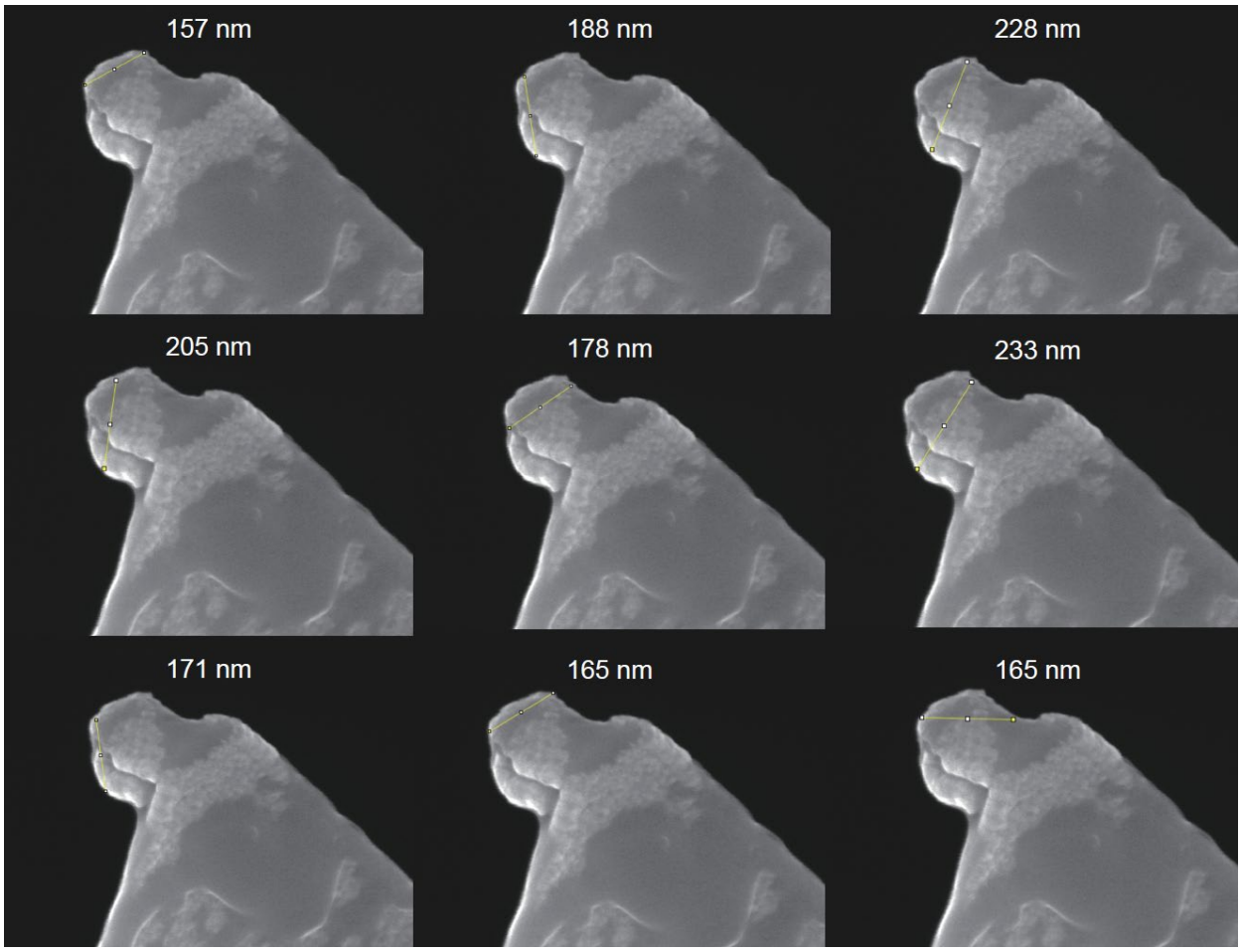

Figure 2.8 The FE-SEM images of hydrothermal organics cantilevers after AFM measurements in Chapter 3. The diameter of the tips is determined to be 192 ± 25 nm. Each yellow line indicates the measured length.

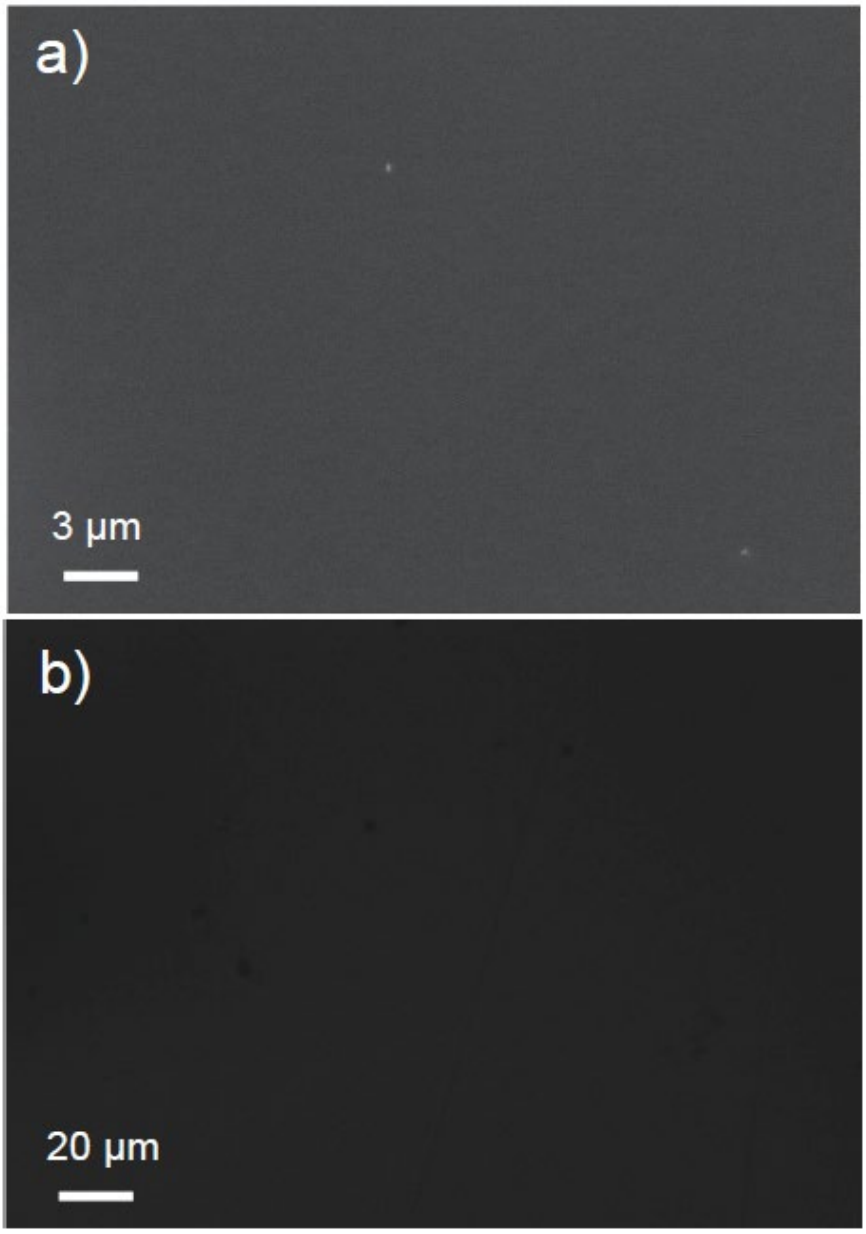

Figure 2.9 The FE-SEM images of (a) Titan tholin and (b) hydrothermal organics on Si wafer substrate after AFM measurements in Chapter 3. The surface of each sample appears to be smooth.

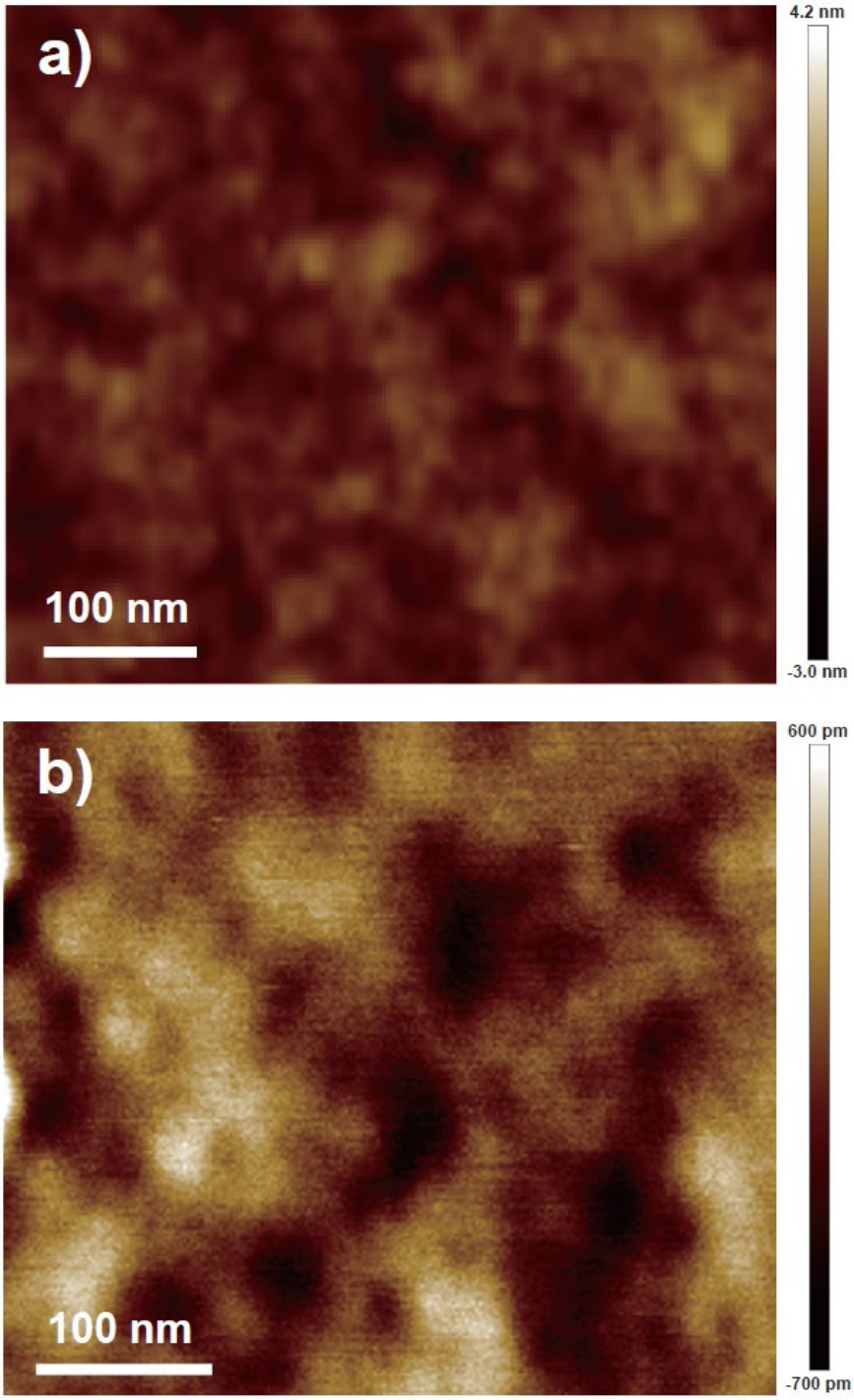

Figure 2.10 The AFM images of (a) Titan tholin and (b) altered on Si wafer substrate obtained in tapping mode of AFM. Each contour shows the topography of each point. White areas show higher topography regions, whereas the black areas shows the depression of the structure. The surface roughness of Titan tholin could be within ~7 nm, whereas the surface roughness of altered tholin could be within ~1 nm.

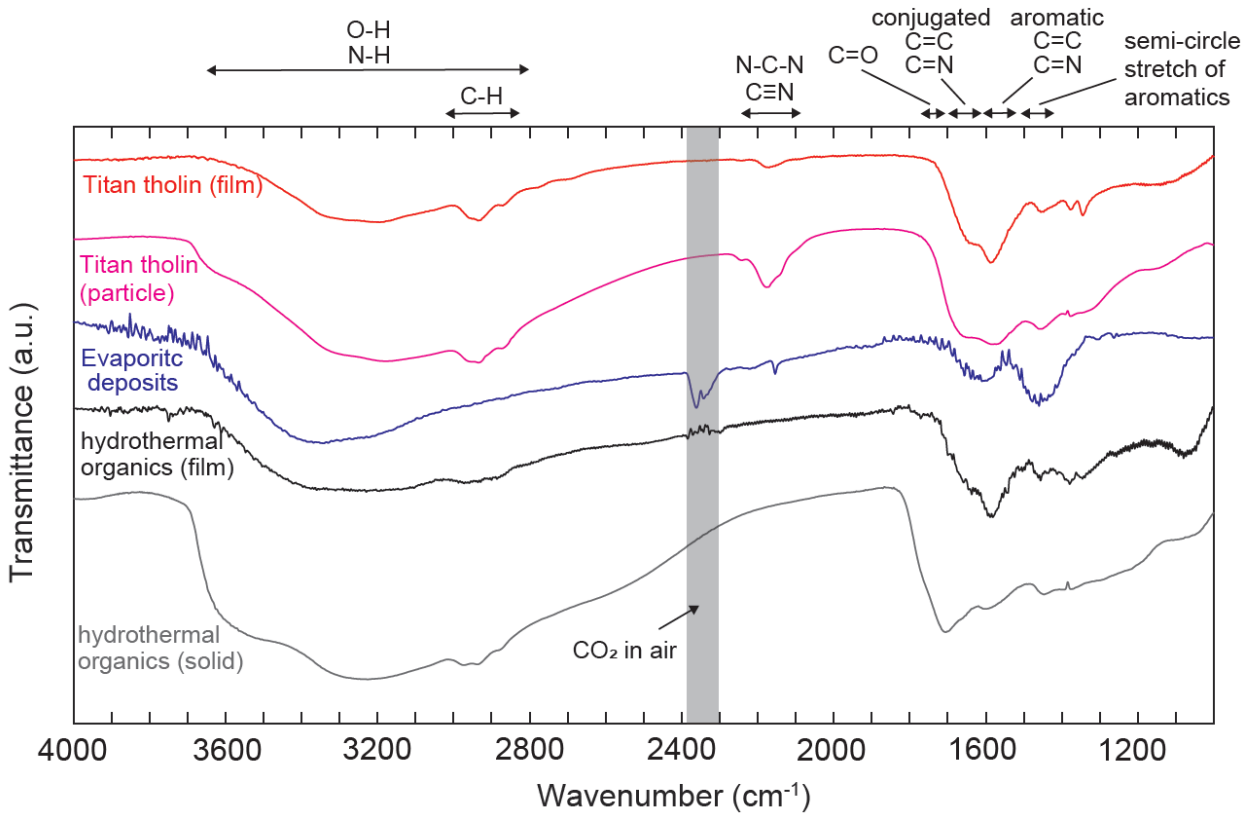

Figure 2.11 Infrared transmittance spectra of Titan tholin (film) (red), Titan tholin (particle) (magenta), hydrothermal organics (liquid) (black), and hydrothermal organic (solid) (gray). The surface of altered tholin would be covered with the evaporitic deposits (blue) (Hirai et al., 2023). Transmittance spectra are normalized and offset for clarity. The signal-to-noise ratio for evaporitic deposits is large because its original absorption is small. Gray hatching indicates absorption owing to CO_2 in air.

Table 2.2 Summary of the results of Elemental analysis of Titan tholin (particle) compared with the results of the previous studies (Imanaka et al., 2004; Sekine et al., 2008).

	sample	C/H	C/N
The present study	Titan tholin (particle)	0.7	2.1
Sekine et al. (2008)	Mid-pressure tholin (160 Pa)	0.6	2.8
Imanaka et al. (2004)	Mid-pressure tholin (150 Pa)	0.8	2

Table 2.3 Summary of the results of Elemental analysis of hydrothermal organics (solid) compared with the results of the previous studies (Kebukawa et al., 2013; Sekine et al., 2018).

	sample	C/H	C/N	C/O
The present study	hydrothermal organics (solid)	0.8	5.3	2
Kebukawa et al. (2013)	F150N	-	12.5	2.9
	F130N	-	10	2.5
Sekine et al. (2018)	high NH_3	-	9.8	-
	low NH_3	-	4.2	-

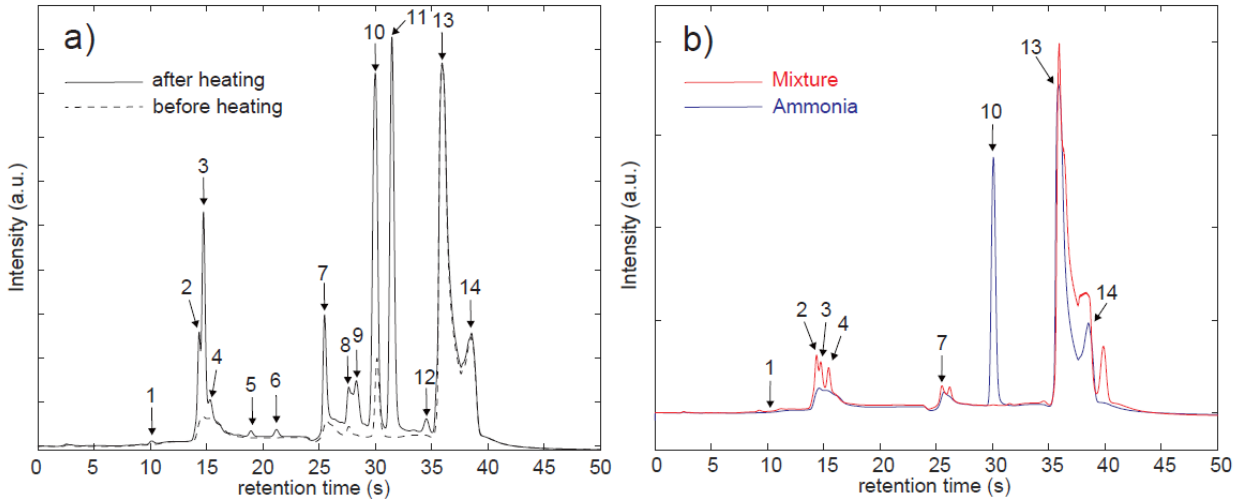

Figure 2.12 Chromatogram of (a) liquid samples of hydrothermal organics formation experiments and (b) standard solutions. After heating the starting solution, amines and amino acids such as glutamic acid, glycine, α-alanine, α-aminobutyric acid, β-alanine, methylamine, and ethylamine are detected. In addition, four unknown peaks are detected that were not present in the standards.

Table 2.4 The list of the detected compounds in Fig. 2.12

Peak #	Retention time (min)	Compounds
1	10.1	Glutamic acid
2	14.3	Glycine
3	14.7	α -alanine
4	15.3	α -aminobutyric acid
5	18.9	Unknown
6	21.2	Unknown
7	25.5	β -alanine
8	27.6	Formaldehyde
9	28.3	Unknown
10	30	Ammonia
11	31.5	Methylamine
12	34.5	Ethylamine
13	35.9	Ammonia
14	38.5	Ammonia

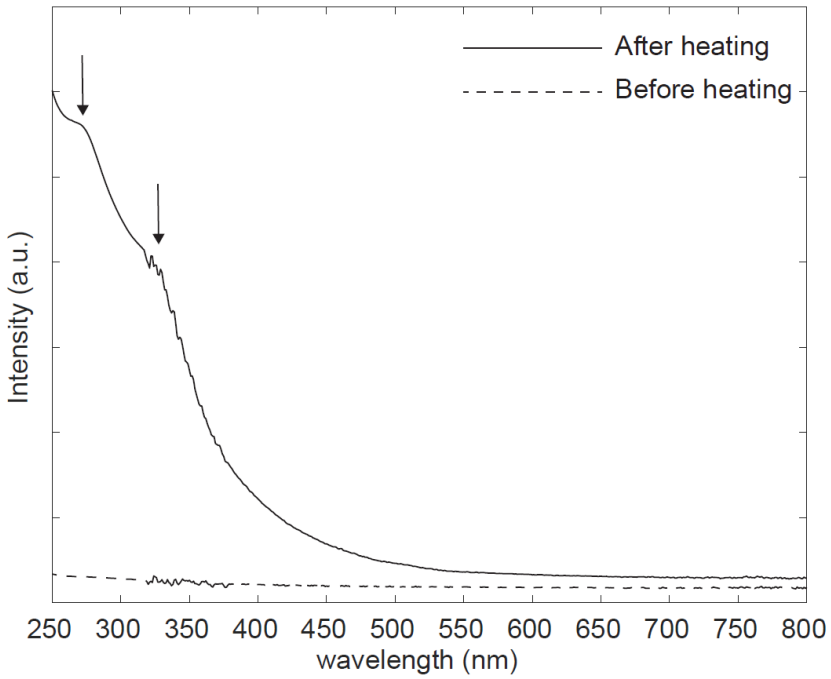

Figure 2.13 UV/Vis spectrum of liquid sample of hydrothermal organics formation experiments. The continuous absorption from 200 to 400 nm in the solution after heating is consistent with the deep red brown color shown in Fig. 2.3c. Two allows indicate the peaks at 260–270 nm and 300–330 nm of polycyclic aromatic compounds.

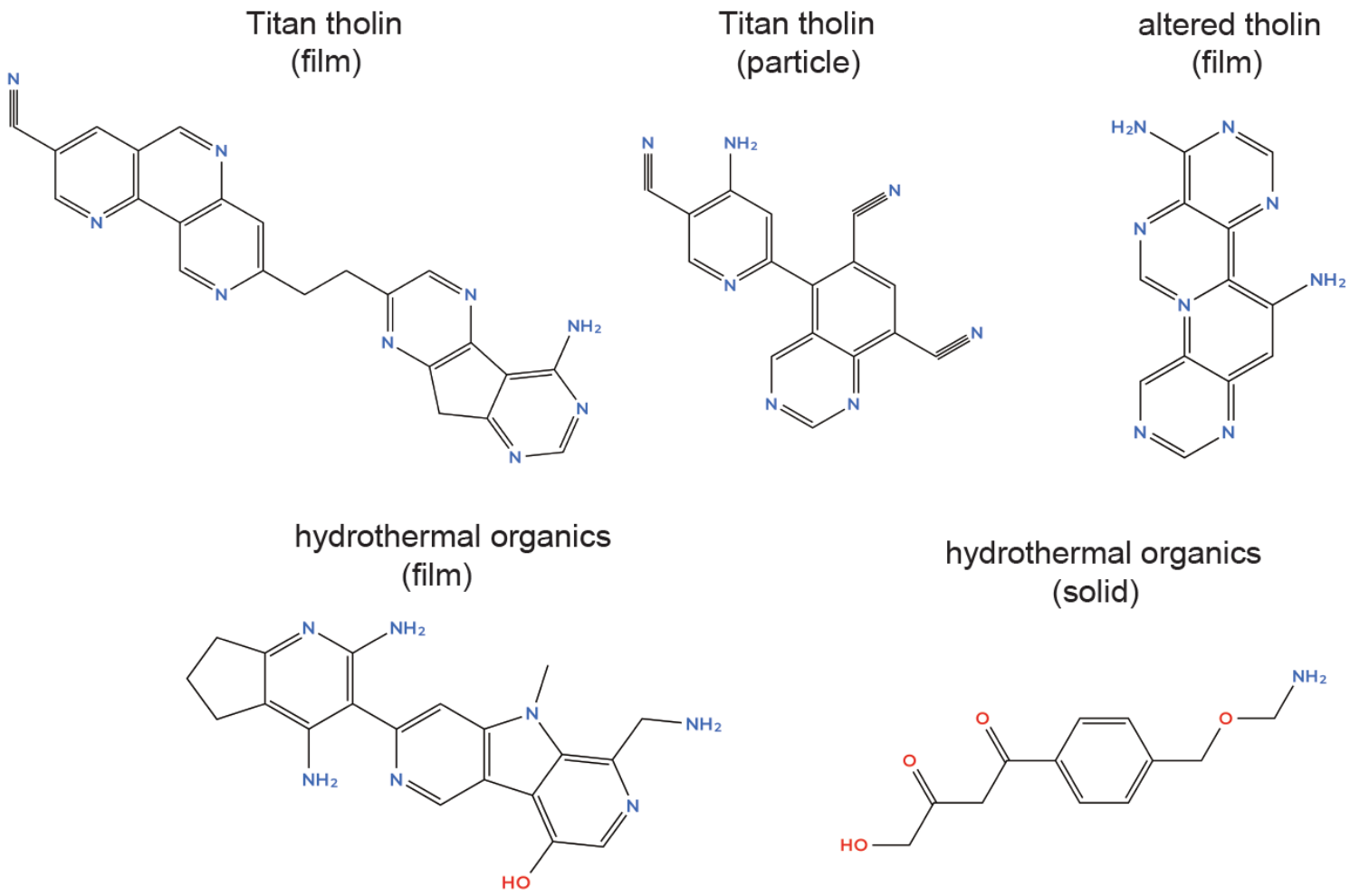

Figure 2.14 Possible explanation for the structure differences between each organic materials produced in the present study. Titan tholin film and Titan tholin particles are composed of combinations of N-bearing polycyclic aromatic compounds (N-PACs) terminated with -CH_3 and -C≡N. Altered tholin could be covered by nitrogen-bearing aromatics with less aliphatic structure. Hydrothermal organic film and solid could contain the poly-olefin with aromatic structure.

2.4. Summary of Chapter 2

In order to investigate surface energy with the AFM measurements (Chapter 3) and elasticity with the elastic wave measurements (Chapter 4) of organic materials on Titan, the present study produced laboratory analogs of Titan's organic materials; 1) films and particles of Titan tholin, 2) films of altered tholin, and 3) films and solids of hydrothermal organics. The aim of this chapter is to characterize the morphology and chemical structure of these organic materials before the AFM and elastic wave measurements. We performed FE-SEM observations and AFM analysis to examine the surface morphology, and FT-IR spectroscopy, elemental analysis, UV/Vis analysis, and HP-LC analysis to investigate the chemical structures.

Our results of morphology analyses show that the tips of the cantilever and Si wafer substrates used in the AFM measurements are covered with films of the organic materials with smooth surface in the scale of several nanometers. The contact radius between the tip and substrate coated with the organic materials in the AFM measurements are also obtained with the results of the microscopic observations.

Figure 2.14 summarizes proposed chemical structures of organic materials. Films and particles of Titan tholin and film of hydrothermal organics would have similar chemical structures as seen from the similarity in the IR spectra. In these three organic materials, N-bearing polycyclic aromatic compounds (N-PACs) would be connected with polymer-like chain structures. Films of Titan tholin would contain more aromatic rings than particles of Titan tholin particles and film of the other. Particles of Titan tholin would contain more polymer-like chain structures with conjugated C=C / C=N and nitrile -C≡N structures than the others. Films of hydrothermal organics contain N-bearing aromatics, e.g., pyrrole, with less C≡N at the termination of polymer-like chain structures than the others. Altered tholin contains N-bearing heterocyclic aromatic structures with little aliphatic compounds. Solids of hydrothermal organics show the poly-olefin with an abundance of C=O bonds in the structure. In Chapters 3 and 4, the differences in the surface energy and elasticity among these organic materials are examined.

Chapter 3. Cohesion force and surface energy of Titan's organic analog materials

3.1 Objectives of Chapter 3

As described in Chapter 1, thick organic sediments exist as dunes at low latitudes of Titan, but they would be absent in the middle latitude regions (e.g., Lorenz et al., 2006; Radebaugh et al., 2008, Rodriguez et al., 2014). Since both low and middle latitude regions are generally arid, deposited organic aerosols at middle latitudes may have been transported spontaneously. Saltation of deposited organic aerosols on Titan would occur by strong winds due to CH_4 storms at low latitudes (Tokano, 2010; Charnay et al., 2015); whereas seasonal winds at middle and low latitudes would be unable to saltate organic sands based on the measured high cohesiveness of Titan tholin at room temperature (Yu et al., 2017). However, the cohesive force should have temperature dependence. In addition, cohesion force should depend on their chemical structures. In fact, wet-and-dry cycles of liquid CH_4 on Titan may have altered deposited organic aerosols through dissolution of a soluble part of aerosols and precipitation as evaporites (Hirai et al., 2023). Hypervelocity impacts on Titan could have induced melting of icy crust at the impact site, which can also induce hydrothermal reactions near the surface. If the icy crust contains simple non-H_2O molecules, such as NH_3 and HCHO, complex organic materials would be formed through the impact-induced hydrothermal reactions.

In this chapter, we conduct cohesion force measurements for Titan's organic analog materials produced and characterized in Chapter 2. Through cohesion force measurements, we aim to investigate both temperature and chemical structure dependence of surface energy of organic analogs. In Sec. 3.2, we describe the principle and methodologies of cohesion force measurement with an AFM. In Sec. 3.3, the results of cohesion forces of films of Titan tholin at temperatures from 300 K to 117 K are reported. The measured cohesion forces of films of altered tholin and hydrothermal organics are also compared in Sec. 3.3. In Chapter 3.4, we initially discuss the uncertainty of the cohesion force and surface energy measurements, and then discuss temperature and chemical structure dependence of cohesion force and surface energy of organic materials.

3.2 Experiments and data analysis

This section describes methodologies of cohesion force measurement of laboratory organic analogs formed in Chapter 2 with an atomic force microscope (AFM) and the methodologies of data analysis.

3.2.1. Atomic Force Microscopy

3.2.1.1. Principles of the measurements and analyses

An AFM can measure cohesion force between a tip of a cantilever and a sample on a Si wafer substrate. In the present study, the AFM was used in the contact mode to measure the cohesion force of organic materials whereby a spherical tip of a cantilever covered with organic materials was pulled off from the flat plane of organic substrate. The morphologies of organic materials were characterized in Chapter 2.

Figure 3.1 shows a typical force curve obtained in the present study with schematic illustrations of interactions between a tip of a cantilever and sample on substrate. First, the tip approaches to the surface of the sample (Figure 3.1A). Due to the attractive force, the tip snaps in the sample. Then, the attractive force can be measured by the bending of the cantilever (i.e., the cantilever deflection from the baseline). (Figure 3.1B). As the distance between the tip and sample becomes close, the cantilever is deflected due to the repulsive force (Figure 3.1C). After the tip measures the repulsive force, the tip is pulled off the sample. Due to the cohesion force between the tip and sample, the cantilever is bent (Figure 3.1D). Finally, the tip and sample are separated, and the cantilever returns to its unperturbed state (baseline). The cohesion force, F_{coh}, can be calculated by the cantilever deflection given for spring constant of the cantilever.

The deflection of the cantilever was measured by optical lever method (e.g., Alexander et al., 1989); The angle of an incident laser beam reflected from the back side of the cantilever and was continuously monitored by a photodetector. To calibrate the deflection of the cantilever and the voltage signal from the photodetector, i.e. the deflection sensitivity [mV/nm], a relationship between the displacement (deflection) of the cantilever on hard substrate, such as a Si wafer substrate, was measured.

Ideally, the spring constant of the cantilever in vacuum can be calculated by the mass of the cantilever and the resonant frequency (Sader et al., 1995). However, for most cantilevers, determination of mass of the cantilever is difficult due to the large uncertainty of the thickness and density. Furthermore, during the resonant frequency measurement, the surrounding fluid such as air and/or liquid can reduce the resonant frequency (Sader et al., 1995). According to Sader et al. (1999), the equation of the spring constant of the cantilever k_s that is taken into

account the effect of fluid, especially the quality factor in fluid, and is independent of thickness and density of the cantilever, can be described as below:

$$k_{\mathrm{s}} = 0.1906\rho_{\mathrm{atm}} b^2 L Q_{\mathrm{f}} \Gamma_{\mathrm{i}}(Re)(2\pi f_{\mathrm{r}})^2, \quad Re = 2\pi f_{\mathrm{r}} \rho_{\mathrm{atm}} b^2/(4\eta), \tag{3.1}$$

where ρ_{atm} is the density of air (ρ_{atm} = 1.3 kg/m^3), b and L are the width and length of the cantilever, respectively, Q_{f} and f_{r} are the quality factor and resonant frequency of the cantilever in the air, respectively, η is the dynamic viscosity of the air (η = 1.8 × 10^{-5} Pa s), and $\Gamma_{\mathrm{i}}(Re)$ is the imaginary part of the hydrodynamic function. The hydrodynamic function $\Gamma(Re)$ can be described as below (Sader, 1998):

$$\Gamma(Re) = 1 + \frac{4iK_1\left(-i\sqrt{i\,Re}\right)}{\sqrt{iRe}K_0\left(-i\sqrt{i\,Re}\right)}, \tag{3.2}$$

where the functions of K_0 and K_1 are modified Bessel functions of the third kind (Abramowitz and Stegun, 1972). $\Gamma_{\mathrm{i}}(Re)$ at each value of *Re* was obtained from Fig. 1 in Sader et al. (1999) (Table 3.1). In the present study, for the width b and length L of the cantilever (Figure 2.4a; SI-DF3-A, Seiko Instruments), the commercial values (b = 55 μm and L = 450 μm) were used. The quality factor Q_{f} and the resonant frequency f_{r} of each cantilever were measured before and after cohesion measurements by measuring the amplitude of oscillation of the cantilever with varying the frequency in dynamic force microscope (DFM) mode of the AFM. The results of the spring constant of the cantilever and each parameter were summarized in Table 3.1.

To derive the surface energy of the organic materials from the measured cohesion force, the DMT theory (Derjaguin et al., 1999) was applied instead of the JKR theory (Johnson et al., 1971), the latter of which can be applied to soft materials. As shown below in Chapter 3, Titan tholin and hydrothermal organics have 9.7 ± 1.8 GPa and 10.4 ± 1.3 GPa of Young's modulus. Materials with Young's modulus of the order of higher than GPa are generally considered as relatively hard materials, to which the DMT theory can be applied (Nakajima et al., 2013). According to the DMT theory, the cohesion force, F_{coh}, can be described as below:

$$F_{\mathrm{coh}} = 2\pi \mathrm{W}_{\mathrm{coh}} R, \tag{3.3}$$

where R is the radius of the material and W_{coh} is the work of cohesion, which is the energy needed to separate two solid surfaces (Israelachvili, 2011). As for the radius, R, of the tip, R was obtained as FE-SEM image analyses from the electron microscopic observations of the tip (see above in Sec. 2.3.1). Concerning the sample, we assumed the surface of sample as flat plane, because the typical roughness of sample was within a few nm, which is the order of less than the R of the tip.

Errors of work of cohesion δW_{coh} were calculated as below:

$$\delta W_{\mathrm{coh}} = W_{\mathrm{coh}} \sqrt{\left(\frac{\delta F_{\mathrm{coh}}}{F_{\mathrm{coh}}}\right)^2 + \left(\frac{\delta R}{R}\right)^2}, \tag{3.4}$$

where δF_{coh} is the error of cohesion force, and δR is the error of the radius of the tip. If the materials on the tip are same as that on the sample, the adhesion energy can be described as below:

$$\mathrm{W}_{\mathrm{coh}} = 2\gamma, \tag{3.5}$$

where γ is the surface energy of the materials. On the other hand, we assumed that the adhesion energy between different materials is equal to the sum of the surface energy of each material:

$$\mathrm{W}_{\mathrm{coh}} = \gamma_1 + \gamma_2, \tag{3.6}$$

where γ_1 and γ_2 was the surface energy of different materials.

3.2.1.2. Experimental setup and parameters

The cohesion force measurements at cryogenic temperatures were carried out at National Institute of Advanced Industrial Science and Technology (AIST). The experimental setup at AIST composed of an AFM (SII Nanonavi E-sweep, SII technology Inc.) (Figure 3.2a), a temperature controller and a thermocouple equipped with the AFM (Figure 3.2c), optical microscopes (MX-51, Olympus Inc.) (Figure 3.2d), a cold cathode gauge (IKR 251, PFEIFFER Inc.), a scroll pump (ISP-250B, ANEST Iwata Inc.) and a molecular turbo pump (STP251S, BOC EDWARDS Inc.). The temperature of the sample stage and a cold finger were measured with a thermocouple and controlled with a heater set under the stage. The cold finger was cooled with liquid N_2 (~77 K) (Figure 3.2b). The pressure of the chamber of the AFM was evacuated and maintained less than 2.0×10^{-4} Pa during the measurements. To avoid the condensation of vapor onto the sample surface, the temperature of the cold finger was initially cooled to 273 K before the measurements, whereas the temperature of the sample stage was maintained above 273 K for a few minutes. This would lead to trapping atmospheric vapor on the cold finger as a cold trap. The deflection sensitivity of the cantilever was calibrated by indenting on a Si wafer substrate (Figure 2.4b; SI-500443, Nilaco Inc.).

Table 3.2 summarizes the combination of materials deposited on the tip of cantilever and Si wafer substrate in our experiments. As explained above in Sec. 2.2.1, Titan tholin or hydrothermal organics were deposited on an Au-coated Si tip (Figure 2.4a; SI-DF3-A, Seiko Instruments). Titan tholin, altered tholin, and hydrothermal organics were also deposited on a Si wafer substrate. The radius of the tip and the surface roughness of the samples on the Si wafer substrate was examined with a field-emission scanning probe microscope (FE-SEM) (LEO1550, ZEISS Inc.) and/or an AFM (Dimension Icon, Bruker Inc.) with the tapping mode as shown in

Chapter 2. The present study measured the cohesion force at temperatures of 118–300 K or 117–300 K for Si tip and Si wafer substrate coated with film of Titan tholin (Run #1 and Run #2) (Table 3.2). The cohesion force between Si tip coated with organic flake and Si wafer substrate coated with film of altered tholin was measured at temperature of 300 K (Run #3) (Table 3.2). The cohesion force for Si tip and Si wafer substrate coated with film of hydrothermal organics (Run #4) was measured at temperatures of 300 K (Table 3.2). As mentioned above in Chapter 2, this organic flake could be composed of film of Titan tholin or film of altered tholin because this flake was found after cohesion force measurement between Si tip without organics and film of Titan tholin and subsequent measurement between the tip and film of altered tholin. The measurements using a Si tip and Si wafer substrate without organic samples (Run #5), together with those using a Si tip coated with film of Titan tholin and Si wafer substrate without organic samples (Run #6), were also conducted to examine the deflection sensitivity (Table 3.2). Although the surface temperature of Titan is 90–95 K, the lower limit of the measurement temperature was 117 K. This is because the temperature of the sample stage was determined by the balance between the cooling by the cold fingers with liquid nitrogen (~77 K) and the ambient heat. The cohesion force at lower temperatures comparable to Titan's surface is estimated by extrapolating the obtained results using the measured activation energy of the cohesion force for the temperature range of 117–300 K. The cohesion force measurements were conducted at a scan duration of 3 seconds in the contact mode of the AFM. There was no significant change (e.g., less than 1 % of cohesion force) in the measured cohesion force for the scan durations of 0.3, 1, 3, 5, and 10 seconds. The force curve measurements were conducted 3–10 times in total at 2–5 different locations on the sample. The errors of cohesion force were calculated by standard deviation of all force curves measured at different timing and location at each temperature condition.

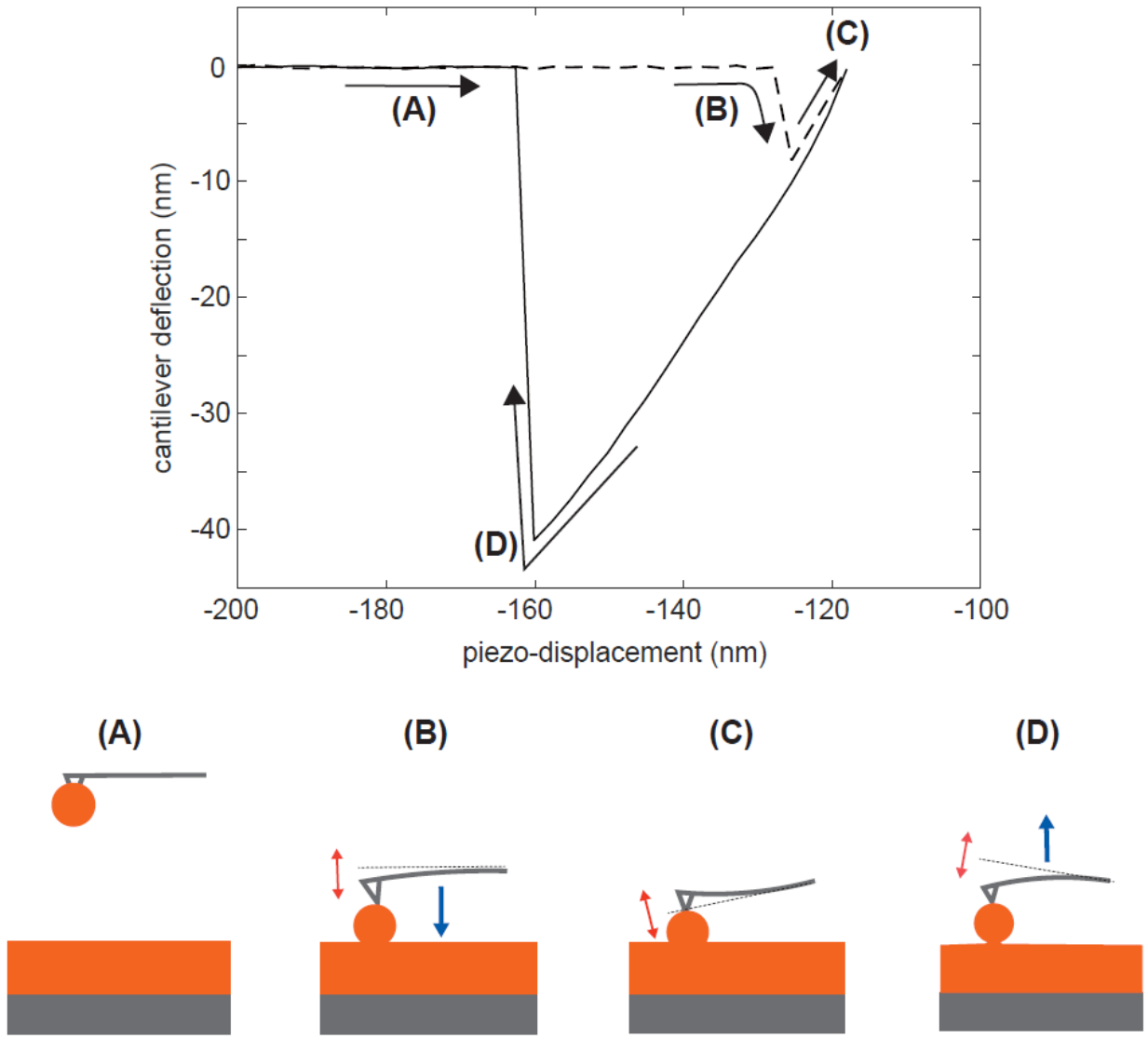

Figure 3.1 (upper) An illustration of force distance curve obtained with an AFM. The solid line represents the approaching phase, whereas the dashed line represents the retraction phase. (bottom) Schematic illustrations of interactions between a tip of cantilever and sample on a substrate during the force curve measurement. (A) The tip is approaching to the surface on substrate. (B) The tip snaps in the sample owing to the attractive force. (C) As the distance between the tip and sample becomes close, the cantilever is deflected due to the repulsive force. (D) The tip is pulled off the sample.

Figure 3.2 The experimental setup for the cohesion force measurement at cryogenic temperatures at AIST. (a) An atomic force microscope (AFM) (SII Nanonavi E-sweep, SII technology Inc.). (b) A cantilever holder and a sample holder indicated solid arrow and dashed arrow, respectively. (c) A temperature controller equipped with AFM and a monitor of a cold cathode gauge (IKR 251, PFEIFFER Inc.). (d) Optical microscopes (MX-51, Olympus Inc.)

Table 3.1 Summary of the calculated spring constants of the cantilever and each parameter of cantilever used each experimental run with Eq. (3.1) and Eq. (3.2). The quality factor Q_f and the resonant frequency f_r of the cantilevers were measured before and after cohesion force measurements as indicated in timing. The width of the cantilever b = 55 μm, the length of the cantilever L = 450 μm, the density of air ρ_{atm} = 1.3 kg/m^3, the dynamic viscosity of the air $\eta = 1.8 \times 10^{-5}$ Pa s were used.

Experimental Run#	timing	tip	Qf	fr (kHz)	Re	Γi(Re)	ks (N/m)
Run#1	before	Titan tholin film	-	-	7.4	1.3	-
	after	Titan tholin film	146	21.6	7.4	1.3	1.2
Run#2	before	Titan tholin film	154	21.2	7.3	1.3	1.2
	after	Titan tholin film	147	21.3	7.3	1.3	1.2
Run#3	before	Au-coated Si	179	24.5	8.4	1.2	1.7
	after	Titan tholin or Altered tholin	162	24.6	8.4	1.2	1.6
Run#4	before	hydrothermal organics	53.3	23.3	8	1.2	0.5
	after	hydrothermal organics	105	21.6	7.4	1.3	0.8

Table 3.2 Experimental conditions for AFM measurements at AIST. * Organic flake could be composed of Titan tholin or altered tholin. ** The order of the temperature indicates the order of the measurements.

Experimental Run#	deflection sensitivity at 300 K (mV/nm)	cantilever	tip	ks (N/m)	tip diameter (nm)*	sample	temperature (K)**
Run#1	4.58	SI-DF3-A	Titan tholin film	1.2	88±4	Titan tholin	300, 118, 210, 240, 270, 300, 270
Run#2	4.32	SI-DF3-A	Titan tholin film	1.2	83±5	Titan tholin	300, 210, 180, 153, 117, 153, 180, 210, 240, 270, 300, 270
Run#3	5.16	SI-DF3-A	Organic flake*	1.6	63±15	altered tholin	300
Run#4	1.5	SI-DF3-A	hydrothermal organics	0.8	192±25	hydrothermal organics	300
Run#5	4.59	SI-DF3-A	Au-coated Si	-	-	Si wafer	300
Run#6	5.63	SI-DF3-A	Titan tholin film	-	-	Si wafer	300

3.3 Results of the experiments

3.3.1. Cohesion force and the surface energy of Titan tholin

Figure 3.3 shows the temperature dependence of deflection sensitivity between (a) Si tip to Si wafer substrate without organic samples (Run #5) and (b) Si tip with Titan tholin to Si wafer substrate without organic samples (Run #6). These figures indicate that the deflection sensitivity decreases linearly with the slope of 0.003 independent of the materials of the tip. These results indicate that the deflection sensitivity decreases as the temperature decreases. Since the output of deflection of cantilever in the instrument is based on the deflection sensitivity at room temperature, it is needed to correct the deflection value by considering the deflection sensitivity at each temperature. The corrected deflection of cantilever at each temperature T was corrected by using equations as follows:

$$(corrected\ deflection) = (output\ of\ deflection) \times \frac{(deflection\ sensitivity\ at\ 300\ K)}{(deflection\ sensitivity\ at\ T\ K)}, \quad (3.7)$$

$$(deflection\ sensitivity\ at\ T\ K) = 0.003(T - 300) + (deflection\ sensitivity\ at\ 300\ K).$$

Figure 3.4 shows results of force curves for Si tip and Si wafer substrate with Titan tholin for different temperatures measured at Run #1 (Fig. 3.4a) and Run #2 (Fig. 3.4b), respectively. The cohesion forces are calculated by the spring constant of the cantilever k_s =1.2 N/m (Table 3.2) and corrected deflection sensitivity with Eq. (3.7). These results indicate that the deflection of the cantilever decreases as the temperature decreases. Since the spring constant of Si cantilever increases only a few percent at 117 K compared to 300 K (Cho, 2009; Shirai, 2013; Liu, 2020), the decreasing of deflection could be derived from the decreasing of cohesion force rather than the increasing of the spring constant of the cantilever. The shape of the force curve at 117 K is different from the force curves measured above 117 K. This would be derived from the intrinsic properties of instrument or the phase change of the sample. Given the cohesion force is defined as the force that is needed to separate materials, the cohesion force at 117 K could be the with considering of the temperature dependence of the deflection sensitivity.

As the temperature decreases, the jump-in of the cantilever tends to occur at smaller cantilever displacements (Figure 3.4). Three possible explanations for this tendency are as follows: 1) temperature dependence of scanner sensitivity, 2) deflection of cantilever due to the difference of thermal expansion coefficient of Si cantilever and film of Titan tholin, and 3) temperature dependence of intermolecular interaction would be responsible. To evaluate the impact of temperature changes on scanner sensitivity, the height change of a grating (STS2-440P, VLSI Standard Inc.) was measured using a cantilever (OMCL-AC200TS-R3, Olympus Inc.) in dynamic force microscopy (DFM) mode with an AFM system (Figure 3.2; SII Nanonavi E-sweep, SII technology Inc.). The results show that the errors remain within 1.7% across

different temperatures, indicating that the temperature dependence of the scanner sensitivity does not significantly affect the results. The thermal expansion coefficient of Si is approximately 10^{-9} K^{-1} (Middelmann et al., 2015), whereas that of amorphous carbon nitride—an analogous material to Titan tholin—is around 10^{-6} K^{-1} (Champi et al., 2002). This significant difference in thermal expansion coefficients likely contributes to the variation in the timing of the cantilever jump-in. Additionally, as discussed later, intermolecular forces may increase as temperature decreases, which could result from a reduction in the thermal energy of molecules (Awada et al., 2011).

The temperature dependence of the cohesion force calculated from the force curves (Fig. 3.4) is shown in Fig. 3.5 for Run #1 and Run #2, respectively. These figures indicate that the cohesion forces decrease as the temperature decreases for both experimental runs using Titan tholin. Using the obtained cohesion force together with the average diameter of the tip, the surface energy of Titan tholin can be obtained through Eqs. (3.3) and (3.5). As discussed later in Sec. 3.4.2, this value represents apparent surface energy, rather than the intrinsic surface energy. Figure 3.6 shows the temperature dependence of the surface energy of Titan tholin for Run #2 (Table 3.1). This figure shows that the surface energy follows an exponential law as temperature changes (the Arrhenius relationship). The fitted curve using the Arrhenius relationship can be expressed as following:

$$\gamma_s = \gamma_0 \exp\left(-\frac{E_{\text{surf}}}{R_{\text{gas}}T}\right), \tag{3.8}$$

where E_{surf} is the activation energy, R_{gas} is the gas constant of 8.31 J mol^{-1} K^{-1}, and T is temperature. The result of the least square fitting shows γ_0 = 180 ± 15 mJ m^{-2} and E_{surf} = 1780 ± 170 kJ mol^{-1}. All experimental results for Run #1 and Run #2 were summarized in Table 3.3.

3.3.2. Cohesion force and surface energy of altered tholin and hydrothermal organics

Figure 3.7a shows the typical result of a force curve measurement for Si tip with organic flake which composed of Titan tholin or altered tholin, and Si wafer substrate with altered tholin at Run #3, whereas Figure 3.7b shows the typical result of a force curve for Si tip with hydrothermal organics and Si wafer substrate with hydrothermal organics at Run #4. The cohesion force and the work of cohesion between Si tip with organic flakes and Si wafer substrate with altered tholin at 300 K are 63 ± 2.3 nN and 318 ± 77 mJ/m^2, respectively, with the tip diameter of 63 ± 15 nm. If the organic flakes are composed of altered tholin, the surface energy of altered tholin could be 159 ± 39 mJ/m^2 based on Eq. (3.5). On the other hand, if the organic flakes are composed of Titan tholin, the surface energy of altered tholin could be 226 ± 77 mJ/m^2 based on Eq. (3.6) and the surface energy of Titan tholin at 300 K obtained in experimental Run #2 (92 ± 6 mJ/m^2). The cohesion force and the surface energy of hydrothermal organics at 300 K are determined to be 69 ± 1.9 nN and 57 ± 8 mJ/m^2, respectively, with the tip

diameter of 192 ± 25 nm. All experimental results for Run #3 and Run #4 were summarized in Table 3.3.

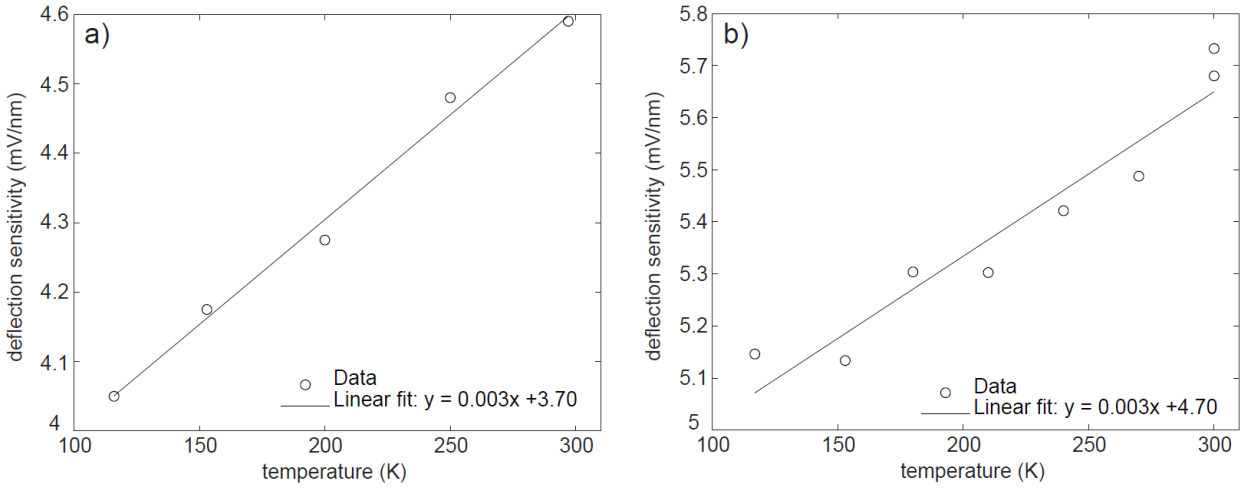

Figure 3.3 The results of Run #5 and Run #6 showing temperature dependence of the deflection sensitivity of (a) SI-DF3-A (Au-coated Si tip) and (b) Titan tholin tip to Si wafer substrate, respectively. Both results show the slope of the curve is 0.003, suggesting that the deflection sensitivity increases as the temperature increases linearly with the slope of 0.003 which does not depend on the presence of Titan tholin on the tip.

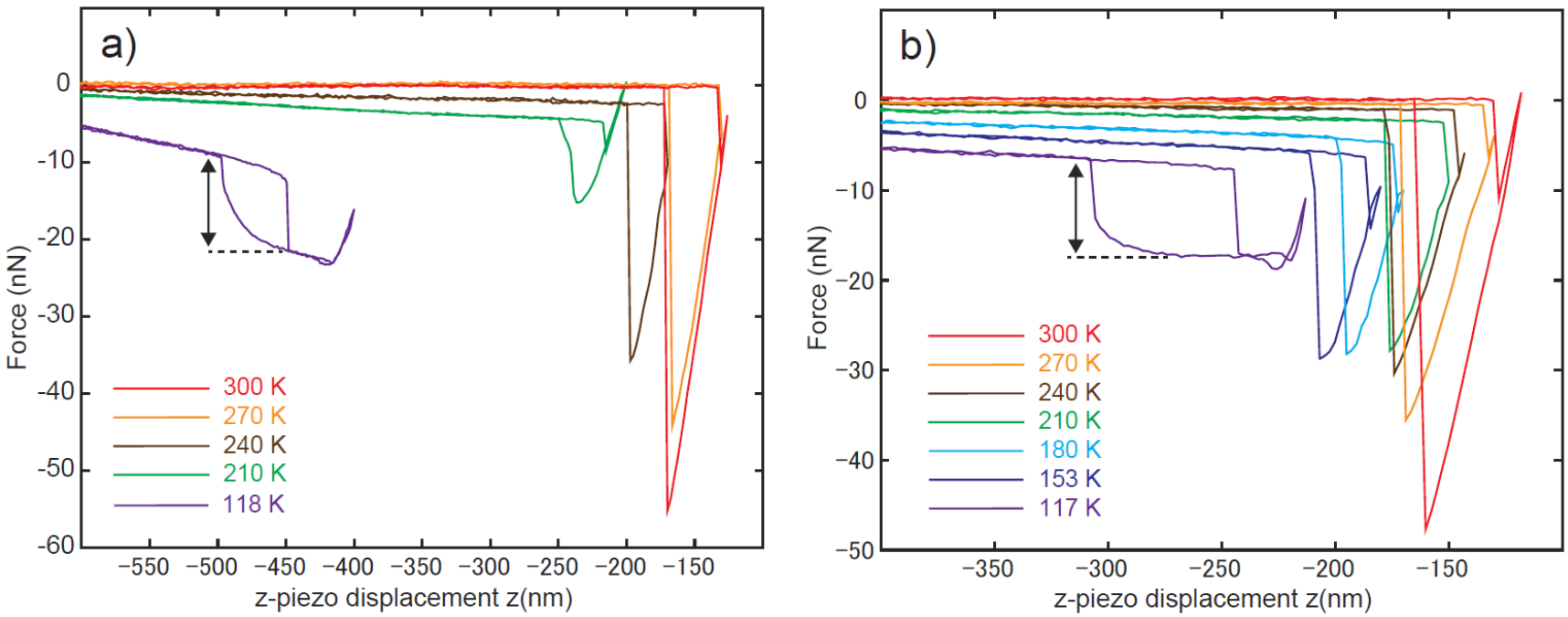

Figure 3.4 Typical results of force curves measured between Si tip and Si wafer substrate coated with Titan tholin at different temperature conditions in (a) Run #1 and (b) Run #2, respectively. Each color indicates the temperature condition of the measurement. The slope of the baseline increases as the temperature decreases. The black double arrows indicate the cohesion force at 117 or 118 K analyzed in the present study.

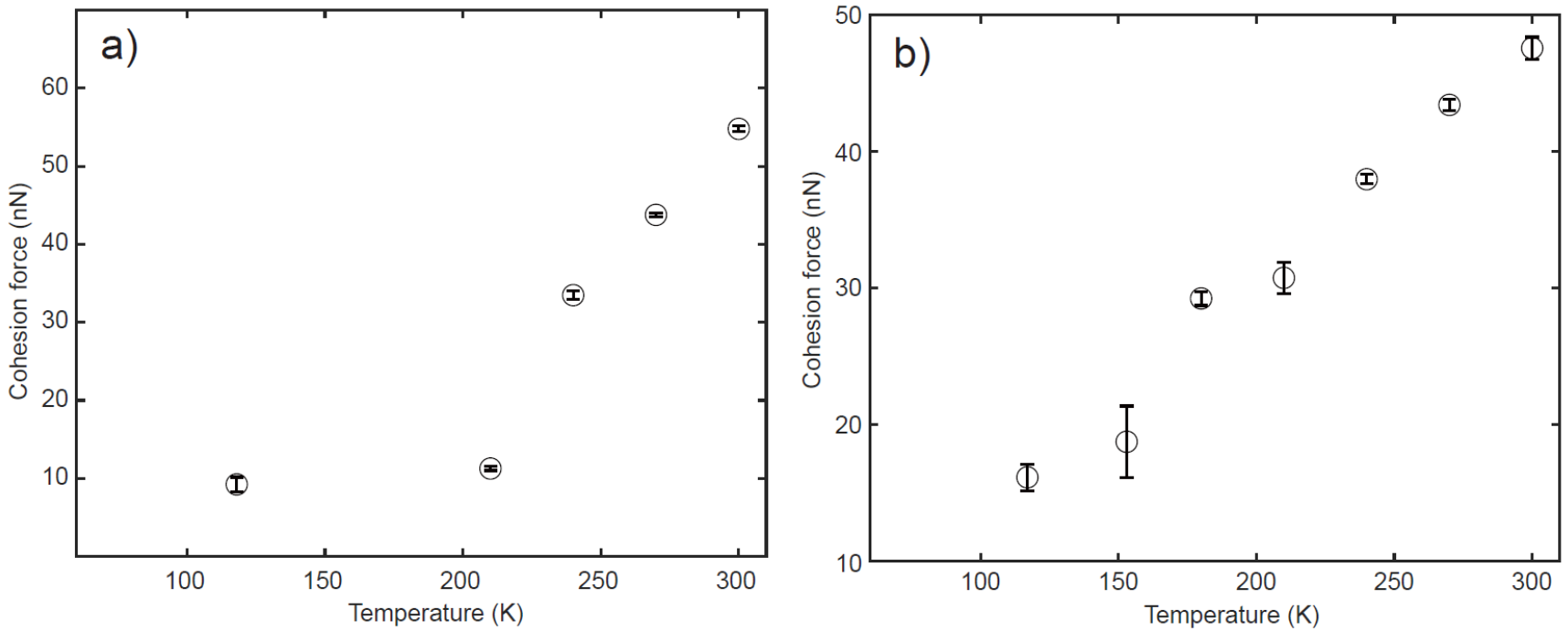

Figure 3.5 Temperature dependence of the cohesion force of Titan tholin obtained in (a) Run #1 and (b) Run #2, respectively. Circle shows the mean value of the cohesion force, whereas each bar shows the error of the standard deviation in each experimental Run. Both results indicate that the cohesion forces decrease as the temperature decreases.

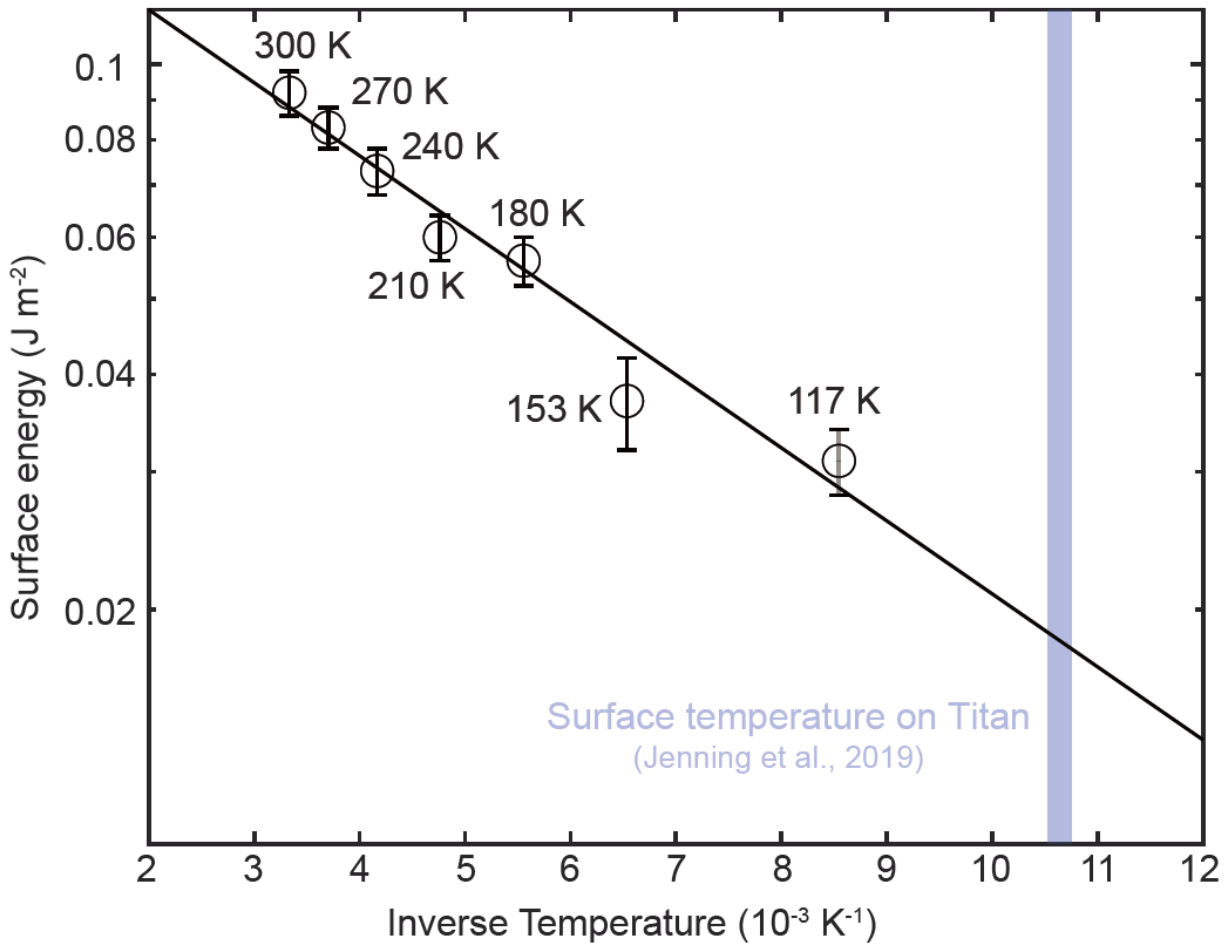

Figure 3.6 Temperature dependence of the surface energy of Titan tholin obtained in the present study. Circle shows the mean value of the cohesion force, whereas each bar shows the error of the standard deviation in Run #2. The blue region shows Titan's surface temperature (Jenning et al., 2019). The black curve shows the fitting results of Arrhenius equation with the value of γ_0 = 180 ± 20 mJ m^{-2} and E_{surf} = 1760 ± 190 kJ mol^{-1}, respectively.

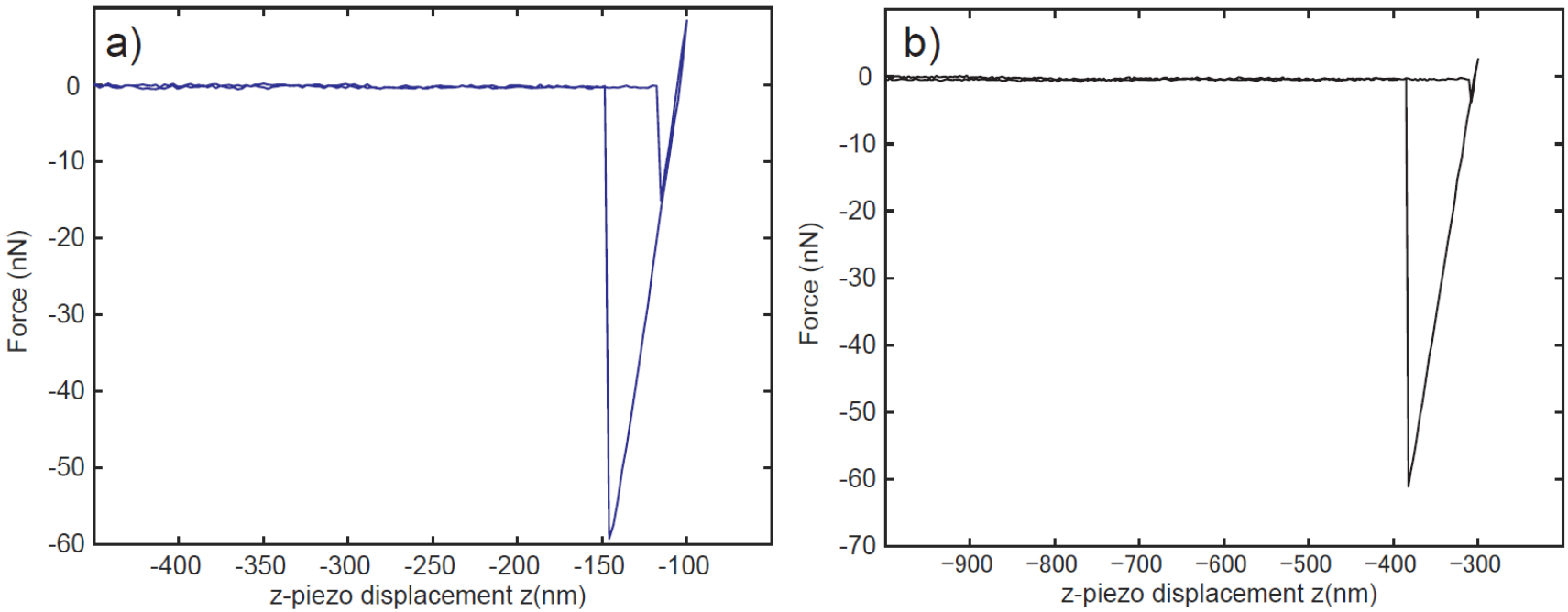

Figure 3.7 Typical results of force curve measurements of (a) altered tholin and (b) hydrothermal organics obtained in Run #3 and Run #4, respectively.

Table 3.3 Summary of surface energy (cohesion force) measurements in the present study. *The organic flakes on the tip of experimental Run #3 could be altered tholin or Titan tholin. For the former case, the surface energy of experimental Run #3 was calculated with Eq. (3.5), whereas, for the latter case, with Eq. (3.6) and the surface energy of Titan tholin obtained in experimental Run #2.

Experimental Run#	sample	temperature (K)	cohesion force (nN)	tip diameter (nm)	work of cohesion (mJ/m^2)	surface energy (mJ/m^2)
Run#1	Titan tholin	300	55±0.4	88±4	200±9	100±5
		270	44±0.2		159±7	80±4
		240	33±0.5		119±6	60±3
		210	11±0.3		40±2	20±1
		118	9.2±0.9		33±4	17±2
Run#2	Titan tholin	300	48±0.8	83±5	184±11	92±6
		270	43±0.4		165±10	83±5
		240	38±0.3		146±9	73±5
		210	31±1.1		119±8	60±4
		180	29±0.5		112±7	56±4
		153	19±2.6		73±9	37±5
		117	16±1		61±5	31±3
Run#3	altered tholin	300	63±2.3	63±15	318±77	159±39 or 226±77*
Run#4	hydrothermal organics	300	69±1.9	192±25	114±15	57±8

3.4. Discussion

In this section, we first discuss the uncertainty in our cohesion force and surface energy measurements (Sec. 3.4.1). Then, the temperature and structure dependence of cohesion force and surface energy are discussed, based on the comparison with the results reported in the previous studies (Sec. 3.4.2).

3.4.1. Uncertainty in the experiments

The uncertainties in the cohesion force and surface energy measurements derived from the uncertainties of spring constant of the cantilever k_s, deflection sensitivity of the cantilever, contact radius of the tip R, and the theory which is applied to derive surface energy.

As shown in the Sec. 3.2.1, the spring constants of the cantilevers are estimated from measured resonant frequency f_r and quality factor Q_f of the cantilevers, respectively. The difference of the estimated spring constants of Si tip with Titan tholin between before and after measurements for Run #2 are within 1 % (Table 3.1), suggesting that the contact of the tip to sample does not affect the surface condition of the tip significantly throughout cohesion force measurement, although the errors of the cohesion force at 153 K and 210 K are larger compare to that measured at other temperature conditions (Fig. 3.5). In Run #1, the spring constant of the cantilever was calculated based on the resonant frequency and quality factor of the cantilevers after measurement. Hence, the difference of the condition of the tip before and after measurements is not unclear. The surface energies of Titan tholin at 300 K and 270 K obtained both Run #1 and Run #2 are within 5 %, whereas those of Titan tholin below 240 K obtained both Run #1 and Run #2 are different significantly. The difference of the values of surface energy at each temperature could be derived from the change of the surface condition of the tip of the cantilever in Run #1 due to deposition of small organic flakes or ablation of the tip during measurement. The spring constant of the cantilever in Run #3 and Run #4 are changed before and after measurements within 5 % and 40 %, respectively. Given the 5 % of errors in Run #3, cohesion force and surface energy of altered tholin could be still larger than other organic materials. On the other hand, hydrothermal organic could show lower cohesion force and surface energy because spring constant of the cantilever $k_s = 0.8$ is the upper limit of the values of the tip with hydrothermal organics.

Deflection sensitivity at 300 K is measured at 2–3 times before each cohesion force measurement. The values are within ~5 %. In addition to this, as mentioned in Sec. 3.3.1, the temperature dependence of deflection sensitivity is considered to calculate deflection of cantilever at each temperature conditions. This error could be also within a few percent.

Therefore, the error of the deflection sensitivity does not change our experimental results of cohesion force measurements significantly.

The radius of the tip (shown in Table 3.2 and Table 3.3 as diameter of the tip) used for estimation of surface energy should be the upper limit of the contact radius. Therefore, the estimated surface energy is the lower limit of surface energy of each organic materials. Although the values of the estimated surface energy are subject to some uncertainty, the trend that the cohesion force of Titan tholin decreases with decreasing temperature, as shown in Figures 3.4 and 3.5, remains unaffected by the contact radius used in the analyses.

The present study analyzes the surface energy of each sample by applying DMT theory instead of JKR theory for simple approximation because Titan tholin has 9.7 ± 1.8 GPa of Young's modulus (see Chapter 4). On the other hand, the contact theory which can be applied to the materials could change depending on the elasticity of the materials following the elasticity parameter λ_E (Haugstad, 2012; Yu et al., 2017) as below:

$$\lambda_E = \frac{2.06}{\xi_0}\left(\frac{R^*{\gamma_s}^2}{\pi K^2}\right)^{1/3}, \tag{3.9}$$

where the interatomic distance ξ_0 = 0.16 nm, the reduced contact radius R*, the bulk modulus $\frac{1}{K} = \frac{3}{2}\frac{1-\nu^2}{Y}$, Y is the Young's modulus, the Poisson's ratio ν, and the surface energy γ_s. If $\lambda_E > 5$, JKR can be applied, whereas $\lambda_E < 0.1$, DMT can be applied. For Titan tholin at 300 K, the bulk modulus K and Poisson's ratio ν are ~7 GPa and ~0.27, respectively (see Chapter 4). Given the surface energy of Titan tholin γ_s is ~100 mJ m^{-2} and R is ~83 nm, the elastic modulus λ_E at 300 K of Titan tholin could be ~2.8. On the other hand, λ_E at 117 K could be different from the value at 300 K based on the temperature dependence of surface energy and elasticity constrained in the present study (Chapter 3 and Chapter 4); With the values of K ~14.7 GPa, ν ~0.27 (constant), γ_s = 31 mJ m^{-2}, R = 83 nm (constant), λ_E would be ~0.6. Therefore, our results would be intermediate; The cohesive property of Titan tholin at room temperature appears to be closer to JKR theory, whereas that at 117 K seems to be closer to DMT theory. Given the estimated surface energy by applying to JKR theory is 4/3 times higher than that of DMT theory, the surface energy of Titan tholin at higher temperature would be larger than the value obtained in the present study. Therefore, the activation energy obtained in the present study could be the lower limit of the activation energy of the surface energy of Titan tholin.

3.4.2. Temperature and structure dependence of cohesion force and surface energy

Temperature dependence: The experimental results of the previous studies on the cohesion force of H_2O ice (Musiolik and Wurm, 2019; Jabaud et al., 2024) and polymers such as

poly(n-butyl methacrylate) and polystyrene (Cappella and Stark, 2006) suggest that the cohesion forces decrease as the temperature decreases. Musiolik and Wurm, (2019) and Jabaud et al. (2024) attribute the decreasing of the cohesion force to the decreasing the surface energy, assuming the constant contact area. On the other hand, Cappella and Stark, (2006) have considered that the cohesion forces could be changed along with the changes of elastic-plastic properties; the decreasing of yielding forces along with increasing the temperature results in plastic deformations and increasing contact area.

However, there are several experimental studies on AFM measurements showing opposite temperature dependence (Awada et al., 2011; Nelson et al., 2003; Tambe and Bhushan, 2004; Lai et al., 2019). Awada et al. (2011) have measured cohesion force between Si tip modified with methyl ($-CH_3$) group and surface of cross-linked polydimethylsiloxanes (PDMS), whereas, other previous studies have measured cohesion force between Si tip and mica (Nelson et al., 2003), Si tip and Si wafer substrate (Lai et al., 2019), and Si_3N_4 tip and various sample including poly(dimethylsiloxane) (PDMS) and poly(methylmethacrylate) (PMMA) (Tambe and Bhushan, 2004) over the temperature range of 300–400 K. All their results indicate that the cohesion force decreases as the temperature increases.

Awada et al. (2011) attribute the temperature dependence to the decreasing of the intermolecular interaction between organic materials on the tip and sample due to increasing thermal energy of molecules. On the other hand, other previous studies (Nelson et al., 2003; Lai et al., 2019; Tambe and Bhushan, 2004) consider that these tendencies could be the evaporation of water film due to the increasing temperature. The atmospheric water would not affect the temperature dependence of cohesion force of Titan tholin because the temperature range of the measurement is 117–300 K.

Decreasing of cohesion force of Titan tholin with decreasing temperature following Arrhenius equation (Fig. 3.4 and Fig. 3.5) would be explained by three potential mechanisms; 1) A reduction in surface energy with decreasing temperature, as shown in Jabaud et al. (2024). 2) A decrease in the contact radius decreases due to increased elasticity as the temperature drops. 3) Energy dissipation caused by thermal activated molecular stick-slip process (Chaudhury, 1995; Kendall, 1975).

For the first case, the surface energy could increase as the temperature decreases. This is because the intermolecular forces between materials could be weakened due to increasing thermal energy as mentioned by Awada et al. (2011) and/or due to lower bond energy due to thermal expansion (Sun, 2007; Cheng et al., 2013; Zhang et al., 2019). Furthermore, according to Tyson, (1975), the surface energy can be described as below:

$$\gamma(T)A_m = \gamma(0)A_m - TS, \tag{3.10}$$

where $\gamma(T)$ and $\gamma(0)$ are the surface energy at temperature T and absolute zero, respectively, A_m is the molar surface area, and S is the entropy. This equation suggests the surface energy decreases as the temperature increases or the entropy increases, assuming the constant A_m. Indeed, the results of several studies show that the surface energy decreases as the temperature increases, based on theoretical model (Aqra and Ayyad, 2011; Beeler et al., 2020; Cheng et al., 2017; Schönecker et al., 2015; Xing et al., 2020; Magomedov, 2024), and experiments (Zhao et al., 2004). Consequently, it is unlikely that intrinsic changes in surface energy are responsible for the observed decrease in cohesion force with temperature.

For the second case, the decrease in cohesion force can be attributed to the reduction in contact radius caused by the increase in elasticity with decreasing temperature. This phenomenon can be explained by time-dependent strain. In this mechanism, the reduction in thermal energy limits the occurrence of thermally activated local rearrangements of side groups and short chain segments at "loose sites" within the amorphous structure, leading to an increase in elasticity (Gilbert et al., 1986). The temperature dependence of elasticity in this mechanism follows an Arrhenius-type equation. Given that Titan tholin is an amorphous material, it is plausible that this mechanism contributes to the observed decrease in cohesion force at lower temperatures.

For the third case, the decrease in cohesion force can be attributed to energy dissipation caused by a molecular stick-slip mechanism during separation. This process involves stress concentration at the edges of the contact interface, where the breaking and the formation of molecular bonds play a key role. When a molecular bond is broken due to an applied external force, the molecular chain reforms a bond with a nearby molecule. The time required for this process, known as the "unsettled life," depends on the thermal energy of the molecules and follows an Arrhenius-type relationship (Kendall, 1975; Chaudhury, 1996). Consequently, as temperature decreases and thermal energy is reduced, less frequent bond formation and breaking results in a lower cohesion force.

In summary, the observed temperature dependence of cohesion force can likely be attributed to either the second or third mechanism discussed above, both of which related to the observed Arrhenius-type behavior of cohesion force. It should be noted that the surface energy values presented in Sec. 3.3.1 represent apparent values, as they inherently include contributions from both molecular interactions and dynamic factors such as energy dissipation and mechanical cohesion.

The cohesion force measurements presented in this study carry significant uncertainty, as they are influenced by various factors, including molecular interactions, mechanical cohesion, and energy dissipation. To better constrain the mechanisms responsible for the temperature dependence of cohesion, further investigations are needed. The temperature dependence of viscoelastic properties of organic materials can be constrained by Dynamic Mechanical Analysis

(DMA) (e.g., Menard & Menard, 2020), rheometry (e.g., Ferry, 1980), and dielectric relaxation spectroscopy (e.g., Ngai & Roland, 1993) from room temperature to low temperatures. This approach allows us to determine whether the cohesion force follows the Arrhenius equation due to temperature-dependent behaviors in the viscoelastic modulus. Additionally, to examine the temperature dependence of cohesion due to interfacial stick-slip phenomena, i.e., frictional effects, it is necessary to examine the temperature dependence of frictional forces. This can be investigated using techniques such as Surface Force Apparatus (SFA) (e.g., Israelachvili et al., 2010) in addition to Atomic Force Microscopy (AFM) (e.g., Carpick & Salmeron, 1997).

Comparison with other materials: Figure 3.8 shows the comparison of the temperature dependence of apparent surface energy of Titan tholin and H_2O ice. Surface energy of H_2O ice decreases as the temperature decreases (Jabaud et al., 2024), which is also considered apparent surface energy. The difference in magnitude of apparent surface energy between two materials would be attributed to the differences in the surface roughness of H_2O ice grains used in Jabaud et al. (2024). This is supported by the fact that the intrinsic surface energy of Titan tholin and H_2O ice, as well as the elasticity of Titan tholin and H_2O ice below 300 K, are within a factor of 2 (Chapter 4).

Table 3.4 presents the surface energy of Titan tholin, altered tholin, and hydrothermal organics compared with that of other organic materials, measured using various experimental techniques, including AFM measurements (the present study), contact angle measurements (Li et al., 2022; Rahman et al., 2011; Israelachvili, 2011 and references therein), surface force balance (SFB) (van Engers et al., 2017), and the Brazilian Disc Test (Bischoff et al., 2020). Surface energy obtained using the same method, particularly contact angle and AFM measurements, is consistent within a factor. In contrast, surface energy derived from the Brazilian Disc Test differs by orders of magnitude. This discrepancy arises because surface energy estimated in the Brazilian Disc Test is calculated indirectly through tensile strength measurements, which are subject to significant error propagation inherent in the method (Bischoff et al., 2020).

Contact angle methods calculate surface energy based solely on intermolecular interactions, whereas AFM cohesion force measurements include additional effects, such as mechanical cohesion caused by energy dissipation from the rheological properties and the influence of molecular chains or shapes. Surface force balance (SFB) measurements, similar to AFM, also directly measure the force required to separate materials, using spring displacement to calculate surface energy. These factors contribute to higher measured cohesion forces and correspondingly elevated surface energy when compared to contact angle measurements.

In addition, Table 3.4 indicates that, within the same measurement method, surface energy tends to be higher when the C/H ratio is larger and the C/N ratio is smaller. This suggests that surface energy may be influenced by the abundance of unsaturated bonds and/or the

presence of nitrogen and oxygen. Indeed, Li et al. (2022) discussed that variations in the surface energy of organic materials arise from the contribution of polar components in their chemical structure. On the other hand, previous studies have shown that surface energy increases with molecular size, such as the number of polycyclic aromatic hydrocarbon (PAH) rings (Lechner and Sax, 2014). This is consistent with the higher surface energy of altered tholin, which has an aromatic-rich composition, compared to other organic materials. Although multiple factors in chemical structure can influence surface energy, if organic sand grains on Titan's surface contain highly polar structures, nitrogen-containing compounds, or large, aromatic-rich molecules, their surface energy could be higher by a factor of several compared to organic molecules composed purely of hydrocarbons.

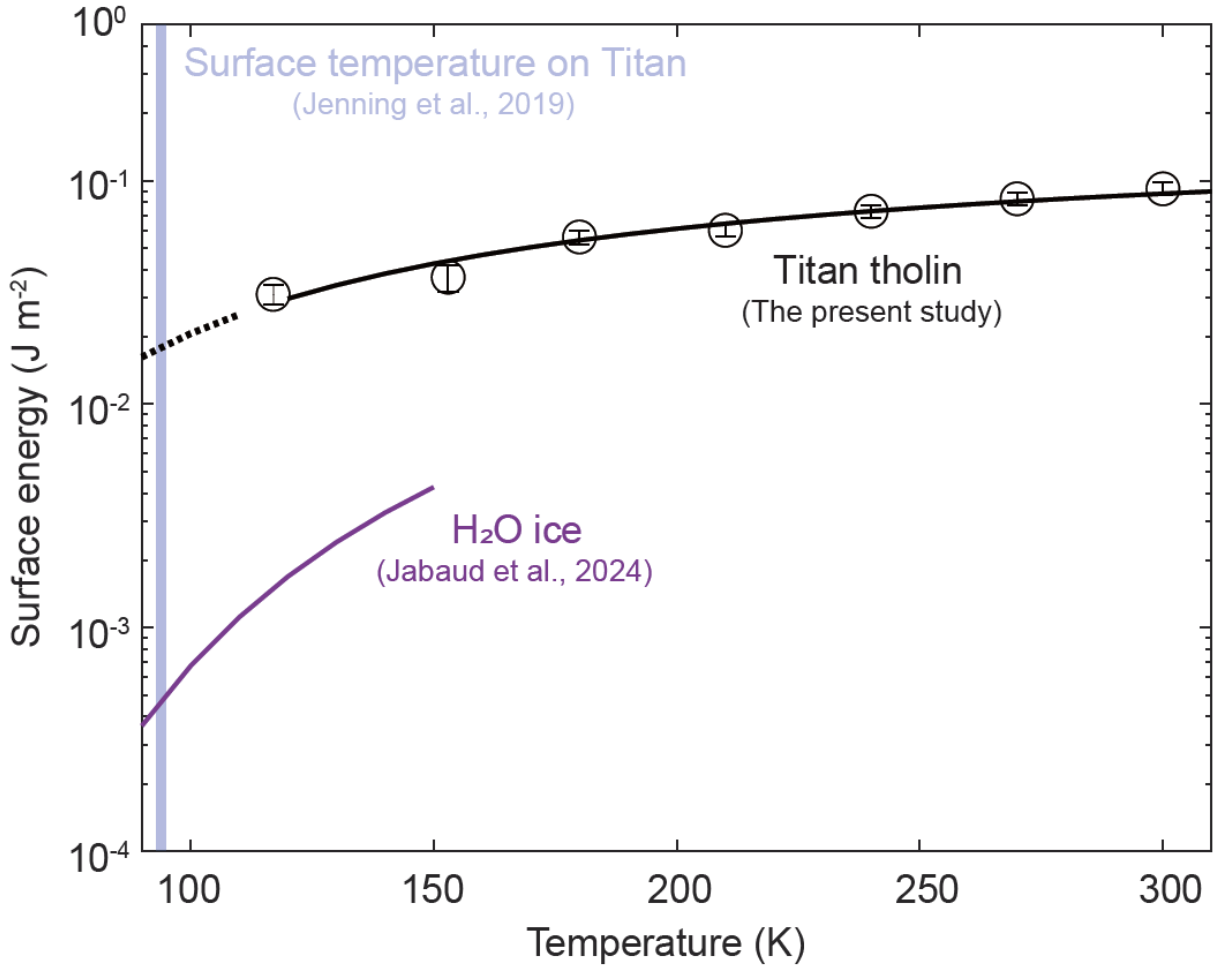

Figure 3.8 Temperature dependence of the surface energy of Titan tholin and H_2O ice (Jabaud et al., 2024). The surface energy of each material decreases as the temperature decreases. Titan tholin shows higher surface energy compared to H_2O ice over all temperature ranges.

Table 3.4 Surface energy values of various materials with C/H and C/N ratios where available. Measurement methods and references are also listed.

material	C/H	C/N	γ_s (mJ m^{-2})	method	reference
Titan tholin	0.7	2.1	100±5	AFM	this study
altered tholin	-	-	159±39 or 226±77	AFM	this study
hydrothermal organics	0.8	5.3	57±8	AFM	this study
Titan tholin	-	1.3	65.8±1.9	contact angle	Li et al. 2022
Titan tholin	-	2.4	53.4±5.2	contact angle	Li et al. 2022
ta-C:N	-	10	32	contact angle	Rahman et al. 2011
benzene	1	-	28	contact angle	Israelachvili 2011
cyclohexane	0.5	-	25	contact angle	Israelachvili 2011
paraffin	0.5	-	25	contact angle	Israelachvili 2011
graphene	-	-	115	surface force balance	van Engers et al. 2017
paraffin	0.5	-	3900 (900–2900)	Brazilian Disc Test	Bischoff et al. 2020
graphene	-	-	210 (150–560)	Brazilian Disc Test	Bischoff et al. 2020

3.5. Summary of Chapter 3

To reveal the temperature and chemical structure dependence of cohesion force and surface energy of Titan's organic analog materials, we performed 1) cohesion force measurements between Si tip and Si wafer substrate covered with Titan tholin over temperature ranges from 300 K to 117 K, and 2) cohesion force measurements between Si tip and Si wafer substrate covered with altered tholin or hydrothermal organics at 300 K by using atomic force microscope (AFM).

Our results suggest that the cohesion force of Titan tholin decreases as the temperature decreases. Given the surface energy of materials would increase with temperature drop, decreasing of contact radius due to increasing of the elasticity (see Chapter 4) and/or the energy dissipation caused by a molecular stick-slip mechanism during separation would be the plausible mechanisms to explain the temperature dependence of the cohesion force. The apparent surface energy of Titan tholin follows the Arrhenius equation with the γ_0 = 180 ± 20 mJ m^{-2} and the activation energy E_{surf} = 1760 ± 190 J mol^{-1}. Additional low-temperature measurements on other Titan's organic analog materials and/or constraints on the contact radius based on indentation depth are needed to clarify the contributions of different factors to the observed temperature-dependent behavior.

The surface energy of altered tholin is 159 ± 39 mJ m^{-2} or 226 ± 77 mJ m^{-2}. The surface energy of hydrothermal organics is determined to be 57 ± 8 mJ m^{-2}. These values are higher than the surface energies of Titan tholin reported in the previous studies measured by contact angle measurements. They are, however, comparable to the surface energy of graphene measured by surface force balance (SFB) and significantly lower than that of paraffin measured by the Brazilian Disc Test. These findings suggest that surface energy estimated from cohesion force measurements may be higher than values obtained from contact angle measurements. This difference likely arises from energy dissipation during separation, such as molecular stick-slip mechanisms, or mechanical adhesion effects, which are not accounted for in static contact angle measurements. Furthermore, a comparison of our results with surface energy values measured using different experimental techniques indicates that surface energy is influenced by multiple factors, including elemental ratios such as C/H and C/N, the abundance of unsaturated bonds, and molecular size. If organic sand grains on Titan's surface contain highly polar structures, nitrogen-containing compounds, or large, aromatic-rich molecules, their surface energy could be several times higher than that of organic molecules composed purely of hydrocarbons.

Chapter 4. Elastic wave velocities of Titan's organic analog materials

4.1 Background of Chapter 4

The shallow subsurface structure on Titan is largely unknown, despite their importance in the past and present meteorology, fate of organics on Titan, and replenishments of the atmospheric CH_4 (see Chapter 1). The subsurface structures include the thickness and inter-structure of organic sediments (dunes), the mixing ratio of H_2O ice and organic materials, and liquid CH_4 aquifer, and the presence of evaporite layer.

NASA's Dragonfly mission will investigate the subsurface structure on Titan with active seismic survey using the onboarded seismometer (Lorenz et al., 2018; 2021; Barnes et al., 2021; MacKenzie et al., 2021). To quantify the subsurface structure, the physical properties, such as elastic wave velocities, of Titan's organic materials are required. Elastic wave velocity can be estimated from a density, Young's modulus, and Poisson's ratio of a material (e.g., Mavco et al., 2009). Many studies performed the density measurements of laboratory analogs of Titan's organic materials (e.g., Titan tholin) (Yu et al. 2023 and references therein); whereas, only a few studies have measured Young's modulus and Poisson's ratio at room temperature (Yu et al., 2017; 2018). There have been no measurements of these parameters at low temperatures, comparable to Titan's surface. In addition, given that the frequency range of the seismometer onboard NASA's Dragonfly is 0.1–10 Hz, which is significantly different from the frequency ranges of laboratory or synchrotron experiments, the frequency dependence of the elastic wave velocity in organic materials should be investigated.

In the present study, two independent methods were applied to measure the elastic wave velocities of Titan's organic analog materials: inelastic X-ray scattering (IXS) method and ultrasonic pulse transmission method. In IXS method, acoustic wave velocities were estimated by determining phonon dispersion, momentum transfer dependence of phonon excitations in materials (e.g., Dorner et al., 1987; Burkel et al., 1987, 2000; Fåk & Dorner, 1997; Sette et al., 1998; Baron et al., 2000). Small amounts of samples (~1 mm^3) were needed to apply this method. Furthermore, phonon excitations can be observed at any energy and momentum transfer. However, available beamlines for IXS experiments are very limited all over the world. On the other hand, by applying the ultrasonic pulse transmission method, P-wave and S-wave velocities can be measured directly based on the determination of their travel times through a sample of known thickness, using waves generated by a piezoelectric transducer (e.g., McSkimin, 1950; Spetzler et al., 1993; Li et al., 1996; Chen et al., 1996; Higo et al., 2009; 2018). This technique can be performed on a laboratory scale. However, the results from ultrasonic measurements reflect not only the intrinsic material properties but also the bulk structures of the sample, as the longer wavelengths of ultrasonic waves could be affected by small structure of samples. By

comparing the results of the IXS method (THz) and the ultrasonic method (MHz), the frequency dependence of the elastic wave velocity can be constrained.

These methods have been applied to measure the elastic wave velocities of materials relevant to Earth's interior under extreme conditions, such as high temperature and high pressure. For instance, the elastic wave velocities of minerals and metals under conditions comparable to those in the Earth's deep mantle, the core-mantle boundary, or the core have been extensively investigated using the IXS method (Fiquet et al., 2004; Shibazaki et al., 2012; Yoneda et al., 2014; Nakajima et al., 2015; Kuwayama et al., 2020; Ikuta et al., 2023) and the ultrasonic method (e.g., Li & Liebermann, 2014, and references therein). However, to the best of our knowledge, elastic wave velocities have not been experimentally measured at cryogenic temperatures comparable to Titan's surface (~93 K) in the context of Earth & Planetary Science. Furthermore, for organic materials relevant to planetary science, no measurements have been conducted even at room temperature.

Here, we investigated phonon dispersion of Titan tholin and hydrothermal organics at 300 K in IXS method to estimate the acoustic wave velocity and elastic properties of these organic materials. Furthermore, phonon dispersions Titan tholin at cryogenic temperature were investigated to reveal the temperature dependence of acoustic wave velocity and intrinsic elastic properties of Titan tholin. On the other hand, P-wave and S-wave velocities of Titan tholin and hydrothermal organics were determined to investigate the modulus of both organic materials. In Sec. 4.2, we describe the methodology of the IXS and ultrasonic pulse methods. In Sec. 4.3, the results of both experiments are shown. In Sec. 4.4, we discuss the material, temperature, and frequency dependence of elastic wave velocities of the organic analogs.

4.2 Methods of elastic wave velocity measurement

4.2.1. Sample preparation

Sample size for IXS experiments must be large enough compared to beam size. Sample thickness for IXS experiments must be smaller than the tolerance of the spectrometer, if X-ray penetration depth of samples is large. Since the beam size at the sample position of BL35XU in SPring-8 is about 0.1 mm in diameter and measured sample is nearly transparent in X-rays for IXS measurements, a few millimeter diameter and 2 mm thickness of the samples in maximum are acceptable for IXS measurements at BL35XU of SPring-8. Particles of Titan tholin and solids of hydrothermal organics (see Chapter 2) were compressed to form pellet samples with 3 mm of diameter and approximately 2 mm of thickness for IXS measurements (Figure 4.1b,c) to obtain sufficient signal rates. On the other hand, the pellets for ultrasonic method were prepared using the same process but with a thickness of approximately 100 μm. The compression was conducted using a hydraulic press (Mini-Pellet Press, Specas Inc.). Pellet of solid of hydrothermal organics was formed under forces of ~700 MPa for 30 sec, whereas pellets of Titan tholin particles were formed under forces of ~700 MPa for 30 sec (Titan tholin A) or ~500 MPa for 30 sec (Titan tholin B), respectively. The density of Titan tholin pellet was determined by measuring the mass of pellet with an electronic balance and the volume of pellet. See Chapter 2 for the characterization of chemical structure of Titan tholin particles and solid of hydrothermal organics.

4.2.2. Inelastic X-ray scattering (IXS) method

Principle of determination of elasticity in IXS method: In the IXS method, acoustic wave velocity of a material can be determined by constraining phonon dispersion, the relationship between energies (angular frequency ω) and momentum (wave number Q) of phonon (lattice vibration), through investigation for the interaction of phonon and X-ray photon (e.g., Burkel, 2000). Incident X-ray can be scattered inelastically (with energy transfer) due to the excitation of phonons (e.g., Dorner et al., 1987; Burkel et al., 1987; Burkel, 2000). With the incident X-ray beam of Energy E_1 and wavevector k_1, and the scattered beam of E_2 and wavevector k_2, the energy and momentum transfer of inelastic scattering of X-ray by interaction with phonons can be described as below (Fig. 4.2a: e.g., Burkel, 2000):

$$\hbar\omega = E_1 - E_2, \tag{4.1}$$

$$\hbar\vec{Q} = \hbar\overrightarrow{k_1} - \hbar\overrightarrow{k_2}, \tag{4.2}$$

where $\hbar$ is Dirac constant ($\hbar = h/(2\pi)$ = 1.054 × 10^{-34} J s), ω is the energy (angular frequency) of phonon, Q is the momentum (wavenumber) of phonon, $\hbar\omega$ is the energy transfer, and $\hbar\vec{Q}$ is the momentum transfer. Q can be described as below (e.g., Burkel, 2000):

$$Q = \left|\overrightarrow{k_2} - \overrightarrow{k_1}\right| = (4\pi/\lambda)\sin\left(\frac{2\theta}{2}\right) = 2k_1\sin\left(\frac{2\theta}{2}\right), \tag{4.3}$$

where 2θ is scattered angle of beam, k_1 is the incident wavenumber of X-ray, and λ is the wavelength of X-ray. Phonon dispersion can be constrained by measuring energy transfer at multiple scattered angles.

Based on the equation of motion of one-dimensional coupled-vibration model of lattice vibration (Fig. 4.2b), the phonon dispersion, the relationship between angular frequency ω and the wavenumber Q of phonon, can be described as below:

$$\omega = 2\sqrt{\frac{k}{m}}\sin\left(\frac{Qa}{2}\right), \tag{4.4}$$

where a is the spacing of the lattice plane, m is the mass of each atom, and k is the spring constant between atoms.

Figure 4.2c shows an example of the phonon dispersion curve over the range between 0 and π/a (so-called the first Brillouin zone). Given the unit of Q is the inverse of the distance, the wave number Q = π/a and $Q \rightarrow 0$ corresponds to the unit cell scale and the macroscopic scale, respectively. Given the slope of the phonon dispersion curve corresponds to the group velocity of phonons, the acoustic wave velocity V_p of a material at macroscopic scale can be described as below (e.g., Fiquet et al., 2004; Shibazaki et al., 2012; Nakajima et al., 2015; Kuwayama et al., 2020):

$$V_\mathrm{p} = \left(\frac{d\omega}{dQ}\right)_{Q\rightarrow 0}. \tag{4.5}$$

Background of IXS measurements: As described later, IXS spectra (phonon spectra), the intensity of scattering X-ray as a function of energy transfer and momentum transfer, are obtained by measuring photon flux scattered with angle 2θ in IXS measurements (e.g., Baron, 2000). The scattering cross-section for a photon to be scattered into a solid angle dΩ and into some energy bandwidth dE can be described as below (e.g., Burkel, 2000; Baron, 2015):

$$\frac{d^2\sigma}{d\Omega dE} = \left(\frac{E_2}{E_1}\right) {r_e}^2 (\boldsymbol{e}_1 \cdot \boldsymbol{e}_2)^2 \cdot S(\boldsymbol{Q}, \omega), \tag{4.6}$$

where r_e is the classical electron radius (r_e = 2.818 × 10^{-13} cm), $\boldsymbol{e}_1$ and $\boldsymbol{e}_2$ are the polarization of X-ray beam before and after scattering, $S(\boldsymbol{Q}, \omega)$ is the dynamical structure factor of crystal. The

term of $(E_2/E_1){r_e}^2(\boldsymbol{e}_1 \cdot \boldsymbol{e}_2)^2$ represents the Thomson scattering cross-section. The dynamical structure factor $S(\boldsymbol{Q}, \omega)$ governs the transition for inelastic scattering. $S(\boldsymbol{Q}, \omega)$ due to phonon excitation in crystals can be described as below (e.g., Burkel, 2000; Baron, 2015):

$$S(\boldsymbol{Q},\omega) = \sum_j \left| \sum_d f_d(\boldsymbol{Q}) \cdot e^{-W_d}[\boldsymbol{Q} \cdot \boldsymbol{e}_d(\boldsymbol{Q},j)] {M_d}^{-\frac{1}{2}} \cdot e^{-i\boldsymbol{Q}\cdot\boldsymbol{r}_d} \right|^2 \times \frac{\langle n(\omega_{\boldsymbol{Q},j},T)\rangle + \frac{1}{2} \pm \frac{1}{2}}{\omega_{\boldsymbol{Q},j}} \delta(\omega \mp \omega_{\boldsymbol{Q},j}), \tag{4.7}$$

where $f_d(\boldsymbol{Q})$ is the atomic form factor of the dth atom at position $\boldsymbol{r}_d$, M_d is its mass, and e^{-W_d} is the Deby-Waller factor to account for bond strength of each atom. The dot product $\boldsymbol{Q} \cdot \boldsymbol{e}_d(\boldsymbol{Q},j)$ represents the projection of the normalized phonon eigenvector $\boldsymbol{e}_d(\boldsymbol{Q},j)$ in the phonon in the mode j with phonon wavevector $\boldsymbol{Q}$ for atom d. Note that for amorphous materials such as Titan tholin, the wavenumber Q is expressed as a scalar rather than as a wavevector $\boldsymbol{Q}$. The term $\frac{\langle n(\omega_{\boldsymbol{Q},j},T)\rangle + \frac{1}{2} \pm \frac{1}{2}}{\omega_{\boldsymbol{Q},j}} \delta(\omega \mp \omega_{\boldsymbol{Q},j})$ represents the probability of phonon excitation normalized by phonon energy $\omega_{\boldsymbol{Q},j}$ due to phonon creation (annhilation). $\langle n(\omega_{\boldsymbol{Q},j},T)\rangle$ is the Bose (occupation) factor and can be described as below (e.g., Burkel, 2000; Baron, 2015):

$$\langle n(\omega_{\boldsymbol{Q},j},T)\rangle = \left(\exp(\hbar\omega_{\boldsymbol{Q},j}/k_BT) - 1\right)^{-1}, \tag{4.8}$$

where T is the temperature, k_B is the Boltzmann constant (k_B = 8.617333262 × 10^{-5} eV K^{-1}). This equation describes that phonons follow Bose-Einstein statistics. The probability of excitation of phonon decreases with decreasing temperature because Bose factor decreases as the temperature decreases. The probability term for phonon excitation in Eq. (4.7) indicates that the probability of phonon creation is greater than that of annihilation. Inversely, the temperature can be estimated from the ratio of the scattering intensity due to phonon creation (Stokes scattering) to that due to annihilation (anti-Stokes scattering).

Momentum transfer dependence of the dynamical structure factor has been investigated to obtain phonon dispersion relations in materials. The IXS spectrometer can also be applied to investigation of static structure factor, say diffraction pattern. When the energy transfer is zero in dynamical structure factor, S(Q, 0) provides elastic contribution of S(Q, ω). Since angle dependence of elastic X-ray scatteroing means diffraction patterns, momentum transfer dependence of S(Q, 0) provides diffraction patterns in materials.

Experimental setups & conditions: The measurements were performed at the beamline of BL35XU in SPring-8. The details of the beamline were described elsewhere (e.g., Baron et al., 2015). Figure 4.3 shows the beam path for IXS measurements at the beamline BL35XU. Initially, the X-ray beam was generated in-vacuum linear undulator system of 4.5 m insertion

devices composed of 32 mm period and 8 mm minimum magnetic gap (Baron, 2000). A roughly monochromatic X-ray beam (~20 keV) was obtained by reflection from a pair of Si (1 1 1) and a pair of Si (4 0 0) monochromators and directed toward the backscattering monochromator. To perform energy scan, the energy of the monochromatic X-ray beam was varied around 21.747 keV with a resolution of 1.5 meV by reflecting on the temperature-controlled backscattering monochromator of Si (11 11 11) (Baron et al., 2000). The reflected X-ray beam was focused onto the sample position through a cylindrical mirror. Avalanche photo diode (APD) was placed upstream (apd3) and downstream (apd2) of sample position to measure the photon flux before and after X-ray scattering. The angle of the goniometer was varied between each measurement to vary the scattered angle 2θ. The scattered beam was passed through slit and analyzed by the 12 analyzers composed of small blocks of perfect silicon ($0.6 \times 0.6 \times 3$ mm^3) glued to a spherically curved substrate (Baron et al., 2000), placed from 10 m of distance with different scattered angle simultaneously. The scattered angles between the top four and the down four analyzer were nearly identical (Fig. 4.3). The scattered beam was only reflected on the analyzers when Bragg conditions are satisfied. The signals were detected by a Cadmium Zinc Telluride (Cd Zn Te) detector placed near the sample.

In the present study, scattered beam was analyzed by the 12 spherical Si analyzers at 1–3 different angles of goniometer, which corresponds to 12–36 independent spectra with 8–24 independent scattered angles (momentum transfer) between 1.97 nm and 11.45 nm. The slits, positioned 6 m away from the sample, were set to an aperture size of 50 mm in both the vertical and horizontal directions, resulting in a momentum resolution $\Delta Q \sim 0.9$ nm^{-1}. According to Eq. (4.7), Stokes and anti-Stokes scattering are expected to appear in positive and negative energy transfer symmetrically due to the sample's energy gain (loss) associated with the creation (annihilation) of phonons. Therefore, the range of energy scan was set to -10 to 25 meV or -10 to 30 meV for $2\theta = 2.062°$, -10 to 30 meV for $2\theta = 2.409°$, and -10 to 30 meV or -10 to 40 meV for $2\theta = 4.861°$ of the goniometer. Measurement time for each spectra is between 1 and 6 hours, depending on the signal rate and scan range at each scattering angle. It also took about 3 hours to measure resolution function of each analyzer, which also provides correction factors of reflectivity in each analyzer crystal. In addition, since the raw data of the spectra in each sample includes signal scattered from the sample area, background measurements are required, which took about 2–4 hours. All experimental conditions were summarized in Table 4.3.

In addition to the dynamical structure factor $S(Q, \omega)$ measurements, $S(Q, 0)$ of Titan tholin at each temperature condition was measured to investigate the temperature dependence of lattice structure of Titan tholin. In these measurements, the intensity of elastic scattering was measured from with various scattered angle 2θ (various momentum transfer) from 2.062° to 9.106°.

Figure 4.4 shows a schematic illustration and pictures of our measurements at room temperature (hereafter setup A). This chamber was initially developed by Sekimoto et al (2019) to minimize the background caused by scattering from the beryllium (Be) window and air. This was achieved by using a polyimide (Kapton) window and purging the chamber with an inert gas, such as helium (He). In addition to minimizing background, we used the chamber to prevent alteration of the samples by atmospheric H_2O and O_2. The chamber of ~100 mm of diameter with ~150 mm of height was placed at sample position in the beamline (Fig. 4.3). The chamber was connected to a He gas cylinder through a tube and connected to the ambient atmosphere. The interior of the chamber was purged with He gas at a rate of a few cm^3 per minute during the experiment. The sample was set in a 3 mm-diameter hole of the sample holder at the center of the chamber (Figure 4.4c). The sample holder, designed by the present study, was made of a Cu substrate (Cu1020) with width of 25 mm, height of 15 mm, and thickness of 2 mm. To prevent the detection of small-angle X-ray scattering from the air around the sample, a collimator was placed upstream of the sample at a distance of 2.5 mm from the sample (Sekimoto et al., 2019). The collimator was made of tantalum (Ta), as materials with a high atomic number, such as Ta, can effectively attenuate X-rays. The incident X-ray beam was focused on the sample holder with an ellipse-shape beam size of 40–50 μm in vertical and 80–100 μm in horizontal. The tolerance of X-ray beam at the sample is about 100 μm. The energy resolution for the experimental setup of Fig. 4.4 was ~1.5 meV. The resolution function was measured using scattering from borosilicate glass (Tempax) (Ishikawa & Baron, 2021). A polyimide film (Kapton, DU PONT - TORAY Inc.) was used to fix the sample on the sample holder. To avoid both oxidization of the sample and atmospheric scattering due to H_2O and CO_2, the chamber was purged with He gas at a constant flow rate (a few cm^3 per minute) continuously during measurements.

Figure 4.5 shows a schematic illustration of our experimental setup for low-temperature measurements (hereafter setup B). The sample was set in a sample holder (Figure 4.5b-g), which was made of Cu (C1020, AS ONE). The sample holder, designed by the present study, had three holes with 3 mm diameter aligned vertically to the sample and two holes with 2 mm diameter in the bottom, the latter of which was connected with a Ta collimator (Figure 4.5d-g). The collimator had three holes with 0.6 mm in the vertical direction and 0.3 mm in the horizontal direction. These holes were aligned vertically and used to collimate the X-ray beam. The collimator also had two holes with 2 mm of diameter below the sample holder (Figure 4.5d-g). The incident X-ray beam was focused on the sample holder with an ellipse-shape beam size of 40–50 μm in vertical and 80–100 μm in horizontal. The tolerance of X-ray beam at the sample is about 100 μm. The sample holder was set to a chamber with a Be window (Figure 4.5a). To enhance the thermal conductivity, the chamber was purged by 1 bar of He gas at room temperature. This was also important to avoid the oxidization of the sample. The temperature of

the sample holder was controlled with a cold head and heater (within 1 K precision) (Figure 4.5a). The temperatures at the top of the sample holder and the bottom of the cold head were monitored (Figure 4.5a). The temperatures of the measurements were set to be 93, 140, 190, 240, and 300 K. The energy resolution was ~1.5 meV. To evaluate the effects of pressure of formation of Titan tholin pellets, irradiation of X-ray, heating-and-cooling cycles, oxidation due to exposure to the atmosphere, and the heterogeneity of the sample, the measurements were performed to different pellets, and the same pellet at multiple positions on the same sample and at the same location before and after cooling (Table 4.3).

Analyses of IXS spectra: As described above, the IXS spectrum is directly related to the dynamical structure factor, as shown in Eq. (4.7), although wavenumber is treated as scalar for amorphous materials such as Titan tholin and hydrothermal organics. The dynamical structure factor consists of terms that are either unrelated or related to phonon energy. At a certain momentum transfer, the energy-independent term can be expressed as a constant value, while the energy-dependent term represents the contribution from phonon excitations. The latter is composed of the probability of phonon excitation and a delta function corresponding to phonon excitation energy. In addition to the inelastic scattering contribution, an elastic scattering peak appears at zero energy transfer. Ideally, both elastic and inelastic peak would be described by a delta function. However, problems related to energy and momentum resolution are inevitable in X-ray scattering experiment. IXS experiments employ analyzer response, which consists of high-energy resolution optics placed upstream of the sample and analyzer placed downstream of the sample. Consequentry, observed IXS spectra contain finite linewidth, which is always wider than resolution of the spectrometer. (e.g., Ishikawa & Baron, 2021). Furthermore, spectral broadening also occurs due to phonon and electron lifetime effects, which reflect the average time a phonon or electron remains in an excited state before scattering. As a result, the actual IXS spectrum is expressed as the sum of elastic and inelastic scattering contributions, both of which can be described using a pseudo-Voigt function, combination of Lorentzian and Gaussian components (Wertheim et al., 1974), with the Bose factor for the inelastic term analytically written as follows:

$$I_{\text{elastic}}(\mathrm{Q},\omega) = I_0(Q)\left\{\frac{1}{\pi}\frac{f_{\mathrm{LF}}\left(\frac{\Gamma_n^{\mathrm{LF}}}{2}\right)^2}{\omega^2+\left(\frac{\Gamma_n^{\mathrm{LF}}}{2}\right)^2}+(1-f_{\mathrm{LF}})\frac{1}{\sqrt{2\pi}\sigma_n^{\mathrm{GF}}}\exp\left(-\frac{\omega^2}{\left(\sigma_n^{\mathrm{GF}}\right)^2}\right)\right\} \quad ,(4.9)$$

$$I_{\text{inelastic}}(Q,\omega) = \sum_j I_j(Q) \left\{ \frac{1}{\pi} \frac{f_{\text{LF}} \left(\frac{\Gamma_j^{\text{LF}}}{2} \right)^2}{\left(\omega - |\omega_{\text{j}}|\right)^2 + \left(\frac{\Gamma_j^{\text{LF}}}{2} \right)^2} \right.$$
$$\left. + (1 - f_{\text{LF}}) \frac{1}{\sqrt{2\pi}\sigma_j^{\text{GF}}} \exp\left(- \frac{\left(\omega - |\omega_{\text{j}}|\right)^2}{\left(\sigma_j^{\text{GF}}\right)^2} \right) \right\} \frac{BF(\omega_{\text{j}}, T)}{\omega_{\text{j}}}, \quad (4.10)$$

$$\Gamma_i^{\text{LF}} = 2\sqrt{ln2}\sigma_i^{\text{GF}} \ (i = n, j), \quad (4.11)$$

$$BF(\omega_{\text{j}}, T) = \begin{cases} \dfrac{\exp\left(\frac{\omega_{\text{j}}}{k_{\text{B}}T}\right)}{\left\{\exp\left(\frac{\omega_{\text{j}}}{k_{\text{B}}T}\right) - 1\right\}} & (\omega > 0), \\ \dfrac{1}{\left\{\exp\left(\frac{\omega_{\text{j}}}{k_{\text{B}}T}\right) - 1\right\}} & (\omega < 0), \end{cases} \quad (4.12)$$

where ω_j is the energy of j$^{\text{th}}$ phonon mode, Γ_i^{LF} is the full width at half maximum (FWHM) in the Lorentzian function, σ_i^{GF} is the FWHM in the Gaussian function, f_{LF} is the ratio of the Lorentzian function and the Gaussian function of resolution function, $I_0(Q)$ is the intensity of the elastic contribution, $I_j(Q)$ is the phonon intensity of j$^{\text{th}}$ phonon mode, and $\Delta\omega$ is the offset of the peaks from the zero energy transfer. In reality, observed spectra may be shifted by offset of the sample position and alignment of the spectrometer.

The measured IXS data with samples were subtracted using the data without sample. This was done because the raw IXS spectra includes the contribution of scattering not only from the sample but also from Be window and polyimide film, as indicated in the blank spectra. In general, the phonon energy of an optical mode is much higher than that of an acoustic mode. Specifically, the minimum phonon energy of an optical mode of Titan tholin can be expected to be approximately 60 meV, as the minimum Raman shift of Titan tholin was observed around 500 cm^{-1} in a previous study (Bernard et al., 2006). Since the energy range of the IXS measurements in the present study is limited to 40 meV, the contribution of optical phonon modes to the IXS spectra would be considered negligible. Therefore, we assumed that each subtracted IXS spectrum $S(Q, \omega)$ is mainly composed of three peaks: One is a quasi-elastic contribution near

zero energy transfer, and the others are a pair of inelastic contributions of Stokes and anti-Stokes components.

Based on the Eq. (4.4), the phonon dispersion should follow a sine curve as below:

$$\omega = A_s \sin(B_s Q), \tag{4.13}$$

where A_s is the energy of the phonon in meV at $Q = \pi/a$, and B_s is the half of the spacing of the lattice plane [m] (see Eq. (4.4)). These constants were determined by fitting of phonon dispersion with Eq. (4.13) by least-square method. Then, V and the error δV of the sample was determined by equations as below:

$$V = A_s B_s \frac{1/4.13567 \times 10^{12}}{1/(2\pi \times 10^{-9})}, \tag{4.14}$$

$$\delta V = \sqrt{(A_s \delta B_s)^2 + (B_s \delta A_s)^2} \frac{1/4.13567 \times 10^{12}}{1/(2\pi \times 10^{-9})}, \tag{4.15}$$

where δA_s and δB_s are the error of the least square fitting of phonon dispersion with Eq. (4.13). Here, 1 THz = 4.13567 meV, (unit of wavenumber) = $1/(2\pi)$ nm^{-1} were considered.

As mentioned later, the acoustic wave velocity estimated in the present study was V_p based on the comparison with the results obtained in ultrasonic pulse transmittance method. The longitudinal modulus M and the error δM of the sample was calculated as below;

$$M = \rho V_\mathrm{p}^2, \tag{4.16}$$

$$\delta M = M \sqrt{\left(\frac{\delta V_\mathrm{p}}{V_\mathrm{p}}\right)^2 + \left(\frac{\delta \rho}{\rho}\right)^2}, \tag{4.17}$$

where ρ and $\delta\rho$ are the density and the error of the sample.

4.2.3. Ultrasonic pulse method

Principle: In this method, ultrasonic pulse generated at the front side of a sample passes through the sample and reaches to the back side. Elastic wave velocities (i.e. longitudinal P-wave velocity and transverse S-wave velocity) are directly obtained by dividing a thickness of the samples over a travel time of elastic waves. The elastic modulus, including bulk modulus K, shear modulus G, Young's modulus Y, and Poisson's ratio ν, and each error δK, δG, δY, and $\delta\nu$ could be extracted from the measured P-wave velocity Vp, S-wave velocity Vs, and the density ρ, and each error $\delta\rho$, δV_p, and δV_s as below (Mavco et al., 2009);

$$K = \rho \left(V_\mathrm{p}^2 - \frac{4}{3} V_\mathrm{s}^2\right), \tag{4.18}$$

$$\delta K = K\sqrt{\left(\frac{\delta V_\mathrm{p}}{V_\mathrm{p}}\right)^2 + \left(\frac{\delta V_\mathrm{s}}{V_\mathrm{s}}\right)^2}, \tag{4.19}$$

$$G = \rho V_\mathrm{s}^2, \tag{4.20}$$

$$\delta G = G\sqrt{\left(\frac{\delta \rho}{\rho}\right)^2 + \left(\frac{\delta V_\mathrm{p}}{V_\mathrm{p}}\right)^2}, \tag{4.21}$$

$$Y = \frac{\rho V_\mathrm{s}^2\left(3V_\mathrm{p}^2 - 4V_\mathrm{s}^2\right)}{V_\mathrm{p}^2 - V_\mathrm{s}^2}, \tag{4.22}$$

$$\delta Y = Y\sqrt{\left(\frac{\delta \rho}{\rho}\right)^2 + \left(\frac{\delta V_\mathrm{p}}{V_\mathrm{p}}\right)^2 + \left(\frac{\delta V_\mathrm{s}}{V_\mathrm{s}}\right)^2}, \tag{4.23}$$

$$\nu = \frac{V_\mathrm{p}^2 - 2V_\mathrm{s}^2}{2\left(V_\mathrm{p}^2 - V_\mathrm{s}^2\right)}, \tag{4.24}$$

$$\delta \nu = \nu\sqrt{\left(\frac{\delta V_\mathrm{p}}{V_\mathrm{p}}\right)^2 + \left(\frac{\delta V_\mathrm{s}}{V_\mathrm{s}}\right)^2}. \tag{4.25}$$

Experimental setup and conditions: The elastic wave velocity measurements with the ultrasonic pulse method were conducted at the beamline BL04B1 in SPring-8. Figure 4.6a,d show the schematic diagram and the picture of the experimental system. Our experimental setup was similar to that of the previous study (Higo et al., 2018). The experimental setup was composed of a pulse generator (33210A, Agilent Inc.), a high-frequency waveform generator (AFG3251C, Tektronix Inc.), a low noise post-amplifier (7T142-4029A, Thamway), a digital oscilloscope (MDO4104C, Tektronix Inc.), an attenuator (920-N732AC, Yuuetsu-Seiki Inc.), a duplexer (N120-3069A, Thamway Inc.) and a cell assembly as a sample holder (Figure 4.6b,c). A sine burst wave was generated from the pulse generator 1000 times per second, following generation of three cycles of sine waves (40 MHz, 60 MHz, or 80 MHz for each experimental condition) by the waveform generator. These waves were amplified by the amplifier and entered the sample cell through the duplexer. Reflected waves were observed by the oscilloscope through the attenuator and duplexer, whereas the transmitted waves were observed by the oscilloscope directly (Figure 4.6d). The cell assembly was composed of a cylinder, piezoelectric transducers, and buffer rods. Crystaline $LiNbO_3$ (10°-Y Cut $LiNbO_3$: Yamaju ceramics Inc.) was used as the piezoelectric transducer (Figure 4.6e) because $LiNbO_3$ shows resonant frequency of S-wave around 40 MHz and P-wave velocity around 60 MHz, which result in the formation of high amplitude of transmitted wave.

We measured elastic wave velocities without sample, SiO_2 and NaCl samples as references, and Titan tholin and hydrothermal organics at room temperature. The thickness of the samples was measured to be 410 μm for NaCl, 1310 μm for SiO_2, 127 μm for Titan tholin, and 171 μm for hydrothermal organics using a micrometer. The sample was located in-between the buffer rods (Figure 4.7a). Elastic wave of burst sine signals with frequencies of 40, 60, and 80 MHz were generated at the front side of the rod (Figure 4.7a). Part of wave reflected at the boundary between the sample and rod. The reflected wave was detected at the front side of the rod with the oscilloscope after passing through attenuator, duplexer (Figure 4.7a). Part passed through the sample and reached the back side of the opposing rod. The wave passing through the sample and rods was detected at the back side of the opposing rod with the oscilloscope. Waveform detected with the oscilloscope was recorded as an average of 512 times burst signals. Travel time of wave was determined by cross correlation methods, which is the method to measure the similarity between two waveforms as a function of time. At the time where the maximum amplitude of cross correlation was analyzed. The elastic wave velocities were determined by dividing the sample thickness by the travel time.

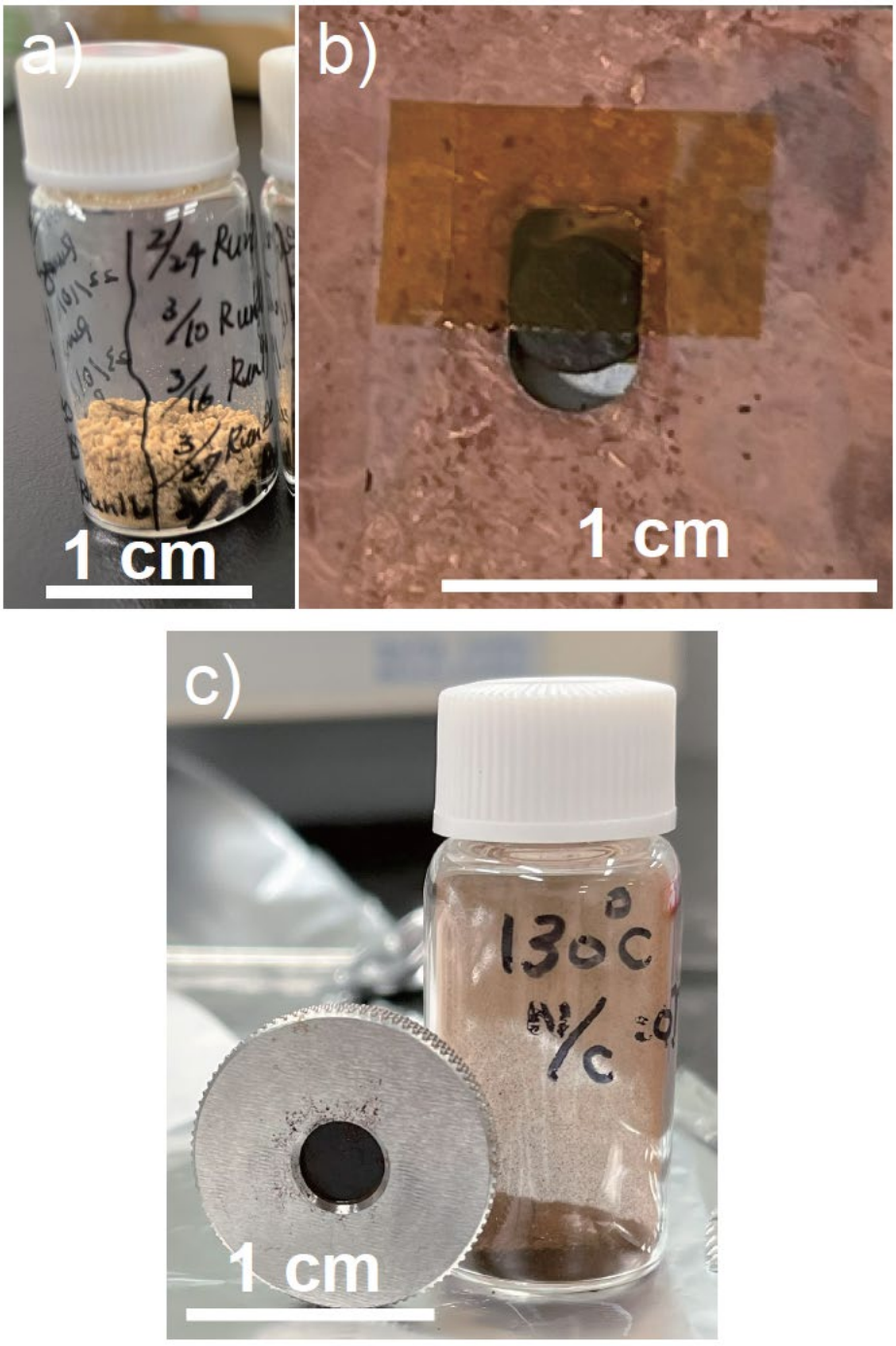

Figure 4.1 (a) Titan tholin particles and (b) pellet, and (c) hydrothermal organic particles and pellet measured in the present study.

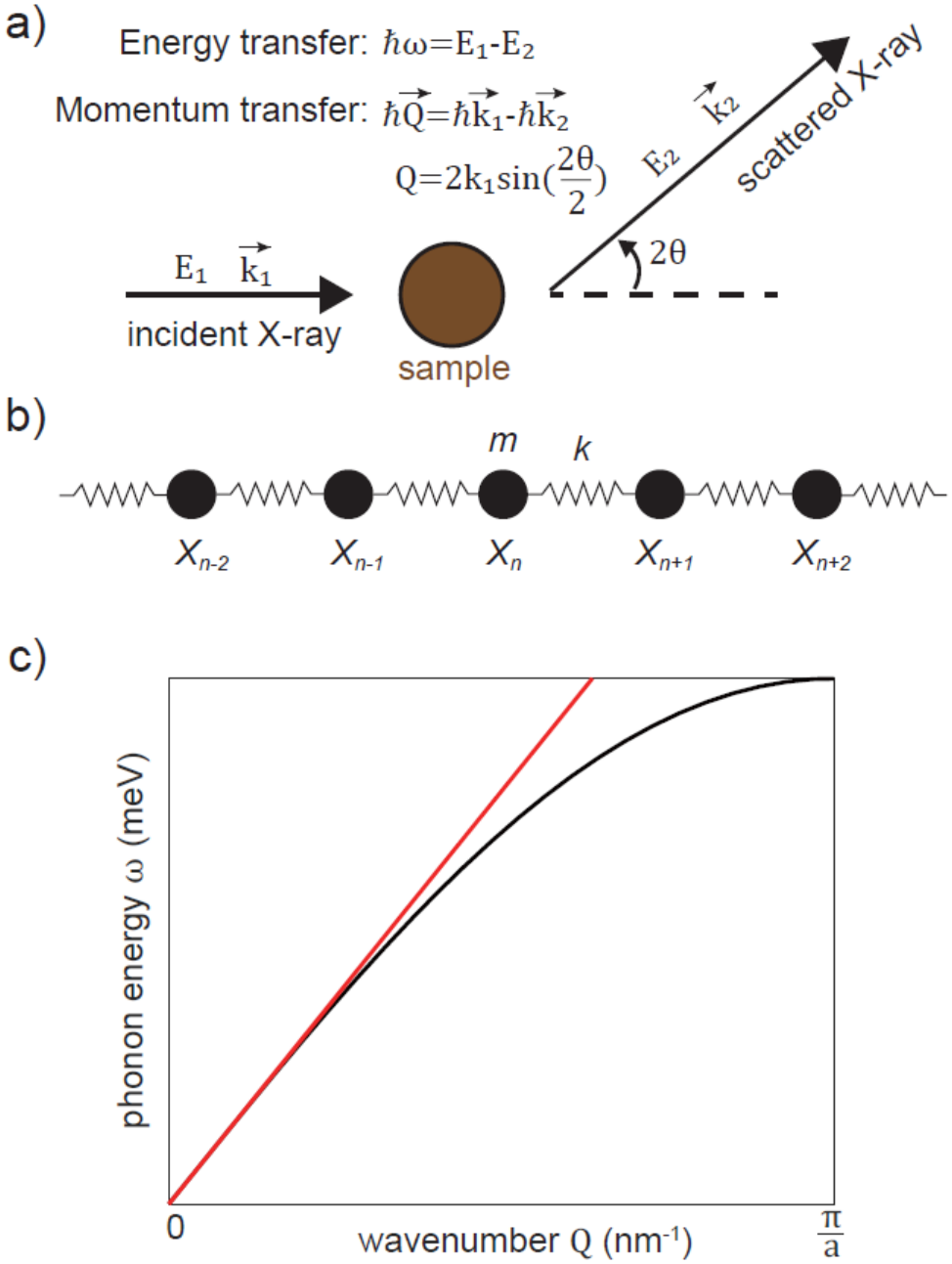

Figure 4.2 (a) Schematic diagram of the principle of IXS measurements. The phonon dispersion of sample was constrained by investigating the energy transfer $\hbar\omega$ at a given momentum tranfer $\hbar\vec{Q}$ between incident X-ray and scattered X-ray. (b) Schematic diagram of the one-dimensional spring-mass model of lattice vibration. The solution of the equation of motion for X_n corresponds to Eq. (4.4). (c) Black line indicates the phonon dispersion curve as a solution of the spring-mass model given Figure 4.2 (b). Red line indicates the slope of the phonon dispersion curve of the spring-mass model at $Q \rightarrow 0$, which corresponds to V_p of a material at macroscopic scale.

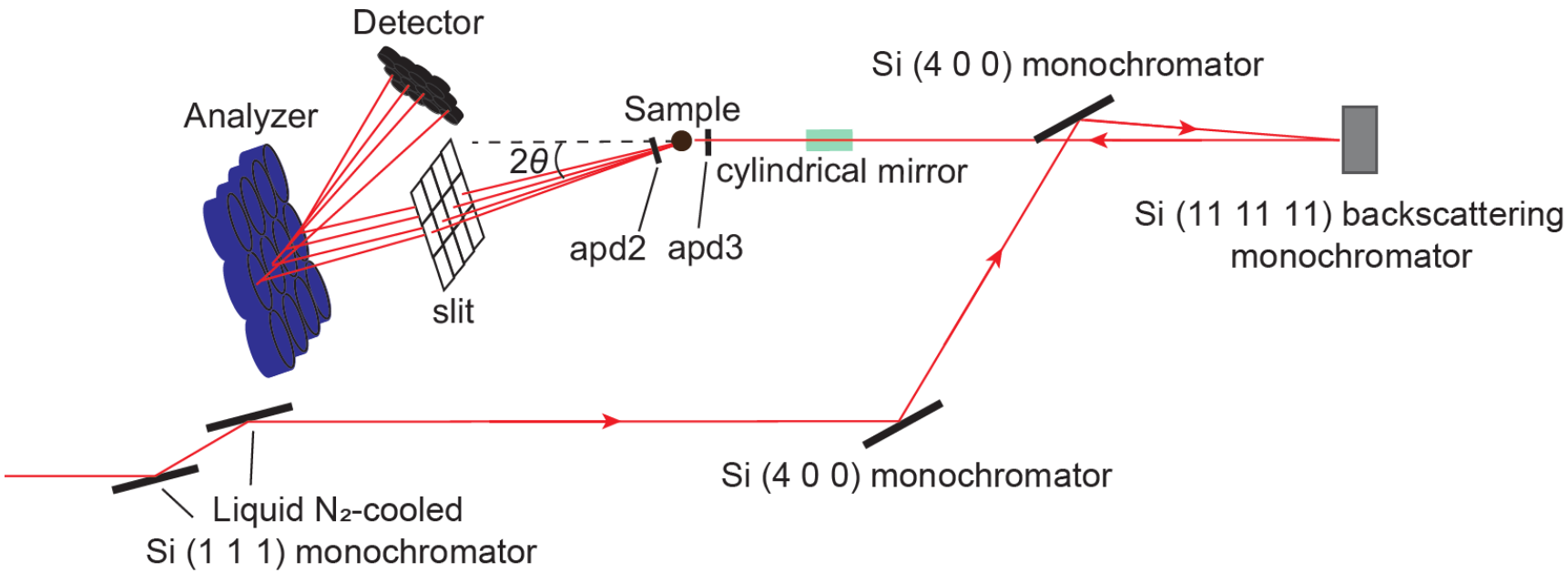

Figure 4.3 Schematic illustration of X-ray beam path (red line and arrows) for IXS measurement at beamline of BL35XU at SPring8 (BL35XU Inelastic X-ray Scattering Setup, http://bl35www.spring8.or.jp/ixs/ixs.html). X-ray beam was reflected on a set of channel cut crystals of Si(4 0 0) placed upstream of the backscattering monochromator. To perform energy scan, the energy of the monochromatic X-ray beam was varied around 21.747 keV with a resolution of 1.5 meV by reflecting on the temperature-controlled backscattering monochromator of Si (11 11 11) (Baron et al., 2000). The reflected X-ray beam was reflected on a cylindrical mirror to focus the beam onto the sample position. Avalanche photo diode (APD) was placed upstream (apd3) and downstream (apd2) of sample position measure the photon flux before and after X-ray scattering. The scattered beam was passed through slit and analyzed by the 12 analyzers with the scattered angle 2θ. The scattered photons reflected on the analyzers were detected by a Cadmium Zinc Telluride (Cd Zn Te) detector.

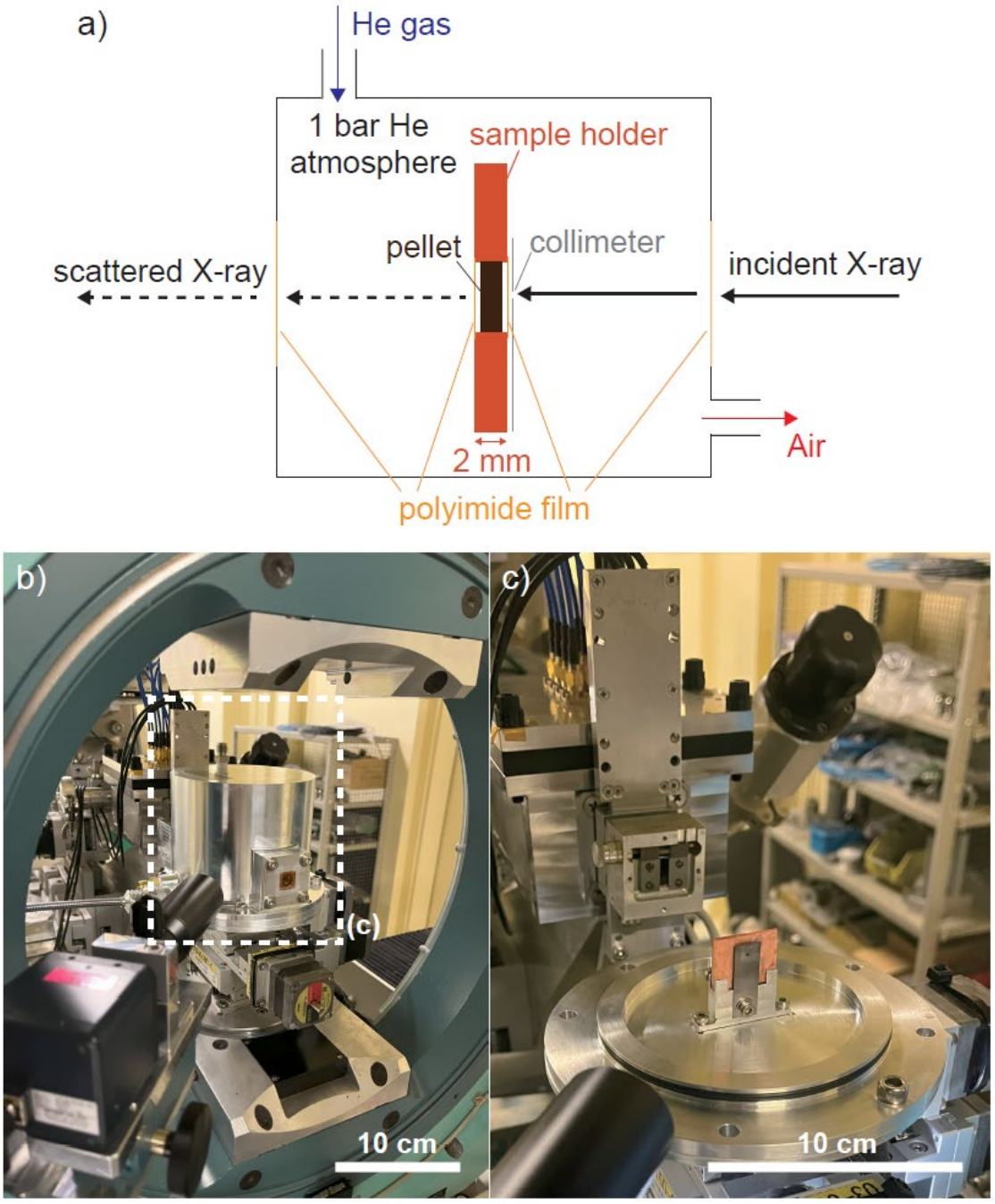

Figure 4.4 (a) A schematic illustration IXS measurements at room temperature (setup A). The sample was set in a 3 mm-diameter hole of the sample holder at the center of the chamber. To avoid both oxidization of the sample and atmospheric scattering due to H_2O and CO_2, the chamber was purged with He gas. The incident X-ray beam was focused on the sample position with an ellipse-shape beam size of 78 μm in the horizontal direction and 100 μm in the vertical direction. (b) A pictures of the chamber. White dashed rectangular indicates the location of (c). (c) A picture of the inside of the chamber with sample holder and collimeter.

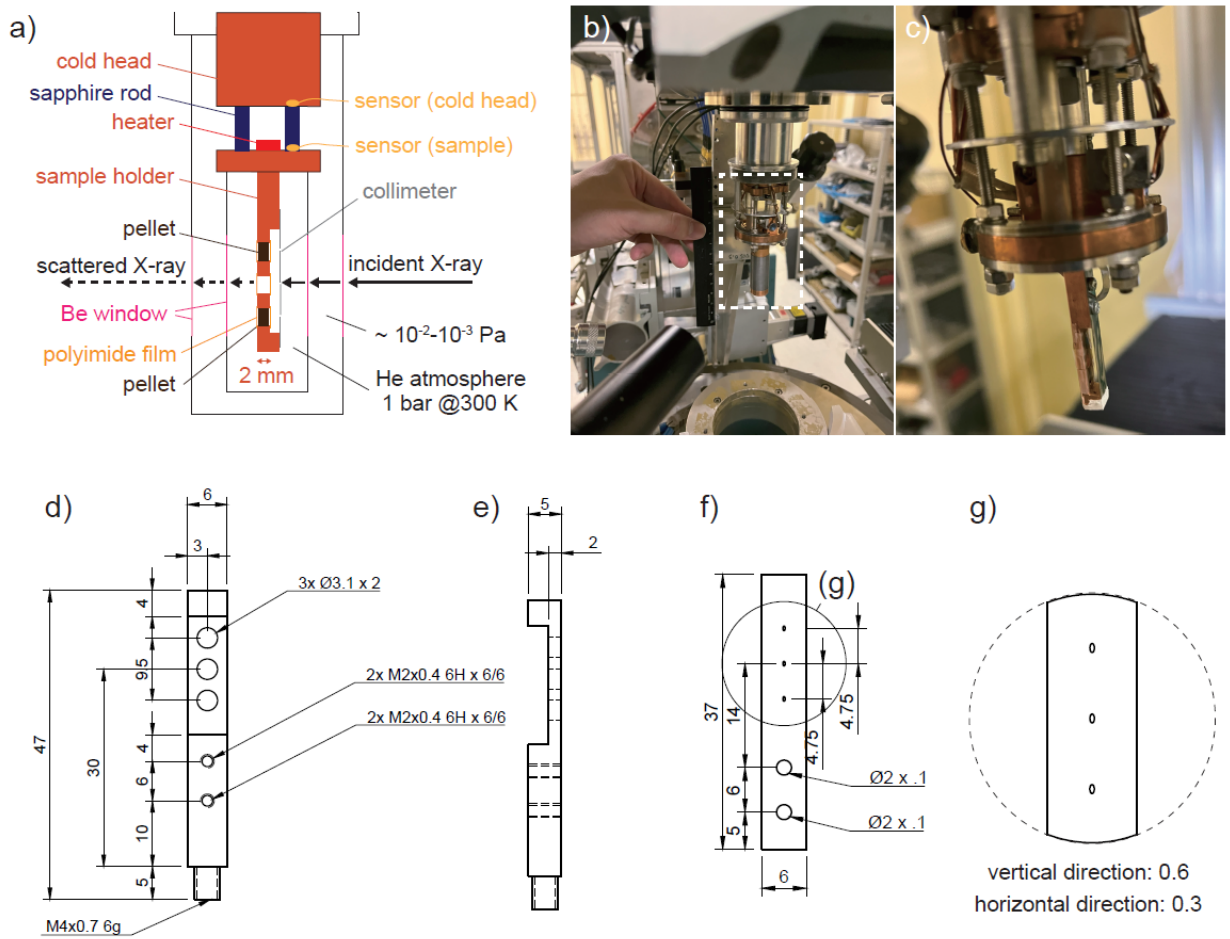

Figure 4.5 (a) A schematic illustration and (b, c) pictures of experimental setup for low-temperature measurements (setup B). The sample was set in a sample holder. The sample holder was set to a chamber with a Be window. To avoid the oxidization of the sample and to enhance thermal conductivity, the chamber was purged by 1 bar of He gas. The temperature of the sample holder was controlled with a cold head and heater. The temperatures at the top of the sample holder and the bottom of the cold head were monitored. (d, e) The sample holder had three holes with 3 mm diameter aligned vertically to the sample and two holes with 2 mm diameter in the bottom, the latter of which was connected with a Ta collimator. (f) The collimator had three holes with 0.6 mm in the vertical direction and 0.3 mm in the horizontal direction. The collimator also had two holes with 2 mm of diameter below the sample holder.

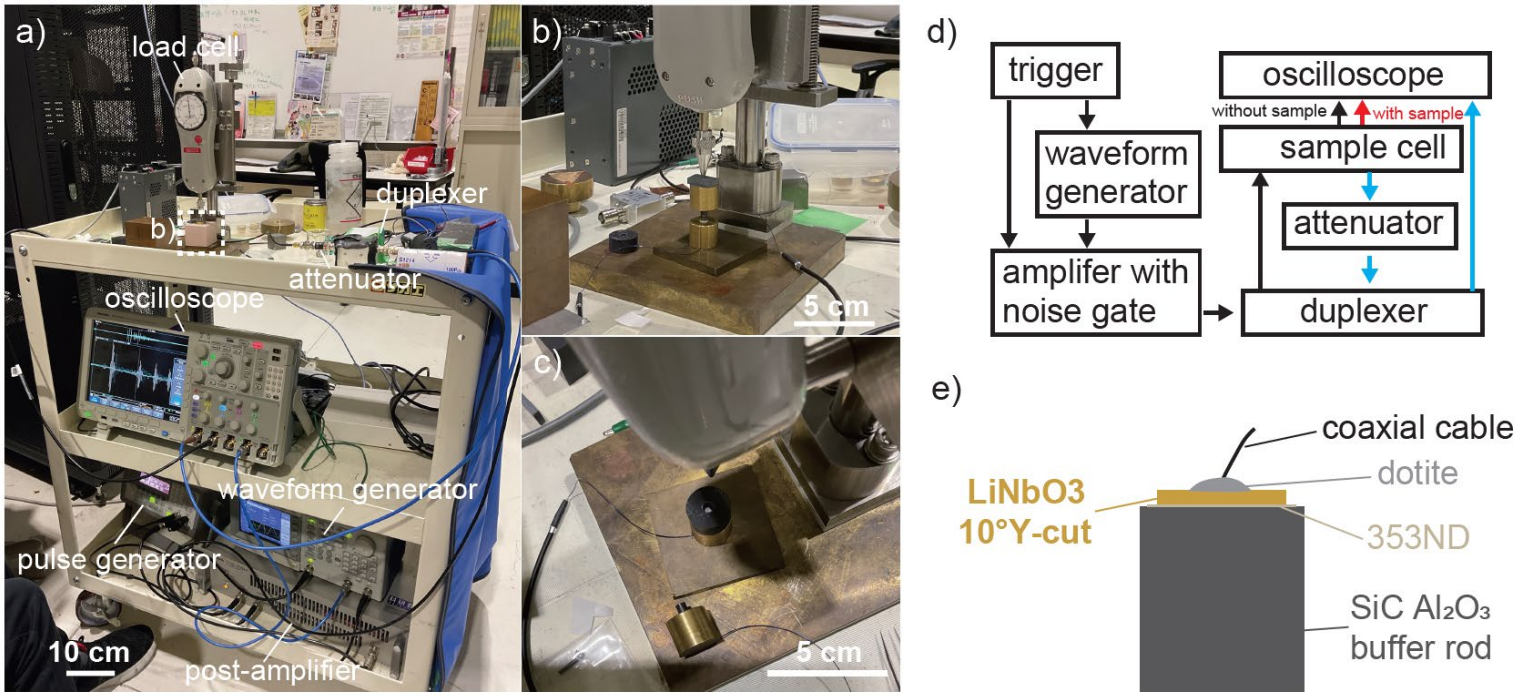

Figure 4.6 (a) A picture of the ultrasonic pulse experimental system. The experimental setup was composed of a pulse generator (33210A, Agilent Inc.), a high-frequency waveform generator (AFG3251C, Tektronix Inc.), a low noise post-amplifier (7T142-4029A, Thamway), a digital oscilloscope (MDO4104C, Tektronix Inc.), an attenuator (920-N732AC, Yuuetsu-Seiki Inc.), a duplexer (N120-3069A, Thamway Inc.) and a cell assembly as a sample holder (b-c). (b-c) Pictures of sample cell. (d) A schematic diagram of the experimental system. A sine burst wave was generated from the pulse generator 1000 times per second, following generation of three cycles of sine waves (40 MHz, 60 MHz, or 80 MHz for each experimental condition) by the waveform generator. These waves were amplified by the amplifier and entered the sample cell through the duplexer. Reflected waves were observed by the oscilloscope through the attenuator and duplexer, whereas the transmitted waves were observed by the oscilloscope directly. (e) The cell assembly was composed of a cylinder, piezoelectric transducers, and buffer rods. Crystaline LiNbO3 (10°-Y Cut LiNbO3: Yamaju ceramics Inc.) was used as the piezoelectric transducer because LiNbO3 shows resonant frequency of S-wave around 40 MHz and P-wave velocity around 60 MHz, which result in the formation of high amplitude of transmitted wave.

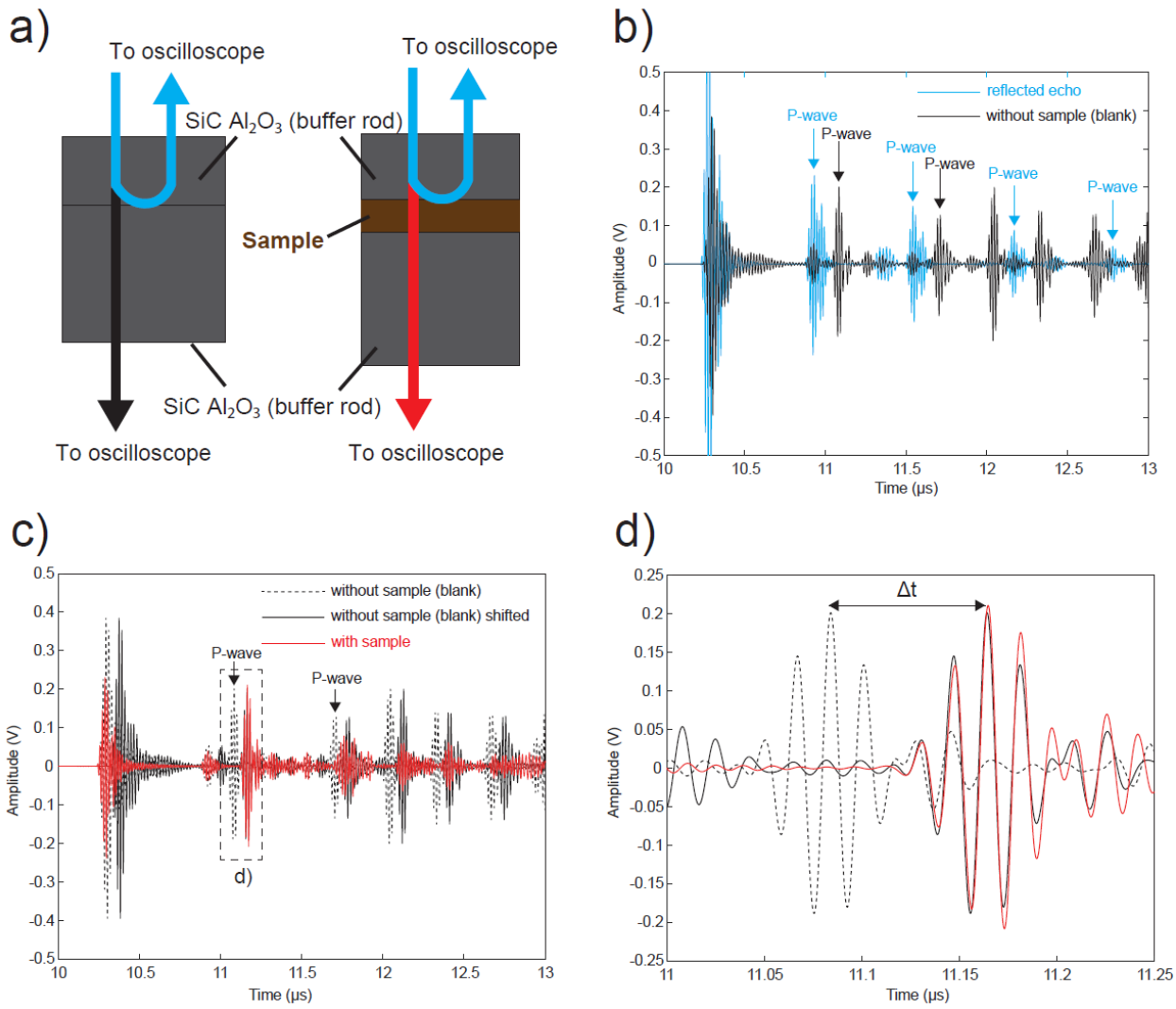

Figure 4.7 A schematic diagram and typical results of ultrasonic pulse measurements. (a) The sample located in-between the buffer rods. Elastic waves of burst sine signals with frequencies of 40, 60, and 80 MHz were generated at the front side of the rod. Part of wave reflected at the boundary between the sample and rod. Part passed through the sample and reached the back side of the opposing rod. (b-d) The wave passing through the rods (b) without sample and (c) with sample were detected at the back side of the opposing rod with the oscilloscope. (d) Waveform detected at the back side of the rod without (black) and with (red) sample. The black dot line shows the raw data of waveform without sample, whereas the black solid line shows the waveform without sample shifted to Δt. Travel time of wave Δt was determined by cross correlation methods, which is the method to measure the similarity between two waveforms as a function of time. At the time where the maximum amplitude of cross correlation was analyzed.

4.3 Results

4.3.1. Density measurements

The thickness and weight of the pellets of Titan tholin and hydrothermal organics were measured to be 1.58 ± 0.02 mm and 12.6 ± 0.1 mg for Titan tholin, and 0.36 ± 0.02 mm and 3.7 ± 0.1 mg for hydrothermal organics, respectively. Consequently, the bulk densities of the pellets, each with a diameter of 3 mm, were estimated to be 1130 ± 60 kg m^{-3} for Titan tholin and 1450 ± 170 kg m^{-3} for hydrothermal organics. For the hydrothermal organics pellet, the sample was cut in half and stacked, resulting in a total thickness of approximately 0.7 mm during IXS measurements.

On the other hand, the density of the Titan tholin pellet at 300 K was also determined based on the Beer-Lambert equation described by the following equation (e.g. Phillips & Lannutti, 1997):

$$T = \frac{I}{I_0} = -\exp(\mu x), \tag{4.26}$$

where T is the transmittance, I and I_0 are the intensities of the incident and transmitted photons, respectively, μ is the linear absorption coefficient, and x is the thickness of the sample.

The X-ray beam transmittance was calculated using the beam intensity ratio between apd2 to apd3. In the density calculation, the linear absorption coefficient was derived from the density and the photoabsorption cross sections of the elemental components (Henke et al., 1993) using the "Compute X-ray Absorption" software (https://11bm.xray.aps.anl.gov/absorb/absorb.php). With an estimated transmittance of 95.8% for the Titan tholin pellet, based on a comparison of X-ray beam transmittance in Run #4 (blank) and Run #5 (Titan tholin at 300 K), along with the pellet thickness of 1.6 mm, an elemental composition of C_2H_3N, and an X-ray beam energy 21.474 keV, the density of Titan tholin was calculated to be 1360 g m^{-3}. This density is higher than the bulk density of Titan tholin pellets derived from the mass and estimated volume of the pellet. This discrepancy may arise because the porosity in the optical path of the X-ray beam would be lower than the bulk porosity, resulting in higher density. Consequently, the density obtained from X-ray transmittance represents the lower limit of the intrinsic density. By comparing the bulk density with this lower limit, the lower limit of porosity of the Titan tholin pellet was estimated to be 17 %.

Given that the thermal expansion coefficient of amorphous carbon nitride, an analog material for Titan tholin, is reported to be 2–9 × 10^{-6} K^{-1} (Champi et al., 2002), the volume change of Titan tholin between 300–93 K is estimated to be 0.4–1.8 % of volume. This implies that the increase in the density of Titan tholin at 93 K compared to 300 K would be, at most,

1.8 %. As shown in Figure 4.15 and discussed later, this result is consistent with the results of $S(Q, 0)$ measurements conducted at different temperatures, indicating that the crystal structure of Titan tholin does not change significantly between 300–93 K.

4.3.2. IXS measurements

Comparison of Titan tholin and hydrothermal organics: Figure 4.8a shows an example of IXS spectrum of Titan tholin B at 300 K with the result of fitting of the data points measured in Run #5 (Table 4.3). Together with the predominant central peak at zero energy transfer of elastic contribution, small peaks of inelastic contribution appear on the shoulder of the central peak (Figure 4.8). The positions of the small peaks correspond to the energy transfer at each momentum transfer. On the other hand, Figure 4.8b shows the same as Figure 4.8a but for hydrothermal organics measured in Run #3 (Table 4.3). As discussed later, small peaks by inelastic contribution in IXS spectra of both Titan tholin and hydrothermal organics should be derived from longitudinal acoustic (LA) mode of phonon, based on the comparison of the acoustic wave velocity at long-wavelength estimated from phonon dispersion with the results of P-wave and S-wave velocities obtained from ultrasonic pulse transmittance method. Therefore, the acoustic wave velocity obtained in IXS measurements should be P-wave velocity (V_p) of organic materials.

All results of fitting of the data point of IXS spectrum at each momentum transfer are shown in Appendix A. The gray areas in the fitting results of the IXS spectra indicate the regions excluded from the fitting process. The analyzed spectra were classified into four categories: (i) analyzable over the entire measured energy scan range, (ii) analyzable only after excluding contributions from optical phonon modes at high energies, (iii) analyzable over a limited or all energy ranges but resulting in questionable results, and (iv) not analyzable due to undetermined energy positions or errors larger by orders of magnitude. Among these, only spectra in categories (i) and (ii) were considered for the analyses of the phonon dispersion described as below, while those in categories (iii) and (iv) were excluded (see Appendix A for details). Several factors may have contributed to the failure of the analysis. Possible reasons include (1) asymmetry in the instrumental function due to analyzer malfunction, (2) fitting difficulties caused by too weak phonon signals, and (3) discrepancies between the model and the actual physical behavior. To address these issues, applying a more realistic model, such as the damped harmonic oscillator (DHO) model (Fåk and Dorner, 1997), and improving the chamber or increasing sample thickness to enhance the probability of phonon signal detection will be necessary in future studies.

Figure 4.9 shows the phonon dispersion of both Titan tholin A, B and hydrothermal organics obtained at 300 K in Run #2, Run #3, and Run #5 (Table 4.3). As described above, we determined the energy of phonon at each momentum transfer from IXS spectra measured at

distinct Titan tholin samples (Titan tholin A and Titan tholin B) and different experimental setups to evaluate the producibility (Table 4.3). According to Eqs. (4.14) and (4.15), V_p values and errors of Titan tholin A measured in setup A and Titan tholin B measured in setup B are estimated to be 2690 ± 240 m/s and 2860 ± 340 m/s, respectively. Within the errors, V_p values of two Titan tholin show a good agreement, which indicates that the formation pressure of Titan tholin pellet and the difference of the experimental setup does not affect the results of IXS measurement significantly. Figure 4.10 shows the phonon dispersion of Titan tholin pellet B before (Run #5) and after (Run #8) cooling, and different areas (Run #9) measured in experimental setup B. In addition to Titan tholin B, the phonon dispersion of Titan tholin A measured in experimental setup B (Run #10) is shown in Figure 4.10. The measurements of IXS spectra of Titan tholin A in experimental setup B (Run #10) was conducted ~6 months later of the measurements in experimental setup A (Run #2). Although the experimental conditions of measurements of IXS spectra of Titan tholin are different, we confirm that the V_p of pellets of Titan tholin before and after heating and cooling cycle, with different irradiation time of X-ray beam, and with different exposure time to the air also does not affect the results significantly (Figure 4.10: Table 4.3–4.4).

Comparing with hydrothermal organics, V_p of two Titan tholin is also consistent with V_p of hydrothermal organics, ~2580 ± 350 m/s, within the errors. Given the densities of Titan tholin and hydrothermal organics (1130 ± 60 kg m^{-3} and 1450 ± 170 kg m^{-3}, respectively: Table 4.2), the longitudinal modules are estimated to be 9.3 ± 2.2 GPa for Titan tholin and 9.7 ± 2.7 GPa for hydrothermal organics (Table 4.4). These longitudinal modules are close in values within the errors, although the mean value of hydrothermal organics is higher than that of Titan tholin. Our longitudinal modulus of Titan tholin agrees with the previous value of Young's modulus of Titan tholin, 10.4 ± 0.5 GPa, determined based on the nano-indentation technique (Yu et al., 2018). The sensitivity of the modulus of organic materials on the seismic survey in the future mission is discussed below in Chapter 5.

Temperature dependence: Figure 4.11 shows examples of inelastic X-ray scattering spectra of Titan tholin B measured at 93–300 K in Run #5, Run #7, Run #13, Run #15, and Run #16, respectively (Table 4.3). Although peaks of inelastic contributions are detected, the intensities of the inelastic scattering contribution are low at low temperatures. This is because the probability of phonon excitation decreases with decreasing temperature, as described by Bose factor shown in Eq. (4.12). All results of fitting of the data point of IXS spectrum of Titan tholin at each momentum transfer at each temperature conditions are also shown in Appendix A. As mentioned above, the analyzed spectra were categorized and selected for the analysis of phonon dispersion.

Figure 4.12 shows the temperature dependence of the phonon dispersion of Titan tholin B and the fitting result of the experimental data obtained at each temperature using Eq. (4.12) with least square method. Based on the comparison of the slope of the fitting curve at zero energy transfer, the temperature dependence of the acoustic wave velocity of Titan tholin can be estimated. Although the error of the energy of each phonon dispersion is relatively large, the slope of the fitting curve at near zero energy transfer tend to increase at lower temperatures, indicating that V_p increases at lower temperatures. The temperature and chemical structure dependence of V_p are shown in Figure 4.13. The mean value of V_p at 93 K becomes 3340 m/s higher than that at 300 K. As mentioned above, the values of V_p of Titan tholin A, B and hydrothermal organics are close within the error.

Figure 4.14 shows the temperature dependence of the longitudinal modulus of Titan tholin B, assuming the density of Titan tholin is constant over the temperature range between 93 K to 300 K. In fact, the phase change of Titan tholin would not occur over these temperature range given the melting point of Titan tholin (e.g., 350 K: He & Smith, 2014; Yu et al., 2018), which suggests that the density would not change dramatically. Figure 4.14 indicates that the longitudinal modulus of Titan tholin becomes larger when the temperature decreases.

The Arrhenius equation for the longitudinal modulus can be described as follows,

$$lnM = lnM_0 - \frac{E_a}{RT}, \tag{4.27}$$

where M_0 and M are longitudinal modulus at absolute zero and the longitudinal modulus, E_a is the activation energy. Non-linear least square fitting of the data points with Eq. (4.27) gives a value of M_0 = 7.3 ± 1.2 GPa and E_a = -500 ± 230 J mol^{-1}. On the other hand, the temperature dependence of elasticity of a material is often described by the following equation (Gilbert et al, 1986; Courtney, 2005):

$$M = M_0\left(1 - \alpha\frac{T}{T_m}\right), \tag{4.28}$$

where M is the elastic modulus (here longitudinal modulus), M_0 is the elastic modulus (here longitudinal modulus) at 0 K, α is a dimension less coefficient (α = 0.5: Courtney, 2005; Yu et al., 2018), T is the temperature and T_m is the melting point (or the glass transition temperature T_g: Gilbert et al., 1986). Least square fitting of the longitudinal modulus of Titan tholin with the Eq. (4.28) results in M_0 = 15 ± 2 GPa and T_m = 340 ± 110 K.

Since it remains unclear which mechanism better explains the temperature dependence of the longitudinal modulus, we performed fittings with both the Arrhenius equation (Eq. (4.27)) and the linear relationship (Eq. (4.28)). Table 4.4 summarizes the results of V_p and the longitudinal modulus of our samples determined with the IXS method and Eq. (4.27), which

have larger errors compared to those obtained using Eq. (4.28). The discussion on which mechanism is more appropriate is presented in Sec. 4.4.

Structure of organic samples: Figure 4.15 shows the temperature dependence of the intensity of elastic scattering of Titan tholin as a function of the spacing of the lattice plane of the unit cells, as determined from $S(Q, 0)$ measurements. All spectra exhibit broad peaks centered at approximately 4–5 Å and possibly beyond 30 Å over the temperature range of 300 K to 93 K, although there are variations in intensity at certain lattice spacings (e.g., around 15 Å in Figure 4.15a). These results indicate that Titan tholin has an amorphous structure characterized by several distinct length scales (4 Å and possibly beyond 30 Å), regardless of temperature.

Table 4.5 summarizes the fitting results of B_s in Eq. (4.13) and the estimated lattice plane spacing. Although the spacing of the lattice plane varies by a few percent across the temperature range of 300 K to 93 K, the estimated d-spacing remains around 3.5–4.5 Å under all conditions. These results are consistent with those from the $S(Q, 0)$ measurements. The lattice plane spacing of hydrothermal organics is slightly larger (5.4 Å), suggesting that the unit cell size of organic molecules in hydrothermal organics is larger than that of Titan tholin.

The amorphous structure of Titan tholin is consistent with previous findings based on X-ray diffraction (XRD) patterns (Quirico et al., 2008). Furthermore, the unit cell sizes of Titan tholin and hydrothermal organics are comparable to the size of 1–2 aromatic rings in Titan tholin and the soluble organic matter (SOM) extracted from the Murchison meteorite, as determined by direct imaging using non-contact AFM (Schulz et al., 2021; Kaiser et al., 2022).

4.3.3. Ultrasonic wave measurements

Figure 4.7a shows the schematic illustration of passage of ultrasonic wave in the sample and corresponding waveform detected with the oscilloscope. In the measurement without the sample (Fig. 4.7b) with 3 cycles of sine burst wave of 60 MHz, part of ultrasonic wave generated at the front side of the rod reflects at the boundary between the rods. On the other hand, part of ultrasonic wave passes through the boundary between the rods. Light blue line in Figure 4.7b shows results of waveform of reflected ultrasonic wave detected at the front side of the rod, whereas black line in Figure 4.7b shows results of waveform of transmitted ultrasonic wave detected at the back side of the rod. The waveform of transmitted ultrasonic wave was offset and aligned with the input of sein burst wave detected as a swarm of large waves at 10.3 μs (Fig. 4.7b). At 10.9 μs, a swarm of P-waves reflected at the boundary between the rods appears. On the other hand, at 11.1 μs, a swarm of large waves is detected at the back side of the rod (Fig. 4.7). This wave swarm is considered to be transmitted P-wave based on the similarity of the shape of the waveform. Then, transmitted waveforms detected at the back side of the rod without and with sample were compared in Fig. 4.16. The red line in Fig. 4.16a shows waveform with

Titan tholin generated by 3 cycles of sine burst wave of 60 MHz and shifted forward by Δt = 42 ns. A swarm of the waveform with Titan tholin appears to be matched with the swarm of P-wave without sample at 11.1 μs (Fig. 4.16b). Thus, the travel time of P-wave t_p of Titan tholin corresponds to the time intervals between 42 ± 0.4 ns. On the other hand, the red line in Fig. 4.16c shows waveform with Titan tholin generated by 3 cycles of sine burst wave of 40 MHz and shifted forward by Δt = 70.8 ns. A swarm of the waveform with Titan tholin appears to be matched with the swarm of S-wave without sample at 12.75 μs (Fig. 4.16d). Thus, the travel time S-wave t_s of Titan tholin corresponds to the time intervals between 70.8 ± 0.4 ns. All results of analyses of the waveforms of other samples (hydrothermal organics, NaCl, and SiO_2) and other frequencies of sine burst wave (40, 60, 80 MHz) are shown in Appendix B.

Given the thickness of the Titan tholin sample, V_p and V_s of Titan tholin are calculated from the measured travel times. V_p and V_s of Titan tholin at 300 K is calculated to be 3260 ± 390 m/s and 1830 ± 60 m/s, respectively by adding the data with frequency of 40, 60, and 80 MHz. The results for each frequency are 3040 ± 60 m/s for 40 MHz, 3020 ± 60 m/s for 60 MHz, and 3710 ± 70 m/s for 80 MHz. Since the frequency dependence is relatively small within this range, we take into account all data for 40–80 MHz to reduce the errors. The relatively large error in V_p is due to large V_p at 80 MHz. This would be because the phase change of the pulse wave could occur during measurements at 80 MHz, resulting in a half-wavelength shift in the determined travel time. Given that the P-wave velocity of Titan tholin determined by IXS measurements is around ~3000 m/s, the analyses at 40 MHz and 60 MHz are likely more accurate than those at 80 MHz. Based on the analysis for the measurements using hydrothermal organics (the data of waveforms are shown in Appendix B). V_p and V_s of hydrothermal organics at 300 K are also calculated to be 2830 ± 60 m/s and 1740 ± 40 m/s, respectively.

The measured V_p at 300 K for both Titan tholin and hydrothermal organics in ultrasonic pulse transmittance method are consistent with the results of the acoustic wave velocities estimated from phonon dispersion obtained with the IXS method within the errors, suggesting that the phonon should be the longitudinal acoustic (LA) mode. Despite the large difference in the frequency (the frequency in the ultrasonic pulse method is approximately four orders lower than that of the IXS method), the V_p of Titan tholin obtaind by both methods are within the errors. This suggests that the frequency dependence of V_p is less than ~10 % of V_p value within the frequency range of ~10 MHz–sub-THz.

Based on the measured V_p and V_s, together with the density of material, the elastic parameters at 300 K (the bulk modulus K, Young's modulus Y, and Poisson's ratio v) are calculated based on Eqs. (4.18–25) above. We obtain K = 7 ± 0.9 GPa, Y = 9.7 ± 1.8 GPa, and v = 0.27 ± 0.03 for Titan tholin, and K = 5.8 ± 0.7 GPa, Y = 10.4 ± 1.3 GPa, and v = 0.20 ± 0.01 for hydrothermal organics. The obtained Young's modulus of Titan tholin in the present study

agrees with the result of the previous study $Y = 10.4 \pm 0.5$ GPa (Yu et al., 2018). However, similar to the results of the IXS measurements, our Titan tholin tend to have a lower Young's modulus than that of Titan tholin in the previous study, which is discussed below in Chapter 4. Comparing Titan tholin with hydrothermal organics, v of Titan tholin is higher than that of hydrothermal organics. In general, materials with low atomic packing density tend to have low v values (Greaves et al., 2011; Rouxel, 2007). The difference in v may be due to the difference in average coordination number in Titan tholin and hydrothermal organics (Greaves et al., 2011; Rouxel, 2007). This is because an increase in the coordination number of atoms in solids results in formation of three-dimensional networks, leading to a low atomic packing density (Greaves et al., 2011; Rouxel, 2007).

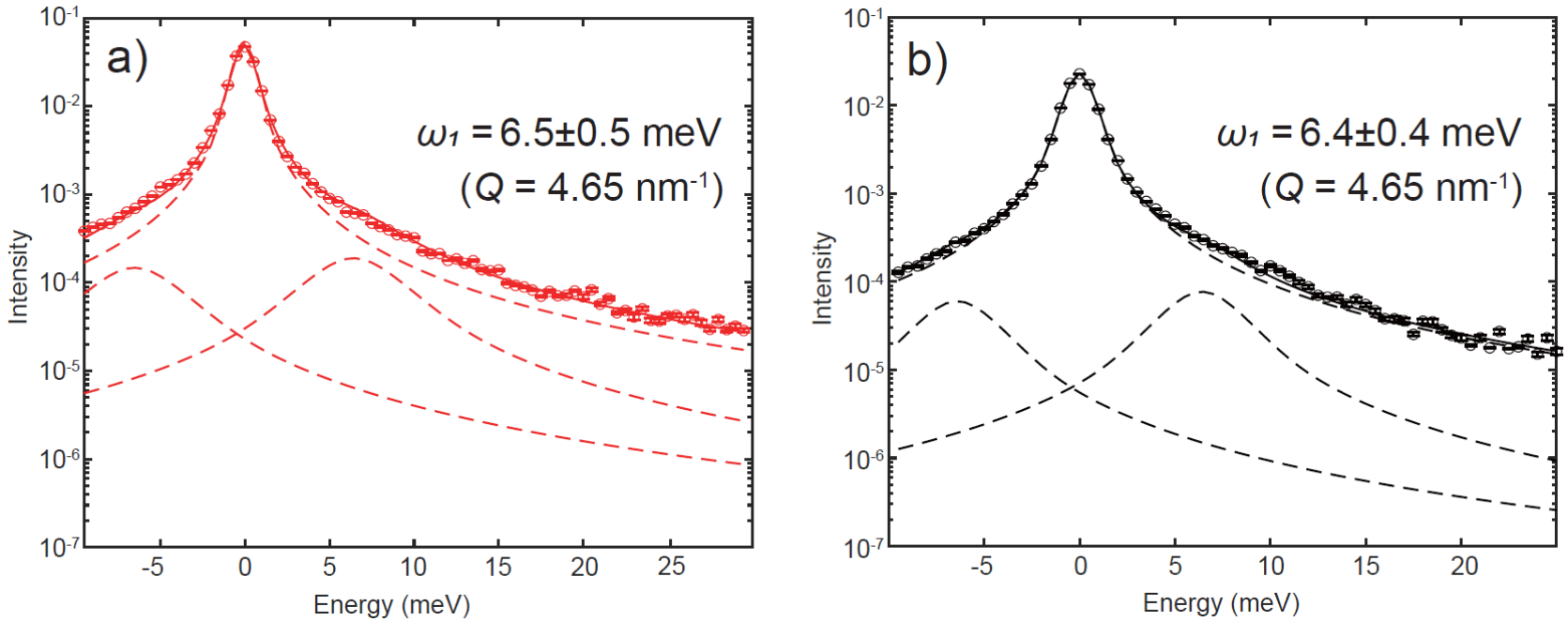

Figure 4.8 (a) An example of IXS spectrum of Titan tholin B at 300 K and momentum transfer Q = 4.65 nm^{-1} measured in Run #5. The circles with errors show data point. Solid curve indicates the fitting results of pseudo-Voigt function with Bose factor. The predominant central peak at zero energy transfer corresponds to elastic contribution, whereas small peaks on the shoulder of the central peak indicate inelastic contribution. The energy of phonon ω_1 = 6.5 ± 0.5 meV at momentum transfer Q = 4.65 nm^{-1} was determined from the positions of the small peaks. (b) An example of IXS spectrum of hydrothermal organics measured in Run #3. The energy of phonon ω_1 = 6.4 ± 0.4 meV at momentum transfer Q = 4.65 nm^{-1} was determined from the positions of the small peaks same as Titan tholin.

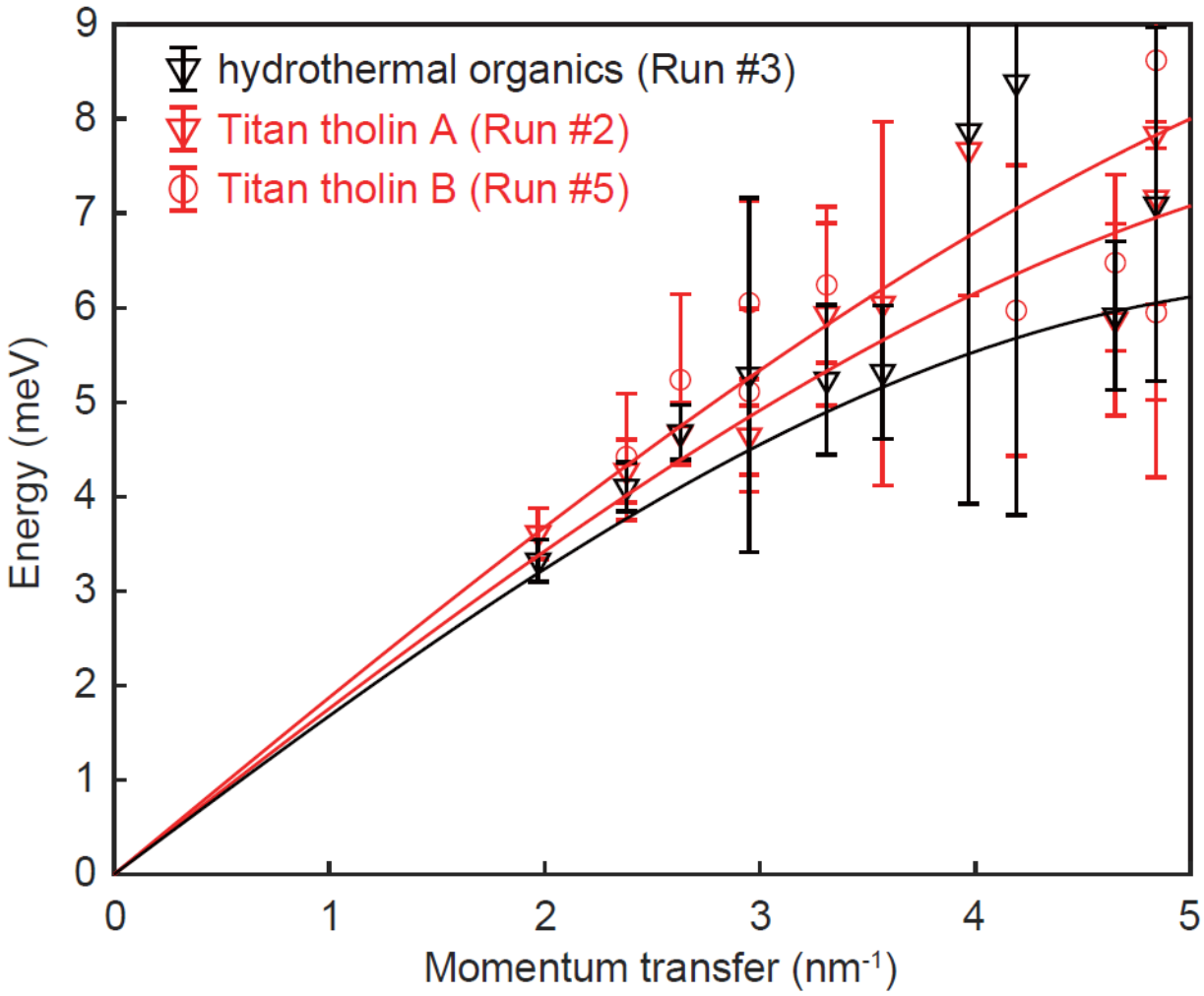

Figure 4.9 Phonon dispersion of Titan tholin A (red inverted triangle), B (red circle) and hydrothermal organics (black inverted triangle) measured at 300 K in Run #2, Run #3, and Run #5. Each solid curve indicates the fitting result of the phonon dispersion curve.

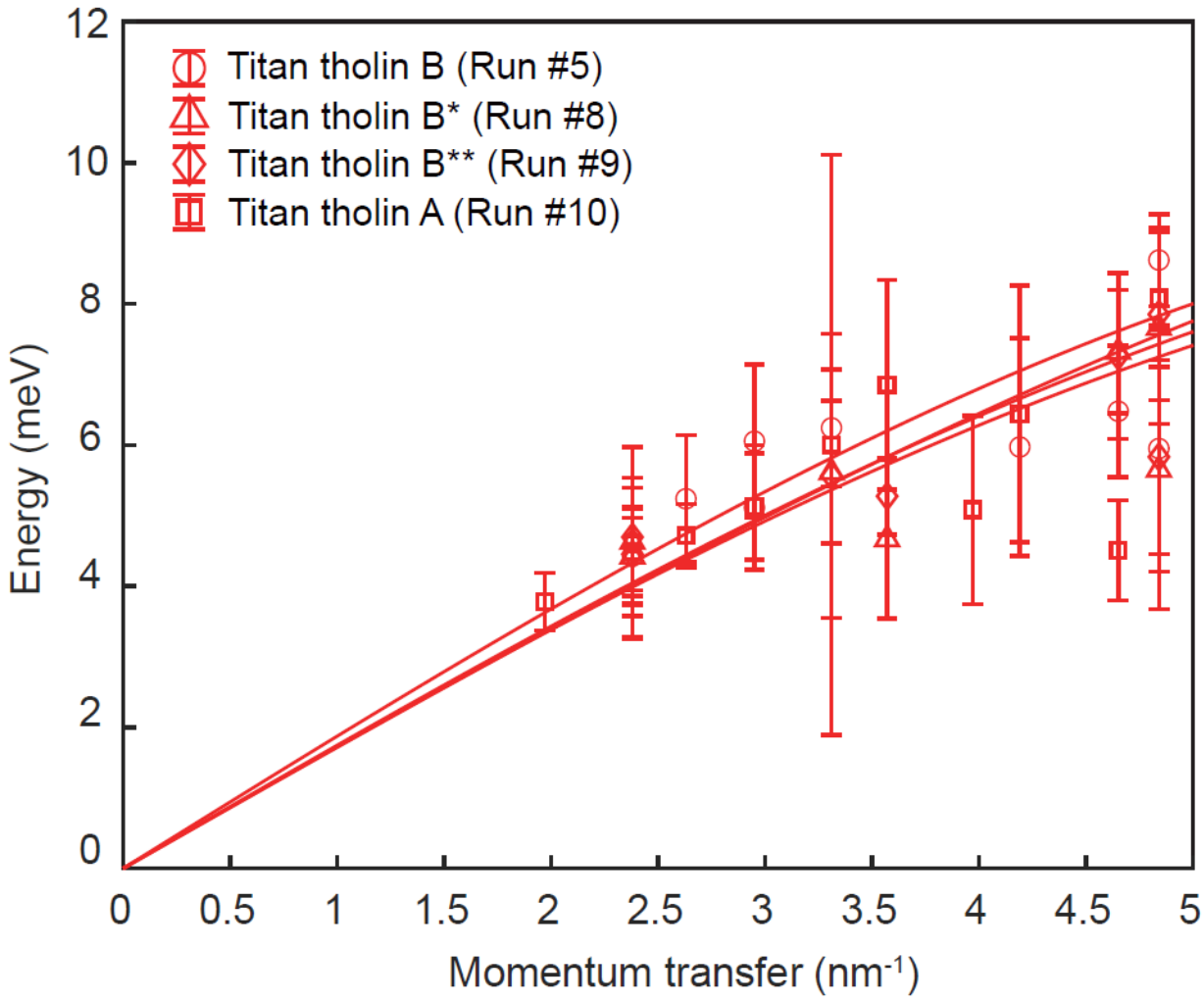

Figure 4.10 Phonon dispersion of Titan tholin pellets of Titan tholin before (red circle, Run #5) and after cooling (red triangle, Run #8), different areas (red diamond, Run #9), and different samples (red square, Run #10). Each solid curve indicates the fitting result of the phonon dispersion curve.

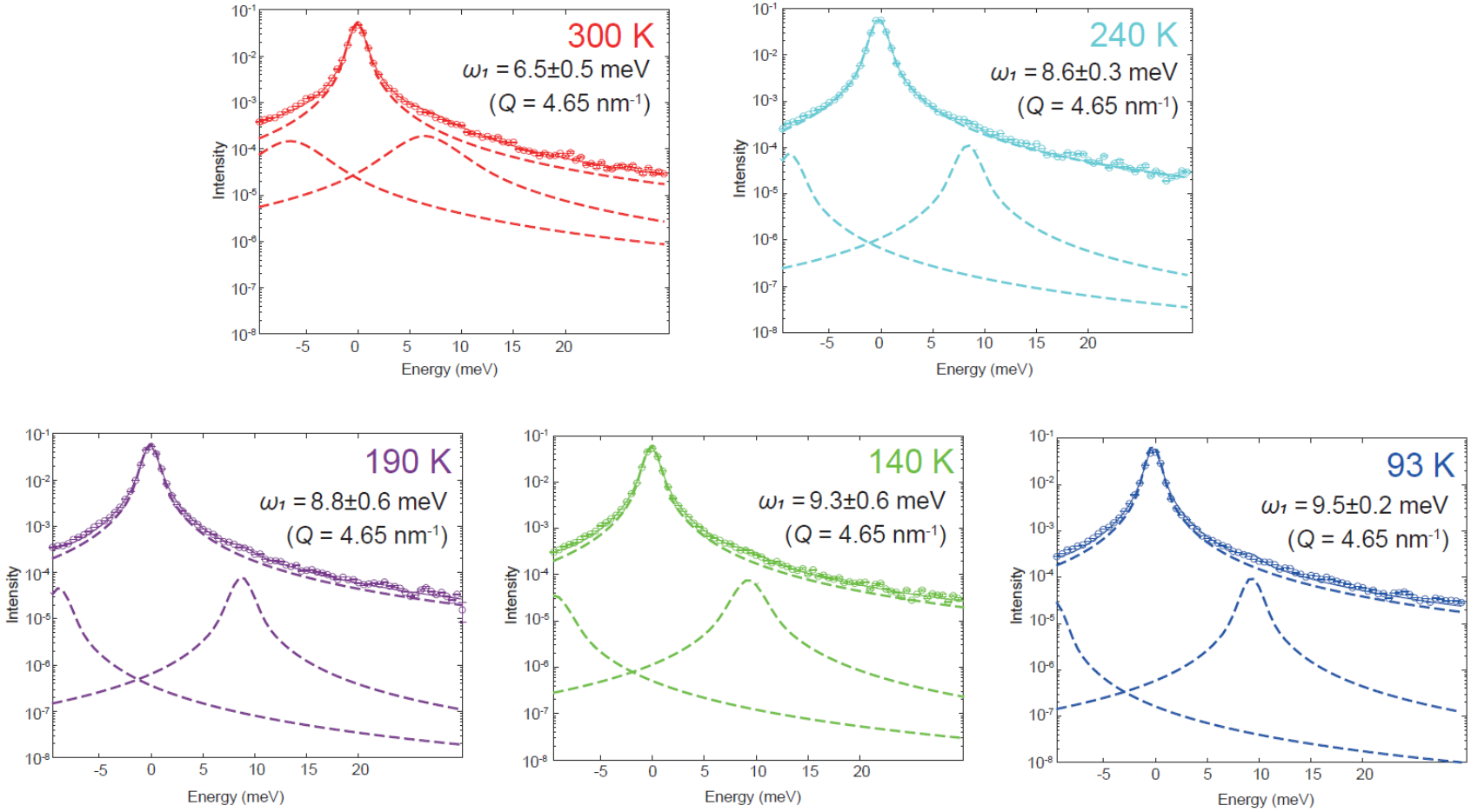

Figure 4.11 Temperature dependence of IXS spectra of Titan tholin (offset) measured at momentum transfer $Q = 4.65$ nm^{-1} and at 300, 240, 190, 140, and 93 K in Run #5, Run #7, Run #13, Run #15, and Run #16, respectively (Table 4.3). The circles with errors show data point. Solid curve indicates the fitting results of pseudo-Voigt function with Bose factor, same as Fig. 4.9. The energy of phonon ω_1 determined by the position of the small peaks appears to increase as the temperature decreases.

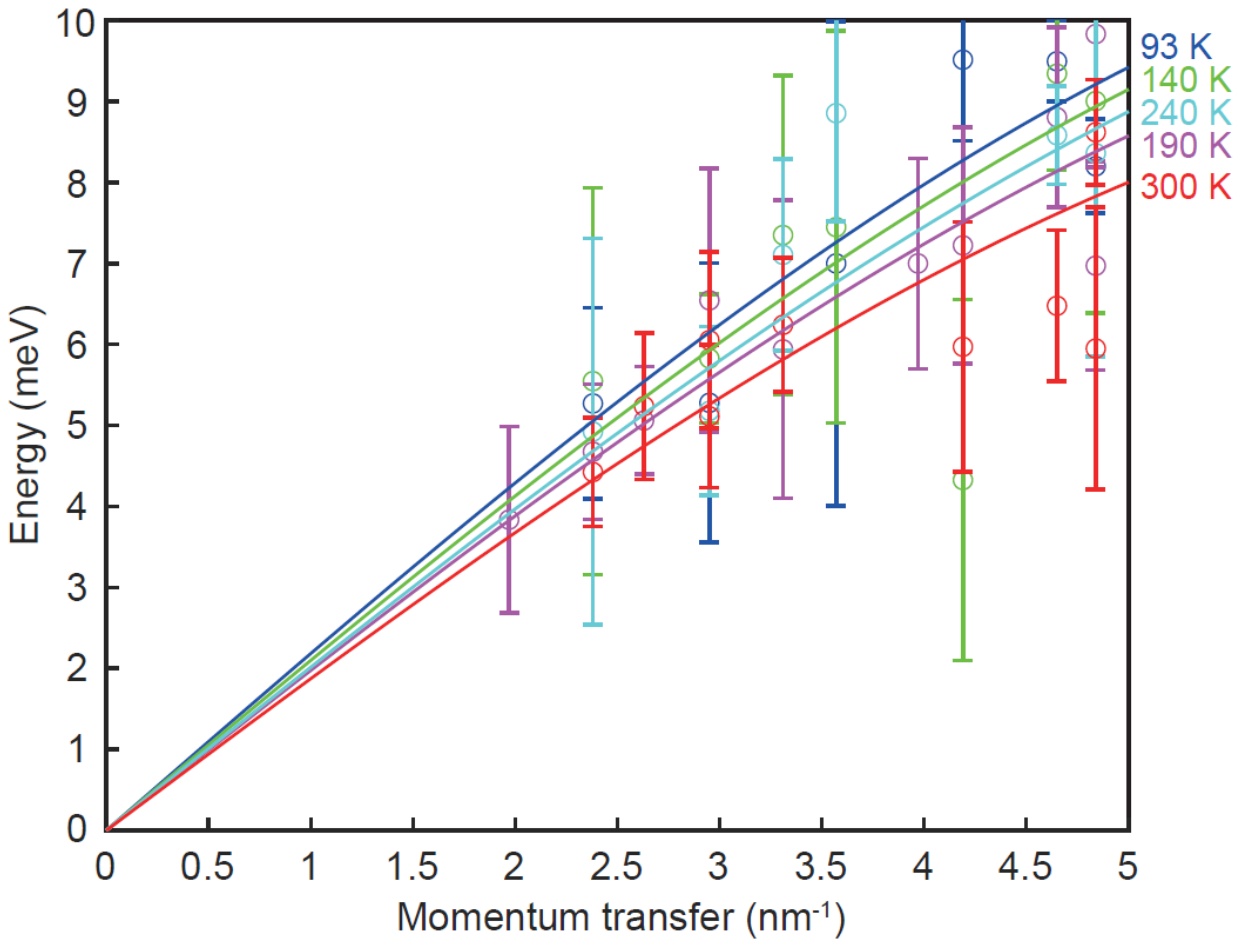

Figure 4.12 Temperature dependence of phonon dispersion between Titan tholin pellet at 300 K (red), 240 K (cyan), 190 K (purple), 140 K (green), and 93 K (blue) obtained in 2024A1609. Each circle indicates the experimental data, whereas each solid curve indicates the fitting result of the phonon dispersion curve. the relationships between the energy and momentum transfer (i.e. phonon dispersion) for Titan tholin B measured at each temperature condition (Run #5, Run #7, Run #13, Run #15, and Run #16). Although the errors of the data points are relatively large, the gradients of the fitting curve at near zero energy transfer tend to be steeper at lower temperatures, indicating higher V_p at lower temperatures.

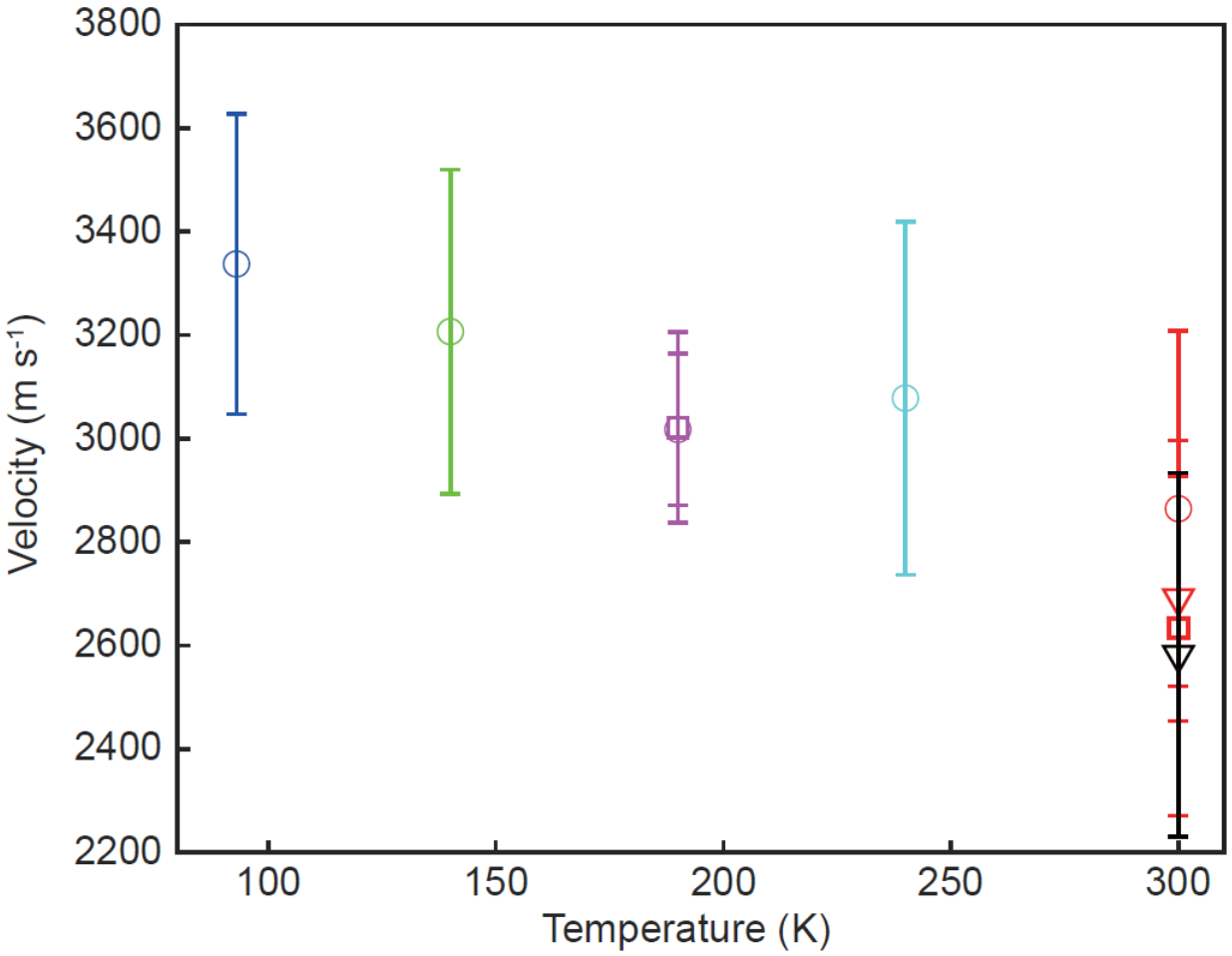

Figure 4.13 Comparison of temperature and chemical structure dependence of V_p. The mean value of V_p at 93 K becomes 3340 m/s higher than that at 300 K. The values of V_p of Titan tholin A in the setup A (red inverted triangle, Run #2) and in the setup B (red square, Run #10), Titan tholin B in the setup B (red circle, Run #5) and hydrothermal organics (black inverted triangle, Run #3) at 300 K are close within the error. The values of V_p of Titan tholin A in the setup B (purple square, Run #12) and Titan tholin B in the setup B (purple circle, Run #13) are also close within the error.

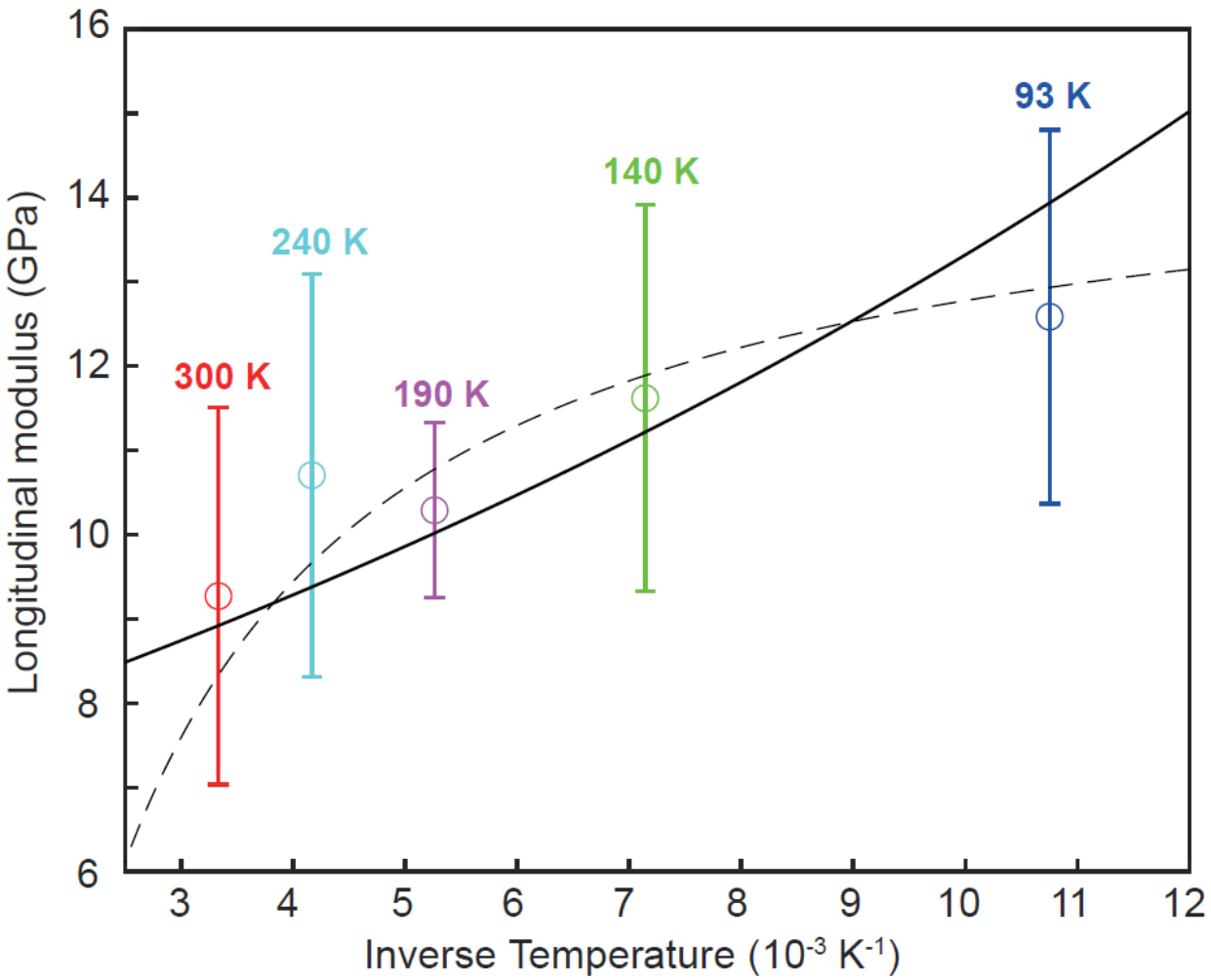

Figure 4.14 Temperature dependence of longitudinal modulus of Titan tholin B, calculated from V_p at each temperature assuming the density of Titan tholin is constant over the temperature range between 93 K to 300 K. The longitudinal modulus of Titan tholin becomes larger when the temperature decreases. The black curve indicates the results of least square fitting of Arrhenius equation (Eq. (4.27)) with a value of M_0 = 7.3 ± 1.2 GPa and E_a = -500 ± 230 J mol^{-1}, respectively. The dased line indicates the results of least square fitting of the linear relationship (Eq. (4.28)) with a value of M_0 = 15 ± 2 GPa and T_m = 340 ± 110 K, respectively.

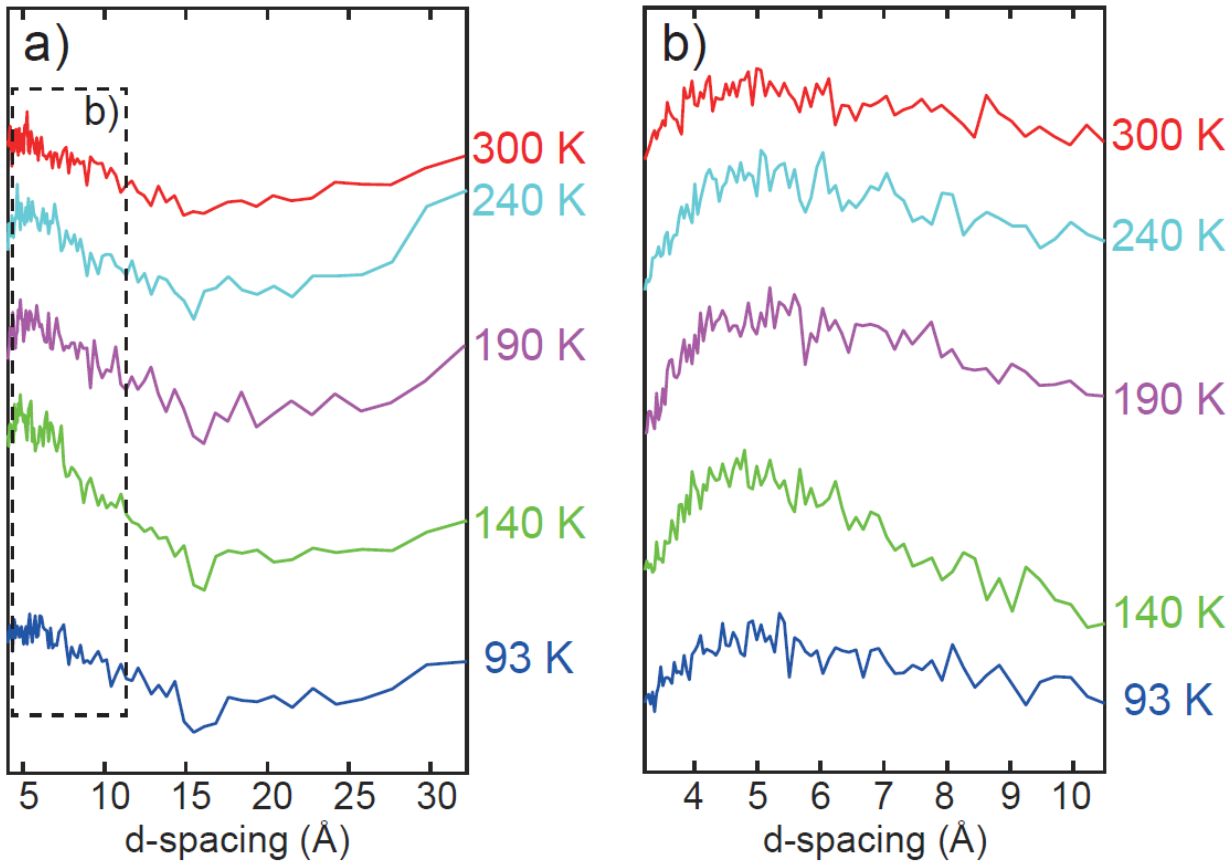

Figure 4.15 Temperature dependence of diffraction pattern of Titan tholin as a function of the distance of the unit cells, shown for (a) a wide range and (b) a close-up view. Each color represents the measurement temperature condition. All spectra are normalized to the minimum d-spacing and offset for clarity. The spectra exhibit broad peaks centered at approximately 4–5 Å and possibly beyond 30 Å. Additionally, the peak near 15 Å becomes weaker as the temperature decreases.

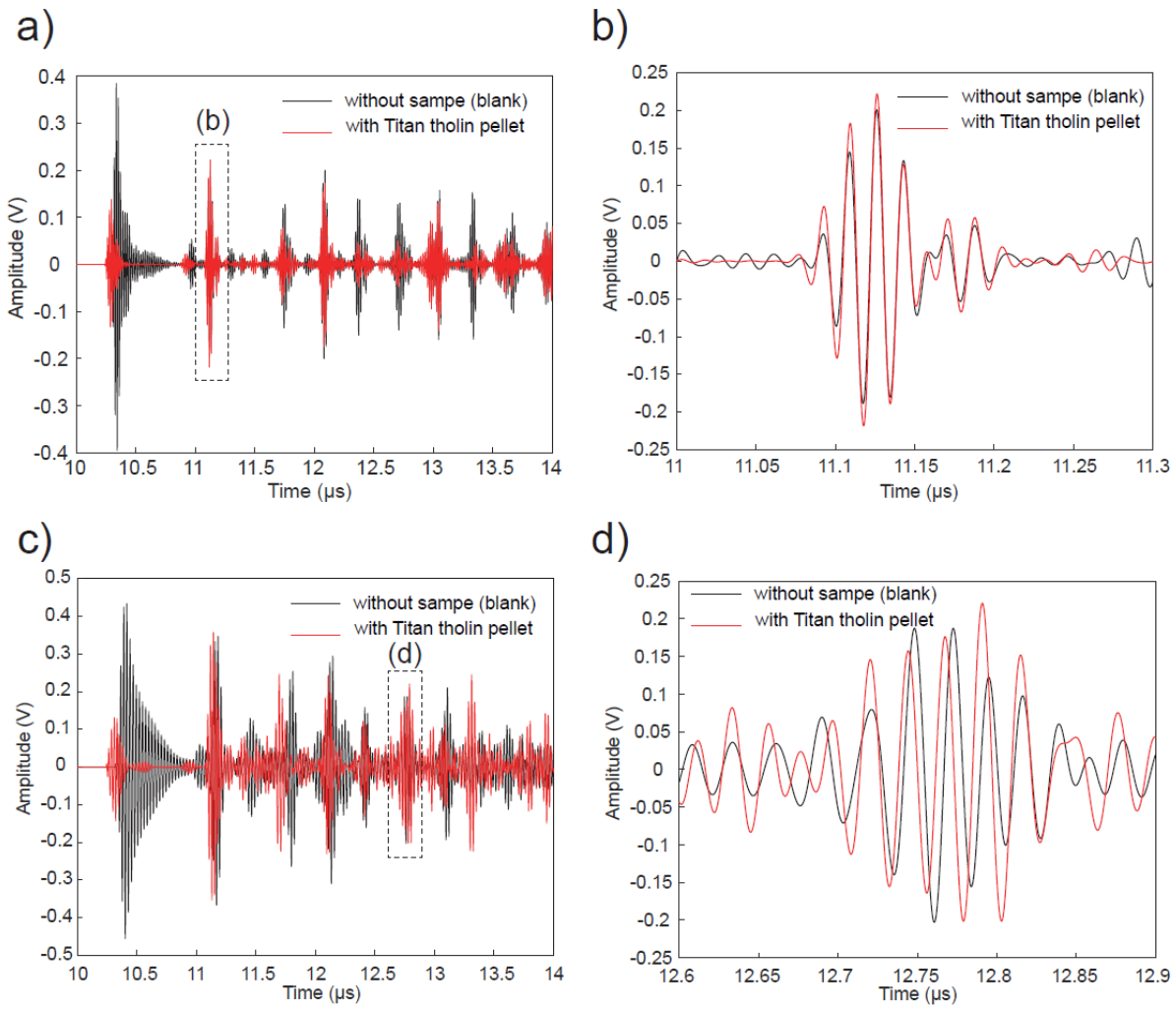

Figure 4.16 Typical results of the transmitted waveforms detected at the back side of the rod without (black) and with sample (red), respectively. (a.b) Waveform generated by 3 cycles of sine burst wave of 60 MHz. Dashed box in (a) indicates the area of (b). Waveform with Titan tholin (red) was shifted forward by Δt = 42 ns. A swarm of the waveform with Titan tholin appears to be matched with the swarm of P-wave without sample at 11.1 μs, suggesting that the travel time of P-wave t_p of Titan tholin corresponds to the time intervals between 42 ± 0.4 ns. (b,c) Waveform generated by 3 cycles of sine burst wave of 40 MHz. Dashed box in (c) indicates the area of (d). Waveform with Titan tholin (red) was shifted forward by Δt = 70.8 nsec. A swarm of the waveform with Titan tholin appears to be matched with the swarm of S-wave without sample at 12.75 μs, suggesting that the travel time S-wave t_s of Titan tholin corresponds to the time intervals between 70.8 ± 0.4 ns.

Table 4.1 Summary of the experimental conditions and results of travel time determination of ultrasonic pulse transmittance measurements. *The error of the length of samples were derived from instrumental error. ** The errors of the travel time were derived from the cross-correlation analysis.

frequency (MHz)	sample	*length (μm)	**tp (s)	**ts (s)
40	NaCl	410±2	77.8±0.4	130.6±0.4
40	SiO_2 glass	1310±2	226±0.4	366.4±0.4
40	Titan tholin	127±2	41.8±0.4	70.4±0.4
40	hydrothermal tholin	171±2	59.4±0.4	96.6±0.4
60	NaCl	410±2	80.2±0.4	134.4±0.4
60	SiO_2 glass	1310±2	226±0.4	380±0.4
60	Titan tholin	127±2	42±0.4	70.8±0.4
60	hydrothermal tholin	171±2	61.4±0.4	99.8±0.4
80	NaCl	410±2	81±0.4	137.4±0.4
80	SiO_2 glass	1310±2	227±0.4	366±0.4
80	Titan tholin	127±2	34.2±0.4	67.2±0.4

Table 4.2 Summary of the results of ultrasonic pulse transmittance measurements. *, ** The density of NaCl and SiO_2 glass were from Jiang et al. (2018) and Carini et al. (2016), respectively.

sample	Vp (m/s)	Vs (m/s)	density (kg/m^3)	Y (Gpa)	K (Gpa)	G (Gpa)	v
NaCl	5150±110	3060±80	2160*	50±3	30±1	20±1.2	0.23±0.01
SiO_2 glass	5790±20	3530±80	2200**	66±3.4	37±0.8	27±1.4	0.20±0.00
Titan tholin	3260±390	1830±60	1130±60	9.7±1.8	7±0.9	3.8±0.3	0.27±0.03
hydrothermal organics	2830±60	1740±40	1450±170	10.4±1.3	5.8±0.7	4.4±0.5	0.20±0.01

Table 4.3 Summary of the experimental conditions for IXS measurement. *The irradiation point was different from other experimental runs. **The chamber was once leaked into the air and then evacuated before measurement.

Experimental Run#	setup	sample	temperature (K)	scattered angle 2θ	Duration (h)
Run #1	A	blank	300	2.062	1
				2.409	1
				4.861	1
Run #2	A	Titan tholin A	300	2.062	4
				2.409	5
				4.861	2
Run #3	A	hydrothermal organics	300	2.062	4
				2.409	3
				4.861	4
Run #4	B	blank	300	2.062	2
				2.409	1
				4.861	1
Run #5	B	Titan tholin B	300	2.062	5
				2.409	3
				4.861	4
Run #6	B	blank	93	2.062	2
				2.409	1
				4.861	1
Run #7	B	Titan tholin B	93	2.062	6
				2.409	5
				4.861	5
Run #8	B	Titan tholin B	300	2.062	2
Run #9	B	Titan tholin B*	300	2.062	2
Run #10	B	Titan tholin A	300	2.062	2
				2.409	2
				4.861	2
Run #11	B	blank	190	2.062	1
				2.409	1
				4.861	1
Run #12	B	Titan tholin A	190	2.062	4
				2.409	4
				4.861	4
Run #13	B	Titan tholin B	190	2.062	2
				2.409	2
				4.861	2
Run #14	B	blank	140	2.062	1
				2.409	1
Run #15	B	Titan tholin B	140	2.062	2
				2.409	2
				4.861	2
Run #16**	B	Titan tholin B	240	2.062	3
				2.409	2
				4.861	3

Table 4.4 Summary of the experimental results of V_p and elasticity of each organic material based on IXS measurements. *Measured after cooling and subsequent increase of temperature. **Measured at different point after cooling and subsequent increase of temperature. Due to the large error of V_p, the longitudinal modulus in Runs #8 and #9 could not be obtained.

sample	temperature (K)	setup	Vp (m/s)	longitudinal modulus (Gpa)
Titan tholin B (Run #7)	93	B	3340±290	12.6±2.2
Titan tholin B (Run #15)	140	B	3210±310	11.6±2.3
Titan tholin B (Run #13)	190	B	3020±150	10.3±1.0
Titan tholin A (Run #12)	190	B	3020±180	10.3±1.3
Titan tholin B (Run #16)	240	B	3080±340	10.7±2.4
Titan tholin B (Run #5)	300	B	2860±340	9.3±2.2
Titan tholin B* (Run #8)	300	B	2620±2160	-
Titan tholin B** (Run #9)	300	B	2670±1980	-
Titan tholin A (Run #10)	300	B	2630±360	7.8±2.2
Titan tholin A (Run #2)	300	A	2690±240	8.2±1.5
hydrothermal organics (Run #3)	300	A	2580±350	9.7±2.7

Table 4.5 Summary of the fitting results of Bs and the estimated lattice plane spacing. *,** Due to the large error of B_s, d-spacing in Runs #8 and #9 could not be obtained.

sample	temperature (K)	setup	Bs (nm)	d-spacing (Å)
Titan tholin B (Run #7)	93	B	0.19±0.02	3.8±0.4
Titan tholin B (Run #15)	140	B	0.18±0.02	3.7±0.4
Titan tholin B (Run #13)	190	B	0.18±0.01	3.7±0.2
Titan tholin A (Run #12)	190	B	0.18±0.01	3.7±0.3
Titan tholin B (Run #16)	240	B	0.18±0.02	3.5±0.4
Titan tholin B (Run #5)	300	B	0.20±0.03	3.9±0.5
Titan tholin B* (Run #8)	300	B	-	-
Titan tholin B** (Run #9)	300	B	-	-
Titan tholin A (Run #10)	300	B	0.19±0.03	3.8±0.6
Titan tholin A (Run #2)	300	A	0.23±0.02	4.5±0.4
hydrothermal organics (Run #3)	300	A	0.27±0.04	5.4±0.7

4.4. Discussion

Comparison with other materials: Figure 4.17 shows the comparison of bulk modulus and density of both Titan tholin and hydrothermal organics measured with the ultrasonic pulse method with various materials (empty circle) including quartz and clay (Blangy, 1992; Han et al., 1986), H_2O ice (Shaw, 1986), polyaromatic hydrocarbons (PAHs) (Richter et al., 2000), high-density polyethylene, low-density polyethylene, and (Jordan et al., 2021), kerogen (Yan and Han, 2013; Zhao et al., 2016 and references therein; Xie et al., 2019 and reference therein), and bamboo (Krzesińska et al., 2006). All materials except PAHs and parts of kerogen were measured by ultrasonic pulse methods (Blangy, 1992; Han et al., 1986; Shaw, 1986; Jordan et al., 2021; Yan and Han, 2013; and Krzesińska et al., 2006). The bulk modulus of PAHs is constrained by nano-indentation techniques (Richter et al., 2000), whereas that of parts of kerogen is constrained by measurements at lower frequency of acoustic wave velocity compared to ultrasonic wave (Zhao et al., 2016 and references therein; Xie et al., 2019 and reference therein). This figure shows that the elastic properties of laboratory analogs of Titan's organic materials (i.e., Titan tholin and hydrothermal organics) are distinguishable from crystalline H_2O ice that would consist of Titan's crust. The bulk modules of both Titan tholin and hydrothermal organics fall within the range of those of kerogen, H_2O ice, polyethylene, kerogen, and/or PAHs; however, considering the density together, kerogen is considered to be the closest material, in the elastic properties, to Titan tholin and hydrothermal organics.

Figure 4.18 compares the Young's modulus of Titan tholin, hydrothermal organics, and other organic materials, including PAHs (Richter et al., 2000), polyethylene (Jordan et al., 2021), adenine (Yu et al., 2018), and biphenyl (Yu et al., 2018), as a function of their C/H ratio. The results indicate that PAHs, which have a higher C/H ratio, exhibit higher Young's modulus values, while polyethylene, a linear hydrocarbon with a lower C/H ratio, displays a lower Young's modulus. This trend suggests that for simple hydrocarbons with either purely aliphatic or aromatic structures, a higher C/H ratio tends to correlate with a higher Young's modulus. On the other hand, adenine, which contains heterocyclic rings and amine ($-NH_2$) groups, and biphenyl, which consists of benzene rings connected by a single bond, exhibit lower Young's modulus values comparable to that of polyethylene. This trend indicates that the Young's modulus of organic materials is not solely determined by elemental ratios or the number of unsaturated bonds but is also influenced by factors such as elemental composition, functional groups, and the molecular configuration of aromatic and aliphatic structures. The Young's modulus of Titan tholin and hydrothermal organics obtained in this study falls between the values of PAHs and other organic materials. As inferred in Chapter 2, the chemical structures of Titan tholin and hydrothermal organics consist of a combination of cyclic hydrocarbons

containing nitrogen and oxygen and linear hydrocarbons. These findings support the idea that the Young's modulus of organic materials is not simply governed by the C/H ratio but is also influenced by elemental composition, functional groups, and the arrangement of cyclic and aliphatic structures within the molecules. To elucidate the relationship between chemical structure and elasticity, such as the Young's modulus of organic materials, further studies are needed. Specifically, a combination of improved constraints on chemical structure using LDMS/MS, which will be onboard NASA's *Dragonfly* mission (e.g., Grubisic et al., 2021), and a systematic comparison of the elasticity of organic materials with different chemical structures will be essential.

Temperature dependence: Our results of the IXS measurements suggest that the longitudinal modulus (and V_p) of Titan tholin becomes larger (and higher) at lower temperatures in the range of 93–300 K (Figure 4.14). The longitudinal modulus of Titan tholin decreases by a factor of ~1.5 from 300 K to 93 K following the Arrhenius equation (Eq. (4.27)) or linear relationship (Eq. (4.28)). This temperature dependence can be explained by two possible mechanisms (Gilbert et al., 1986); 1) a decrease in molecular distance as the temperature decreases due to thermal shrink, which results in strengthening the Van der Waals interactions of each atom and force required for intermolecular deformation by bond stretching (Yannas and Luise, 1982). The temperature dependence in this case follows a linear relationship as described by Eq. (4.28). 2) a decrease in thermal energy of molecules, which prevents relaxation of amorphous by thermally-activated rearrangements of side branches or short segments at deficit in the amorphous structure below glass transition temperature (Gilbert et al., 1986). In this latter case, temperature dependence follows Arrhenius relation (Eq. (4.27)). Given the large errors in both fitting results of the longitudinal modulus of Titan tholin with Eqs. (4.27) and Eq. (4.28), the dominant mechanism which is responsible for the temperature dependence is uncertainty. However, the linear relationship is more likely because the elasticity estimated using the IXS method reflects the unit cell scale, where intermolecular forces such as van der Waals interactions cannot be neglected. Nonetheless, the analysis in this study is insufficient and requires further refinement. Additional low-temperature experiments using alternative methods, such as ultrasonic techniques or Brillouin scattering, are necessary to enable a comparative evaluation of the results.

Frequency dependence: Figure 4.19 compares the phonon dispersion of different orders obtained using the IXS (Run #2) and ultrasonic methods for Titan tholin. The phonon dispersion curves are approximated as a linear relationship near the zero point, based on the assumption that a sine curve can be approximated by a linear function in this region. The phonon dispersion obtained by the IXS method is shown at $Q = 1.97$ nm^{-1}, while the dispersion obtained via the ultrasonic method was derived using the relationships $Q = 2\pi/\lambda_p$ and $E = (2\pi\hbar/e)\,f$, considering a

frequency range of 40–80 MHz and a sound speed of 3260 ± 390 m/s. Here, λ_p is the wavelength of phonon, e is the elementary charge, and f is the phonon frequency.

At Q = 1.97 nm^{-1}, the phonon dispersion corresponds to a scale of approximately 1 nm, which is on the order of a few times the unit cell size of Titan tholin (4–5 Å), as estimated by $S(Q, 0)$ and the parameter Bs in the least-squares fitting results of the phonon dispersion curve (Eq.(4.13)) (see Sec. 4.3.2). In contrast, the ultrasonic method probes phonons on a scale of several hundred micrometers. Despite this difference in length scales, the phonon dispersion measured using the ultrasonic method falls within the phonon dispersion curve obtained by IXS, within the errors. This suggests that the long-wavelength approximation holds well within the phonon scale of a few unit cells. Indeed, the P-wave velocity of Titan tholin determined by the ultrasonic method is consistent with that constrained by the IXS method, within the errors (see Tables 4.2, 4.3). This result implies that the results of ultrasonic methods can be extrapolated to the 0.1–10 Hz frequency band, relevant to the seismograph aboard NASA's *Dragonfly* mission.

Implications for Titan's organic materials: If the chemical structures of Titan's organic materials are similar to Titan tholin and/or hydrothermal organics, their elastic properties at Titan's surface temperature (~93 K; Jennings et al., 2019) are estimated as follows: K = 11 ± 3.8 GPa and G = 6 ±2.0 GPa for Titan tholin-like structure, and K = 9.1 ± 3.1 GPa and G = 6.9 ± 2.4 GPa for hydrothermal organic-like structure. These values assume an Arrhenius-type temperature dependence (considered as the maximum error) of elasticity and a density of ρ = 1130 ± 60 kg m^{-3} of Titan tholin or ρ = 1450 ± 170 kg m^{-3} of hydrothermal organics.

As discussed in Chapter 5, the elasticities of Titan's organic analog materials are essential to analyze the data obtained in future seismic surveys, such as those planned for NASA's *Dragonfly* mission (e.g., Lorenz et al., 2018). By analyzing the travel times of seismic waves artificially generated and reflected from subsurface boundaries, the thickness of the organic regolith on Titan can be estimated. This information is essential for understanding Titan's organic cycles, including the age of its atmosphere. Our measurements of the elastic properties of Titan's organic analog materials involve an error factor of approximately 2. Consequently, the estimated thickness of the organic regolith from an active seismic survey would also include an error factor of 2, suggesting that the constrained age of the atmospheric CH_4 cycle would inherit a similar level of uncertainty. However, it is important to note that the current estimates for Titan's atmospheric age carry significant uncertainties, ranging from 100 Myr to a few Gyr. These estimates are derived from various constraints, including the $^{12}C/^{13}C$ ratio of atmospheric CH_4 (Nixon et al., 2012; Mandt et al., 2012), the estimated amount of organic material on Titan's surface (Lorenz et al., 2008; Nixon et al., 2018), crater counting (Neish & Lorenz, 2012), and interior models predicting episodic major CH_4 replenishments (Tobie et al., 2006). In this context, determining the age of organic sediments with an uncertainty factor as low as 2

represents a significant improvement. Such results would provide valuable insights into the CH_4 cycle on Titan, including the duration over which atmospheric CH_4 has been consumed and converted into organic material.

4.5. Summary of Chapter 4

The present study investigated the elastic wave velocity of Titan's organic analog materials by inelastic X-ray scattering (IXS) measurements and ultrasonic pulse transmittance measurements, respectively. Before each measurement, organic pellets of Titan tholin particles and solids of hydrothermal organics were formed by using hydraulic press. In IXS measurements, the phonon dispersion of both pellets of Titan tholin and hydrothermal organics were determined by measuring IXS spectra at 300 K. IXS spectra of Titan tholin pellet at 300 K, 240 K, 190 K, 140 K, 93 K were measured to investigate temperature dependence of the phonon dispersion and elastic properties of Titan tholin. In ultrasonic measurements, V_p and V_s of pellets of Titan tholin and hydrothermal organics were measured at 300 K.

We find that the acoustic wave velocity estimated from phonon dispersion of Titan tholin is 2860 ± 340 m/s based on IXS measurements, which is consistent with the results of V_p of Titan tholin at 300 K determined to be 3260 ± 390 m/s within the errors. Therefore, the acoustic wave velocity determined in IXS measurements should be P-wave velocity of Titan tholin. V_s of Titan tholin at 300 K is also determined to be 1830 ± 60 m/s, based the ultrasonic measurements. Acoustic wave velocity (V_p) estimated from phonon dispersion of hydrothermal organics, and V_p, and V_s of hydrothermal organics determined by ultrasonic wave experiments are 2580 ± 350 m/s, 2830 ± 60 m/s and 1740 ± 40 m/s, respectively. Given the densities of Titan tholin and hydrothermal organics (1130 ± 60 kg m^{-3} and 1450 ± 170 kg m^{-3}, respectively: Table 4.2), the elastic parameters at 300 K (the bulk modulus K, Young's modulus Y, and Poisson's ratio v) are calculated to be K = 7 ± 0.9 GPa, G = 3.8 ± 0.3 GPa, Y = 9.7 ± 1.8 GPa, and v = 0.27 ± 0.03 for Titan tholin, and K = 5.8 ± 0.7 GPa, G = 4.4 ± 0.5 GPa, Y = 10.4 ± 1.3 GPa, and v = 0.20 ± 0.01 for hydrothermal organics, respectively. The Young modulus of Titan tholin agrees with the previous value of Young's modulus of Titan tholin, 10.4 ± 0.5 GPa.

We also find that the overall crystal structure of Titan tholin does not change significantly and is characterized by the distinct length scale (4–5 Å) between 300 K and 93 K based on the $S(Q, 0)$ measurements and the phonon dispersion curve. The acoustic wave velocity of Titan tholin becomes larger with decreasing the temperature based on the temperature dependence of phonon dispersion. Estimated longitudinal modulus of Titan tholin also becomes larger when the temperature decreases. We performed the least square fittings with both Arrhenius equation and linear relationship, resulting in the values of M_0 = 7.3 ± 1.2 GPa and E_a = -500 ± 230 J mol^{-1} for Arrhenius equation and in M_0 = 15 ± 2 GPa and T_m = 340 ± 110 K for linear relationship. Given the large errors in both fitting results, the dominant mechanism which is responsible for the temperature dependence is uncertainty. Additional analyses of experimental data and/or

additional measurements such as ultrasonic measurements or Brillouin scattering at cryogenic conditions are necessary to evaluate the results obtained in the present study.

Based on the comparison of bulk modulus and density of both Titan tholin and hydrothermal organics with various materials, kerogen is considered to be the closest material, in the elastic properties, to Titan tholin and hydrothermal organics. Our comparison of the Young's modulus of Titan tholin and hydrothermal organics with various organic materials as a function of their C/H ratio suggests that the elemental ratio is not the sole factor determining Young's modulus. Instead, factors such as elemental composition, functional groups, and the molecular configuration of aromatic and aliphatic structures play a crucial role in determining the elastic properties of organic materials. Further investigation, combining improved constraints on chemical structure using LDMS/MS and a systematic comparison of organic materials with different chemical structures, will be essential.

The comparison of phonon dispersion obtained using the IXS and ultrasonic methods for Titan tholin shows that the ultrasonic measurements fall within the IXS phonon dispersion curve near the zero point, within the errors. This indicates that the long-wavelength approximation holds at the phonon scale of a few unit cells, suggesting that results of the ultrasonic method can be extrapolated to the frequency range of seismometer (0.1–10 Hz) onboard NASA's *Dragonfly* mission.

If the chemical structures of Titan's organic materials are similar to Titan tholin and/or hydrothermal organics, the elastic properties of Titan's organic materials at Titan's surface temperature (~93 K: Jenning et al., 2019) would be $K = 11 \pm 3.8$ GPa and $G = 6 \pm 2.0$ GPa for Titan tholin-like structure, and $K = 9.1 \pm 3.1$ GPa and $G = 6.9 \pm 2.4$ GPa for hydrothermal organic-like structure, assuming the Arrhenius type of temperature dependence of elasticity and the density $\rho = 1130 \pm 60$ kg m^{-3} of Titan tholin or $\rho = 1450 \pm 170$ kg m^{-3} of hydrothermal organics.

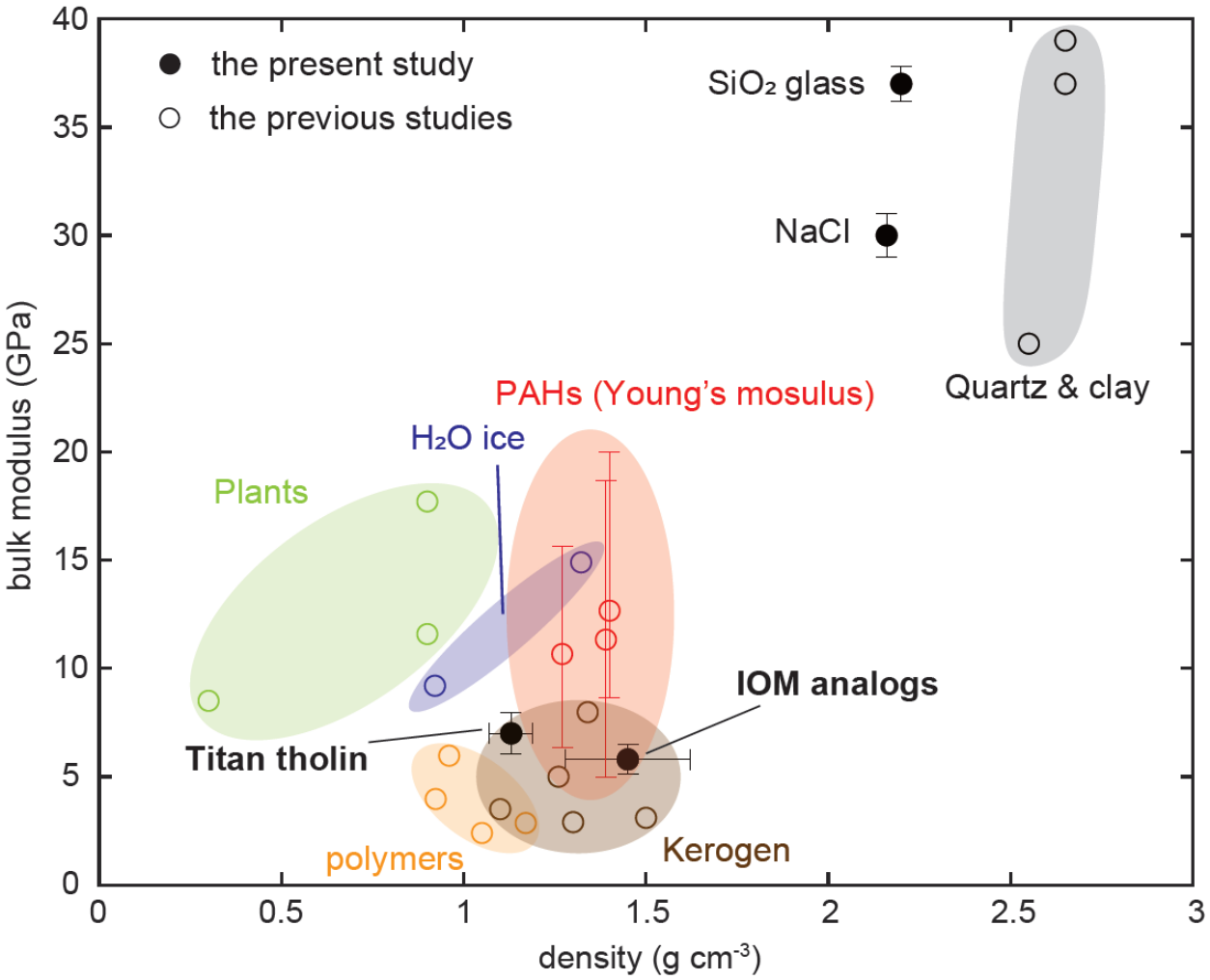

Figure 4.17 Comparison of bulk modulus and densities of various materials measure in the present study (filled circle) and the present studies (empty circle). The reference data includes quartz and clay (Blangy, 1992; Han et al., 1986), H_2O ice (Shaw, 1986), PAHs (Richter et al., 2000), high-density polyethylene (HDPE), low-density polyethylene (LEPE) (Jordan et al., 2021), kerogen (Yan and Han, 2013; Zhao et al., 2016 and references therein; Xie et al., 2019 and reference therein), and plants (Krzesińska et al., 2006). Titan tholin and hydrothermal organics are located near the data of polymers, PAHs, and kerogen.

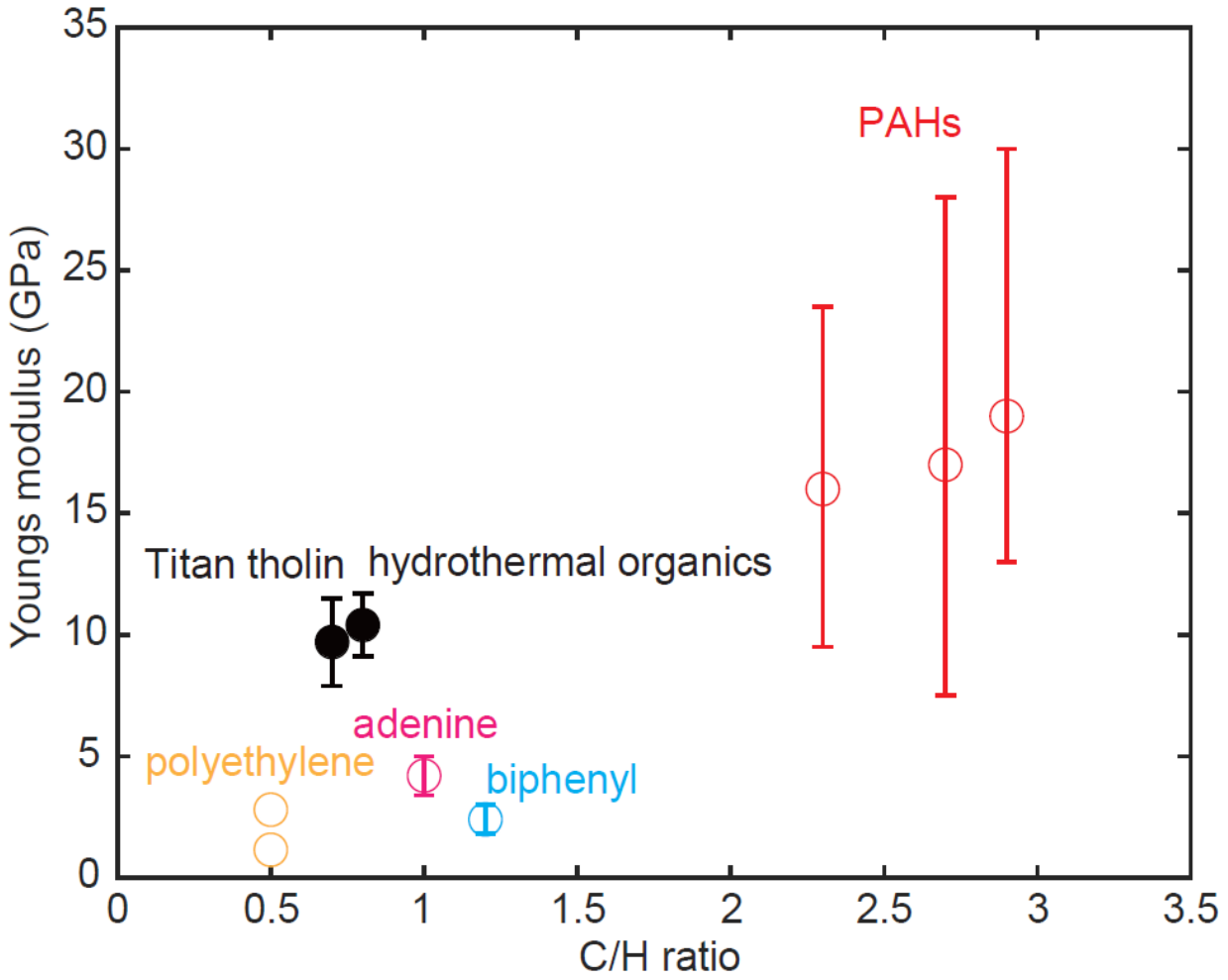

Figure 4.18 Young's modulus versus C/H ratio for Titan tholin and hydrothermal organics, compared with various organic materials, including PAHs (Richter et al. 2000), polyethylene (Jordan et al. 2021), adenine (Yu et al., 2018), and biphenyl (Yu et al., 2018).

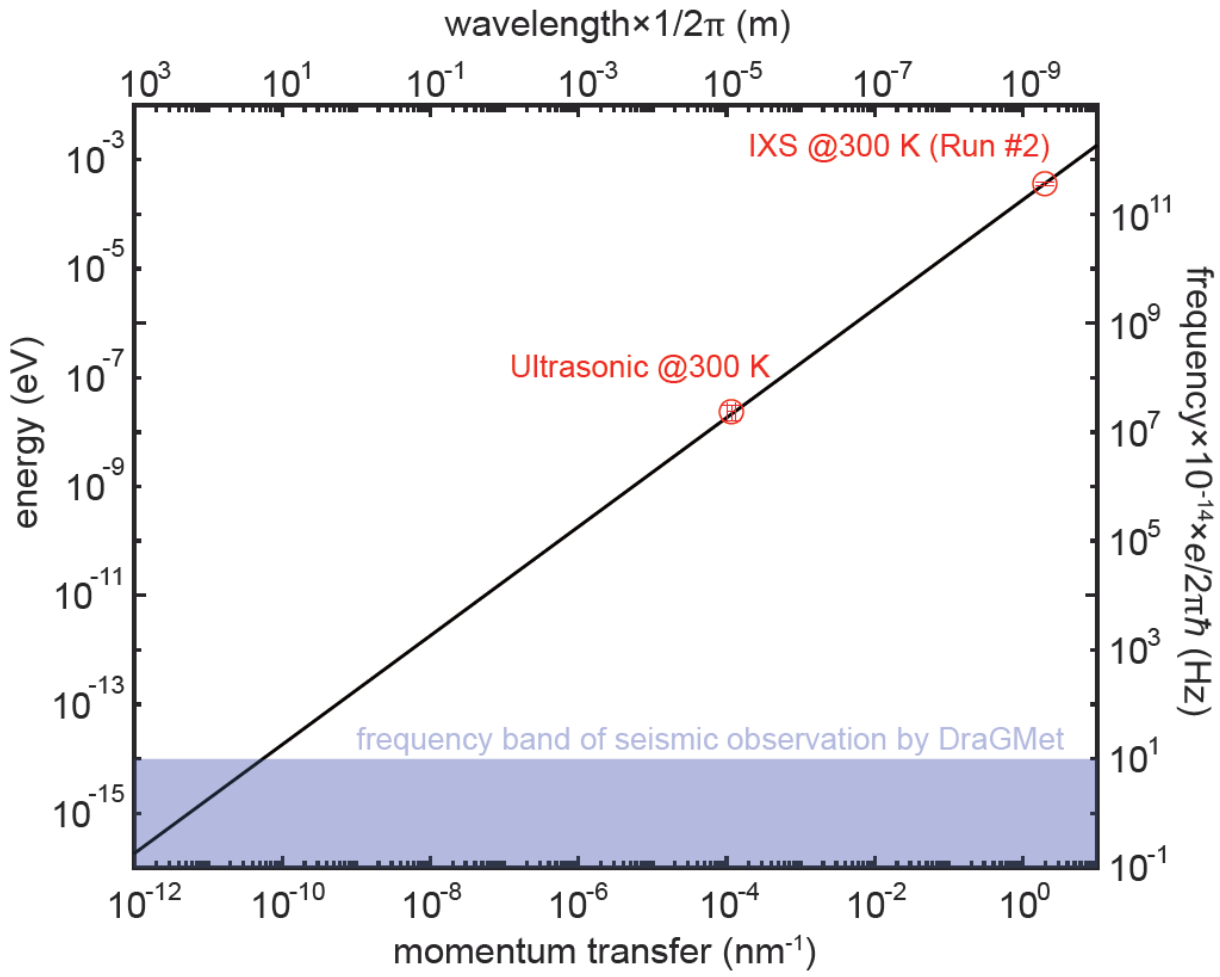

Figure 4.19 Comparison of the phonon dispersion of different orders obtained using the IXS (Run #2) and ultrasonic methods for Titan tholin. The black curve represents the phonon dispersion curve, approximated as a linear relationship near the zero point. The red circles indicate the phonon dispersion obtained by the IXS method at $Q = 1.97$ nm^{-1} and that obtained by the ultrasonic method, considering the relationships $Q = 2\pi/\lambda$ and $E = (2\pi\hbar/e)f$, a frequency range of 40–80 MHz, and a sound speed of 3260 ± 390 m/s. Here, λ_p is the wavelength of phonon, e is the elementary charge, and f is the phonon frequency. The blue region represents the frequency band of seismic observations in future missions.

Chapter 5. Applications to Titan's surface processes

5.1 Objective of Chapter 5

As described in Chapter 1, thick aeolian sediments of dunes of organic materials occur at low latitudes of Titan (Lorenz et al., 2006; Radebaugh et al., 2008, Rodriguez et al. 2014). In contrast, at middle latitudes, there is a significant variation in the thickness of organic materials on the surface. Hummocky, labyrinth, and plains in middle latitude regions exhibit surface H_2O ice absorption, suggesting that thickness of organic materials in these regions are thin; whereas, plains in near the low latitude regions are covered with organic materials (Solomonidou et al., 2018; Malaska et al., 2016). These are two fundamental questions concerning these observations: 1) What would the surface process transport surface organic materials at middle latitude to explain the exposure of H_2O ice at particular regions? 2) How thick are the organic materials in plains at middle and low latitutdes of Titan? Regarding the question 1), saltation of organic materials by winds was not expected to occur based on the high cohesiveness of Titan tholin at room temperature (Yu et al., 2017). However, our results of AFM measurements at low temperatures indicate that the cohesion force and the surface energy of Titan tholin decrease with temperature (Chapter 3), suggesting that the saltation threshold wind speed u^* (see Eq. (1.1) in Chapter 1) of organic materials on Titan may become lower than expected given the surface temperature of ~93 K on Titan (Jenning et al., 2019). Concerning the question 2) above, seismic measurements of shallow subsurface will be conducted in NASA's *Dragonfly* mission. Our data on the elastic wave velocities of Titan tholin at low temperatures obtained in Chapter 4 is crucial to estimate the detectability of the seismic echo in the active seismic survey in the *Dragonfly* mission.

In this chapter, we estimate the saltation and transportation of organic materials by winds at middle latitudes of Titan (Sec. 5.2). Saltation threshold wind speed u^* is calculated based on the temperature dependence of cohesiveness obtained in the present study (Chapter 3). The flux of organic materials from middle latitudes (45° latitude) to low ones (< 30° latitude) is compared with the deposition rates of organic aerosols from the atmosphere. We also estimated elastic wave velocities of seismic wave in organic sediments on Titan based on the results obtained in the present study (Chapter 4). To this end, we employ one dimensional wave propagation model, which has been used for rocky sediments on Earth (Dvorkin et al., 1999) (Sec. 5.3). We performed a sensitivity study of detection limit of depths of reflected echo during seismic measurements assuming the waveform and intensity of active survey in the *Dragonfly* mission with a noise curve model of the onboarded seismometer (Sec. 5.3).

5.2 Saltation of organic materials on Titan

In Chapter 3, the temperature dependence of surface energy of Titan tholin has been obtained in the form of the Arrhenius relationship (Eq. (3.8)). Assuming that Q_{surf} and γ_0 of organic materials on Titan are same as those obtained in Chapter 3, the cohesion coefficient on Titan (at temperature of 93 K), γ_{Titan}, can be calculated using Eq. (1.2). Then, the threshold velocity, u_*, on Titan (at 93 K) can be also obtained by introducing γ_{Titan} into Eq. (1.1) for the same values for the other parameters as those described in Chapter 1.

Figure 5.1 shows the calculated u^* at 93 K based on our experimental results as a function of particle diameter, d, compared with the estimated u_* using the cohesion force at room temperature in the previous study (Yu et al., 2017). As for small particles (< 700 μm), u_* becomes higher at smaller particles because the effects of cohesion force become larger. On the other hand, u_* becomes greater at larger particles for size > 700 μm due to the effect of gravity becoming larger. Thereby, a minimum u^* appears at d ~ 700 μm (Figure 5.1). Our results suggest that the u^* based on our experiments decreases approximately by factor of 3 for a given particle diameter from the previous estimates for the same particle diameter. This is because the u^* depends on the square root of the surface energy, which decreases approximately by a factor of 6 at 93 K compared to that of at 300 K. The range of the estimated u^* is shown in Figure 5.1. Given the minimum u^* at 700 μm, organic materials can saltate by the wind speed > 0.05 m s^{-1}. In contrast, using the u_* estimated based on the previous study (Yu et al., 2017), the wind speed needs to exceed 0.08 m/s for saltation; however, this wind speed would be rarely achieved at middle latitudes. The wind speed of > 0.05 m/s for the u_* based on our experiments can be achieved owing to tidal winds in summer of middle latitudes (Tokano, 2008). Given the fact that the direction of the tidal wind is equatorward (Tokano, 2002; 2008), organic materials can be transported toward low latitudes from middle ones in summer.

Bagnold (1941) found that the mass flux of sand Q_{mass} in steady-state saltation is proportional to the cube of the saltation threshold wind speed u^* based on wind tunnel experiments. The sand mass flux was measured by weighing the total amount of sand transported by wind during the experiments. Three types of sand conditions were tested: uniform sand with an average diameter of 250 μm, naturally graded sand typical of Earth's dune fields, and sand with a wide range of grain sizes. Based on the results of the wind tunnel experiment, the scaling of the steady-state saltation mass flux Q_{mass} (kg/s/m) can be obtained as follows (Bagnold, 1941; Kok, 2012):

$$Q_{\mathrm{mass}} = C_{\mathrm{B}} \sqrt{\frac{d}{D_{250}}} \frac{\rho_{\mathrm{f}}}{g} u_*^3 \tag{5.1}$$

where the empirical factor C_B = 1.5, 1.8, and 2.8 for uniform, naturally graded, and poorly sorted sand, respectively, d is particle diameter, D_{250} is a reference diameter of 250 μm, ρ_f = 5.4 kg m^{-3} is the density of the atmosphere on Titan's surface, g = 1.352 m s^{-2} is the gravitational constant of Titan, and u_* is the saltation threshold windspeed. Indeed, this scaling with C_B = 1.8, well explains sand mass flux observed on Earth's dunes (Bagnold, 1941). Figure 5.1 shows that the minimum u_* would range 0.05–0.07 m s^{-1} for particle size of 750 μm. Thus, the lower limit of Q_{mass} can be estimated to be 1–2 g s^{-1} for different C_B.

Tidal winds at velocity > 0.05 m/s may occur on Titan in a limited time period, such as during summer seasons. Previous work estimated the probability of occurrence of a given wind speed near the surface at different latitudes (Fig. 3 in Tokano, 2008) (also shown as Figure 5.2 of this thesis, which is obtained based on Fig. 3 of Tokano (2008) to read the data points using WebPlotDigitizer software (ver. 4.7)). Figure 5.2 shows the probability of the duration of the wind of speed blowing per Titan year at each latitude bins. Based on the results of GCM calculations shown in Tokano (2008), the fastest winds reach to 0.07 m/s which occur in summer. Table 5.1 shows the results of the analysis for the probability of wind speed >0.05 m s^{-1} for different latitude bins. The probability of wind speed >0.05 m s^{-1} is 1.6 % at 45° latitude (middle latitudes), which corresponds to ~1 × 10^7 seconds per one Titan year (one Titan year = 29.5 Earth year). Together with the estimated Q_{mass} above (1–2 g s^{-1} m^{-1}), the lower limit of mass of transportation at middle latitudes toward low ones per one Titan year would be ~(1–2) ×10^7 g m^{-1}. Considering that Titan has a radius of approximately 2570 km, the total amount of sand transported from latitude 45° toward the equator per Titan year is estimated to be ~2 × 10^{13} g. On the other hand, based on the photochemical models in Titan's atmosphere, the aerosol production rate in the atmosphere is estimated to be on the order of 10^{-14} g cm^{-2} s^{-1} (McKay et al., 1989, 2001; Rannou et al., 2003; Lavvas et al., 2009; 2011; Larson et al., 2014). If these organic aerosols deposit on the surface of Titan globally, the flux of aerosols in middle latitude region (30–60°) would be approximately 1 × 10^8 g per one Titan year. Accordingly, the flux of the aeolian transportation at middle latitudes by tidal winds is much greater than the proposed deposition rate of organic aerosols at middle latitudes.

The fact that the high potential of aeolian transportation of organic materials by tidal winds implies that the growth of deposited aerosols with size of 0.1–1 μm to sands with size of ~10^2–10^3 μm would be the limiting factor of transportation. The proposed mechanisms of the growth of particle size on Titan include evaporitic cementation (Hirai et al., 2023) or polymerization by external energy (Abplanalp et al., 2019). Based on a modeled vertical profile of aerosol number density in Titan's troposphere (Tomasko & West, 2009), the number of aerosols at altitude below 30 km would be 2–4 particles/cm^3 for ~1 μm-sized aerosol. Assuming the diameter of raindrop on Titan as ~1 cm (Lorenz, 1995) and the altitude of CH_4 cloud

formation as ~15–20 km (Rannou et al., 2006), the number of aerosols that can be swept by one falling raindrop might be the order of 10^6 particles until reaching to the surface. If all swept particles are incorporated into the raindrop and coagulate upon drying similar to our experiments, then the size of one aggregate formed by drying of one raindrop would be around the order of 10^2 μm. Thereby, one cycle of falling and evaporation of a raindrop could account for the growth of aerosols to larger aggregates. Our results in Chapter 3 show that the cohesion force and, thereby, $u*$ would not strongly depend on the chemical structures within the possibility of Titan's surface organic materials (Fig. 3.9). For instance, $u*$ of altered tholin would be 1.2–1.4 times higher than Titan tholin given the surface energy of altered tholin is comparable to 1.5–2 times higher than that of Titan tholin. Given the $u*$ for Titan tholin at Titan would be 0.04 m/s for 700 μm, $u*$ for aggregates of organic aerosols covered with evaporitic deposits of 700 μm diameter would be 0.05–0.07 m/s, which are comparable to the wind speed of tidal wind in the summer (Tokano, 2008).

Given that the (apparent) surface energy of H_2O ice (the order of 10^{-4} J/m^2 at 93 K: Jabaud et al., 2024) is significantly smaller than the Titan tholin, organic aerosols on H_2O-ice crust on Titan's surface would saltate easily compared to saltation on other organic sediments due to the difference of the saltation threshold wind speed. As a results, organic particles would tend to remain and be concentrated on the organic sediments rather than on H_2O-ice crust. Indeed, thick organic sediments only exist in the low latitude regions as organic dunes, whereas plains, labyrinth, hummocky in higher latitudes (30–50°N) in middle latitude regions, and hummocky and interdunes in low latitude regions are mainly composed of H_2O-ice based on IR and Radar observation as mentioned above in Chapter 1 (Solomonidou et al., 2018; Bonnefoy et al., 2016).

If the chemical structures of organic evaporites and organic materials formed through hydrothermal reactions on Titan are similar to organic aerosols, the saltation threshold $u*$ would not change dramatically, given that the surface energy of organic materials does not change significantly (by a factor of 2–3) across various elemental compositions, the abundance of unsaturated bonds, and molecular sizes, as mentioned above in Chapter 3.

In the past, the surface temperature of Titan would be different depending on the amount of atmospheric CH_4 (McKay, 1991; Lorenz et al., 1997; Charnay et al., 2014). If the surface temperature of Titan in the past is higher today with a larger amount of CH_4, the surface energy of organic particles would be larger than that of current surface temperature (McKay, 1991), which results in larger saltation threshold wind speed $u*$. On the other hand, if the surface temperature of Titan in the past is colder than today due to atmospheric collapse of CH_4 (Lorenz et al., 1997; Charnay et al., 2014), surface energy of organic particles would be lower than today, which results in lower saltation threshold wind speed $u*$. To constrain the conditions for the sand

transportation on Titan in the past, surface temperature should be considered in addition to the wind regime (Lora et al., 2014).

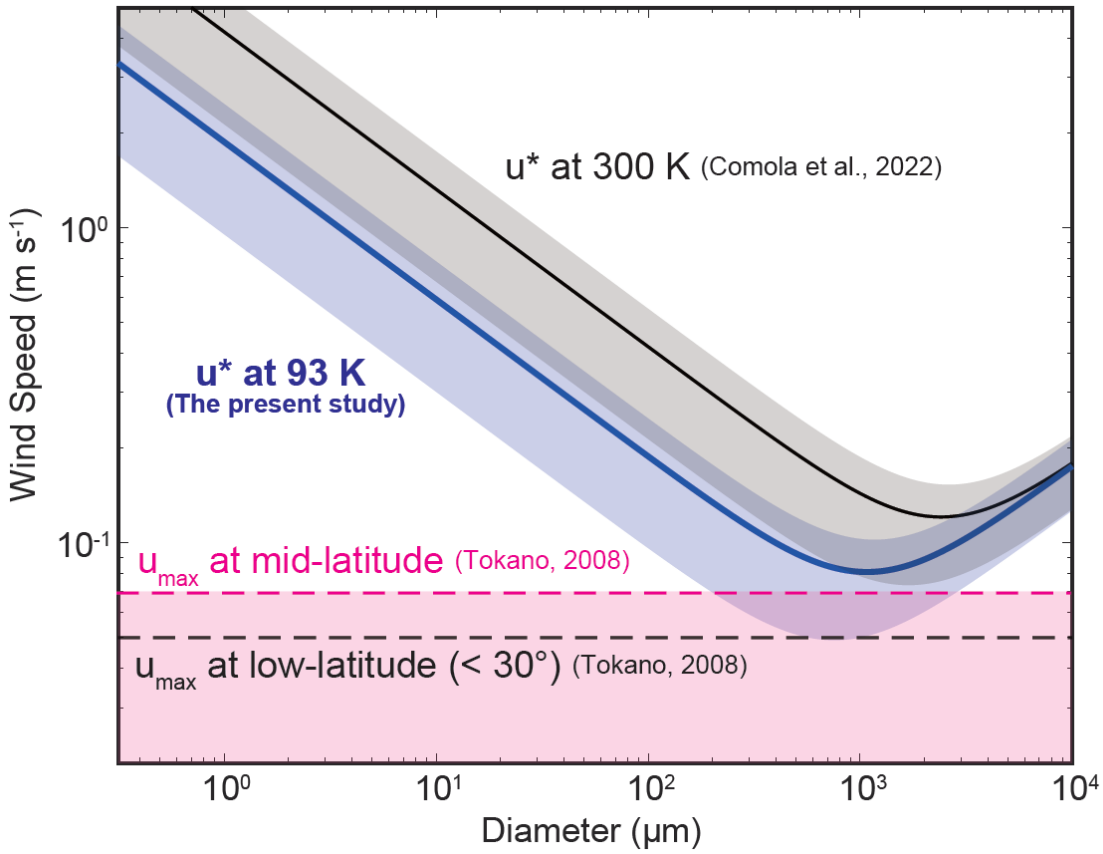

Figure 5.1 The saltation threshold wind speed u_* at 93 K (blue) estimated based on our experimental results as a function of particle diameter, compared with that estimated based on the previous data obtained at room temperature (black; Comola et al., 2022). The hatches of these two curves indicate the error of the cohesion coefficient. The predicted maximum wind speeds u_{max} on Titan's low (black dash line) and middle latitudes (pink dash line) are also shown (Tokano, 2008). Below these dashed lines, organic particles cannot saltate.

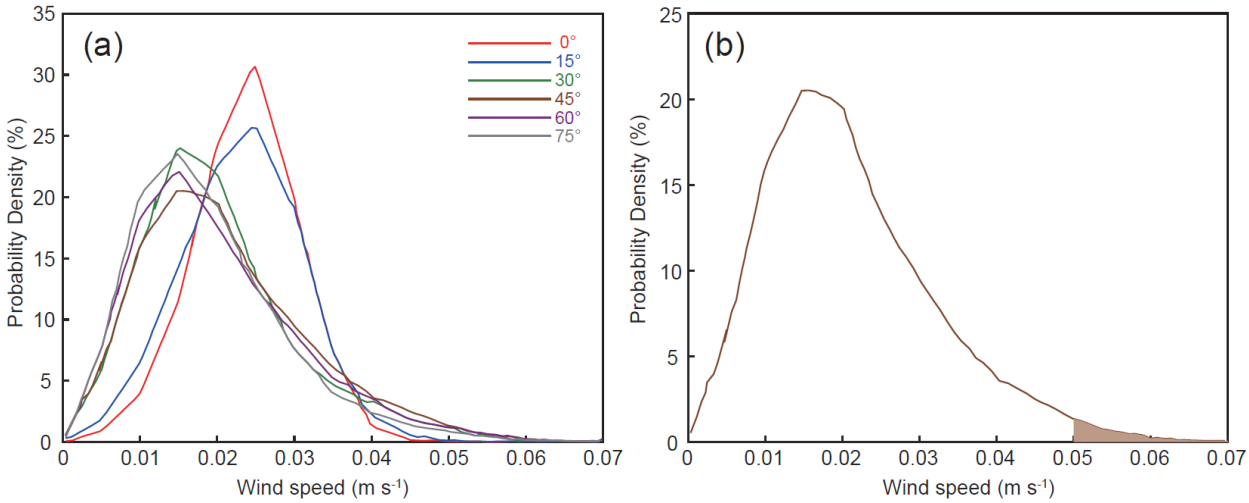

Figure 5.2 (a) Probability density of the wind speed during one Titan-year at different latitudes (Tokano, 2008). (b) The probability density of wind speed at 45° latitude. The brown area indicates the probability of wind speed > 0.05 m s^{-1}.

Table 5.1 The results of the analysis for the probability of wind speed > 0.05 m s^{-1} at different latitudes.

latitude	Probability (%)
0°	0.24
15°	0.23
30°	1.2
45°	1.6
60°	1.6
75°	1.1

5.3 Estimation of detection limits in seismic survey on Titan

In an active survey of seismology on Titan, a spacecraft (e.g., *Dragonfly* spacecraft) makes artificial seismic (elastic) waves by hammering the surface with a drill (Lorenz et al., 2018). A seismometer onboarded on the spacecraft measures elastic waves reflected within the subsurface. In order to constrain the thickness of organic sediments in an active seismic survey, the boundary of organic materials and overlaid icy crust in the subsurface needs to be determined based on a reflected echo at the boundary with the seismometer. Detectability of the reflected echo is determined by a comparison of the amplitude of the seismic wave with the noise of the seismometer. Attenuation of seismic waves during propagation is controlled by the properties of subsurface materials (Q_a value), frequency of wave, reflected depth, and a seismic wave velocity (see Sec. 5.3.2) (e.g., Kedar et al., 2017). Here, we perform a sensitivity study on numerical simulations on propagation of artificial seismic waves within a layered structure of Titan's shallow subsurface; that is, the upper organic sediments and the bottom H_2O ice. Organic materials on Titan would be porous, regolith-like materials (Hayes et al., 2008), rather than organic solids without a significant porosity. We examine how the detection limit of depths of organic sediments depends on the possible range of the parameters, such as an elasticity of organic materials and a porosity of organic sediments. To this end, we consider a one dimentional model of seismic wave propagation, which takes into account an attenuation of seismic waves and the elastic modulus of high-porosity sediments based on a model used in active seismic surveys on Earth (Dvorkin et al., 1999). The calculated results of the amplitude of the reflected echo are compared to the noise model of *Dragonfly* Geophysics and Meteorology Package (DraGMet) seismometer (SEIS), which has been developed by JAXA and will be onboarded on NASA's *Dragonfly* spacecraft. Finally, we discuss the parameters of subsurface materials that can be detected based on a reflected echo from the boundary.

5.3.1 Model description

A schematic illustration of our seismic wave propagation model is shown in Fig. 5.3. The model assumed the presence of organic sediments overlying on H_2O ice crust. The organic sediments and overlaid H_2O ice crust were divided into multiple layers with 1000 layers as total with a thickness of 1 m for each layer. The boundary between the organic sediments and H_2O ice was varied from 1 m to 1000 m depth (Fig. 5.3). The top of the organic sediment layer was connected to the atmosphere (Fig. 5.3). The thickness of organic sediments on Titan is poorly constrained, although the maximum height of linear dunes in the equatorial regions is estimated to be ~150 m based on the radar altimetry observation by Cassini (Lorenz et al., 2006). The effective pressure, i.e. a sum of the lithostatic and hydrostatic pressures and the effective elastic modulus of the organic sediments were calculated in each layer (see Sec. 5.3.1.1). The elastic

properties of the organic sediments were also varied assuming the values for Titan tholin and hydrothermal organics obtained in Chapter 4. Vertically isothermal structure at 300 K or 93 K was assumed within the organic sediments for simplicity. We assumed a box model for the elastic wave velocity propagates in one layer of organic sediments in the organic sediment was constant during the seismic wave propagation. The elastic wave velocity was calculated from the elasticity and pressure at the depth of the boundary. Part of elastic wave was reflected on the subsurface boundary depending on the reflection coefficient C_r, whereas the other part of elastic wave transmitted toward the subsurface layer. The porosity of the H_2O-ice bedrock was assumed to be zero for simplicity.

5.3.1.1 Basic equations

When the seismic wave reaches the top layer of H_2O ice, or CH_4 aquifer, at depth d_r, the seismic wave reflects at the boundary. The amplitude $A(f)$ of the reflected wave at the surface with frequency f can be described as below (Keder et al., 2017):

$$A = A_0 exp\left(-\frac{\pi f \times (2d_r/v)}{Q_a}\right)\frac{1}{4\pi \times (2d_r)}C_r, \tag{5.2}$$

where $A_0(f)$ is the amplitude of the initial, artificial seismic wave from the top of the layers of organic sediments, v is the seismic wave velocity, Q_a is the quality factor of the sediment, and C_r is the reflection coefficient. The exponential term of Eq. (5.2) represents the energy dissipation due to scattering and intrinsic properties of the organic materials. The term of $1/\{4\pi \times (2d_r)\}$ in Eq. (5.2) represents geometric attenuation, where the energy dissipates as the wavefront spreads three dimensionally. The reflection coefficient C_r can be described as below:

$$C_r = \frac{\rho_B v - \rho_2 v_2}{\rho_B v + \rho_2 v_2}, \tag{5.3}$$

where ρ_B is the bulk density of the organic sediments, and ρ_2 and v_2 are the bulk density and velocity of the H_2O ice crust, or organic sediments with CH_4 aquifer, respectively. The value of ρ_B was calculated as a linear mixing of the densities of the organic materials (Titan tholin or hydrothermal organics) and Titan's air (5.2 kg m^{-3}) for a given porosity Φ. The value of ρ_2 for H_2O ice crust was the density of H_2O ice (1000 kg m^{-3}). The values of v_2, the P-wave and S-wave velocities of H_2O ice, were extrapolated to be 4200 m/s and 2130 m/s, respectively. These values were derived from experimental measurements of V_p and V_s conducted at temperatures ranging approximately from 270 K to 210 K (Kohnen, 1974).

We assumed that Q_a of the regolith follows the following relationship based on the equation derived from energy dissipation of lunar regolith (Nakamura & Koyama, 1982):

$$Q_a = Q_0 f^{0.7}, \tag{5.4}$$

where Q_0 is the attenuation coefficient. The value of Q_0 for organic materials on Titan is unknown; thereby, we assumed $Q_0 = 20$ as a nominal value, based on the value of kerogen on Earth (Carcione, 2000). Additionally, we investigated the effect of Q_0 on the detectability of reflected echoes, considering a range of values from $Q_0 = 2$ to $Q_0 = 2000$, as discussed later.

Using Eq. (5.2) with Eq. (5.3), $A(f)$ can be estimated when v and v_2 are obtained. The seismic wave velocity v in the organic sediments with porosity Φ is determined by the bulk elastic modulus and density of the organic materials, and coordination number n. At the critical porosity ϕ_c, above which grains exist as a suspension, the effective bulk modulus at the critical porosity ϕ_c, K_{HM} and the effective shear modulus at the critical porosity ϕ_c, G_{HM} can be described as below (Dvorkin et al., 1999):

$$K_{HM} = \left[\frac{n^2(1-\phi_c)^2 G^2}{18\pi^2(1-\nu)^2} P\right]^{\frac{1}{3}},$$
$$G_{HM} = \frac{5-4\nu}{5(2-\nu)}\left[\frac{3n^2(1-\phi_c)^2 G^2}{2\pi^2(1-\nu)^2} P\right]^{\frac{1}{3}}, \tag{5.5}$$

where P is the effective pressure, K, G, and ν are the bulk and shear modulus of zero porosity (i.e. intrinsic modulus), and Poisson's ratio, respectively. K and ν at room temperature and 93 K were obtained in our measurements in Chapter 4. n is the coordination number of each grain, which is the average number of contacts per grain.

According to Dvorkin et al. (1999), the bulk modulus and shear modulus of porous sediments without fluid in the pore can be classified into two regimes; that is, the porosity $\phi \leq \phi_c$ and the porosity $\phi > \phi_c$ (Fig. 5.3). In the regime of $\phi \leq \phi_c$, each grain loses contact and behaves as suspended in fluid. The effective bulk modulus K_{Dry} and the effective shear modulus G_{Dry} can be described as below (Dvorkin et al., 1999):

$$K_{Dry} = \left[\frac{\phi/\phi_c}{K_{HM} + \frac{4}{3}G_{HM}} + \frac{1-\phi/\phi_c}{K_{HM} + \frac{4}{3}G_{HM}}\right]^{-1} - \frac{4}{3}G_{HM},$$
$$G_{Dry} = \left[\frac{\phi/\phi_c}{G_{HM} + Z} + \frac{1-\phi/\phi_c}{G + Z}\right]^{-1} - Z, \tag{5.6}$$
$$Z = \frac{G_{HM}}{6}\left(\frac{9K_{HM} + 8G_{HM}}{K_{HM} + 2G_{HM}}\right).$$

In the regime of $\phi > \phi_c$, each grain is densely packed. The effective bulk modulus K_{Dry} and the effective shear modulus G_{Dry} can be described as below (Dvorkin et al., 1999):

$$K_{\mathrm{Dry}} = \left[\frac{(1-\phi)/(1-\phi_{\mathrm{c}})}{K_{\mathrm{HM}} + \frac{4}{3}G_{\mathrm{HM}}} + \frac{(\phi-\phi_{\mathrm{c}})/(1-\phi_{\mathrm{c}})}{\frac{4}{3}G_{\mathrm{HM}}}\right]^{-1} - \frac{4}{3}G_{\mathrm{HM}},$$
$$G_{\mathrm{Dry}} = \left[\frac{(1-\phi)/(1-\phi_{\mathrm{c}})}{G_{\mathrm{HM}} + Z} + \frac{(1-\phi)/(1-\phi_{\mathrm{c}})}{Z}\right]^{-1} - Z, \quad (5.7)$$
$$Z = \frac{G_{\mathrm{HM}}}{6}\left(\frac{9K_{\mathrm{HM}} + 8G_{\mathrm{HM}}}{K_{\mathrm{HM}} + 2G_{\mathrm{HM}}}\right).$$

The bulk modulus and shear modulus of organic sediments filled with fluid in the pore, K_{sat} and G_{sat}, can be described as below (Dvorkin et al., 1999):

$$G_{\mathrm{sat}} = G_{\mathrm{Dry}},$$
$$K_{\mathrm{sat}} = K\frac{\phi K_{\mathrm{Dry}} - (1+\phi)\,K_{\mathrm{f}}K_{\mathrm{Dry}}/K + K_{\mathrm{f}}}{(1-\phi)K_{\mathrm{f}} + \phi K - K_{\mathrm{f}}K_{\mathrm{Dry}}/K}, \quad (5.8)$$

where K_{f} is the bulk modulus of the fluid in the pore. Here, we assumed that the pore is filled with N_2 and CH_4 of Titan's atmosphere. The elastic wave velocities of regolith can be described as below (Dvorkin et al., 1999):

$$V_{\mathrm{p}} = \sqrt{\left(K_{\mathrm{sat}} + {}^{4}/_{3}\,G_{\mathrm{sat}}\right)/\rho_{\mathrm{B}}}\,,$$
$$V_{\mathrm{s}} = \sqrt{G_{\mathrm{sat}}/\rho_{\mathrm{B}}}\,, \quad (5.9)$$

where ρ_{B} is the bulk density of regolith.

The effective pressure is determined to be lithostatic and hydrostatic pressure (Dvorkin et al, 1999). In the present study, we assumed the effective pressure is described as below,

$$P = P_{\mathrm{atm}} + [(1-\phi)\rho_1 + \phi\rho_{\mathrm{f}}]g|z|, \quad (5.10)$$

where P_{atm} is Titan's surface pressure.

5.3.1.2 Parameters

In our calculations, we varied four parameters, including two experimentally obtained values in Chapter 4; that is, (1) the bulk modulus *K* and shear modulus *G* of the organic materials constrained in the present study (Chapter 4), (2) Poisson's ratio *v* constrained in the present study (Chapter 4), (3) the critical porosity Φ_{c}, and (4) the coordination number *n*. Table 5.2 summarizes the range of these parameters varied in the calculation. In Chapter 4, the bulk modulus *K* and the Poisson's ratio *v* of Titan tholin at 300 K were determined to be $K = 7 \pm 1$ GPa, $G = 3.8 \pm 0.3$ GPa, and $v = 0.27 \pm 0.5$, respectively. Those of hydrothermal organics were 300 $K = 5.8 \pm 0.7$ GPa, $G = 4.4 \pm 0.5$ GPa, and $v = 0.20 \pm 0.01$, respectively. Assuming that the

bulk modulus K and shear modulus G of each organic materials follow the Arrhenius equation with E_a = -500 ± 230 J mol^{-1} in Eq. (4.27), the values of K and G at 93 K are estimated to be K = 11 ± 3.8 GPa and G = 6 ±2.0 GPa for Titan tholin, and K = 9.1 ± 3.1 GPa and G = 7 ±2.4 GPa for hydrothermal organics. The porosity of organic sediments on Titan was assumed to be 0.3–0.5 based on those of dunes on Earth (Dickinson & Ward, 1994; Atkins & McBride, 1992). The critical porosity Φ_c and the coordination number n of the organic sediments were assumed to be 0.36–0.4 and 6–9, respectively, based on the previous studies on unconsolidated rocks on Earth and/or sphere pack (Dvorkin et al., 1999; Andrä et al., 2013). We varied these parameters within the suggested ranges to investigate the sensitivity of the results on these parameter sets.

As for the initial artificial seismic wave, we used the data of hammering by NASA's *InSight* mission to Mars as an analog for the source of artificial seismic waves for an active seismic survey on other extraterrestrial bodies beyond Earth, although the drilling system will be used for the *Dragonfly* mission. Figure 5.4 shows a comparison of the amplitude spectral density (ASD) of hammering by Insight-HP^3 of the InSight lander Mars (SEIS Data Service. 2019; Brinkman et al., 2022; Spohn et al., 2022) and a noise model of DraGMet SEIS (personal communication with Dr. Keisuke Onodera) used in the present study. The noise model considered the instrumental self-noise, such as Johnson-Nyquist noise and suspension noise of the seismometer, voltage noise, and current noise of the pre-amplifier (personal communication with Dr. Keisuke Onodera).

5.3.2 Results for modeling of seismic measurements

Figure 5.5 shows the vertical profile of effective pressure in Titan's organic regolith calculated with Eq. (5.10). In the present study, the fluid density was neglected, assuming that the pores are filled with air, which has a much lower density than the organic regolith. Solid line, dashed line and dotted line correspond to the porosity Φ = 0.3, Φ = 0.4, and Φ = 0.5, respectively. This figure indicates that the effective pressure of Titan's organic regolith increases as the depth increases and reaches at most 8.5 × 10^5 Pa which corresponds to ~6 times larger than the atmospheric pressure. Thus, the grains composing of the organic regolith does not deform due to the effective pressure.

Figure 5.6 shows the vertical profile of the elastic wave velocities of organic regolith at 93 K calculated using K = 11 GPa, G = 6 GPa and ν = 0.27, the intrinsic elasticity of Titan tholin as constrained in Chapter 4, and based on the rock physics modelling described in Sec. 5.3.1.1 at each porosity condition. These results indicate that the bulk elastic wave velocities decrease by a factor of 4–5 compared to intrinsic elastic wave velocity. On the other hand, the elastic wave velocity does not increase significantly at most by a factor of 1.1–1.2 as the deeper depth down to 1000 m.

Figure 5.7 shows the typical result of the amplitude spectral density (ASD) of the reflected seismic echo with initial amplitude of the hammering was used as the Insight hammering (Brinkman et al., 2022; Spohn et al., 2022) passing through organic regolith and reflected from subsurface boundary layer composed of H_2O ice bedrock (v_2 = 4200 m s^{-1}, ρ_2 = 1000 kg m^{-3}) at each depth over a range from 1 to 1000 m depth. These results are compared to ASD of the noise curve model shown in black curve. The results indicate that the ASD of noise curve tends to be larger than that of reflected echoes from all depth at lower frequency range. On the other hand, the ASD of the reflected echoes from ~10–30 m at higher frequency exceeds that of noise curve. There is no significant difference between all porosity conditions. Figure 5.8 shows the comparison of the amplitude of the echo and the noise model at 0.1 Hz, 1 Hz, and 10 Hz for each porosity condition, shown in Figure 5.7. Each black curve indicates the amplitude of the noise model at each frequency. Based on the comparison, the detection limit of depths of this condition is around 30 m shown in 10 Hz. Therefore, the detection limit of depth of the reflected echo at this condition could be 30 m. The detection limits for depth under the other calculation conditions were analyzed following the same protocol as described above.

Figure 5.9 shows the results of the sensitivity study of detection limit of depths to the bulk modulus and the shear modulus of each organic material constrained in Chapter 4, assuming a porosity of organic regolith Φ = 0.4. The detection limits of depths of P-wave could be approximately 30 m, which are independent of temperature and structure dependence of elasticity of organic materials. On the other hand, the detection limits of depths of S-wave could be approximately 25 m for Titan tholin and 20–25 m for hydrothermal organics at all temperature conditions. On the other hand, Fig 5.10 shows the results of the sensitivity study of detection limits of depths to Poisson's ratio v, the porosity of regolith Φ, the critical porosity Φ_c, and the coordination number n. In all calculations, P-wave velocity based on the bulk modulus and the shear modulus of Titan tholin at 93 K was considered. The results indicate that the detection limits of depths of P-wave remain largely unchanged (~30 m) across the range of parameters, except for porosity, which affects the detection limit as follows: 25 m for Φ = 0.5, 30 m for Φ = 0.4, and 33 m for Φ = 0.3. The thickness of organic material with zero porosity at each detection limit depth ranges from approximately 12.5 to 23 m. This is larger than the estimated thickness of organic aerosols deposited on Titan's surface over a few billion years, which is on the order of a few meters. This estimate is based on the predicted haze production rate (~10^{-14} g cm^{-2} s^{-1}) from photochemical models (e.g., McKay et al., 1989, 2001; Rannou et al., 2003; Lavvas et al., 2009, 2011; Larson et al., 2014) and the density of Titan's organic aerosol analog materials (Titan tholins) (~1000 kg m^{-3}) (Chapter 4 of this study; Yu et al., 2023, and references therein). Therefore, during an active seismic survey in Titan's low-latitude regions, reflected waves from the subsurface boundary could be detected in relatively thin areas (<30 m), rather than in thicker regions such as dune ridges (~100 m thickness; Lorenz et al., 2006).

Figure 5.11 shows the dependence of the energy dissipation term $exp\left(-\frac{\pi f(2d_r/v)}{Q_a}\right)$ in Eq. (5.2) on the reflection depth, considering different values of Q_0 values of 2, 20, 200, and 2000. This range of attenuation factors was selected based on comparisons with attenuation factors of Earth's lithosphere (~10–1000), the Moon's megaregolith (~1–10), Martian regolith (~100–1000), and Earth's volcanic regions (~1–100) (Onodera et al., 2023, and references therein). The attenuation term represents the seismic wave energy loss due to the properties of the regolith, as mentioned above. The calculations were conducted at f = 10 Hz, using K = 11 GPa, G = 6 GPa and v = 0.27, the intrinsic elasticity of Titan tholin as constrained in Chapter 4, with a critical porosity Φ_c = 0.4 and a coordination number n = 6. For Q_0 = 20, corresponding to the attenuation factor of kerogen (Carcione, 2000), the energy dissipation term varies by less than 5% at all depths relative to its maximum value. In contrast, for Q_0 = 2, representing a pessimistic scenario with attenuation coefficient similar to the Moon's megaregolith or Earth's volcanic regions, energy dissipation increases significantly, with up to 40% of seismic wave energy lost at greater depths. These findings indicate that for attenuation factors equivalent to or greater than Q_0 = 20, the expected reflection amplitudes are sufficient to detect seismic echoes at depths up to 30 m.

To summarize the results of the sensitivity study performed in the present study, the detection limits of depths of P-wave would be 25–33 m, whereas that of S-wave would be 21–27 m assuming the temperature and structure dependence of the elasticity of organic materials measured in Chapter 4. Our sensitivity study suggests that the elasticity of organic materials such as bulk modulus, shear modulus, and Poisson's ratio v, and other parameters such as coordination number n, the critical porosity Φ_c, and the porosity of regolith Φ does not change the detection limits of depths significantly. This is because a factor of difference of the elastic wave velocity does not affect the attenuation of the amplitude of the seimic wave (see Eq. (5.2)). On the other hand, the Q_0 value of organic sediments will affect the detection limit of depth (e.g., approximately 30 m) when Q_0 is as low as 2, as shown in Figure 5.11. Initial input A_0 could also affect the results of the detection limits of depths significantly, because this value directly determines the initial amplitude of the seismic wave and, consequently, the amplitude of the reflected echoes after accounting for attenuation and geometric spreading (see Eq. (5.2)). Therefore, to characterize the amplitude spectral density of drilling of DrACO which will onboarded on *Dragonfly* are important to estimate the detection limits of depths of Titan's shallow surface during seismic measurements in the future mission. Finally, the elastic wave velocities of organic materials constrained in this study are essential for interpreting the thickness of organic sediments from the travel time of reflected echoes, which will be obtained during the active seismic survey conducted as part of NASA's *Dragonfly* mission.

5.4. Summary of Chapter 5

The present study estimated the saltation threshold wind speed u_* based on the temperature dependence of the surface energy of Titan tholin obtained in Chapter 3. Our results show that u_* would be 0.05 m/s for particles with diameter of 700 μm at 93 K, which is a factor of 3 lower than the previous estimate at room temperature. Given this u_* at 93 K, organic particles at middle latitudes of Titan can saltate due to tidal winds in summer. Based on the estimation of saltation mass flux Q_{mass}, the amount of organic sand transported from latitude 45° toward the equator by tidal winds in summer would be ~2×10^{13} g per Titan year. This amount is higher than the estimated deposition rate of organic aerosols in middle latitude regions (30–60°), which is approximately 1×10^8 g per one Titan year. Thereby, effective removal of organic aerosols would occur in middle latitudes. On the other hand, the size of organic particles should be larger than approximately 700 μm, requiring size growth mechanisms from 1 μm-sized aggregates of organic aerosols in the atmosphere on Titan. In other words, growth of size would be a limiting factor of aeolian transport of organic materials.

Active seismic measurements of the shallow subsurface structure on Titan will be performed in the *Dragonfly* mission. We also performed a sensitivity study of the detection limit of depths of organic sediments. Our results suggest that the detection limits of depths of P-wave and S-wave would be ~30 m at 10 Hz of frequency, assuming a porosity of organic regolith Φ = 0.4. The detection limits would be insensitive to the elastic parameters, such as the bulk and shear modulus, and geological parameters, such as critical porosity and overlaid materials. Our results confirm that V_p and V_s are sensitive to the porosity as previously suggested. Notably, the calculated detection limit of depth of organic sediments with zero porosity exceeds the estimated thickness of organic aerosols accumulated on Titan's surface over billions of years, implying that seismic echoes reflected from the subsurface boundary could be detectable in relatively thin regions (<30 m) during an active seismic survey. The elastic wave velocities of organic materials determined in this study are critical for estimating the thickness of organic sediments based on the travel time of reflected seismic echoes, which will be measured during the active seismic survey of NASA's *Dragonfly* mission. In addition, our findings of elasticities of Titan's organic analog materials would be essential to provide insight into the compaction and sintering history of organic materials on Titan.

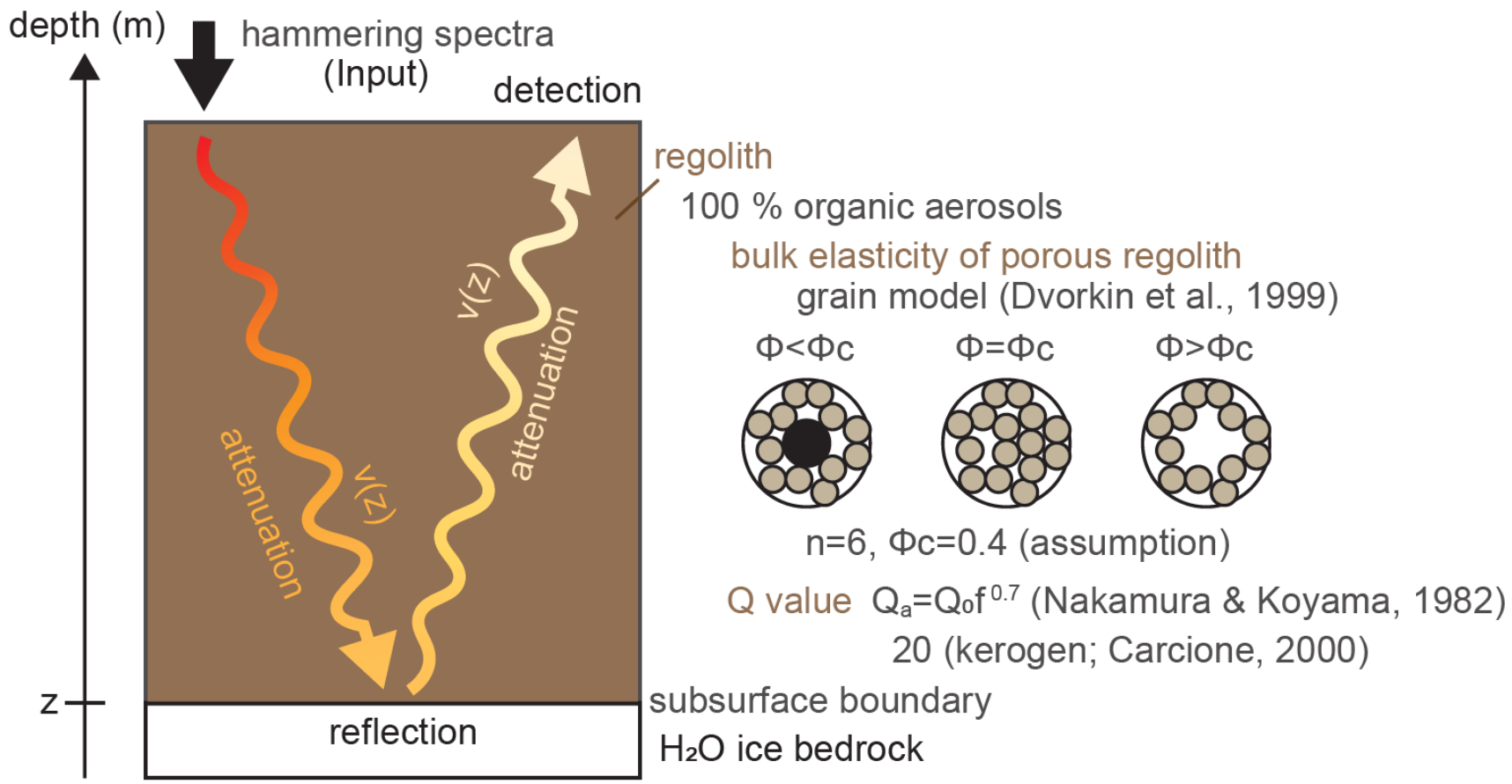

Figure 5.3 A schematic illustrations of seismic wave propagation model. The wavy line indicates the propagation of seismic wave. The gradation color suggests attenuation of the elastic wave. The effective pressure, the effective modulus, and the effective elastic wave velocities of organic regolith were calculated based on the grain model reported in Dvorkin et al. (1999). The elastic wave velocity was assumed to be the velocity at the depth of the subsurface boundary. We calculated the attenuation of artificial seismic wave generated by Insight-HP^3 (InSight Mars SEIS Data Service. 2019; Brinkman et al., 2022; Spohn et al., 2022). Subsurface structure was assumed to be H_2O ice bedrock with porosity $\Phi = 0$. The Q_0 value was assumed to be of organic materials on Titan would be comparable to the kerogen on Earth (Q_0 =20; Carcione, 2000) and depends on frequency (Nakamura & Koyama, 1982).

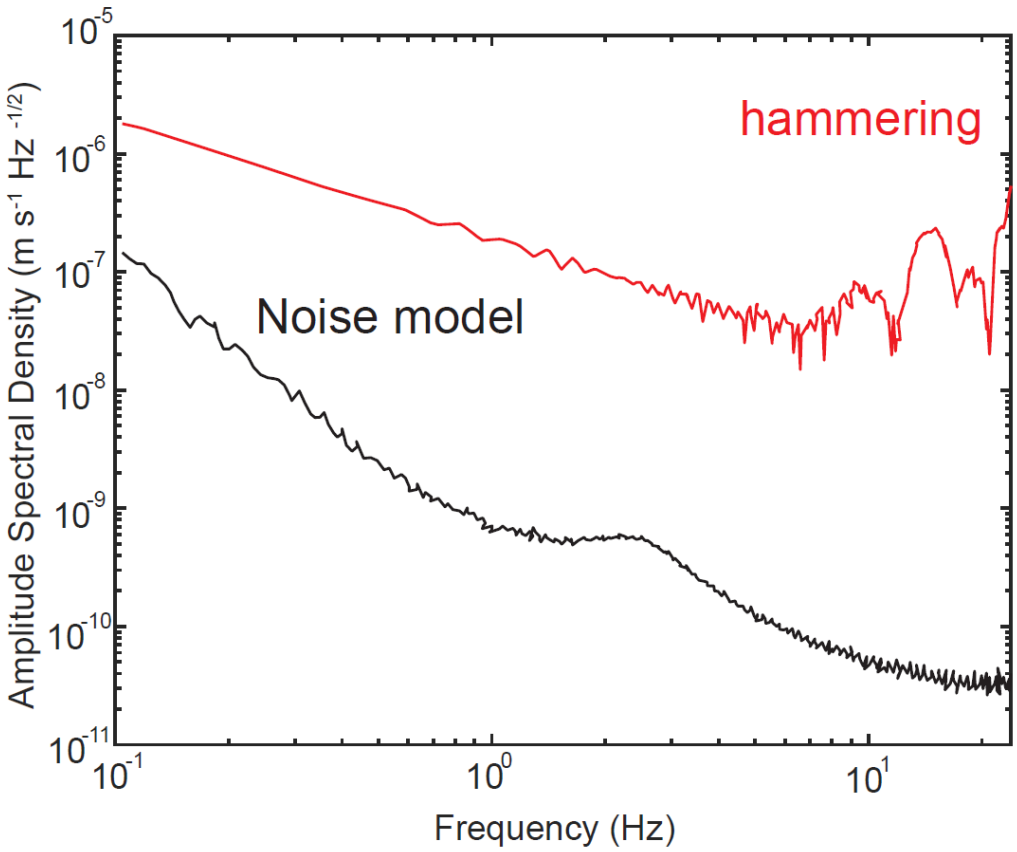

Figure 5.4 Comparison of the ASD of hammering by Insight-HP^3 (red) and Noise model of the seismometer of DraGMet SEIS (black).

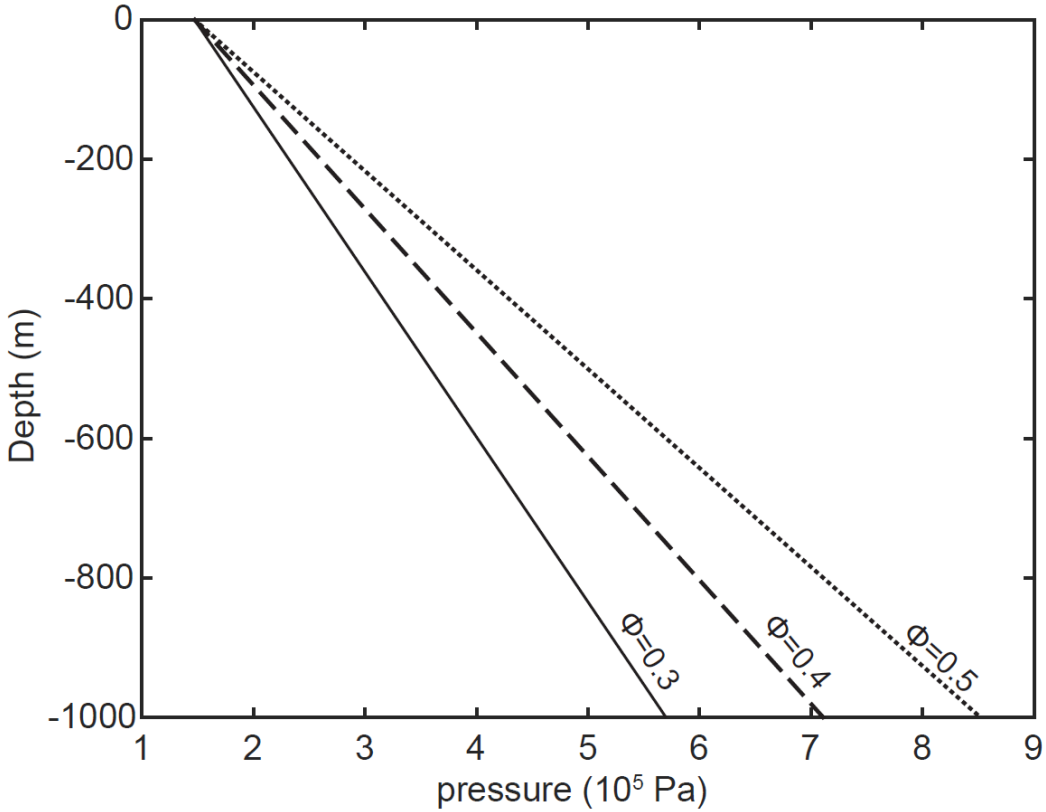

Figure 5.5 The vertical profile of effective pressure in Titan's organic regolith calculated with Eq. (5.10). Solid line, dashed line and dot line correspond to the porosity $\Phi = 0.3$, $\Phi = 0.4$, and $\Phi = 0.5$, respectively.

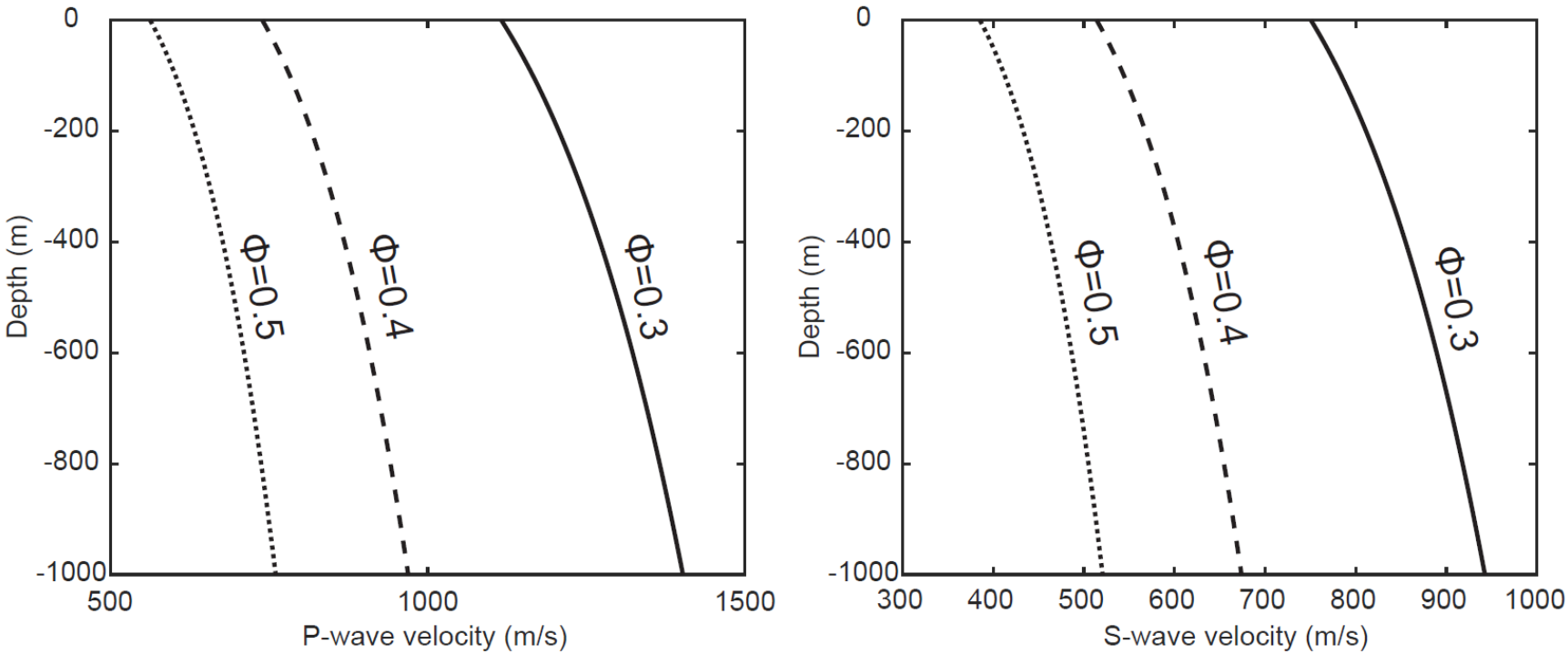

Figure 5.6 Vertical profiles of P-wave velocity and S-wave velocity in Titan's organic regolith at 93 K calculated based on the rock physics modeling described in the main text. Solid line, dashed line and dotted line correspond to the porosity $\Phi = 0.3$, $\Phi = 0.4$, and $\Phi = 0.5$, respectively. The critical porosity Φ_c is assumed to be 0.4.

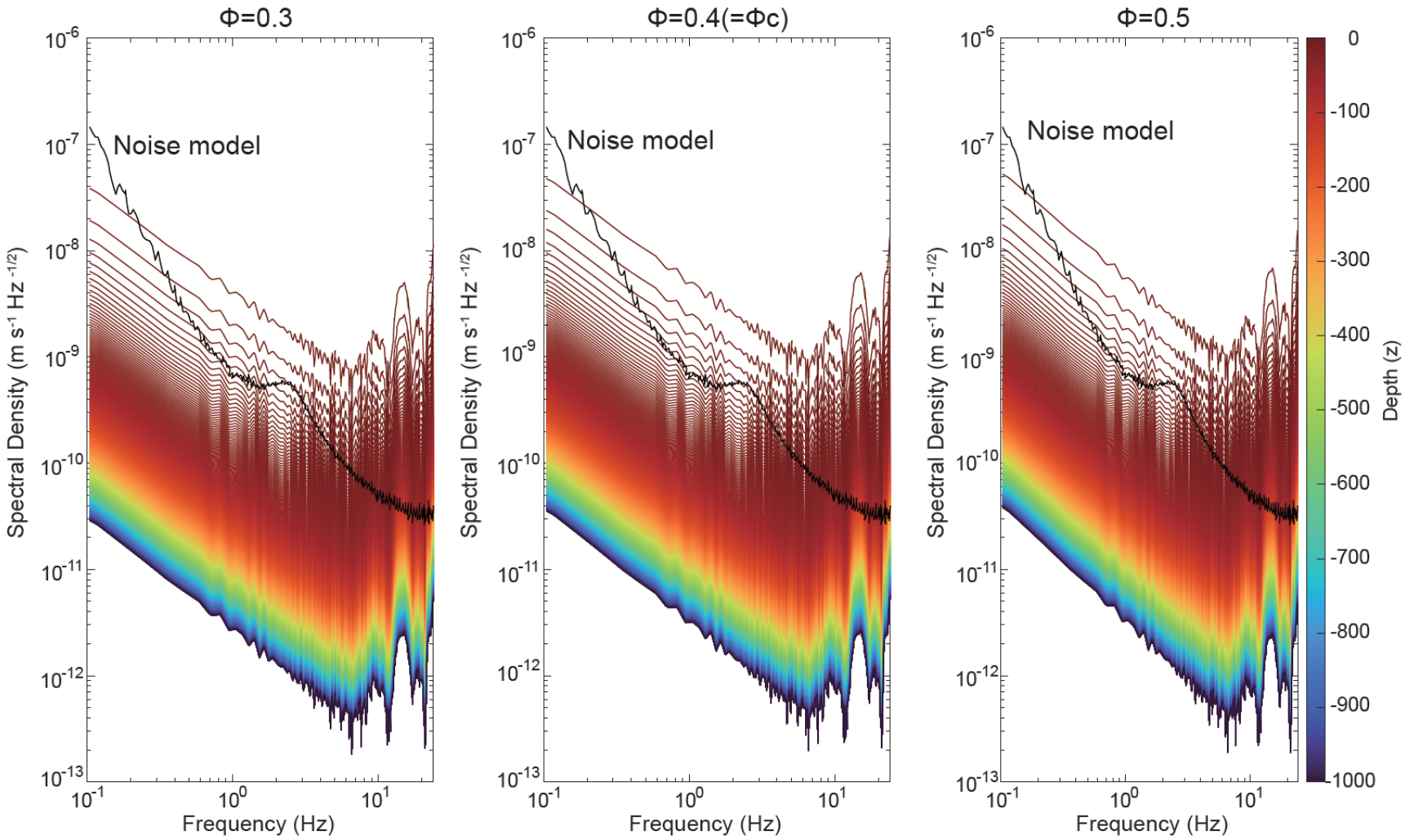

Figure 5.7 Comparison of ASD of reflected echo from the subsurface boundary at each depth vs. seismic noise model at $\Phi = 0.3$, $\Phi = 0.4$, and $\Phi = 0.5$, respectively. Each solid line indicates the ASD of the seismic echo. Each color suggests the reflected depth in the subsurface. Black line indicates the ASD of noise model.

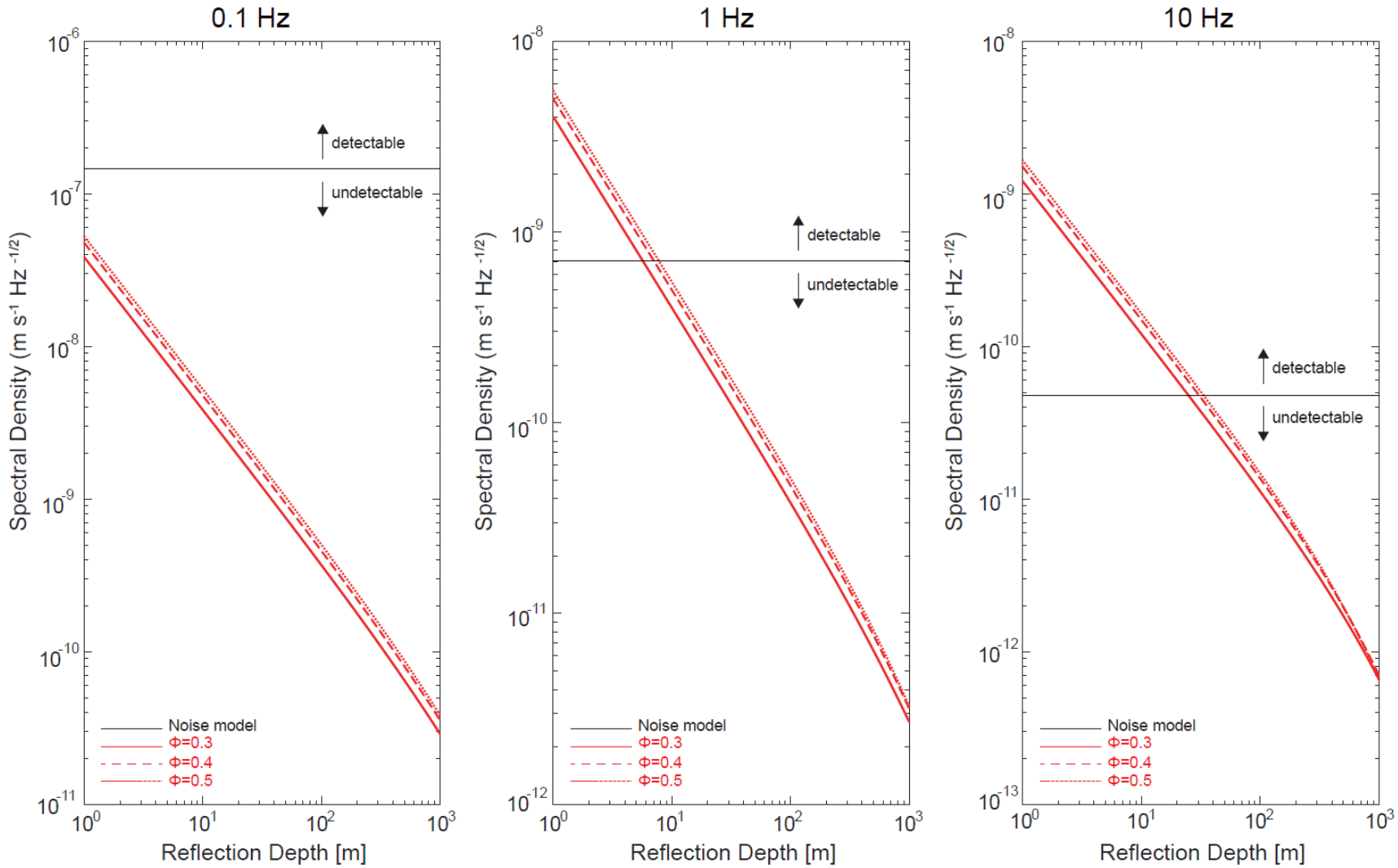

Figure 5.8 Comparison of amplitude spectral density of the echo vs. the noise model at 0.1 Hz, 1 Hz, and 10 Hz for each porosity condition. The critical porosity of the regolith is assumed to be $\Phi_c = 0.4$. Each black curve indicates the amplitude of the noise model at each frequency. Based on the comparison, the detection limit of depth of this condition is around 30 m shown in 10 Hz.

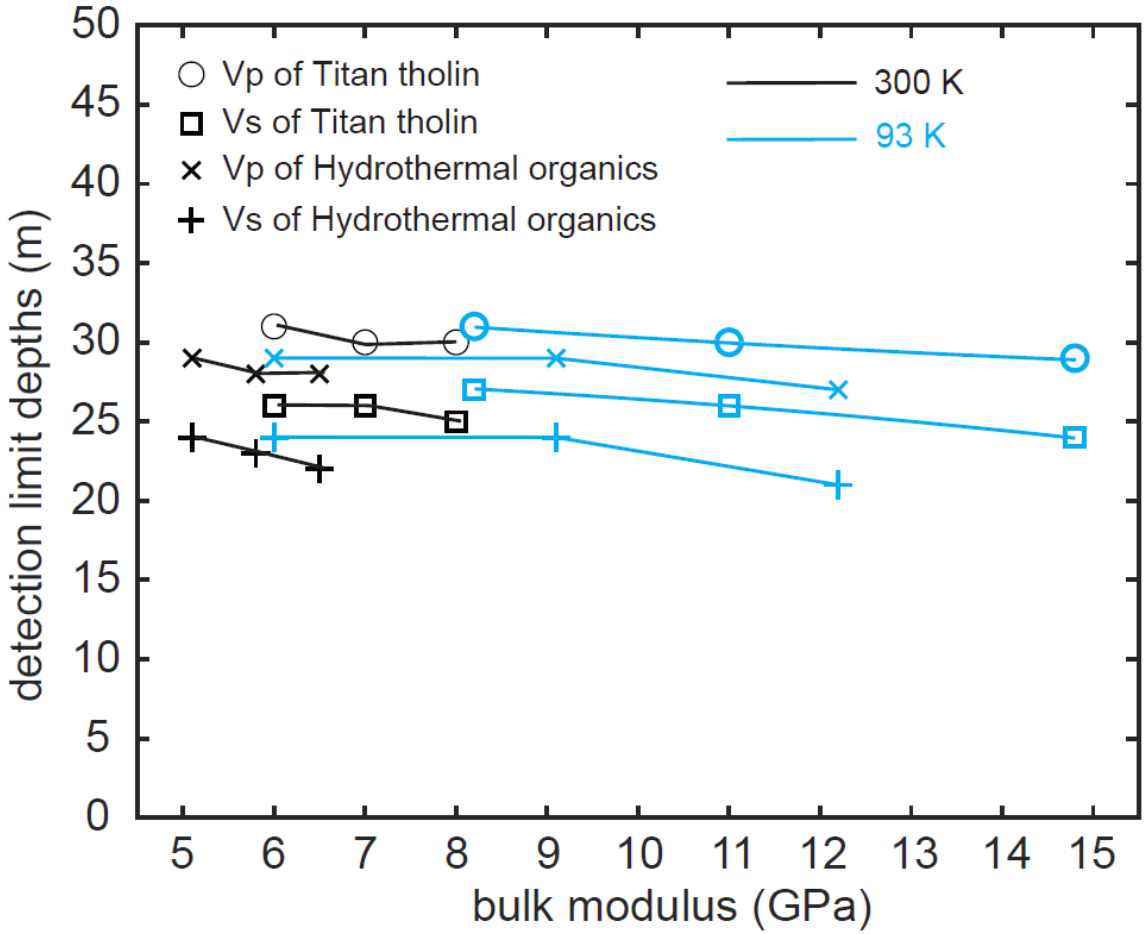

Figure 5.9 The results of the sensitivity study of detection limit of depths to bulk modulus and shear modulus of each organic material constrained in Chapter 4. Each symbol corresponds to each type of wave (i.e. P-wave or S-wave) and sample (Titan tholin or hydrothermal organics), respectively. The black color shows the results considering elasticity at 300 K, whereas the blue color indicates the results considering elasticity at 93 K, respectively. Each line indicates the same type of wave, the same sample, and the same temperature conditions. The detection limits of depths of P-wave could be approximately 30 m, which are independent of temperature and structure dependence of bulk modulus and shear modulus of organic materials. On the other hand, the detection limits of depths of S-wave could be approximately 20–25 m for Titan tholin and hydrothermal organics at all temperature conditions.

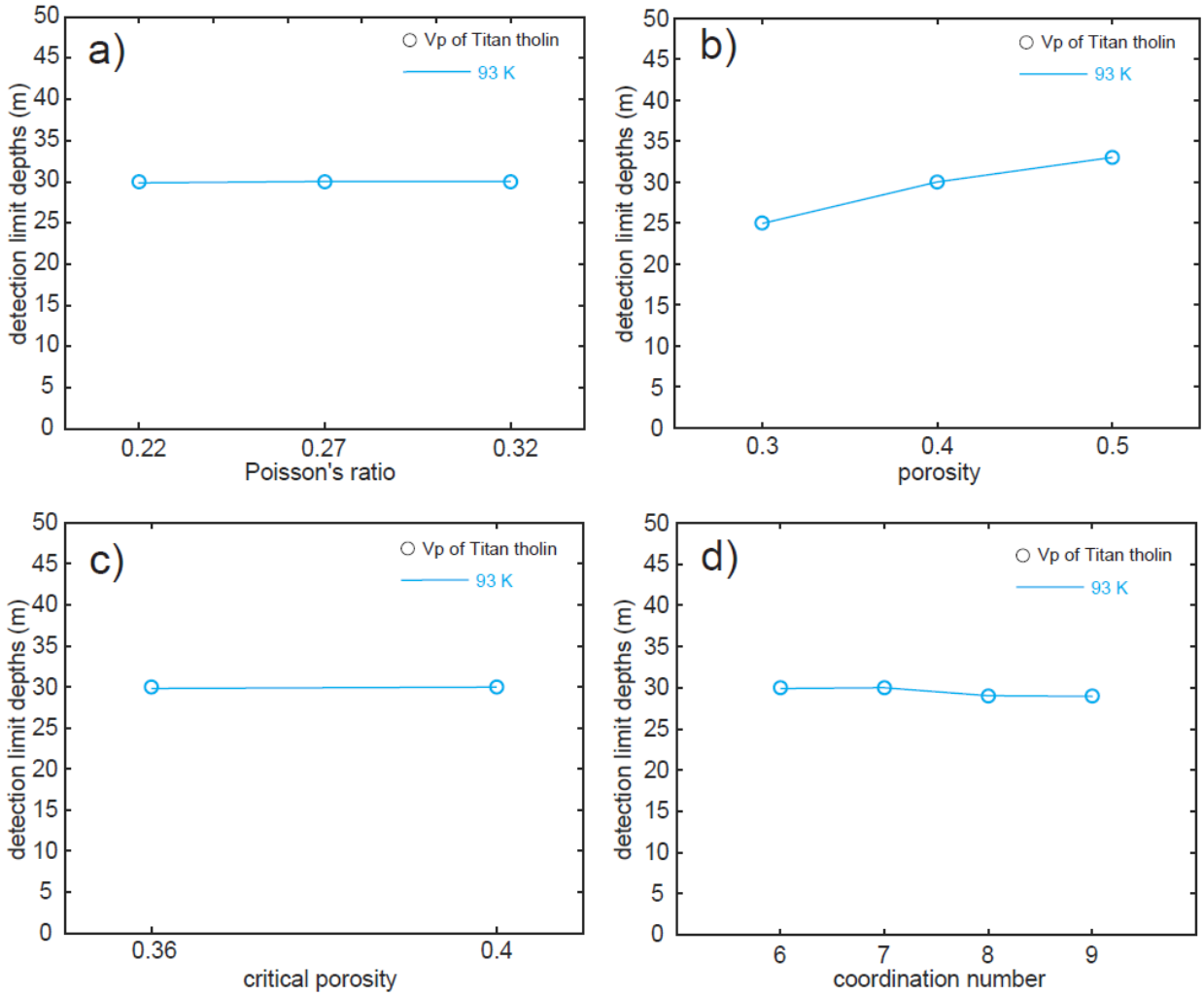

Figure 5.10 The results of the sensitivity study of detection limits of depths to (a) Poisson's ratio, (b) the porosity Φ, (c) the critical porosity Φ_c, and (d) the coordination number n. In all calculations, P-wave velocity based on the bulk modulus and the shear modulus of Titan tholin at 93 K was considered. All results except (b) indicate that the detection limits of depths of P-wave of Titan tholin at 93 K could be approximately 30 m, which are independent on other parameters except porosity Φ. The results of (b) suggest that the detection limits of depths of P-wave of Titan tholin at 93 K could be approximately 25–33 m.

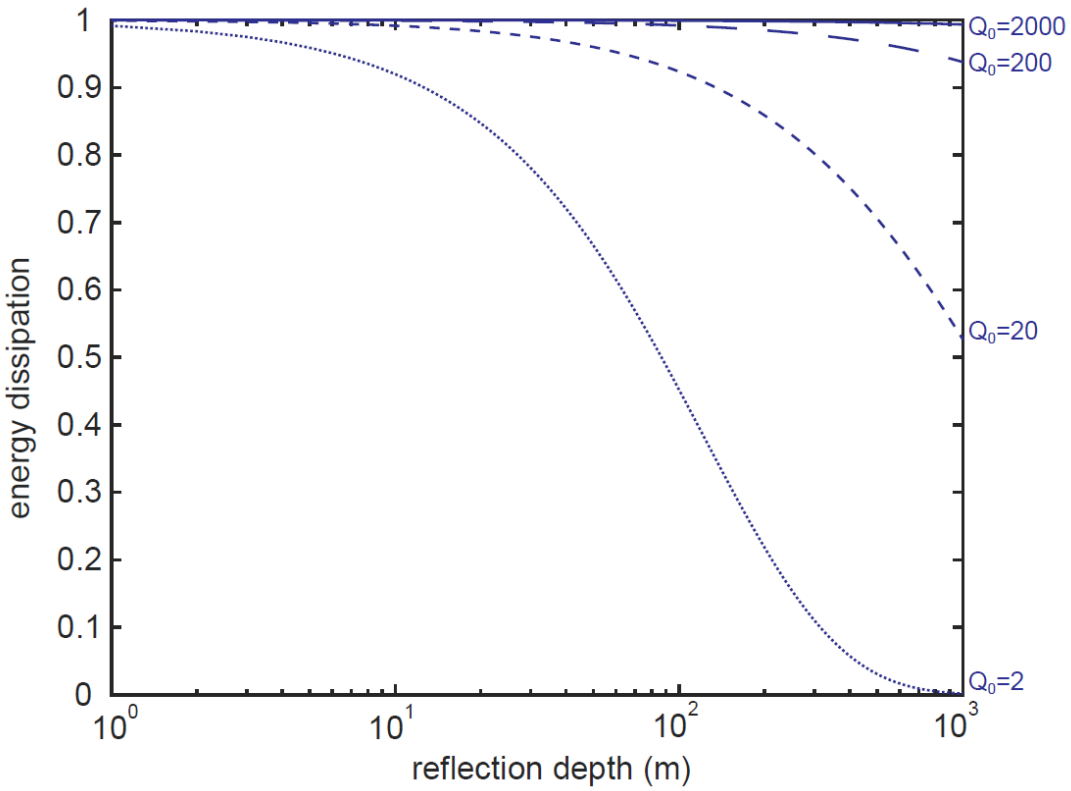

Figure 5.11 Dependence of energy dissipation on reflection depth for different Q_0 values (Q_0 = 2, 20, 200, and 2000). The energy dissipation term is calculated using Eq. (5.2) for a frequency of f = 10 Hz, considering the elastic properties of Titan tholin (K = 11 GPa, G = 6 GPa and ν = 0.27) at 93 K, and typical regolith conditions (Φ_c = 0.4, Φ = 0.4 and a coordination number n = 6). Results show that for lower Q_0 values (e.g., Q_0 = 2), energy dissipation increases significantly with depth, resulting in reduced reflected wave amplitudes at greater depths. In contrast, for Q_0 values above 20, energy dissipation remains low, allowing reflected wave amplitudes to be preserved at greater depths.

Table 5.2 Ranges of parameter values considered in the calculations.

Parameter	sample	Range	Unit	Reference
bulk modulus K	Titan tholin	6–8 (300 K), 7.2–14.8 (93 K)	GPa	The present study
	hydrothermal organics	5.1–6.5 (300 K), 6–12.2 (93 K)	GPa	The present study
shear modulus G	Titan tholin	3.5–4.1 (300 K), 4–8 (93 K)	GPa	The present study
	hydrothermal organics	3.9–4.9 (300 K), 4.5–9.3 (93 K)	GPa	The present study
Poisson's ratio v	Titan tholin	0.22–0.32	-	The present study
	hydrothermal organics	0.19–0.21	-	The present study
porosity of regolith Φ		0.3–0.5	-	Dickinson & Ward, 1994 Atkins & McBride, 1992
critical porosity Φ_C		0.36–0.4	-	Nur et al., 1998
coordination number n		6–9	-	Dvorkin et al., 1999 Andra et al., 2013

Chapter 6. General Conclusions

6.1. Synthesis of findings of the present study and their implications for the transport and accumulation of organic sands on Titan

This thesis aimed to constrain the temperature and chemical structure dependence of cohesiveness, which depends on the surface energy and elasticity, of organic material analogs on Titan. The present study initially produced organic analog materials and characterized their chemical structures and morphologies by multiple chemical analyses and microscopic observations (Chapter 2). Then, the present study investigated the cohesion force at different temperatures using an atomic force microscope (AFM) to obtain apparent surface energy (Chapter 3) and elastic wave velocities of the organic materials by synchrotron radiation X-ray experiments and ultrasonic wave experiments to obtain the information about elasticity (Chapter 4). Using the obtained cohesion force and apparent surface energy, the present study discussed the saltation threshold velocity, u_*, of organic particles on Titan (Chapter 5). Then, we compared the mass flux of sand transportation based on the saltation threshold velocity, u_*, and the mass flux of production of organic aerosols in the atmosphere to explain why thick organic sediments are absent in middle latitude regions. Using the obtained elastic wave velocities and elasticity, we also discussed the detection limit of depths of organic sediments in shallow subsurface with active seismic measurements assuming the seismometer of the Dragonfly Geophysics and Meteorology Package (DraGMet) (Chapter 5). This chapter describes the synthesis of findings in Chapters 2−5 of this thesis and future perspectives of this thesis, including the role of the stickiness of organic matters in the fragmentation velocity of collisional dust grains in the protoplanetary disks and reducing atmospheres of early Earth and exoplanets based on the results of this thesis in Sec. 6.2.

As discussed in Chapter 1, thick organic sediments exist as dunes only at low latitude regions of Titan, but not in the middle latitude regions (e.g., Lorenz et al., 2006; Radebaugh et al., 2008, Rodriguez et al., 2014), although both low and middle latitude regions are generally arid. Given that no thick organic sediments exist on middle latitude regions where potentially H_2O ice crust exposed (Solomonidou et al., 2018), organic aerosols at middle latitudes may have been transported spontaneously. Previous studies, however, have considered that saltation of organic aerosols would occur only by strong winds due to CH_4 storms at low latitudes (Tokano, 2010; Charnay et al., 2015) but would not occur by seasonal wind at low and middle latitudes (Tokano, 2008) based on the high cohesiveness of Titan tholin measured at room temperature (Yu et al., 2017; Comola et al., 2022). However, the cohesive force should have temperature dependence. Given the Titan's surface temperature is ~93 K (Jenning et al., 2019), the cohesiveness of organics would be different from at room temperature. In addition, cohesion force should depend on their chemical structures. In fact, wet-and-dry cycles of liquid CH_4 on Titan may have altered deposited organic aerosols through dissolution of a soluble part of

aerosols and precipitation as evaporites (Hirai et al., 2023). Hypervelocity impacts on Titan could have induced melting of icy crust at the impact site, which can also induce hydrothermal reactions near the surface. If the icy crust contains simple non-H_2O molecules, such as NH_3 and HCHO, complex organic materials would be formed through the impact-induced hydrothermal reactions. However, the temperature dependence and chemical structure dependence of cohesion force, surface energy, and elasticity of Titan's organic analog materials have been poorly understood.

In Chapter 2, the present study performed laboratory experiments to generate three types of organic materials; the present study produced laboratory analogs of Titan's organic materials; 1) films and particles of Titan tholin, 2) films of altered tholin, and 3) films and solids of hydrothermal organics. The morphologies of these organic materials were observed by FE-ESM observations and AFM analysis. The chemical structure of these organic materials was characterized by FT-IR spectroscopy, elemental analysis, UV/Vis analysis, and HP-LC analysis. The conclusions of our characterizations of morphology and chemical structures of organic analog materials are summarized as follows:

(1) The tip of the cantilever and Si wafer substrates used in the AFM measurements are covered with films of organic materials with smooth surface in the scale of several nanometers. The contact radius between the tip and substrate coated with the organic materials in the AFM measurements are also obtained with the results of the microscopic observations.

(2) Films and particles of Titan tholin and film of hydrothermal organics would be N-bearing polycyclic aromatic compounds (N-PACs) connected with polymer-like chain structures. Films of Titan tholin would contain more aromatic rings than particles of Titan tholin particles and film of the other. Particles of Titan tholin would contain more polymer-like chain structures with conjugated C=C / C=N and nitrile -C≡N structures than the others. Films of hydrothermal organics contain N-bearing aromatics with less C≡N at the termination of polymer-like chain structures than the others. Altered tholin contains N-bearing heterocyclic aromatic structures with little aliphatic compounds. Solids of hydrothermal organics show the polyolefin with an abundance of C=O bonds in the structure. Proposed chemical structures of organic materials are summarized in Figure 2.14.

In Chapter 3, the present study performed 1) cohesion force measurements between Si tip and Si wafer substrate covered with Titan tholin over temperature ranges from 300 K to 117 K, and 2) cohesion force measurements between Si tip and Si wafer substrate covered with altered tholin or hydrothermal organics at 300 K by using atomic force microscope (AFM). The conclusions of our measurements are summarized as follows:

(3) The cohesion force of Titan tholin decreases as the temperature decreases. The apparent surface energy of Titan tholin also decreases as the temperature decreases following the

Arrhenius equation with the γ_0 = 180 ± 20 mJ m^{-2} and the activation energy E_{surf} = 1760 ± 190 J mol^{-1}. Given the surface energy of materials would increase with temperature drop, decreasing of contact radius due to increasing of the elasticity and/or the energy dissipation caused by a molecular stick-slip mechanism during separation would be the plausible mechanism to account for the observed temperature dependence of cohesion force.

(4) The surface energy of altered tholin is 159 ± 39 mJ m^{-2} or 226 ± 77 mJ m^{-2}. The surface energy of hydrothermal organics is determined to be 57 ± 8 mJ m^{-2}. These values are higher than values obtained by contact angle measurements but are comparable to graphene measured by surface force balance (SFB) and lower than that of paraffin estimated from tensile strength measurement. The difference arises from energy dissipation during separation, such as molecular stick-slip and mechanical adhesion effects, which are not considered in static contact angle measurements. Surface energy is influenced by multiple factors, including elemental ratios such as C/H and C/N, the abundance of unsaturated bonds, and molecular size.

In Chapter 4, the present study performed synchrotron radiation X-ray experiments (inelastic X-ray scattering (IXS) measurements) to estimate 1) acoustic wave velocities of Titan tholin and hydrothermal organics at 300 K and 2) acoustic wave velocities of Titan tholin at 300 K, 240 K, 190 K, 140 K, 93 K by investigating phonon dispersion from IXS spectra. The present study also performed ultrasonic measurements to investigate 3) V_p and V_s of Titan tholin and hydrothermal organics at 300 K. The conclusions of our measurements are summarized as follows:

(5) V_p and V_s of Titan tholin and hydrothermal organics at 300 K are 3260 ± 390 m/s and 1830 ± 60 m/s for Titan tholin and 2830 ± 60 m/s and 1740 ± 40 m/s for hydrothermal organics, respectively, based on ultrasonic measurements. These results are consistent with value and error of acoustic wave velocities of Titan tholin and hydrothermal organics are 2860 ± 340 m/s and 2580 ± 350 m/s, respectively, based on IXS measurements. Given the densities of Titan tholin and hydrothermal organics (1130 ± 60 kg m^{-3} and 1450 ± 170 kg m^{-3}, respectively), the elastic parameters at 300 K (the bulk modulus K, Young's modulus Y, and Poisson's ratio ν) are calculated to be K = 7 ± 0.9 GPa, G = 3.8 ± 0.3 GPa, Y = 9.7 ± 1.8 GPa, and ν = 0.27 ± 0.03 for Titan tholin, and K = 5.8 ± 0.7 GPa, G = 4.4 ± 0.5 GPa, Y = 10.4 ± 1.3 GPa, and ν = 0.20 ± 0.01 for hydrothermal organics, respectively.

(6) The mean value of acoustic wave velocities of Titan tholin (V_p) becomes larger with decreasing the temperature based on the temperature dependence of phonon dispersion. The overall lattice structure of Titan tholin does not change significantly between 300 K and 93 K based on the $S(Q, 0)$ measurements and phonon dispersion curve. With assuming a constant density of Titan tholin between the temperature range, temperature dependence of the longitudinal modulus of Titan tholin is estimated. We fitted the data using both the Arrhenius

equation and a linear relationship, yielding M_0 = 7.3 ± 1.2 GPa and E_a = -500 ± 230 J mol^{-1} for Arrhenius equation and in M_0 = 15 ± 2 GPa and T_m = 340 ± 110 K for linear relationship. However, large errors indicate significant uncertainty in the temperature-dependent mechanism, requiring further analysis and alternative measurements.

(7) Based on the comparison of bulk modulus and density of both Titan tholin and hydrothermal organics with various materials, kerogen is considered to be the closest material, in the elastic properties, to Titan tholin and hydrothermal organics. Our comparison of the Young's modulus of Titan tholin and hydrothermal organics with various organic materials as a function of their C/H ratio suggests that the elemental ratio is not the sole factor determining Young's modulus. Instead, factors such as elemental composition, functional groups, and the molecular configuration of aromatic and aliphatic structures play a crucial role in determining the elastic properties of organic materials.

(8) The comparison of phonon dispersion obtained using the IXS and ultrasonic methods for Titan tholin shows that the ultrasonic measurements align with the IXS phonon dispersion curve near the zero point, within the errors. This suggests that the long-wavelength approximation remains valid at the phonon scale of a few unit cells, indicating that the results of the ultrasonic method can be extrapolated to the 0.1–10 Hz frequency range of the seismometer onboard NASA's *Dragonfly* mission. At Titan's surface temperature (~93 K), the elastic properties are estimated to be K = 11 ± 3.8 GPa and G = 6 ± 2.0 GPa for Titan tholin-like structure, and K = 9.1 ± 3.1 GPa and G = 6.9 ± 2.4 GPa for hydrothermal organic-like structure.

In Chapter 5, the present study estimated 1) the saltation threshold wind speed u^* based on the temperature dependence of the surface energy of Titan tholin (Chapter 3) and compared mass flux of sand transports from middle latitude regions toward lower latitude regions. The present study also performed sensitivity study of the detection limit of depths of organic sediments in shallow subsurface to the elasticity of organic materials (Chapter 4) with a rock physics model (Dvorkin, 1999). The conclusions of our estimations are summarized as follows

(9) The saltation threshold wind speed u^* would decrease by a factor ~3 than values previously expected. At this conditions, saltation would occur by seasonal wind of speed > 0.05 m s^{-1}, such as tidal wind at middle latitude regions in the summer, if the particle size is comparable to 700 μm. Wind speed of 0.05 m s^{-1} would result in mass flux of sand transportation of ~2×10^{13} g per Titan year from latitude 45° toward the equator by tidal winds in summer, which is larger than the estimated deposition rate of organic aerosols in middle latitude regions (30–60°) (approximately 1×10^8 g per one Titan year). Given that the size of organic aerosols in the troposphere are approximately 1 μm aggregates, growth of size would be a limiting factor of aeolian transport of organic materials. The effective removal of organic aerosols from middle latitude regions toward low latitude regions by tidal wind in the summer would explain the

absence of thick organic sediments in the middle latitude regions where potentially H_2O ice crust is exposed (Solomonidou et al., 2018).

(10) The detection limits of depths of P-wave would be 25–33 m, whereas that of S-wave would be 21–27 m assuming the temperature and structure dependence of the elasticity of organic analog materials (Chapter 4). Our sensitivity study suggests that the elasticity of organic materials such as bulk modulus, shear modulus, and Poisson's ratio v, and other parameters such as coordination number n, the critical porosity Φ_c, and the porosity of regolith Φ does not change the detection limits of depths significantly. On the other hand, the attenuation factor Q_0 and the amplitude of initial input A_0 could affect the detectability of the reflected echoes. The elastic wave velocities of organic materials determined in this study are critical for estimating the thickness of organic sediments based on the travel time of reflected seismic echoes measured in the future mission.

NASA's *Dragonfly* will onboard several instruments beside DraGMet such as tandem mass spectrometer LD-MSMS, infrared camera (DragCAM), and Gamma and Neutron Spectrometer (DraGNS) to constrain the composition and chemical structure of surface organic materials (Lorenz et al., 2018; Barnes et al., 2021). If the chemical structure of organic materials on the surface of Titan is similar to our organic analogs, the intrinsic elastic wave velocity could be comparable to our organic analogs. Furthermore, the porosity of the surface organic regolith can be constrained based on morphology observation. If Titan's organic porous regolith (such as porosity Φ = 0.3–0.5) is thinner than 10–30 m, we could constrain the CH_4 cycle on Titan by determining the thickness of the organic sediments during *Dragonfly* mission.

6.2. Implication to collisional growth of dust particles: fragmentation velocity of dust aggregates

The cohesive properties of organic materials are important for discussing not only Titan's sand transportation and accumulation but also the collisional growth of dust particles in the protoplanetary disks and reducing atmospheres of early Earth, Pluto, Triton and exoplanets. We discuss the implication to the role of the stickiness of organic matters in terms of the fragmentation velocity of collisional dust grains based on the results of this thesis.

Mechanisms responsible for size growth from dusts to planetesimals in a protoplanetary disk is a long-standing question in planetary formation. One of the possible mechanisms is collisional growth of small dust particles (<μm size) to larger aggregates (e.g., Okuzumi et al., 2012; Kataoka et al., 2013). Previous works have suggested that effective growth of dust via collision could occur if cohesive organic matter covers the surface of dust particles (Kudo et al.,

2002; Bekaert et al., 2018; Homma et al., 2019). The origin of the organic matters is considered to be derived from the diffused and molecular clouds incorporated in H_2O ice mantle on silicate core and subsequent UV irradiation (Greenberg, 1989). Then, organic mantle grains (OMG) formed along with the H_2O sublimation (Poch et al., 2016), by precipitating into the inner warm region of disks. The cohesiveness of these organic matter is expected to vary along with the temperature profile of the disks owing to the temperature dependence of elasticity (Kudo et al., 2002; Homma et al., 2019). However, in protoplanetary disks, a variety of organic materials can be produced under different formation conditions, such as photochemical reactions on the disk surface (e.g., Kuga et al., 2015) and hydrothermal reactions in the planetesimals (e.g., Yabuta et al., 2023). Furthermore, surface energy could also show temperature dependence, as shown in Chapter 3.

Homma et al. (2019) have considered collisional growth of OMGs with finite thickness of organic mantle and proposed that the results of the collisional growth could depend on the thickness of the organic mantle and their temperature dependence of elasticity (Kudo et al., 2002). This is because contact between softer particles makes a larger contact area, resulting in higher stickiness between particles. The fragmentation velocity of dust aggregates v_{frag} can be described as below (e.g., Wada et al., 2013):

$$v_{\mathrm{frag}} = 20\sqrt{\frac{E_{\mathrm{break}}}{m_{mon}}}, \tag{6.1}$$

where E_{break} is the breakup energy to break the bond between two grains (so-called monomer), and m_{mon} is mass of each monomer. Mass of the monomer can be described as below (Homma et al., 2019):

$$m_{mon} = \frac{4\pi}{3}\{\rho_{\mathrm{sil}}(R - \Delta R_{\mathrm{or}})^3 + \rho_{\mathrm{or}}(R^3 - (R_{mon} - \Delta R_{\mathrm{or}})^3)\}, \tag{6.2}$$

where ρ_{sil} is the density of silicate, ρ_{or} is the density of organic mantle, R_{mon} is the radius of each monomer, ΔR_{or} is the ratio of thickness of organic mantle over R_{mon}. As mentioned above, softer materials tend to form larger contact area, requiring larger displacement of organic mantle. If the thickness of organic mantle is too thin or too soft, the contribution of hard silicate core should be considered. Therefore, the breakup energy of organic mantle dust can be divided into two cases: 1) thick organic mantle and 2) thin or elastic organic mantle. In the former case, the breakup energy of OMGs can be described as below:

$$E_{\mathrm{or}} = 23\frac{{\gamma_{\mathrm{or}}}^{5/3}{R_{mon}}^{4/3}(1 - {\nu_{\mathrm{or}}}^2)^{2/3}}{{Y_{\mathrm{or}}}^{2/3}}, \tag{6.3}$$

where γ_{or} is surface energy of organics, ν_{or} is Poisson's ratio of organics, and Y_{or} is Young's modulus of organics. On the other hand, in the latter case, the breakup energy of OMGs can be written as belows:

$$|\Delta U_{\mathrm{or}}| = 2\pi\gamma_{\mathrm{or}}(2R_{mon} - \Delta R_{\mathrm{or}})\Delta R_{\mathrm{or}}, \tag{6.4}$$

$$E_{\mathrm{sil}} = 23\frac{{\gamma_{\mathrm{sil}}}^{5/3}(R_{mon} - \Delta R_{\mathrm{or}})^{4/3}(1 - {\nu_{\mathrm{sil}}}^{2})^{2/3}}{{Y_{\mathrm{sil}}}^{2/3}}, \tag{6.5}$$

where ΔU_{or} is the binding energy of organic mantle, E_{sil} is breakup energy of silicates, γ_{sil} is surface energy of silicates, ν_{sil} is Poisson's ratio of silicate, and Y_{sil} is Young's modulus of silicates.

Figure 6.1 shows the comparison of the maximum collisional velocity in a typical turbulent disks (gray region in Figure 6.1) and fragmentation velocities of OMGs for the case of organic mantle with 1) the surface energy of silicate (2.5×10^{-2} N m^{-1}) and the elasticity of an interstellar organic analog measured in Kudo et al. (2002) (Homma et al., 2019; Red curves in Figure 6.1) and 2) with the values constrained in the present study (Blue curves in Figure 6.1) with various $\Delta R_{\mathrm{or}}/R_{mon}$. The result of previous study indicates that if the thickness of organic mantle is comparable to or thicker than the thickness of typical interplanetary dust particles (IDPs) (which corresponds to $\Delta R_{\mathrm{or}}/R_{mon}$ = 0.03), collisional growth of dusts aggregate would be proceed aided by soft organic materials inner regions of a protoplanetary disk (Homma et al., 2019; Figure 6.1). On the other hand, the fragmentation velocity of OMGs with considering the temperature dependence of the surface energy and elasticity (Young's modulus), and constant Poisson's ratio (ν = 0.27) constrained in the present study would be lower than or comparable to the results shown in the present study over all temperature range.

The difference between Homma et al. (2019) and the present study is due to the difference of the temperature dependence of the elasticity of organic materials (Kudo et al., 2002). The elasticity of interstellar organic matter analogs measured by Kudo et al. (2002) increases dramatically with the temperature decreases over the temperature range from 300 K to 200 K. This could be because more than 10 wt.% of their initial organic matter shows the melting point under room temperature (300 K), such as ethylene glycol (1.2 wt.%), glycerol (1.4 wt.%), indene (4.7 wt.%), 1,2-Dimethylnaphthalene (1.6 wt.%), and 1,4-Diisopropenylbenzene (2.0 wt.%). Phase transitions of these organic materials could result in significant increasing of the elasticity. On the other hand, the phase of our laboratory analogs would not change based on the molecular structure measurement in Chapter 4. The fragmentation velocity of OMGs based on our results decreases below 200 K significantly because the elasticity and the surface energy of our laboratory analogs follows Arrhenius equation (Chapter 3 and Chapter 4).

Given organic matters could be formed via photochemical reaction near the surface of disks (e.g., Kuga et al., 2015), the chemical structure of organic matter would be similar to our laboratory analogs. Furthermore, the chemical analyses of insoluble organic matter (IOM) in Ryugu sample suggest that the chemical structure of IOM is enriched in polyaromatic hydrocarbons (Yabuta et al., 2023). If OMGs are covered with such organic materials, the temperature dependence of the fragmentation velocity would be similar to results with our physical parameters. This suggests that the collisional growth of OMGs would not proceed efficiently even inner warm region compared to previously expected, if the organic mantle is derived from the photochemistry in the disk surface or hydrothermal reactions in the parent body of asteroids.

On the other hand, in reducing planetary atmospheres, organic aerosols are formed or expected to be formed via photochemical reactions in early Earth, Pluto, Triton and exoplanet (e.g., Khare et al., 1984; Sagan & Chyba, 1997; Wolf & Toon, 2010; Trainer et al., 2006; Gladstone et al., 2016; Cheng et al., 2017; Grundy et al., 2018; Ohno et al., 2021). These aerosols determine atmospheric temperature structure by absorbing sunlight and heat ambient atmosphere (e.g., Barnes et al., 2018; McKay et al., 1989, 1993; Rannou et al., 2003, 2004).

Recent observations of exoplanets suggest that the haziness of the exoplanet atmosphere depends on the equilibrium temperature (e.g., Knutson et al., 2014; Kreidberg et al., 2014). Haziness of the atmosphere is determined by the balance between the production and removal of haze particles (Yu et al., 2021). Previous study compares surface energy of organic haze analogs formed at different temperatures and initial gas mixtures. Their results indicate that the surface energy and contact radius with water of organic haze analogs depends on the formation temperature, suggesting that the temperature dependence of contact radius to water controls the removal of haze particles as a cloud condensation nuclei (CCN) and haziness of the atmosphere (Yu et al., 2021). They also propose dry deposition of haze particles as another possible mechanism to remove the haze particles from the atmosphere. Haze particles with higher surface energy will collide and growth to larger particles more efficiently, resulting in the rapid removal of the haze particles. However, our results suggest the opposite trend: the surface energy of haze particles could be larger if the temperature of atmosphere is higher. This suggests that the surface energy of the haze particles does not control the removal rate of the particles as previously thought (Yu et al., 2021), requiring other factors to explain the haziness of the reducing atmosphere.

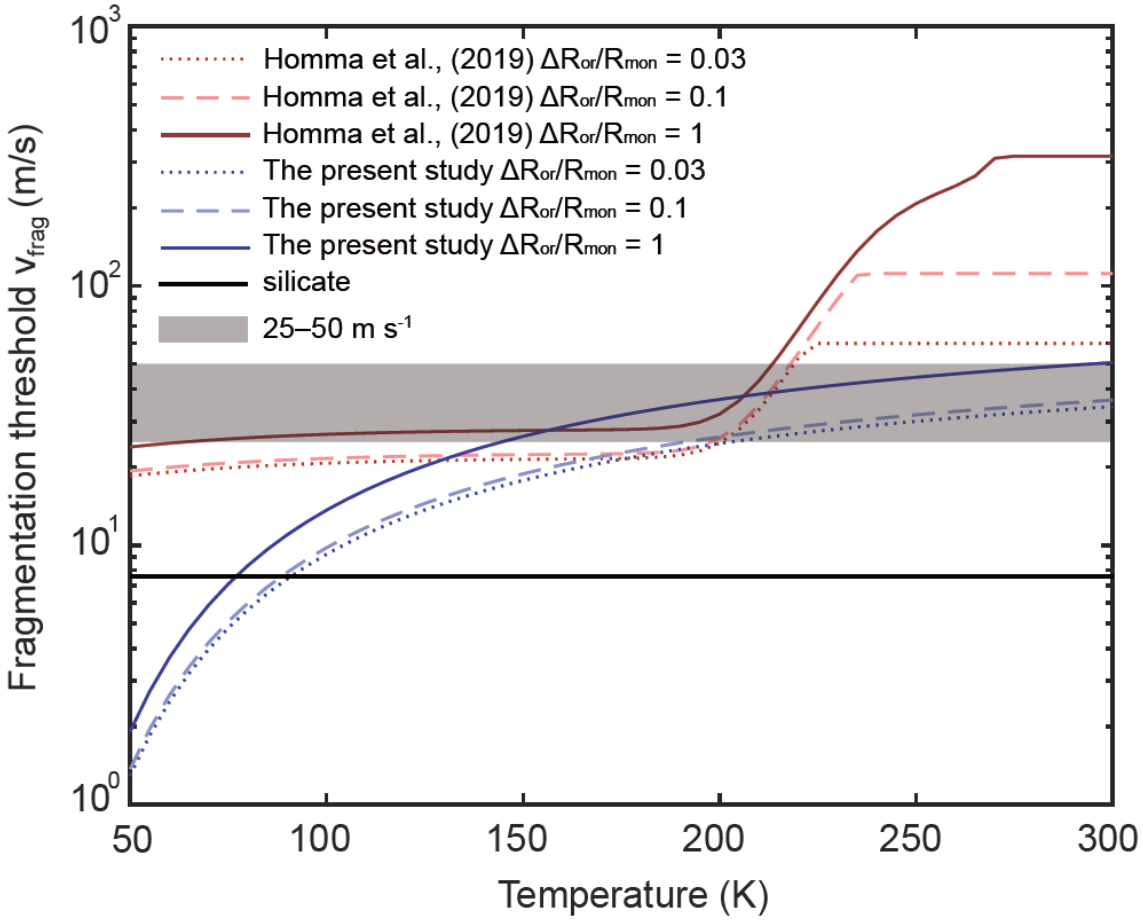

Figure 6.1 Temperature dependence of fragmentation threshold velocity $v_{\rm frag}$ for dust aggregates composed of 100 nm-sized OMGs. The pink, red, and dark red lines are for $\Delta R_{\rm or}/R_{mon}$ = 1, 0.1 and 0.03, respectively. The black line shows the fragmentation threshold for aggregates of 100 nm-sized silicate grains assuming constant physical parameters. The gray area indicates 25–50 m s^{-1}, which corresponds to the maximum velocity of collision in weakly turbulent disks.

References

Abplanalp, M.J., Frigge, R., Kaiser, R.I., 2019. Low-temperature synthesis of polycyclic aromatic hydrocarbons in Titan's surface ices and on airless bodies. *Sci. Adv. 5*, eaaw5841. https://doi.org/10.1126/sciadv.aaw5841

Abramowitz, M., Stegun, I.A., 1972. Handbook of Mathematical Functions with Formulas, Graphs, and Mathematical Tables. *National Bureau of Standards Applied Mathematics Series 55*. Tenth Printing.

Aharonson, O., Hayes, A.G., Hayne, P.O., Lopes, R.M., Lucas, A., Perron, J.T., 2014. Titan's surface geology, in: Müller-Wodarg, I., Griffith, C.A., Lellouch, E., Cravens, T.E. (Eds.), Titan. *Cambridge University Press*, pp. 63–101. https://doi.org/10.1017/CBO9780511667398.005

Aharonson, O., Hayes, A.G., Lunine, J.I., Lorenz, R.D., Allison, M.D., Elachi, C., 2009. An asymmetric distribution of lakes on Titan as a possible consequence of orbital forcing. *Nature Geosci 2*, 851–854. https://doi.org/10.1038/ngeo698

Alexander, S., Hellemans, L., Marti, O., Schneir, J., Elings, V., Hansma, P.K., Longmire, M., Gurley, J., 1989. An atomic-resolution atomic-force microscope implemented using an optical lever. *Journal of Applied Physics 65*, 164–167. https://doi.org/10.1063/1.342563

Anderson, O.L., 1966. Derivation of Wachtman's Equation for the Temperature Dependence of Elastic Moduli of Oxide Compounds. *Phys. Rev. 144*, 553–557. https://doi.org/10.1103/PhysRev.144.553

Andrä, H., Combaret, N., Dvorkin, J., Glatt, E., Han, J., Kabel, M., Keehm, Y., Krzikalla, F., Lee, M., Madonna, C., Marsh, M., Mukerji, T., Saenger, E.H., Sain, R., Saxena, N., Ricker, S., Wiegmann, A., Zhan, X., 2013. Digital rock physics benchmarks—Part I: Imaging and segmentation. *Computers & Geosciences 50*, 25–32. https://doi.org/10.1016/j.cageo.2012.09.005

Aqra, F., Ayyad, A., 2011. Surface energies of metals in both liquid and solid states. *Applied Surface Science 257*, 6372–6379. https://doi.org/10.1016/j.apsusc.2011.01.123

Artemieva, N., Lunine, J., 2003. Cratering on Titan: impact melt, ejecta, and the fate of surface organics. *Icarus 164*, 471–480. https://doi.org/10.1016/S0019-1035(03)00148-9

Artemieva, N., Lunine, J.I., 2005. Impact cratering on Titan II. Global melt, escaping ejecta, and aqueous alteration of surface organics. *Icarus 175*, 522–533. https://doi.org/10.1016/j.icarus.2004.12.005

Atkins, J.E., McBride, E.F., 1992. Porosity and packing of Holocene river, dune, and beach sands. *AAPG bulletin, 76*(3), pp.339-355. https://doi.org/10.1306/BDFF87F4-1718-11D7-8645000102C1865D

Awada, H., Noel, O., Hamieh, T., Kazzi, Y., Brogly, M., 2011. Contributions of chemical and mechanical surface properties and temperature effect on the adhesion at the nanoscale. *Thin Solid Films 519*, 3690–3694. https://doi.org/10.1016/j.tsf.2011.01.261

Awaja, F., Gilbert, M., Kelly, G., Fox, B., Pigram, P.J., 2009. Adhesion of polymers. *Progress in Polymer Science 34*, 948–968. https://doi.org/10.1016/j.progpolymsci.2009.04.007

Bagnold R A 1941 The Physics of Blown Sand and Desert Dunes (*New York: Methuen*)

Baldan, A., 2012. Adhesion phenomena in bonded joints. *International Journal of Adhesion and Adhesives 38*, 95–116. https://doi.org/10.1016/j.ijadhadh.2012.04.007

Barnes, J.W., Brown, R.H., Soderblom, L., Buratti, B.J., Sotin, C., Rodriguez, S., Le Mouèlic, S., Baines, K.H., Clark, R., Nicholson, P., 2007. Global-scale surface spectral variations on Titan seen from Cassini/VIMS. *Icarus 186*, 242–258. https://doi.org/10.1016/j.icarus.2006.08.021

Barnes, J.W., Bow, J., Schwartz, J., Brown, R.H., Soderblom, J.M., Hayes, A.G., Vixie, G., Le Mouélic, S., Rodriguez, S., Sotin, C., Jaumann, R., Stephan, K., Soderblom, L.A., Clark, R.N., Buratti, B.J., Baines, K.H., Nicholson, P.D., 2011. Organic sedimentary deposits in Titan's dry lakebeds: Probable evaporite. *Icarus 216*, 136–140. https://doi.org/10.1016/j.icarus.2011.08.022

Barnes, J.W., Brown, R.H., Soderblom, L., Sotin, C., Le Mouèlic, S., Rodriguez, S., Jaumann, R., Beyer, R.A., Buratti, B.J., Pitman, K., Baines, K.H., Clark, R., Nicholson, P., 2008. Spectroscopy, morphometry, and photoclinometry of Titan's dunefields from Cassini/VIMS. *Icarus 195*, 400–414. https://doi.org/10.1016/j.icarus.2007.12.006

Barnes, J.W., Lorenz, R.D., Radebaugh, J., Hayes, A.G., Arnold, K., Chandler, C., 2015. Production and global transport of Titan's sand particles. *planet. sci. 4*, 1. https://doi.org/10.1186/s13535-015-0004-y

Barnes, J.W., MacKenzie, S.M., Young, E.F., Trouille, L.E., Rodriguez, S., Cornet, T., Jackson, B.K., Ádámkovics, M., Sotin, C., Soderblom, J.M., 2018. Spherical Radiative Transfer in C++ (SRTC++): A Parallel Monte Carlo Radiative Transfer Model for Titan. *AJ 155*, 264. https://doi.org/10.3847/1538-3881/aac2db

Barnes, J.W., Turtle, E.P., Trainer, M.G., Lorenz, R.D., MacKenzie, S.M., Brinckerhoff, W.B., Cable, M.L., Ernst, C.M., Freissinet, C., Hand, K.P., Hayes, A.G., Hörst, S.M., Johnson, J.R., Karkoschka, E., Lawrence, D.J., Le Gall, A., Lora, J.M., McKay, C.P., Miller, R.S., Murchie, S.L., Neish, C.D., Newman, C.E., Núñez, J., Panning, M.P., Parsons, A.M., Peplowski, P.N., Quick, L.C., Radebaugh, J., Rafkin, S.C.R., Shiraishi, H., Soderblom, J.M., Sotzen, K.S., Stickle, A.M., Stofan, E.R., Szopa, C., Tokano, T., Wagner, T., Wilson, C., Yingst, R.A., Zacny, K., Stähler, S.C., 2021. Science Goals and Objectives for the Dragonfly Titan Rotorcraft Relocatable Lander. *Planet. Sci. J. 2*, 130. https://doi.org/10.3847/PSJ/abfdcf

Baron, A.Q.R., Tanaka, Y., Goto, S., Takeshita, K., Matsushita, T., Ishikawa, T., 2000. An X-ray scattering beamline for studying dynamics. *Journal of Physics and Chemistry of Solids 61*, 461–465. https://doi.org/10.1016/S0022-3697(99)00337-6

Baron, A.Q.R., 2015. Introduction to high-resolution inelastic x-ray scattering. arXiv preprint arXiv:1504.01098.

Baron, A.Q.R., Tsutsui, S., Uchiyama, H., and Ishikawa, D., 2015, Present Status of BL35XU (2014), *SPring-8 / SACLA Research Report 3*, 212.

Beeler, B., Casagranda, A., Aagesen, L., Zhang, Y., Novascone, S., 2020. Atomistic calculations of the surface energy as a function of composition and temperature in γ U–Zr to inform fuel performance modeling. *Journal of Nuclear Materials 540*, 152271. https://doi.org/10.1016/j.jnucmat.2020.152271

Bekaert, D.V., Derenne, S., Tissandier, L., Marrocchi, Y., Charnoz, S., Anquetil, C., Marty, B., 2018. High-temperature Ionization-induced Synthesis of Biologically Relevant Molecules in the Protosolar Nebula. *ApJ 859*, 142. https://doi.org/10.3847/1538-4357/aabe7a

Bernard, J., Quirico, E., Brissaud, O., Montagnac, G., Reynard, B., Mcmillan, P., Coll, P., Nguyen, M., Raulin, F., Schmitt, B., 2006. Reflectance spectra and chemical structure of Titan's tholins: Application to the analysis of Cassini–Huygens observations. *Icarus 185*, 301–307. https://doi.org/10.1016/j.icarus.2006.06.004

Biot, M., 1956. Theory of propagation of elastic waves in a fluid-saturated porous solid. II. Higher frequency range. *Journal of the Acoustical Society of America 28*, 179–191. https://doi.org/10.1121/1.1908241

Birch, S.P.D., Hayes, A.G., Dietrich, W.E., Howard, A.D., Bristow, C.S., Malaska, M.J., Moore, J.M., Mastrogiuseppe, M., Hofgartner, J.D., Williams, D.A., White, O.L., Soderblom, J.M., Barnes, J.W., Turtle, E.P., Lunine, J.I., Wood, C.A., Neish, C.D., Kirk, R.L., Stofan, E.R., Lorenz, R.D., Lopes, R.M.C., 2017. Geomorphologic mapping of titan's polar terrains: Constraining surface processes and landscape evolution. *Icarus 282*, 214–236. https://doi.org/10.1016/j.icarus.2016.08.003

Birch, S.P.D., Hayes, A.G., Howard, A.D., Moore, J.M., Radebaugh, J., 2016. Alluvial Fan Morphology, distribution and formation on Titan. *Icarus 270*, 238–247. https://doi.org/10.1016/j.icarus.2016.02.013

Bischoff, D., Kreuzig, C., Haack, D., Gundlach, B., Blum, J., 2020. Sticky or not sticky? Measurements of the tensile strength of microgranular organic materials. *Monthly Notices of the Royal Astronomical Society 497*, 2517–2528. https://doi.org/10.1093/mnras/staa2126

Blangy, J.P., Strandenes, S., Moos, D., Nur, A., 1993. Ultrasonic velocities in sands—revisited. *GEOPHYSICS 58*, 344–356. https://doi.org/10.1190/1.1443418

Bonnefoy, L.E., Hayes, A.G., Hayne, P.O., Malaska, M.J., Le Gall, A., Solomonidou, A., Lucas, A., 2016. Compositional and spatial variations in Titan dune and interdune regions from Cassini VIMS and RADAR. *Icarus 270*, 222–237. https://doi.org/10.1016/j.icarus.2015.09.014

Bouchez, A.H., Brown, M.E., 2005. Statistics of Titan's South Polar Tropospheric Clouds. *ApJ 618*, L53–L56. https://doi.org/10.1086/427693

Boyd, R.H., 1983. The mechanical moduli of lamellar semicrystalline polymers. *J. Polym. Sci. Polym. Phys. Ed. 21*, 493–504. https://doi.org/10.1002/pol.1983.180210401

Bragg, W.L., 1913. The structure of some crystals as indicated by their diffraction of X-rays. *Proc. R. Soc. Lond. A Math. Phys. Sci. 89*, 248–277. https://doi.org/10.1098/rspa.1913.0083

Brinkman, N., Schmelzbach, C., Sollberger, D., Pierick, J.T., Edme, P., Haag, T., Kedar, S., Hudson, T., Andersson, F., Van Driel, M., Stähler, S., Nicollier, T., Robertsson, J., Giardini, D., Spohn, T., Krause, C., Grott, M., Knollenberg, J., Hurst, K., Rochas, L., Vallade, J., Blandin, S., Lognonné, P., Pike, W.T., Banerdt, W.B., 2022. In Situ Regolith Seismic Velocity Measurement at the InSight Landing Site on Mars. *JGR Planets 127*, e2022JE007229. https://doi.org/10.1029/2022JE007229

Broadfoot, A.L., Sandel, B.R., Shemansky, D.E., Holberg, J.B., Smith, G.R., Strobel, D.F., McConnell, J.C., Kumar, S., Hunten, D.M., Atreya, S.K., Donahue, T.M., Moos, H.W., Bertaux, J.L., Blamont, J.E., Pomphrey, R.B., Linick, S., 1981. Extreme Ultraviolet Observations from Voyager 1 Encounter with Saturn. *Science 212*, 206–211. https://doi.org/10.1126/science.212.4491.206

Brossier, J.F., Rodriguez, S., Cornet, T., Lucas, A., Radebaugh, J., Maltagliati, L., Le Mouélic, S., Solomonidou, A., Coustenis, A., Hirtzig, M., Jaumann, R., Stephan, K., Sotin, C., 2018. Geological Evolution of Titan's Equatorial Regions: Possible Nature and Origin of the Dune Material. *JGR Planets 123*, 1089–1112. https://doi.org/10.1029/2017JE005399

Burkel, E., 2000. Phonon spectroscopy by inelastic x-ray scattering. *Rep. Prog. Phys. 63*, 171–232. https://doi.org/10.1088/0034-4885/63/2/203

Burkel, E., Peisl, J., Dorner, B., 1987. Observation of Inelastic X-Ray Scattering from Phonons. *Europhys. Lett. 3*, 957–961. https://doi.org/10.1209/0295-5075/3/8/015

Burr, D.M., Bridges, N.T., Marshall, J.R., Smith, J.K., White, B.R., Emery, J.P., 2015. Higher-than-predicted saltation threshold wind speeds on Titan. *Nature 517*, 60–63. https://doi.org/10.1038/nature14088

Cable, M.L., Hörst, S.M., Hodyss, R., Beauchamp, P.M., Smith, M.A., Willis, P.A., 2012. Titan Tholins: Simulating Titan Organic Chemistry in the Cassini-Huygens Era. *Chem. Rev. 112*, 1882–1909. https://doi.org/10.1021/cr200221x

Cappella, B., Stark, W., 2006. Adhesion of amorphous polymers as a function of temperature probed with AFM force–distance curves. *Journal of Colloid and Interface Science 296*, 507–514. https://doi.org/10.1016/j.jcis.2005.09.043

Carcione, J.M., 2000. A model for seismic velocity and attenuation in petroleum source rocks. *GEOPHYSICS 65*, 1080–1092. https://doi.org/10.1190/1.1444801

Carini, Giovanni, Jr, Carini, Giuseppe, Cosio, D., D'Angelo, G., Rossi, F., 2016. Low temperature heat capacity of permanently densified SiO2 glasses. *Philos. Mag. (Abingdon) 96*, 761–773. https://doi.org/10.1080/14786435.2015.1122845

Carpick, R.W., Salmeron, M., 1997. Scratching the Surface: Fundamental Investigations of Tribology with Atomic Force Microscopy. *Chem. Rev. 97*, 1163–1194. https://doi.org/10.1021/cr960068q

Carrasco, N., Schmitz-Afonso, I., Bonnet, J.-Y., Quirico, E., Thissen, R., Dutuit, O., Bagag, A., Laprévote, O., Buch, A., Giulani, A., Adandé, G., Ouni, F., Hadamcik, E., Szopa, C., Cernogora, G., 2009. Chemical Characterization of Titan's Tholins: Solubility, Morphology and Molecular Structure Revisited. *J. Phys. Chem. A 113*, 11195–11203. https://doi.org/10.1021/jp904735q

Champi, A., Lacerda, R.G., Marques, F.C., 2002. Thermal expansion coefficient of amorphous carbon nitride thin films deposited by glow discharge. *Thin Solid Films 420–421*, 200–204. https://doi.org/10.1016/S0040-6090(02)00797-6

Charnay, B., Barth, E., Rafkin, S., Narteau, C., Lebonnois, S., Rodriguez, S., Courrech Du Pont, S., Lucas, A., 2015. Methane storms as a driver of Titan's dune orientation. *Nature Geosci 8*, 362–366. https://doi.org/10.1038/ngeo2406

Charnay, B., Forget, F., Tobie, G., Sotin, C., Wordsworth, R., 2014. Titan's past and future: 3D modeling of a pure nitrogen atmosphere and geological implications. *Icarus 241*, 269–279. https://doi.org/10.1016/j.icarus.2014.07.009

Chaudhury, M.K., 1996. Interfacial interaction between low-energy surfaces. *Materials Science and Engineering: R: Reports 16*, 97–159. https://doi.org/10.1016/0927-796X(95)00185-9

Chen, K.-C., Chiu, J.-M., Yang, Y.-T., 1996. Shear-wave velocity of the sedimentary basin in the upper Mississippi embayment usingS-to-Pconverted waves. *Bull. Seismol. Soc. Am. 86*, 848–856. https://doi.org/10.1785/bssa0860030848

Cheng, A.F., Summers, M.E., Gladstone, G.R., Strobel, D.F., Young, L.A., Lavvas, P., Kammer, J.A., Lisse, C.M., Parker, A.H., Young, E.F., Stern, S.A., Weaver, H.A., Olkin, C.B., Ennico, K., 2017. Haze in Pluto's atmosphere. *Icarus 290*, 112–133. https://doi.org/10.1016/j.icarus.2017.02.024

Cheng, Y., Maria Pugno, N., Shi, X., Chen, B., Gao, H., 2013. Surface energy-controlled self-collapse of carbon nanotube bundles with large and reversible volumetric deformation. *J. Appl. Mech. 80*, 040902. https://doi.org/10.1115/1.4024174

Cho, C.-H., 2009. Characterization of Young's modulus of silicon versus temperature using a "beam deflection" method with a four-point bending fixture. *Current Applied Physics 9*, 538–545. https://doi.org/10.1016/j.cap.2008.03.024

Choukroun, M., Grasset, O., 2010. Thermodynamic data and modeling of the water and ammonia-water phase diagrams up to 2.2 GPa for planetary geophysics. *J. Chem. Phys. 133*, 144502. https://doi.org/10.1063/1.3487520

Clarke, D.W., Ferris, J.P., 1997. Titan Haze: Structure and Properties of Cyanoacetylene and Cyanoacetylene–Acetylene Photopolymers. *Icarus 127*, 158–172. https://doi.org/10.1006/icar.1996.5667

Cody, G.D., Heying, E., Alexander, C.M.O., Nittler, L.R., Kilcoyne, A.L.D., Sandford, S.A., Stroud, R.M., 2011. Establishing a molecular relationship between chondritic and cometary organic solids. *Proc. Natl. Acad. Sci. U.S.A. 108*, 19171–19176. https://doi.org/10.1073/pnas.1015913108

Coll, P., Navarro-González, R., Szopa, C., Poch, O., Ramírez, S.I., Coscia, D., Raulin, F., Cabane, M., Buch, A., Israël, G., 2013. Can laboratory tholins mimic the chemistry producing Titan's aerosols? A review in light of ACP experimental results. *Planetary and Space Science 77*, 91–103. https://doi.org/10.1016/j.pss.2012.07.006

Comola, F., Kok, J.F., Lora, J.M., Cohanim, K., Yu, X., He, C., McGuiggan, P., Hörst, S.M., Turney, F., 2022. Titan's Prevailing Circulation Might Drive Highly Intermittent, Yet Significant Sediment Transport. *Geophysical Research Letters 49*. https://doi.org/10.1029/2022GL097913

Cordier, D., Barnes, J.W., Ferreira, A.G., 2013. On the chemical composition of Titan's dry lakebed evaporites. *Icarus 226*, 1431–1437. https://doi.org/10.1016/j.icarus.2013.07.026

Cordier, D., Mousis, O., Lunine, J.I., Lavvas, P., Vuitton, V., 2009. AN ESTIMATE OF THE CHEMICAL COMPOSITION OF TITAN's LAKES. *ApJ 707*, L128–L131. https://doi.org/10.1088/0004-637X/707/2/L128

Corn, M., 1961. The Adhesion of Solid Particles to Solid Surfaces, I. a Review. *Journal of the Air Pollution Control Association 11*, 523–528. https://doi.org/10.1080/00022470.1961.10468032

Courtney, T.H., 2005. Mechanical Behavior of Materials: Second Edition. *Waveland Press*.

Crist, B., Fisher, C.J., Howard, P.R., 1989. Mechanical properties of model polyethylenes: tensile elastic modulus and yield stress. *Macromolecules 22*, 1709–1718. https://doi.org/10.1021/ma00194a035

Curtis, D.B., Hatch, C.D., Hasenkopf, C.A., Toon, O.B., Tolbert, M.A., McKay, C.P., Khare, B.N., 2008. Laboratory studies of methane and ethane adsorption and nucleation onto organic particles: Application to Titan's clouds. *Icarus 195*, 792–801. https://doi.org/10.1016/j.icarus.2008.02.003

Derjaguin, B.V., Muller, V.M., Toporov, Y.P., 1975. Effect of contact deformations on the adhesion of particles. *J. Colloid Interface Sci. 53*, 314–326. https://doi.org/10.1016/0021-9797(75)90018-1

Dorner, B., Burkel, E., Illini, Th., Peisl, J., 1987. First measurement of a phonon dispersion curve by inelastic X-ray scattering. Z. *Physik B - Condensed Matter 69*, 179–183. https://doi.org/10.1007/BF01307274

Dvorkin, J., Prasad, M., Sakai, A., Lavoie, D., 1999. Elasticity of marine sediments: Rock physics modeling. *Geophysical Research Letters 26*, 1781–1784. https://doi.org/10.1029/1999GL900332

Elachi, C., Wall, S., Allison, M., Anderson, Y., Boehmer, R., Callahan, P., Encrenaz, P., Flamini, E., Franceschetti, G., Gim, Y., Hamilton, G., Hensley, S., Janssen, M., Johnson, W., Kelleher, K., Kirk, R., Lopes, R., Lorenz, R., Lunine, J., Muhleman, D., Ostro, S., Paganelli, F., Picardi, G., Posa, F., Roth, L., Seu, R., Shaffer, S., Soderblom, L., Stiles, B., Stofan, E., Vetrella, S., West, R., Wood, C., Wye, L., Zebker, H., 2005. Cassini Radar Views the Surface of Titan. *Science 308*, 970–974. https://doi.org/10.1126/science.1109919

Ewing, R.C., Hayes, A.G., Lucas, A., 2015. Sand dune patterns on Titan controlled by long-term climate cycles. *Nature Geosci 8*, 15–19. https://doi.org/10.1038/ngeo2323

Faulk, S.P., Mitchell, J.L., Moon, S., Lora, J.M., 2017. Regional patterns of extreme precipitation on Titan consistent with observed alluvial fan distribution. *Nature Geosci 10*, 827–831. https://doi.org/10.1038/ngeo3043

Ferrari, A.C., Robertson, J., Beghi, M.G., Bottani, C.E., Ferulano, R., Pastorelli, R., 1999. Elastic constants of tetrahedral amorphous carbon films by surface Brillouin scattering. *Applied Physics Letters 75*, 1893–1895. https://doi.org/10.1063/1.124863

Ferry, J. D. 1980. Viscoelastic Properties of Polymers (Vol. 264). *Wiley*.

Fiquet, G., Badro, J., Guyot, F., Bellin, C., Krisch, M., Antonangeli, D., Requardt, H., Mermet, A., Farber, D., Aracne-Ruddle, C., Zhang, J., 2004. Application of inelastic X-ray scattering to the measurements of acoustic wave velocities in geophysical materials at very high pressure. *Physics of the Earth and Planetary Interiors 143–144*, 5–18. https://doi.org/10.1016/j.pepi.2003.10.005

Folkner, W.M., Asmar, S.W., Border, J.S., Franklin, G.W., Finley, S.G., Gorelik, J., Johnston, D.V., Kerzhanovich, V.V., Lowe, S.T., Preston, R.A., Bird, M.K., Dutta-Roy, R., Allison, M., Atkinson, D.H., Edenhofer, P., Plettemeier, D., Tyler, G.L., 2006. Winds on Titan from ground-based tracking of the Huygens probe. *J. Geophys. Res. 111*, 2005JE002649. https://doi.org/10.1029/2005JE002649

Fåk, B., Dorner, B., 1997. Phonon line shapes and excitation energies. *Physica B: Condensed Matter 234–236*, 1107–1108. https://doi.org/10.1016/S0921-4526(97)00121-X

Gilbert, D.G., Ashby, M.F., Beaumont, P.W.R., 1986. Modulus-maps for amorphous polymers. *J Mater Sci 21*, 3194–3210. https://doi.org/10.1007/BF00553357

Gladstone, G.R., Stern, S.A., Ennico, K., Olkin, C.B., Weaver, H.A., Young, L.A., Summers, M.E., Strobel, D.F., Hinson, D.P., Kammer, J.A., Parker, A.H., Steffl, A.J., Linscott, I.R., Parker, J.Wm., Cheng, A.F., Slater, D.C., Versteeg, Maarten H., Greathouse, T.K., Retherford, K.D., Throop, H., Cunningham, N.J., Woods, W.W., Singer, K.N., Tsang, C.C.C., Schindhelm, R., Lisse, C.M., Wong, M.L., Yung, Y.L., Zhu, X., Curdt, W., Lavvas, P., Young, E.F., Tyler, G.L., the New Horizons Science Team, Bagenal, F., Grundy, W.M., McKinnon, W.B., Moore, J.M., Spencer, J.R., Andert, T., Andrews, J., Banks, M., Bauer, B., Bauman, J., Barnouin, O.S., Bedini, P., Beisser, K., Beyer, R.A., Bhaskaran, S., Binzel, R.P., Birath, E., Bird, M., Bogan, D.J., Bowman, A., Bray, V.J., Brozovic, M., Bryan, C., Buckley, M.R., Buie, M.W., Buratti, B.J., Bushman, S.S., Calloway, A., Carcich, B., Conard, S., Conrad, C.A., Cook, J.C., Cruikshank, D.P., Custodio, O.S., Ore, C.M.D., Deboy, C., Dischner, Z.J.B., Dumont, P., Earle, A.M., Elliott, H.A., Ercol, J., Ernst, C.M., Finley, T., Flanigan, S.H., Fountain, G., Freeze, M.J., Green, J.L., Guo, Y., Hahn, M., Hamilton, D.P., Hamilton, S.A., Hanley, J., Harch, A., Hart, H.M., Hersman, C.B., Hill, A., Hill, M.E., Holdridge, M.E., Horanyi, M., Howard, A.D., Howett, C.J.A., Jackman, C., Jacobson, R.A., Jennings, D.E., Kang, H.K., Kaufmann, D.E., Kollmann, P., Krimigis, S.M., Kusnierkiewicz, D., Lauer, T.R., Lee, J.E., Lindstrom, K.L., Lunsford, A.W., Mallder, V.A., Martin, N., McComas, D.J., McNutt, R.L., Mehoke, D., Mehoke, T., Melin, E.D., Mutchler, M., Nelson, D., Nimmo, F., Nunez, J.I., Ocampo, A., Owen, W.M., Paetzold, M., Page, B., Pelletier, F., Peterson, J., Pinkine, N., Piquette, M., Porter, S.B., Protopapa, S., Redfern, J., Reitsema, H.J., Reuter, D.C., Roberts, J.H., Robbins, S.J., Rogers, G., Rose, D., Runyon, K., Ryschkewitsch, M.G., Schenk, P., Sepan, B., Showalter, M.R., Soluri, M., Stanbridge, D., Stryk, T., Szalay, J.R., Tapley, M., Taylor, A., Taylor, H., Umurhan, O.M., Verbiscer, A.J., Versteeg, M. H., Vincent, M., Webbert, R., Weidner, S., Weigle, G.E., White, O.L., Whittenburg, K., Williams, B.G., Williams, K., Williams, S., Zangari, A.M., Zirnstein, E., 2016. The atmosphere of Pluto as observed by New Horizons. *Science 351*, aad8866. https://doi.org/10.1126/science.aad8866

Glein, C.R., Shock, E.L., 2013. A geochemical model of non-ideal solutions in the methane–ethane–propane–nitrogen–acetylene system on Titan. *Geochimica et Cosmochimica Acta 115*, 217–240. https://doi.org/10.1016/j.gca.2013.03.030

Glenzer, S.H., Redmer, R., 2009. X-ray Thomson scattering in high energy density plasmas. *Rev. Mod. Phys. 81*, 1625–1663. https://doi.org/10.1103/RevModPhys.81.1625

Goesmann, F., Rosenbauer, H., Bredehöft, J.H., Cabane, M., Ehrenfreund, P., Gautier, T., Giri, C., Krüger, H., Le Roy, L., MacDermott, A.J., McKenna-Lawlor, S., Meierhenrich, U.J., Caro, G.M.M., Raulin, F., Roll, R., Steele, A., Steininger, H., Sternberg, R., Szopa, C., Thiemann, W., Ulamec, S., 2015. Organic compounds on comet 67P/Churyumov-Gerasimenko revealed by COSAC mass spectrometry. *Science 349*, aab0689. https://doi.org/10.1126/science.aab0689

Greaves, G.N., Greer, A.L., Lakes, R.S., Rouxel, T., 2011. Poisson's ratio and modern materials. *Nature Mater 10*, 823–837. https://doi.org/10.1038/nmat3134

Greeley, R.J. D. Iversen, 1985. Wind as a Geologic Process, 333, *Cambridge University Press*, Cambridge.

Greenberg, J.M., 1989. The Core-Mantle Model of Interstellar Grains and the Cosmic Dust Connection. *Symp. - Int. Astron. Union 135*, 345–356. https://doi.org/10.1017/S0074180900125355

Grubisic, A., Trainer, M.G., Li, X., Brinckerhoff, W.B., Van Amerom, F.H., Danell, R.M., Costa, J.T., Castillo, M., Kaplan, D., Zacny, K., 2021. Laser Desorption Mass Spectrometry at Saturn's moon Titan. *International Journal of Mass Spectrometry 470*, 116707. https://doi.org/10.1016/j.ijms.2021.116707

Grundy, W.M., Bertrand, T., Binzel, R.P., Buie, M.W., Buratti, B.J., Cheng, A.F., Cook, J.C., Cruikshank, D.P., Devins, S.L., Dalle Ore, C.M., Earle, A.M., Ennico, K., Forget, F., Gao, P., Gladstone, G.R., Howett, C.J.A., Jennings, D.E., Kammer, J.A., Lauer, T.R., Linscott, I.R., Lisse, C.M., Lunsford, A.W., McKinnon, W.B., Olkin, C.B., Parker, A.H., Protopapa, S., Quirico, E., Reuter, D.C., Schmitt, B., Singer, K.N., Spencer, J.A., Stern, S.A., Strobel, D.F., Summers, M.E., Weaver, H.A., Weigle, G.E., Wong, M.L., Young, E.F., Young, L.A., Zhang, X., 2018. Pluto's haze as a surface material. *Icarus 314*, 232–245. https://doi.org/10.1016/j.icarus.2018.05.019

Han, D.-H., Nur, A., Morgan, D., 1986. Effects of porosity and clay content on wave velocities in sandstones. *Geophysics 51*, 2093–2107. https://doi.org/10.1190/1.1442062

Haugstad, G., 2012. Atomic force microscopy: Understanding basic modes and advanced applications. *John Wiley & Sons*, Nashville, TN.

Hayes, A., Aharonson, O., Callahan, P., Elachi, C., Gim, Y., Kirk, R., Lewis, K., Lopes, R., Lorenz, R., Lunine, J., Mitchell, K., Mitri, G., Stofan, E., Wall, S., 2008. Hydrocarbon lakes on Titan: Distribution and interaction with a porous regolith. *Geophysical Research Letters 35*, 2008GL033409. https://doi.org/10.1029/2008GL033409

Hayes, A.G., 2016. The Lakes and Seas of Titan. *Annu. Rev. Earth Planet. Sci. 44*, 57–83. https://doi.org/10.1146/annurev-earth-060115-012247

Hayes, A.G., Aharonson, O., Lunine, J.I., Kirk, R.L., Zebker, H.A., Wye, L.C., Lorenz, R.D., Turtle, E.P., Paillou, P., Mitri, G., Wall, S.D., Stofan, E.R., Mitchell, K.L., Elachi, C., 2011. Transient surface liquid in Titan's polar regions from Cassini. *Icarus 211*, 655–671. https://doi.org/10.1016/j.icarus.2010.08.017

Hayes, A.G., Birch, S.P.D., Dietrich, W.E., Howard, A.D., Kirk, R.L., Poggiali, V., Mastrogiuseppe, M., Michaelides, R.J., Corlies, P.M., Moore, J.M., Malaska, M.J., Mitchell, K.L., Lorenz, R.D., Wood, C.A., 2017. Topographic Constraints on the Evolution and Connectivity of Titan's Lacustrine Basins: Topography of Titan's Lacustrine Basins. *Geophys. Res. Lett. 44*, 11,745-11,753. https://doi.org/10.1002/2017GL075468

Hayes, A.G., Lorenz, R.D., Lunine, J.I., 2018. A post-Cassini view of Titan's methane-based hydrologic cycle. *Nature Geosci 11*, 306–313. https://doi.org/10.1038/s41561-018-0103-y

He, C., Hörst, S.M., Riemer, S., Sebree, J.A., Pauley, N., Vuitton, V., 2017. Carbon Monoxide Affecting Planetary Atmospheric Chemistry. *ApJ 841*, L31. https://doi.org/10.3847/2041-8213/aa74cc

He, C., Smith, M.A., 2014. Solubility and stability investigation of Titan aerosol analogs: New insight from NMR analysis. *Icarus 232*, 54–59. https://doi.org/10.1016/j.icarus.2014.01.007

Henke, B.L., Gullikson, E.M., Davis, J.C., 1993. X-ray interactions: Photoabsorption, scattering, transmission, and reflection at E = 50-30,000 eV, Z = 1-92. *At. Data Nucl. Data Tables 54*, 181–342. https://doi.org/10.1006/adnd.1993.1013

Higo, Y., Kono, Y., Inoue, T., Irifune, T., Funakoshi, K., 2009. A system for measuring elastic wave velocity under high pressure and high temperature using a combination of ultrasonic measurement and the multi-anvil apparatus at SPring-8. *J Synchrotron Rad 16*, 762–768. https://doi.org/10.1107/S0909049509034980

Hirai, E., Sekine, Y., Zhang, N., Noda, N., Tan, S., Takahashi, Y., Kagi, H., 2023. Rapid Aggregation and Dissolution of Organic Aerosols in Liquid Methane on Titan. *Geophysical Research Letters 50*, e2023GL103015. https://doi.org/10.1029/2023GL103015

Homma, K.A., Okuzumi, S., Nakamoto, T., Ueda, Y., 2019. Rocky Planetesimal Formation Aided by Organics. *ApJ 877*, 128. https://doi.org/10.3847/1538-4357/ab1de0

Hong, P., Sekine, Y., Sasamori, T., Sugita, S., 2018. Experimental study of heterogeneous organic chemistry induced by far ultraviolet light: Implications for growth of organic aerosols by CH3 addition in the atmospheres of Titan and early Earth. *Icarus 307*, 25–39. https://doi.org/10.1016/j.icarus.2018.02.019

Horvath, D.G., Andrews-Hanna, J.C., Newman, C.E., Mitchell, K.L., Stiles, B.W., 2016. The influence of subsurface flow on lake formation and north polar lake distribution on Titan. *Icarus 277*, 103–124. https://doi.org/10.1016/j.icarus.2016.04.042

Hosokawa, S., 2008. Modern X-ray Spectroscopy VI. Using X-rays to probe phonons — mainly in disordered materials., *J. of SPSJ. 57*, 6, 301–312. https://doi.org/10.5111/bunkou.57.301

Hunten, D.M., 2006. The sequestration of ethane on Titan in smog particles. *Nature 443*, 669–670. https://doi.org/10.1038/nature05157

Hörst, S.M., 2017. Titan's atmosphere and climate: TITAN'S ATMOSPHERE. *J. Geophys. Res. Planets 122*, 432–482. https://doi.org/10.1002/2016JE005240

Hörst, S.M., Tolbert, M.A., 2013. IN SITU MEASUREMENTS OF THE SIZE AND DENSITY OF TITAN AEROSOL ANALOGS. *ApJ 770*, L10. https://doi.org/10.1088/2041-8205/770/1/L10

Ikuta, D., Ohtani, E., Fukui, H., Sakamaki, T., Heid, R., Ishikawa, D., Baron, A.Q.R., 2023. Density deficit of Earth's core revealed by a multimegabar primary pressure scale. *Sci. Adv. 9*, eadh8706. https://doi.org/10.1126/sciadv.adh8706

Imanaka, H., Cruikshank, D.P., Khare, B.N., McKay, C.P., 2012. Optical constants of Titan tholins at mid-infrared wavelengths (2.5–25μm) and the possible chemical nature of Titan's haze particles. *Icarus 218*, 247–261. https://doi.org/10.1016/j.icarus.2011.11.018

InSight Mars SEIS Data Service. 2019. SEIS raw data, Insight Mission. IPGP, JPL, CNES, ETHZ, ICL, MPS, ISAE-Supaero, LPG, MFSC. https://doi.org/10.18715/SEIS.INSIGHT.XB_2016

Ishikawa, D., Baron, A.Q.R., 2021. Practical measurement of the energy resolution for meV-resolved inelastic X-ray scattering. *J Synchrotron Rad 28*, 804–811. https://doi.org/10.1107/S1600577521003234

Israelachvili, J., Min, Y., Akbulut, M., Alig, A., Carver, G., Greene, W., Kristiansen, K., Meyer, E., Pesika, N., Rosenberg, K., Zeng, H., 2010. Recent advances in the surface forces apparatus (SFA) technique. *Rep. Prog. Phys. 73*, 036601. https://doi.org/10.1088/0034-4885/73/3/036601

Israelachvili, J.N., 2011. Intermolecular and Surface Forces. *Elsevier Science & Technology*.

Israël, G., Szopa, C., Raulin, F., Cabane, M., Niemann, H.B., Atreya, S.K., Bauer, S.J., Brun, J.-F., Chassefière, E., Coll, P., Condé, E., Coscia, D., Hauchecorne, A., Millian, P., Nguyen, M.-J., Owen, T., Riedler, W., Samuelson, R.E., Siguier, J.-M., Steller, M., Sternberg, R., Vidal-Madjar, C., 2005. Complex organic matter in Titan's atmospheric aerosols from in situ pyrolysis and analysis. *Nature 438*, 796–799. https://doi.org/10.1038/nature04349

Iversen, J.D., White, B.R., 1982. Saltation threshold on Earth, Mars and Venus. *Sedimentology 29*, 111–119. https://doi.org/10.1111/j.1365-3091.1982.tb01713.x

Jabaud, B., Artoni, R., Tobie, G., Le Menn, E., Richard, P., 2024. Cohesive properties of ice powders analogous to fresh plume deposits on Enceladus and Europa. *Icarus 409*, 115859. https://doi.org/10.1016/j.icarus.2023.115859

Janssen, M.A., Le Gall, A., Lopes, R.M., Lorenz, R.D., Malaska, M.J., Hayes, A.G., Neish, C.D., Solomonidou, A., Mitchell, K.L., Radebaugh, J., Keihm, S.J., Choukroun, M., Leyrat, C., Encrenaz, P.J., Mastrogiuseppe, M., 2016. Titan's surface at 2.18-cm wavelength imaged by the Cassini RADAR radiometer: Results and interpretations through the first ten years of observation. *Icarus 270*, 443–459. https://doi.org/10.1016/j.icarus.2015.09.027

Jennings, D.E., Tokano, T., Cottini, V., Nixon, C.A., Achterberg, R.K., Flasar, F.M., Kunde, V.G., Romani, P.N., Samuelson, R.E., Segura, M.E., Gorius, N.J.P., Guandique, E., Kaelberer, M.S., Coustenis, A., 2019. Titan Surface Temperatures during the Cassini Mission. *ApJL 877*, L8. https://doi.org/10.3847/2041-8213/ab1f91

Jiang, H., Haji-Akbari, A., Debenedetti, P.G., Panagiotopoulos, A.Z., 2018. Forward flux sampling calculation of homogeneous nucleation rates from aqueous NaCl solutions. *J. Chem. Phys. 148*, 044505. https://doi.org/10.1063/1.5016554

Johnson, K.L., Kendall, K., Roberts, A.D., 1971. Surface energy and the contact of elastic solids. *Proc. R. Soc. Lond. 324*, 301–313. https://doi.org/10.1098/rspa.1971.0141

Jordan, J.L., Rowland, R.L., Greenhall, J., Moss, E.K., Huber, R.C., Willis, E.C., Hrubiak, R., Kenney-Benson, C., Bartram, B., Sturtevant, B.T., 2021. Elastic properties of polyethylene from high pressure sound speed measurements. *Polymer 212*, 123164. https://doi.org/10.1016/j.polymer.2020.123164

Kaiser, K., Schulz, F., Maillard, J.F., Hermann, F., Pozo, I., Peña, D., Cleaves, H.J., Burton, A.S., Danger, G., Afonso, C., Sandford, S., Gross, L., 2022. Visualization and identification of single meteoritic organic molecules by atomic force microscopy. *Meteorit & Planetary Scien 57*, 644–656. https://doi.org/10.1111/maps.13784

Kataoka, A., Tanaka, H., Okuzumi, S., Wada, K., 2013. Fluffy dust forms icy planetesimals by static compression. *A&A 557*, L4. https://doi.org/10.1051/0004-6361/201322151

Kebukawa, Y., David Kilcoyne, A.L., Cody, G.D., 2013. EXPLORING THE POTENTIAL FORMATION OF ORGANIC SOLIDS IN CHONDRITES AND COMETS THROUGH POLYMERIZATION OF INTERSTELLAR FORMALDEHYDE. *ApJ 771*, 19. https://doi.org/10.1088/0004-637X/771/1/19

Kedar, S., Andrade, J., Banerdt, B., Delage, P., Golombek, M., Grott, M., Hudson, T., Kiely, A., Knapmeyer, M., Knapmeyer-Endrun, B., Krause, C., Kawamura, T., Lognonne, P., Pike, T., Ruan, Y., Spohn, T., Teanby, N., Tromp, J., Wookey, J., 2017. Analysis of Regolith Properties Using Seismic Signals Generated by InSight's HP3 Penetrator. *Space Sci Rev 211*, 315–337. https://doi.org/10.1007/s11214-017-0391-3

Kendall, K., 1975. Rolling friction and adhesion between smooth solids. *Wear 33*, 351–358. https://doi.org/10.1016/0043-1648(75)90288-4

Khare, B.N., Sagan, C., Arakawa, E.T., Suits, F., Callcott, T.A., Williams, M.W., 1984. Optical constants of organic tholins produced in a simulated Titanian atmosphere: From soft x-ray to microwave frequencies. *Icarus 60*, 127–137. https://doi.org/10.1016/0019-1035(84)90142-8

Knutson, H.A., Benneke, B., Deming, D., Homeier, D., 2014. A featureless transmission spectrum for the Neptune-mass exoplanet GJ 436b. *Nature 505*, 66–68. https://doi.org/10.1038/nature12887

Kohnen, H., 1974. The temperature dependence of seismic waves in ice. *J. Glaciol. 13*, 144–147. https://doi.org/10.3189/S0022143000023467

Kok, J.F., Parteli, E.J.R., Michaels, T.I., Karam, D.B., 2012. The physics of wind-blown sand and dust. *Rep. Prog. Phys. 75*, 106901. https://doi.org/10.1088/0034-4885/75/10/106901

Kostiuk, T., Fast, K.E., Livengood, T.A., Hewagama, T., Goldstein, J.J., Espenak, F., Buhl, D., 2001. Direct measurement of winds on Titan. *Geophysical Research Letters 28*, 2361–2364. https://doi.org/10.1029/2000GL012617

Kostiuk, T., Hewagama, T., Fast, K.E., Livengood, T.A., Annen, J., Buhl, D., Sonnabend, G., Schmülling, F., Delgado, J.D., Achterberg, R., 2010. High spectral resolution infrared studies of Titan: Winds, temperature, and composition. *Planetary and Space Science 58*, 1715–1723. https://doi.org/10.1016/j.pss.2010.08.004

Kostiuk, T., Livengood, T.A., Hewagama, T., Sonnabend, G., Fast, K.E., Murakawa, K., Tokunaga, A.T., Annen, J., Buhl, D., Schmülling, F., 2005. Titan's stratospheric zonal wind, temperature, and ethane abundance a year prior to Huygens insertion. *Geophysical Research Letters 32*, 2005GL023897. https://doi.org/10.1029/2005GL023897

Kostiuk, T., Livengood, T.A., Sonnabend, G., Fast, K.E., Hewagama, T., Murakawa, K., Tokunaga, A.T., Annen, J., Buhl, D., Schmülling, F., Luz, D., Witasse, O., 2006.

Stratospheric global winds on Titan at the time of Huygens descent. *J. Geophys. Res. 111*, 2005JE002630. https://doi.org/10.1029/2005JE002630

Kouchi, A., Kudo, T., Nakano, H., Arakawa, M., Watanabe, N., Sirono, S., Higa, M., Maeno, N., 2002. Rapid Growth of Asteroids Owing to Very Sticky Interstellar Organic Grains. *The Astrophysical Journal 566*, L121–L124. https://doi.org/10.1086/339618

Krasnopolsky, V.A., 1993. On the haze model for Triton. *J. Geophys. Res. 98*, 17123–17124. https://doi.org/10.1029/93JE01459

Krasnopolsky, V.A., Sandel, B.R., Herbert, F., 1992. Properties of haze in the atmosphere of Triton. *J. Geophys. Res. 97*, 11695–11700. https://doi.org/10.1029/92JE00945

Kreidberg, L., Bean, J.L., Désert, J.-M., Benneke, B., Deming, D., Stevenson, K.B., Seager, S., Berta-Thompson, Z., Seifahrt, A., Homeier, D., 2014. Clouds in the atmosphere of the super-Earth exoplanet GJ 1214b. *Nature 505*, 69–72. https://doi.org/10.1038/nature12888

Krigas, T.M., Carella, J.M., Struglinski, M.J., Crist, B., Graessley, W.W., Schilling, F.C., 1985. Model copolymers of ethylene with butene-1 made by hydrogenation of polybutadiene: Chemical composition and selected physical properties. *J. Polym. Sci. Polym. Phys. Ed. 23*, 509–520. https://doi.org/10.1002/pol.1985.180230308

Krzesinska, M., Pilawa, B., Pusz, S., Ng, J., 2006. Physical characteristics of carbon materials derived from pyrolysed vascular plants. *Biomass and Bioenergy 30*, 166–176. https://doi.org/10.1016/j.biombioe.2005.11.009

Kudo, T., Kouchi, A., Arakawa, M., Nakano, H., 2002. The role of sticky interstellar organic material in the formation of asteroids. *Meteorit & Planetary Scien 37*, 1975–1983. https://doi.org/10.1111/j.1945-5100.2002.tb01178.x

Kuga, M., Marty, B., Marrocchi, Y., Tissandier, L., 2015. Synthesis of refractory organic matter in the ionized gas phase of the solar nebula. *Proc. Natl. Acad. Sci. U.S.A. 112*, 7129–7134. https://doi.org/10.1073/pnas.1502796112

Kuwayama, Y., Morard, G., Nakajima, Y., Hirose, K., Baron, A.Q.R., Kawaguchi, S.I., Tsuchiya, T., Ishikawa, D., Hirao, N., Ohishi, Y., 2020. Equation of State of Liquid Iron under Extreme Conditions. *Phys. Rev. Lett. 124*, 165701. https://doi.org/10.1103/PhysRevLett.124.165701

Lai, T., Shi, K., Huang, P., 2020. Adhesion force behaviors between two silica surfaces with varied water thin film due to substrate temperature studied by AFM. *The Journal of Adhesion 96*, 855–872. https://doi.org/10.1080/00218464.2018.1523725

Lancaster, N., 1995. Origin of the gran desierto sand sea, Sonora, Mexico: Evidence from dune morphology and sedimentology, in: Desert Aeolian Processes. *Springer* Netherlands, Dordrecht, pp. 11–35. https://doi.org/10.1007/978-94-009-0067-7_2

Lapôtre, M.G.A., Malaska, M.J., Cable, M.L., 2022. The Role of Seasonal Sediment Transport and Sintering in Shaping Titan's Landscapes: A Hypothesis. *Geophysical Research Letters 49*. https://doi.org/10.1029/2021GL097605

Larkin, P. (2017). Infrared and Raman spectroscopy: Principles and spectral interpretation. *Elsevier*.

Larson, E.J.L., Toon, O.B., Friedson, A.J., 2014. Simulating Titan's aerosols in a three dimensional general circulation model. *Icarus 243*, 400–419. https://doi.org/10.1016/j.icarus.2014.09.003

Lavvas, P., Sander, M., Kraft, M., Imanaka, H., 2011. SURFACE CHEMISTRY AND PARTICLE SHAPE: PROCESSES FOR THE EVOLUTION OF AEROSOLS IN TITAN's ATMOSPHERE. *ApJ 728*, 80. https://doi.org/10.1088/0004-637X/728/2/80

Lavvas, P.P., Coustenis, A., Vardavas, I.M., 2008. Coupling photochemistry with haze formation in Titan's atmosphere, Part I: Model description. *Planetary and Space Science 56*, 27–66. https://doi.org/10.1016/j.pss.2007.05.026

Lebonnois, S., Burgalat, J., Rannou, P., Charnay, B., 2012. Titan global climate model: A new 3-dimensional version of the IPSL Titan GCM. *Icarus 218*, 707–722. https://doi.org/10.1016/j.icarus.2011.11.032

Li, B., Jackson, I., Gasparik, T., Liebermann, R.C., 1996. Elastic wave velocity measurement in multi-anvil apparatus to 10 GPa using ultrasonic interferometry. *Phys. Earth Planet. Inter. 98*, 79–91. https://doi.org/10.1016/s0031-9201(96)03173-1

Li, B., Liebermann, R.C., 2014. Study of the Earth's interior using measurements of sound velocities in minerals by ultrasonic interferometry. *Physics of the Earth and Planetary Interiors 233*, 135–153. https://doi.org/10.1016/j.pepi.2014.05.006

Li, J., Yu, X., Sciamma-O'Brien, E., He, C., Sebree, J.A., Salama, F., Hörst, S.M., Zhang, X., 2022. A Cross-laboratory Comparison Study of Titan Haze Analogs: Surface Energy. *Planet. Sci. J. 3*, 2. https://doi.org/10.3847/PSJ/ac3d27

Li, Y., Kurokawa, H., Sekine, Y., Kebukawa, Y., Nakano, Y., Kitadai, N., Zhang, N., Zang, X., Ueno, Y., Fujimori, G., Nakamura, R., Fujishima, K., Isa, J., 2023. Aqueous breakdown of aspartate and glutamate to n-ω-amino acids on the parent bodies of carbonaceous chondrites and asteroid Ryugu. *Sci. Adv. 9*, eadh7845. https://doi.org/10.1126/sciadv.adh7845

Lindal, G.F., Wood, G.E., Hotz, H.B., Sweetnam, D.N., Eshleman, V.R., Tyler, G.L., 1983. The atmosphere of Titan: An analysis of the Voyager 1 radio occultation measurements. *Icarus 53*, 348–363. https://doi.org/10.1016/0019-1035(83)90155-0

Liu, Z., 2021. Temperature-dependent elastic constants and Young's modulus of silicon single crystal. *JACoW Publishing*, Geneva, Switzerland. https://doi.org/10.18429/JACOW-MEDSI2020-WEPC09

Lognonné, P., Banerdt, W.B., Pike, W.T., Giardini, D., Christensen, U., Garcia, R.F., Kawamura, T., Kedar, S., Knapmeyer-Endrun, B., Margerin, L., Nimmo, F., Panning, M., Tauzin, B., Scholz, J.-R., Antonangeli, D., Barkaoui, S., Beucler, E., Bissig, F., Brinkman, N., Calvet, M., Ceylan, S., Charalambous, C., Davis, P., Van Driel, M., Drilleau, M., Fayon, L., Joshi, R., Kenda, B., Khan, A., Knapmeyer, M., Lekic, V., McClean, J., Mimoun, D., Murdoch, N., Pan, L., Perrin, C., Pinot, B., Pou, L., Menina, S., Rodriguez, S., Schmelzbach, C., Schmerr, N., Sollberger, D., Spiga, A., Stähler, S., Stott, A., Stutzmann, E., Tharimena, S., Widmer-Schnidrig, R., Andersson, F., Ansan, V., Beghein, C., Böse, M., Bozdag, E., Clinton, J., Daubar, I., Delage, P., Fuji, N., Golombek, M., Grott, M., Horleston, A., Hurst, K., Irving, J., Jacob, A., Knollenberg, J., Krasner, S., Krause, C., Lorenz, R., Michaut, C., Myhill, R., Nissen-Meyer, T., Ten Pierick, J., Plesa, A.-C., Quantin-Nataf, C., Robertsson, J., Rochas, L., Schimmel, M., Smrekar, S., Spohn,

T., Teanby, N., Tromp, J., Vallade, J., Verdier, N., Vrettos, C., Weber, R., Banfield, D., Barrett, E., Bierwirth, M., Calcutt, S., Compaire, N., Johnson, C.L., Mance, D., Euchner, F., Kerjean, L., Mainsant, G., Mocquet, A., Rodriguez Manfredi, J.A., Pont, G., Laudet, P., Nebut, T., De Raucourt, S., Robert, O., Russell, C.T., Sylvestre-Baron, A., Tillier, S., Warren, T., Wieczorek, M., Yana, C., Zweifel, P., 2020. Constraints on the shallow elastic and anelastic structure of Mars from InSight seismic data. *Nat. Geosci. 13*, 213–220. https://doi.org/10.1038/s41561-020-0536-y

Lopes, R.M.C., Malaska, M.J., Schoenfeld, A.M., Solomonidou, A., Birch, S.P.D., Florence, M., Hayes, A.G., Williams, D.A., Radebaugh, J., Verlander, T., Turtle, E.P., Le Gall, A., Wall, S.D., 2019. A global geomorphologic map of Saturn's moon Titan. *Nat Astron 4*, 228–233. https://doi.org/10.1038/s41550-019-0917-6

Lopes, R.M.C., Malaska, M.J., Solomonidou, A., Le Gall, A., Janssen, M.A., Neish, C.D., Turtle, E.P., Birch, S.P.D., Hayes, A.G., Radebaugh, J., Coustenis, A., Schoenfeld, A., Stiles, B.W., Kirk, R.L., Mitchell, K.L., Stofan, E.R., Lawrence, K.J., 2016. Nature, distribution, and origin of Titan's Undifferentiated Plains. *Icarus 270*, 162–182. https://doi.org/10.1016/j.icarus.2015.11.034

Lopes, R.M.C., Mitchell, K.L., Stofan, E.R., Lunine, J.I., Lorenz, R., Paganelli, F., Kirk, R.L., Wood, C.A., Wall, S.D., Robshaw, L.E., Fortes, A.D., Neish, C.D., Radebaugh, J., Reffet, E., Ostro, S.J., Elachi, C., Allison, M.D., Anderson, Y., Boehmer, R., Boubin, G., Callahan, P., Encrenaz, P., Flamini, E., Francescetti, G., Gim, Y., Hamilton, G., Hensley, S., Janssen, M.A., Johnson, W.T.K., Kelleher, K., Muhleman, D.O., Ori, G., Orosei, R., Picardi, G., Posa, F., Roth, L.E., Seu, R., Shaffer, S., Soderblom, L.A., Stiles, B., Vetrella, S., West, R.D., Wye, L., Zebker, H.A., 2007. Cryovolcanic features on Titan's surface as revealed by the Cassini Titan Radar Mapper. *Icarus 186*, 395–412. https://doi.org/10.1016/j.icarus.2006.09.006

Lopes, R.M.C., Stofan, E.R., Peckyno, R., Radebaugh, J., Mitchell, K.L., Mitri, G., Wood, C.A., Kirk, R.L., Wall, S.D., Lunine, J.I., Hayes, A., Lorenz, R., Farr, T., Wye, L., Craig, J., Ollerenshaw, R.J., Janssen, M., LeGall, A., Paganelli, F., West, R., Stiles, B., Callahan, P., Anderson, Y., Valora, P., Soderblom, L., 2010. Distribution and interplay of geologic processes on Titan from Cassini radar data. *Icarus 205*, 540–558. https://doi.org/10.1016/j.icarus.2009.08.010

Lora, J.M., Lunine, J.I., Russell, J.L., Hayes, A.G., 2014. Simulations of Titan's paleoclimate. *Icarus 243*, 264–273. https://doi.org/10.1016/j.icarus.2014.08.042

Lora, J.M., Mitchell, J.L., 2015. Titan's asymmetric lake distribution mediated by methane transport due to atmospheric eddies. *Geophysical Research Letters 42*, 6213–6220. https://doi.org/10.1002/2015GL064912

Lora, J.M., Tokano, T., Vatant d'Ollone, J., Lebonnois, S., Lorenz, R.D., 2019. A model intercomparison of Titan's climate and low-latitude environment. *Icarus 333*, 113–126. https://doi.org/10.1016/j.icarus.2019.05.031

Lora, J.M., Ádámkovics, M., 2017. The near-surface methane humidity on Titan. *Icarus 286*, 270–279. https://doi.org/10.1016/j.icarus.2016.10.012

Lorenz, R.D., 1995. Raindrops on Titan. *Adv. Space Res. 15*, 317–320. https://doi.org/10.1016/s0273-1177(99)80103-3

Lorenz, R.D., MacKenzie, S.M., Neish, C.D., Gall, A.L., Turtle, E.P., Barnes, J.W., Trainer, M.G., Werynski, A., Hedgepeth, J., Karkoschka, E., 2021. Selection and Characteristics of the Dragonfly Landing Site near Selk Crater, Titan. *Planet. Sci. J. 2*, 24. https://doi.org/10.3847/PSJ/abd08f

Lorenz, R.D., McKay, C.P., Lunine, J.I., 1997. Photochemically Driven Collapse of Titan's Atmosphere. *Science 275*, 642–644. https://doi.org/10.1126/science.275.5300.642

Lorenz, R.D., Mitchell, K.L., Kirk, R.L., Hayes, A.G., Aharonson, O., Zebker, H.A., Paillou, P., Radebaugh, J., Lunine, J.I., Janssen, M.A., Wall, S.D., Lopes, R.M., Stiles, B., Ostro, S., Mitri, G., Stofan, E.R., 2008. Titan's inventory of organic surface materials. *Geophysical Research Letters 35*, 2007GL032118. https://doi.org/10.1029/2007GL032118

Lorenz, R.D., Radebaugh, J., 2009. Global pattern of Titan's dunes: Radar survey from the Cassini prime mission: PATTERN OF TITAN'S DUNES. *Geophys. Res. Lett. 36*. https://doi.org/10.1029/2008GL036850

Lorenz, R.D., Turtle, E.P., Barnes, J.W., Trainer, M.G., 2018. Dragonfly: A Rotorcraft Lander Concept for Scientific Exploration at Titan. *Johns Hopkins APL Technical Digest 34*.

Lorenz, R.D., Wall, S., Radebaugh, J., Boubin, G., Reffet, E., Janssen, M., Stofan, E., Lopes, R., Kirk, R., Elachi, C., Lunine, J., Mitchell, K., Paganelli, F., Soderblom, L., Wood, C., Wye, L., Zebker, H., Anderson, Y., Ostro, S., Allison, M., Boehmer, R., Callahan, P., Encrenaz, P., Ori, G.G., Francescetti, G., Gim, Y., Hamilton, G., Hensley, S., Johnson, W., Kelleher, K., Muhleman, D., Picardi, G., Posa, F., Roth, L., Seu, R., Shaffer, S., Stiles, B., Vetrella, S., Flamini, E., West, R., 2006. The Sand Seas of Titan: Cassini RADAR Observations of Longitudinal Dunes. *Science 312,* 724–727. https://doi.org/10.1126/science.1123257

Lu, W., Komvopoulos, K., 1999. Microstructure and nanomechanical properties of nitrogenated amorphous carbon thin films synthesized by reactive radio frequency sputtering. *Journal of Applied Physics 85*, 2642–2651. https://doi.org/10.1063/1.369581

Lucas, A., Rodriguez, S., Narteau, C., Charnay, B., Du Pont, S.C., Tokano, T., Garcia, A., Thiriet, M., Hayes, A.G., Lorenz, R.D., Aharonson, O., 2014. Growth mechanisms and dune orientation on Titan. *Geophys. Res. Lett. 41*, 6093–6100. https://doi.org/10.1002/2014GL060971

Luz, D., Civeit, T., Courtin, R., Lebreton, J. -P., Gautier, D., Witasse, O., Kaufer, A., Ferri, F., Lara, L., Livengood, T., Kostiuk, T., 2006. Characterization of zonal winds in the stratosphere of Titan with UVES: 2. Observations coordinated with the Huygens Probe entry. *J. Geophys. Res. 111*, 2005JE002617. https://doi.org/10.1029/2005JE002617

Luz, D., Civeit, T., Courtin, R., Lebreton, J., Gautier, D., Rannou, P., Kaufer, A., Witasse, O., Lara, L., Ferri, F., 2005. Characterization of zonal winds in the stratosphere of Titan with UVES. *Icarus 179*, 497–510. https://doi.org/10.1016/j.icarus.2005.07.021

MacKenzie, S.M., Barnes, J.W., 2016. COMPOSITIONAL SIMILARITIES AND DISTINCTIONS BETWEEN TITAN'S EVAPORITIC TERRAINS. *ApJ 821*, 17. https://doi.org/10.3847/0004-637X/821/1/17

MacKenzie, S.M., Barnes, J.W., Sotin, C., Soderblom, J.M., Le Mouélic, S., Rodriguez, S., Baines, K.H., Buratti, B.J., Clark, R.N., Nicholson, P.D., McCord, T.B., 2014. Evidence

of Titan's climate history from evaporite distribution. *Icarus 243*, 191–207. https://doi.org/10.1016/j.icarus.2014.08.022

MacKenzie, S.M., Birch, S.P.D., Hörst, S., Sotin, C., Barth, E., Lora, J.M., Trainer, M.G., Corlies, P., Malaska, M.J., Sciamma-O'Brien, E., Thelen, A.E., Turtle, E., Radebaugh, J., Hanley, J., Solomonidou, A., Newman, C., Regoli, L., Rodriguez, S., Seignovert, B., Hayes, A.G., Journaux, B., Steckloff, J., Nna-Mvondo, D., Cornet, T., Palmer, M.Y., Lopes, R.M.C., Vinatier, S., Lorenz, R., Nixon, C., Czaplinski, E., Barnes, J.W., Sittler, E., Coates, A., 2021. Titan: Earth-like on the Outside, Ocean World on the Inside. *Planet. Sci. J. 2*, 112. https://doi.org/10.3847/PSJ/abf7c9

MacKenzie, S.M., Lora, J.M., Lorenz, R.D., 2019. A Thermal Inertia Map of Titan. *JGR Planets 124*, 1728–1742. https://doi.org/10.1029/2019JE005930

Magomedov, M.N., 2024. Nanocrystalline surface energy studied within the Gibbs thermodynamic framework. *Phys. Rev. B 109*, 035405. https://doi.org/10.1103/PhysRevB.109.035405

Maillard, J., Carrasco, N., Schmitz-Afonso, I., Gautier, T., Afonso, C., 2018. Comparison of soluble and insoluble organic matter in analogues of Titan's aerosols. *Earth and Planetary Science Letters 495*, 185–191. https://doi.org/10.1016/j.epsl.2018.05.014

Malaska, M.J., Lopes, R.M., Hayes, A.G., Radebaugh, J., Lorenz, R.D., Turtle, E.P., 2016. Material transport map of Titan: The fate of dunes. *Icarus 270*, 183–196. https://doi.org/10.1016/j.icarus.2015.09.029

Malaska, M.J., Radebaugh, J., Lopes, R.M.C., Mitchell, K.L., Verlander, T., Schoenfeld, A.M., Florence, M.M., Le Gall, A., Solomonidou, A., Hayes, A.G., Birch, S.P.D., Janssen, M.A., Schurmeier, L., Cornet, T., Ahrens, C., Farr, T.G., 2020. Labyrinth terrain on Titan. *Icarus 344*, 113764. https://doi.org/10.1016/j.icarus.2020.113764

Mandt, K., Waite, J., Teolis, B., Magee, B., Bell, J., Westlake, J., Nixon, C., Mousis, O., Lunine, J., 2012. The 12C/13C ratio on Titan from cassini inms measurements and implications for the evolution of methane. *The Astrophysical Journal 749*. https://doi.org/10.1088/0004-637X/749/2/160

Mason, I.B., Knibbs, R.H., 1967. The Young's modulus of carbon and graphite artefacts. *Carbon 5*, 493–506. https://doi.org/10.1016/0008-6223(67)90026-7

Mavco, G., Mukerji, T., Dvorkin, J., 2009. The Rock Physics Handbook. 2nd edition. *Cambridge University Press*.

McKay, C.P., Coustenis, A., Samuelson, R.E., Lemmon, M.T., Lorenz, R.D., Cabane, M., Rannou, P., Drossart, P., 2001. Physical properties of the organic aerosols and clouds on Titan. *Planetary and Space Science 49*, 79–99. https://doi.org/10.1016/S0032-0633(00)00051-9

McKay, C.P., Pollack, J.B., Courtin, R., 1989. The thermal structure of Titan's atmosphere. *Icarus 80*, 23–53. https://doi.org/10.1016/0019-1035(89)90160-7

McKay, C.P., Pollack, J.B., Courtin, R., 1991. The Greenhouse and Antigreenhouse Effects on Titan. *Science 253*, 1118–1121. https://doi.org/10.1126/science.11538492

McKay, C.P., Pollack, J.B., Lunine, J.I., Courtin, R., 1993. Coupled atmosphere-ocean models of Titan's past. *Icarus 102*, 88–98. https://doi.org/10.1006/icar.1993.1034

McLean, M., Mykura, H., 1966. The temperature dependence of the surface energy anisotropy of platinum. *Surface Science 5*, 466–481. https://doi.org/10.1016/0039-6028(66)90042-2

McSkimin, H.J., 1950. Ultrasonic measurement techniques applicable to small solid specimens. *Journal of the Acoustical Society of America 22*, 413–418. https://doi.org/10.1121/1.1906618

Menard, K.P., & Menard, N. 2020. Dynamic Mechanical Analysis (3rd ed.). *CRC Press*. https://doi.org/10.1201/9780429190308

Middelmann, T., Walkov, A., Bartl, G., Schödel, R., 2015. Thermal expansion coefficient of single-crystal silicon from 7 K to 293 K. *Phys. Rev. B 92*, 174113. https://doi.org/10.1103/PhysRevB.92.174113

Mitchell, J.L., Lora, J.M., 2016. The Climate of Titan. *Annu. Rev. Earth Planet. Sci. 44*, 353–380. https://doi.org/10.1146/annurev-earth-060115-012428

Mohamed, R.M., Mishra, M.K., AL-Harbi, L.M., Al-Ghamdi, M.S., Ramamurty, U., 2015. Anisotropy in the mechanical properties of organic crystals: temperature dependence. *RSC Adv. 5*, 64156–64162. https://doi.org/10.1039/C5RA11656B

Mohr, M., Maultzsch, J., Dobardžić, E., Reich, S., Milošević, I., Damnjanović, M., Bosak, A., Krisch, M., Thomsen, C., 2007. Phonon dispersion of graphite by inelastic x-ray scattering. *Phys. Rev. B 76*, 035439. https://doi.org/10.1103/PhysRevB.76.035439

Moreno, R., Marten, A., Hidayat, T., 2005. Interferometric measurements of zonal winds on Titan. *A&A 437*, 319–328. https://doi.org/10.1051/0004-6361:20042117

Mumma, M.J., Charnley, S.B., 2011. The Chemical Composition of Comets—Emerging Taxonomies and Natal Heritage. *Annu. Rev. Astron. Astrophys. 49*, 471–524. https://doi.org/10.1146/annurev-astro-081309-130811

Musiolik, G., Wurm, G., 2019. Contacts of Water Ice in Protoplanetary Disks—Laboratory Experiments. *ApJ 873*, 58. https://doi.org/10.3847/1538-4357/ab0428

Nakajima K., Liu H., Ito M., Fujinami S., 2013. Development of Quantitative Evaluation Method for Elastic Modulus of Soft-Materials by Atomic Force Microscopy. *J. Vac. Soc. Jpn. 56*, 258–266. https://doi.org/10.3131/jvsj2.56.258

Nakajima, Y., Imada, S., Hirose, K., Komabayashi, T., Ozawa, H., Tateno, S., Tsutsui, S., Kuwayama, Y., Baron, A.Q.R., 2015. Carbon-depleted outer core revealed by sound velocity measurements of liquid iron–carbon alloy. *Nat Commun 6*, 8942. https://doi.org/10.1038/ncomms9942

Nakamura, Y., Koyama, J., 1982. Seismic Q of the lunar upper mantle. *J. Geophys. Res. 87*, 4855–4861. https://doi.org/10.1029/JB087iB06p04855

Neish, C.D., Barnes, J.W., Sotin, C., MacKenzie, S., Soderblom, J.M., Le Mouélic, S., Kirk, R.L., Stiles, B.W., Malaska, M.J., Le Gall, A., Brown, R.H., Baines, K.H., Buratti, B., Clark, R.N., Nicholson, P.D., 2015. Spectral properties of Titan's impact craters imply

chemical weathering of its surface. *Geophys. Res. Lett. 42*, 3746–3754. https://doi.org/10.1002/2015GL063824

Neish, C.D., Somogyi, Á., Smith, M.A., 2010. Titan's Primordial Soup: Formation of Amino Acids via Low-Temperature Hydrolysis of Tholins. *Astrobiology 10*, 337–347. https://doi.org/10.1089/ast.2009.0402

Nelson, B.A., Poggi, M.A., Bottomley, L.A., King, W.P., 2003. Temperature-Dependence of Water Bridge Formation in Atomic Force Microscopy, in: *Microelectromechanical Systems.* Presented at the ASME 2003 International Mechanical Engineering Congress and Exposition, ASMEDC, Washington, DC, USA, pp. 629–636. https://doi.org/10.1115/IMECE2003-41762

Nelson, R.M., Kamp, L.W., Matson, D.L., Irwin, P.G.J., Baines, K.H., Boryta, M.D., Leader, F.E., Jaumann, R., Smythe, W.D., Sotin, C., Clark, R.N., Cruikshank, D.P., Drossart, P., Pearl, J.C., Hapke, B.W., Lunine, J., Combes, M., Bellucci, G., Bibring, J.-P., Capaccioni, F., Cerroni, P., Coradini, A., Formisano, V., Filacchione, G., Langevin, R.Y., McCord, T.B., Mennella, V., Nicholson, P.D., Sicardy, B., 2009. Saturn's Titan: Surface change, ammonia, and implications for atmospheric and tectonic activity. *Icarus 199*, 429–441. https://doi.org/10.1016/j.icarus.2008.08.013

Ngai, K.L., Roland, C.M., 1993. Chemical structure and intermolecular cooperativity: dielectric relaxation results. Macromolecules 26, 6824–6830. https://doi.org/10.1021/ma00077a019

Nixon, C.A., 2024. The Composition and Chemistry of Titan's Atmosphere. *ACS Earth Space Chem. 8*, 406–456. https://doi.org/10.1021/acsearthspacechem.2c00041

Nixon, C.A., Lorenz, R.D., Achterberg, R.K., Buch, A., Coll, P., Clark, R.N., Courtin, R., Hayes, A., Iess, L., Johnson, R.E., Lopes, R.M.C., Mastrogiuseppe, M., Mandt, K., Mitchell, D.G., Raulin, F., Rymer, A.M., Todd Smith, H., Solomonidou, A., Sotin, C., Strobel, D., Turtle, E.P., Vuitton, V., West, R.A., Yelle, R.V., 2018. Titan's cold case files - Outstanding questions after Cassini-Huygens. *Planetary and Space Science 155*, 50–72. https://doi.org/10.1016/j.pss.2018.02.009

Nixon, C.A., Temelso, B., Vinatier, S., Teanby, N.A., Bézard, B., Achterberg, R.K., Mandt, K.E., Sherrill, C.D., Irwin, P.G.J., Jennings, D.E., Romani, P.N., Coustenis, A., Flasar, F.M., 2012. Isotopic ratios in Titan's methane: measurements and modeling. *Astrophys. J. 749*, 159. https://doi.org/10.1088/0004-637x/749/2/159

Ohno, K., Zhang, X., Tazaki, R., Okuzumi, S., 2021. Haze Formation on Triton. *ApJ 912*, 37. https://doi.org/10.3847/1538-4357/abee82

Okuzumi, S., Tanaka, H., Kobayashi, H., Wada, K., 2012. RAPID COAGULATION OF POROUS DUST AGGREGATES OUTSIDE THE SNOW LINE: A PATHWAY TO SUCCESSFUL ICY PLANETESIMAL FORMATION. *ApJ 752*, 106. https://doi.org/10.1088/0004-637X/752/2/106

Onodera, K., Maeda, T., Nishida, K., Kawamura, T., Margerin, L., Menina, S., Lognonné, P., Banerdt, W.B., 2023. Seismic Scattering and Absorption Properties of Mars Estimated Through Coda Analysis on a Long-Period Surface Wave of S1222a Marsquake. *Geophysical Research Letters 50*, e2022GL102716. https://doi.org/10.1029/2022GL102716

Phillips, D.H., Lannutti, J.J., 1997. Measuring physical density with X-ray computed tomography. *NDT & E International 30*, 339–350. https://doi.org/10.1016/S0963-8695(97)00020-0

Poch, O., Pommerol, A., Jost, B., Carrasco, N., Szopa, C., Thomas, N., 2016. Sublimation of water ice mixed with silicates and tholins: Evolution of surface texture and reflectance spectra, with implications for comets. *Icarus 267*, 154–173. https://doi.org/10.1016/j.icarus.2015.12.017

Pope, C.G., 1997. X-Ray Diffraction and the Bragg Equation. *J. Chem. Educ. 74*, 129. https://doi.org/10.1021/ed074p129

Porco, C.C., Baker, E., Barbara, J., Beurle, K., Brahic, A., Burns, J.A., Charnoz, S., Cooper, N., Dawson, D.D., Del Genio, A.D., Denk, T., Dones, L., Dyudina, U., Evans, M.W., Fussner, S., Giese, B., Grazier, K., Helfenstein, P., Ingersoll, A.P., Jacobson, R.A., Johnson, T.V., McEwen, A., Murray, C.D., Neukum, G., Owen, W.M., Perry, J., Roatsch, T., Spitale, J., Squyres, S., Thomas, P., Tiscareno, M., Turtle, E.P., Vasavada, A.R., Veverka, J., Wagner, R., West, R., 2005. Imaging of Titan from the Cassini spacecraft. *Nature 434*, 159–168. https://doi.org/10.1038/nature03436

Qasim, A.M., Ruan, Q., Fu, R.K.Y., Ali, F., Mehrjou, B., Wu, H., Liu, L., Wu, Z., Chu, P.K., 2019. Enhanced oxygen-induced properties of bulk oxygenated amorphous carbon films deposited with an anode layer ion source. *Vacuum 169*, 108915. https://doi.org/10.1016/j.vacuum.2019.108915

Rabbani, A., Schmitt, D.R., 2019. The longitudinal modulus of bitumen: Pressure and temperature dependencies. *GEOPHYSICS 84*, MR139–MR151. https://doi.org/10.1190/geo2018-0344.1

Radebaugh, J., Lorenz, R.D., Lunine, J.I., Wall, S.D., Boubin, G., Reffet, E., Kirk, R.L., Lopes, R.M., Stofan, E.R., Soderblom, L., Allison, M., Janssen, M., Paillou, P., Callahan, P., Spencer, C., The Cassini Radar Team, 2008. Dunes on Titan observed by Cassini Radar. *Icarus 194*, 690–703. https://doi.org/10.1016/j.icarus.2007.10.015

Radebaugh, J., Lorenz, R.D., Wall, S.D., Kirk, R.L., Wood, C.A., Lunine, J.I., Stofan, E.R., Lopes, R.M.C., Valora, P., Farr, T.G., Hayes, A., Stiles, B., Mitri, G., Zebker, H., Janssen, M., Wye, L., LeGall, A., Mitchell, K.L., Paganelli, F., West, R.D., Schaller, E.L., 2011. Regional geomorphology and history of Titan's Xanadu province. *Icarus 211*, 672–685. https://doi.org/10.1016/j.icarus.2010.07.022

Rahman, Md.A., Soin, N., Maguire, P., D'Sa, R.A., Roy, S.S., Mahony, C.M.O., Lemoine, P., McCann, R., Mitra, S.K., McLaughlin, J.A.D., 2011. Structural and surface energy analysis of nitrogenated ta-C films. *Thin Solid Films 520*, 294–301. https://doi.org/10.1016/j.tsf.2011.06.031

Rannou, P., Hourdin, F., McKay, C.P., Luz, D., 2004. A coupled dynamics-microphysics model of Titan's atmosphere. *Icarus 170*, 443–462. https://doi.org/10.1016/j.icarus.2004.03.007

Rannou, P., McKay, C.P., Lorenz, R.D., 2003. A model of Titan's haze of fractal aerosols constrained by multiple observations. *Planetary and Space Science 51*, 963–976. https://doi.org/10.1016/j.pss.2003.05.008

Rannou, P., Montmessin, F., Hourdin, F., Lebonnois, S., 2006. The Latitudinal Distribution of Clouds on Titan. *Science 311*, 201–205. https://doi.org/10.1126/science.1118424

Rannou, P., Toledo, D., Lavvas, P., D'Aversa, E., Moriconi, M.L., Adriani, A., Le Mouélic, S., Sotin, C., Brown, R., 2016. Titan's surface spectra at the Huygens landing site and Shangri-La. *Icarus 270*, 291–306. https://doi.org/10.1016/j.icarus.2015.09.016

Richeton, J., Schlatter, G., Vecchio, K.S., Rémond, Y., Ahzi, S., 2005. A unified model for stiffness modulus of amorphous polymers across transition temperatures and strain rates. *Polymer (Guildf.) 46*, 8194–8201. https://doi.org/10.1016/j.polymer.2005.06.103

Richter, A., Ries, R., Smith, R., Henkel, M., Wolf, B., 2000. Nanoindentation of diamond, graphite and fullerene films. *Diamond and Related Materials 9*, 170–184. https://doi.org/10.1016/S0925-9635(00)00188-6

Rodriguez, S., Garcia, A., Lucas, A., Appéré, T., Le Gall, A., Reffet, E., Le Corre, L., Le Mouélic, S., Cornet, T., Courrech Du Pont, S., Narteau, C., Bourgeois, O., Radebaugh, J., Arnold, K., Barnes, J.W., Stephan, K., Jaumann, R., Sotin, C., Brown, R.H., Lorenz, R.D., Turtle, E.P., 2014. Global mapping and characterization of Titan's dune fields with Cassini: Correlation between RADAR and VIMS observations. *Icarus 230*, 168–179. https://doi.org/10.1016/j.icarus.2013.11.017

Rouxel, T., 2007. Elastic Properties and Short-to Medium-Range Order in Glasses. *Journal of the American Ceramic Society 90*, 3019–3039. https://doi.org/10.1111/j.1551-2916.2007.01945.x

Rubin, D.M., Hesp, P.A., 2009. Multiple origins of linear dunes on Earth and Titan. *Nature Geosci 2*, 653–658. https://doi.org/10.1038/ngeo610

Sader, J., Chon, J., Mulvaney, P., 1999. Calibration of rectangular atomic force microscope cantilevers. *Review of Scientific Instruments 70*, 3967–3969. https://doi.org/10.1063/1.1150021

Sader, J.E., Larson, I., Mulvaney, P., White, L.R., 1995. Method for the calibration of atomic force microscope cantilevers. *Rev. Sci. Instrum. 66*, 3789–3798. https://doi.org/10.1063/1.1145439

Sagan, C., Chyba, C., 1997. The Early Faint Sun Paradox: Organic Shielding of Ultraviolet-Labile Greenhouse Gases. *Science 276*, 1217–1221. https://doi.org/10.1126/science.276.5316.1217

Sagan, C., Thompson, W.R., Khare, B.N., 1992. Titan: a laboratory for prebiological organic chemistry. *Acc. Chem. Res. 25*, 286–292. https://doi.org/10.1021/ar00019a003

Schneider, T., Graves, S.D.B., Schaller, E.L., Brown, M.E., 2012. Polar methane accumulation and rainstorms on Titan from simulations of the methane cycle. *Nature 481*, 58–61. https://doi.org/10.1038/nature10666

Schoenfeld, A.M., Lopes, R.M.C., Malaska, M.J., Solomonidou, A., Williams, D.A., Birch, S.P.D., Hayes, A.G., Corlies, P., Le Gall, A., Janssen, M.A., Le Mouélic, S., Turtle, E., Florence, M., Verlander, T., 2021. Geomorphological map of the South Belet Region of Titan. *Icarus 366*, 114516. https://doi.org/10.1016/j.icarus.2021.114516

Schultrich, B., Scheibe, H.-J., Grandremy, G., Drescher, D., Schneider, D., 1996. Elastic modulus as a measure of diamond likeness and hardness of amorphous carbon films. *Diamond and Related Materials 5*, 914–918. https://doi.org/10.1016/0925-9635(95)00439-4

Schulz, F., Maillard, J., Kaiser, K., Schmitz-Afonso, I., Gautier, T., Afonso, C., Carrasco, N., Gross, L., 2021. Imaging Titan's Organic Haze at Atomic Scale. *ApJL 908*, L13. https://doi.org/10.3847/2041-8213/abd93e

Schönecker, S., Li, X., Johansson, B., Kwon, S.K., Vitos, L., 2015. Thermal surface free energy and stress of iron. *Sci Rep 5*, 14860. https://doi.org/10.1038/srep14860

Sekimoto, Y., Tsutsui S., Min-Cherl, J. and Nakamura M., 2019. Analysis of Phonon Propagation Velocity in Inelastic X-ray Scattering of Carbon Nanotube Composite Yarn with High Thermal Conductivity Using Inelastic X-ray Scattering. *SPring-8/SACLA Science Research Report*.

Sekine, Y., Genda, H., Kamata, S., Funatsu, T., 2017. The Charon-forming giant impact as a source of Pluto's dark equatorial regions. *Nat Astron 1*, 0031. https://doi.org/10.1038/s41550-016-0031

Sekine, Y., Genda, H., Sugita, S., Kadono, T., Matsui, T., 2011. Replacement and late formation of atmospheric N2 on undifferentiated Titan by impacts. *Nature Geosci 4*, 359–362. https://doi.org/10.1038/ngeo1147

Sekine, Y., Imanaka, H., Matsui, T., Khare, B.N., Bakes, E.L.O., McKay, C.P., Sugita, S., 2008. The role of organic haze in Titan's atmospheric chemistry. *Icarus 194*, 186–200. https://doi.org/10.1016/j.icarus.2007.08.031

Sekine, Y., Kodama, K., Kobayashi, T., Obata, S., Chang, Y., Ogawa, N.O., Takano, Y., Ohkouchi, N., Saiki, K., Sekine, T., 2018. An experimental study on impact-induced alterations of planetary organic simulants. *Meteorit & Planetary Scien 53*, 1267–1282. https://doi.org/10.1111/maps.13075

Sette, F., Krisch, M.H., Masciovecchio, C., Ruocco, G., Monaco, G., 1998. Dynamics of Glasses and Glass-Forming Liquids Studied by Inelastic X-ray Scattering. *Science 280*, 1550–1555. https://doi.org/10.1126/science.280.5369.1550

Shao, Y., Lu, H., 2000. A simple expression for wind erosion threshold friction velocity. *J. Geophys. Res. 105*, 22437–22443. https://doi.org/10.1029/2000JD900304

Shaw, G.H., 1986. Elastic properties and equation of state of high pressure ice. *The Journal of Chemical Physics 84*, 5862–5868. https://doi.org/10.1063/1.449897

Shibazaki, Y., Ohtani, E., Fukui, H., Sakai, T., Kamada, S., Ishikawa, D., Tsutsui, S., Baron, A.Q.R., Nishitani, N., Hirao, N., Takemura, K., 2012. Sound velocity measurements in dhcp-FeH up to 70 GPa with inelastic X-ray scattering: Implications for the composition of the Earth's core. *Earth and Planetary Science Letters 313–314*, 79–85. https://doi.org/10.1016/j.epsl.2011.11.002

Shirai, K., 2013. Temperature Dependence of Young's Modulus of Silicon. *Jpn. J. Appl. Phys. 52*, 088002. https://doi.org/10.7567/JJAP.52.088002

Soderblom, L.A., Kirk, R.L., Lunine, J.I., Anderson, J.A., Baines, K.H., Barnes, J.W., Barrett, J.M., Brown, R.H., Buratti, B.J., Clark, R.N., Cruikshank, D.P., Elachi, C., Janssen, M.A., Jaumann, R., Karkoschka, E., Mouélic, S.L., Lopes, R.M., Lorenz, R.D., McCord, T.B., Nicholson, P.D., Radebaugh, J., Rizk, B., Sotin, C., Stofan, E.R., Sucharski, T.L., Tomasko, M.G., Wall, S.D., 2007. Correlations between Cassini VIMS spectra and RADAR SAR images: Implications for Titan's surface composition and the character of

the Huygens Probe Landing Site. *Planetary and Space Science 55*, 2025–2036. https://doi.org/10.1016/j.pss.2007.04.014

Solomonidou, A., Coustenis, A., Lopes, R.M.C., Malaska, M.J., Rodriguez, S., Drossart, P., Elachi, C., Schmitt, B., Philippe, S., Janssen, M., Hirtzig, M., Wall, S., Sotin, C., Lawrence, K., Altobelli, N., Bratsolis, E., Radebaugh, J., Stephan, K., Brown, R.H., Le Mouélic, S., Le Gall, A., Villanueva, E.V., Brossier, J.F., Bloom, A.A., Witasse, O., Matsoukas, C., Schoenfeld, A., 2018. The Spectral Nature of Titan's Major Geomorphological Units: Constraints on Surface Composition. *J. Geophys. Res. Planets 123*, 489–507. https://doi.org/10.1002/2017JE005477

Sotin, C., Jaumann, R., Buratti, B., Brown, R.H., Clark, R.N., Soderblom, L., Baines, K., Bellucci, G., Bibring, J., Capaccioni, F., Cerroni, P., Combes, M., Coradini, A., Cruikshank, D., Drossart, P., Formisano, V., Langevin, Y., Matson, D.L., McCord, T., Nelson, R.M., Nicholson, P., Sicardy, B., Lemouélic, S., Rodriguez, S., Stephan, K., Scholz, C., 2005. Release of volatiles from a possible cryovolcano from near-infrared imaging of Titan. *Nature 435*, 786–789. https://doi.org/10.1038/nature03596

Sotin, C., Lawrence, K.J., Reinhardt, B., Barnes, J.W., Brown, R.H., Hayes, A.G., Le Mouélic, S., Rodriguez, S., Soderblom, J.M., Soderblom, L.A., Baines, K.H., Buratti, B.J., Clark, R.N., Jaumann, R., Nicholson, P.D., Stephan, K., 2012. Observations of Titan's Northern lakes at 5μm: Implications for the organic cycle and geology. *Icarus 221*, 768–786. https://doi.org/10.1016/j.icarus.2012.08.017

Spohn, T., Hudson, T.L., Witte, L., Wippermann, T., Wisniewski, L., Kedziora, B., Vrettos, C., Lorenz, R.D., Golombek, M., Lichtenheldt, R., Grott, M., Knollenberg, J., Krause, C., Fantinati, C., Nagihara, S., Grygorczuk, J., 2022. The InSight-HP3 mole on Mars: Lessons learned from attempts to penetrate to depth in the Martian soil. *Advances in Space Research 69*, 3140–3163. https://doi.org/10.1016/j.asr.2022.02.009

Stofan, E.R., Elachi, C., Lunine, J.I., Lorenz, R.D., Stiles, B., Mitchell, K.L., Ostro, S., Soderblom, L., Wood, C., Zebker, H., Wall, S., Janssen, M., Kirk, R., Lopes, R., Paganelli, F., Radebaugh, J., Wye, L., Anderson, Y., Allison, M., Boehmer, R., Callahan, P., Encrenaz, P., Flamini, E., Francescetti, G., Gim, Y., Hamilton, G., Hensley, S., Johnson, W.T.K., Kelleher, K., Muhleman, D., Paillou, P., Picardi, G., Posa, F., Roth, L., Seu, R., Shaffer, S., Vetrella, S., West, R., 2007. The lakes of Titan. *Nature 445*, 61–64. https://doi.org/10.1038/nature05438

Stähler, S.C., Panning, M.P., Vance, S.D., Lorenz, R.D., van Driel, M., Nissen-Meyer, T., Kedar, S., 2018. Seismic Wave Propagation in Icy Ocean Worlds. *JGR Planets 123*, 206–232. https://doi.org/10.1002/2017JE005338

Sun, C.Q., 2007. Size dependence of nanostructures: Impact of bond order deficiency. *Progress in Solid State Chemistry 35*, 1–159. https://doi.org/10.1016/j.progsolidstchem.2006.03.001

Tambe, N.S., Bhushan, B., 2004. Scale dependence of micro/nano-friction and adhesion of MEMS/NEMS materials, coatings and lubricants. *Nanotechnology 15*, 1561–1570. https://doi.org/10.1088/0957-4484/15/11/033

Tan, S.P., Kargel, J.S., Marion, G.M., 2013. Titan's atmosphere and surface liquid: New calculation using Statistical Associating Fluid Theory. *Icarus 222*, 53–72. https://doi.org/10.1016/j.icarus.2012.10.032

Thomson, J.J., 1906. Conduction of electricity through gases. *Cambridge University Press*.

Tobie, G., Grasset, O., Lunine, J.I., Mocquet, A., Sotin, C., 2005. Titan's internal structure inferred from a coupled thermal-orbital model. *Icarus 175*, 496–502. https://doi.org/10.1016/j.icarus.2004.12.007

Tobie, G., Lunine, J.I., Sotin, C., 2006. Episodic outgassing as the origin of atmospheric methane on Titan. *Nature 440*, 61–64. https://doi.org/10.1038/nature04497

Tokano, T., 2002. Tidal Winds on Titan Caused by Saturn. *Icarus 158*, 499–515. https://doi.org/10.1006/icar.2002.6883

Tokano, T., 2008. Dune-forming winds on Titan and the influence of topography. *Icarus 194*, 243–262. https://doi.org/10.1016/j.icarus.2007.10.007

Tokano, T., 2010. Relevance of fast westerlies at equinox for the eastward elongation of Titan's dunes. *Aeolian Research 2*, 113–127. https://doi.org/10.1016/j.aeolia.2010.04.003

Toksöz, M.N., Cheng, C.H., Timur, A., 1976. Velocities of seismic waves in porous rocks. *Geophysics 41*, 621–645. https://doi.org/10.1190/1.1440639

Tomasko, M.G., West, R.A., 2009. Aerosols in Titan's Atmosphere, in: Titan from Cassini-Huygens. *Springer Netherlands, Dordrecht*, pp. 297–321. https://doi.org/10.1007/978-1-4020-9215-2_12

Trainer, M.G., Pavlov, A.A., DeWitt, H.L., Jimenez, J.L., McKay, C.P., Toon, O.B., Tolbert, M.A., 2006. Organic haze on Titan and the early Earth. *Proc. Natl. Acad. Sci. U.S.A. 103*, 18035–18042. https://doi.org/10.1073/pnas.0608561103

Turtle, E.P., Perry, J.E., Barbara, J.M., Del Genio, A.D., Rodriguez, S., Le Mouélic, S., Sotin, C., Lora, J.M., Faulk, S., Corlies, P., Kelland, J., MacKenzie, S.M., West, R.A., McEwen, A.S., Lunine, J.I., Pitesky, J., Ray, T.L., Roy, M., 2018. Titan's Meteorology Over the Cassini Mission: Evidence for Extensive Subsurface Methane Reservoirs. *Geophysical Research Letters 45*, 5320–5328. https://doi.org/10.1029/2018GL078170

Turtle, E.P., Perry, J.E., Hayes, A.G., Lorenz, R.D., Barnes, J.W., McEwen, A.S., West, R.A., Del Genio, A.D., Barbara, J.M., Lunine, J.I., Schaller, E.L., Ray, T.L., Lopes, R.M.C., Stofan, E.R., 2011. Rapid and Extensive Surface Changes Near Titan's Equator: Evidence of April Showers. *Science 331*, 1414–1417. https://doi.org/10.1126/science.1201063

Tyson, W.R., 1975. Surface energies of solid metals. *Canadian Metallurgical Quarterly 14*, 307–314. https://doi.org/10.1179/000844375795049997

Van Engers, C.D., Cousens, N.E.A., Babenko, V., Britton, J., Zappone, B., Grobert, N., Perkin, S., 2017. Direct Measurement of the Surface Energy of Graphene. *Nano Lett. 17*, 3815–3821. https://doi.org/10.1021/acs.nanolett.7b01181

Varshni, Y.P., 1970. Temperature Dependence of the Elastic Constants. *Phys. Rev. B 2*, 3952–3958. https://doi.org/10.1103/PhysRevB.2.3952

Wachtman, J.B., Tefft, W.E., Lam, D.G., Apstein, C.S., 1961. Exponential Temperature Dependence of Young's Modulus for Several Oxides. *Phys. Rev. 122*, 1754–1759. https://doi.org/10.1103/PhysRev.122.1754

Wada, K., Tanaka, H., Okuzumi, S., Kobayashi, H., Suyama, T., Kimura, H., Yamamoto, T., 2013. Growth efficiency of dust aggregates through collisions with high mass ratios. *A&A 559*, A62. https://doi.org/10.1051/0004-6361/201322259

Waite, J.H., Young, D.T., Cravens, T.E., Coates, A.J., Crary, F.J., Magee, B., Westlake, J., 2007. The Process of Tholin Formation in Titan's Upper Atmosphere. *Science 316*, 870–875. https://doi.org/10.1126/science.1139727

Wall, S., Hayes, A., Bristow, C., Lorenz, R., Stofan, E., Lunine, J., Le Gall, A., Janssen, M., Lopes, R., Wye, L., Soderblom, L., Paillou, P., Aharonson, O., Zebker, H., Farr, T., Mitri, G., Kirk, R., Mitchell, K., Notarnicola, C., Casarano, D., Ventura, B., 2010. Active shoreline of Ontario Lacus, Titan: A morphological study of the lake and its surroundings. *Geophysical Research Letters 37*, 2009GL041821. https://doi.org/10.1029/2009GL041821

Warren W. Dickinson (1), John D. Wa, 1994. Low Depositional Porosity in Eolian Sands and Sandstones, Namib Desert. *SEPM JSR Vol. 64A*. https://doi.org/10.1306/D4267D66-2B26-11D7-8648000102C1865D

Wasson, R.J., Hydet, R., 1983. Factors determining desert dune type., *Nature 304*, 337–339. https://doi.org/10.1038/304337a0

Wertheim, G.K., Butler, M.A., West, K.W., Buchanan, D.N.E., 1974. Determination of the Gaussian and Lorentzian content of experimental line shapes. *Review of Scientific Instruments 45*, 1369–1371. https://doi.org/10.1063/1.1686503

Wilson, E.H., Atreya, S.K., 2004. Current state of modeling the photochemistry of Titan's mutually dependent atmosphere and ionosphere. *J. Geophys. Res. 109*, 2003JE002181. https://doi.org/10.1029/2003JE002181

Wolf, E.T., Toon, O.B., 2010. Fractal Organic Hazes Provided an Ultraviolet Shield for Early Earth. *Science 328*, 1266–1268. https://doi.org/10.1126/science.1183260

Xie, J., Cao, J., Schmitt, D.R., Di, B., Xiao, L., Wang, X., Wang, K., Chen, Y., 2019. Effects of Kerogen Content on Elastic Properties-Based on Artificial Organic-Rich Shale (AORS). *JGR Solid Earth 124*, 12660–12678. https://doi.org/10.1029/2019JB017595

Xing, M., Pathak, A.-D., Sanyal, S., Peng, Q., Liu, X., Wen, X., 2020. Temperature-dependent surface free energy and the Wulff shape of iron and iron carbide nanoparticles: A molecular dynamics study. *Applied Surface Science 509*, 144859. https://doi.org/10.1016/j.apsusc.2019.144859

Xu, S., Flynn, D., Tay, B.K., Prawer, S., Nugent, K.W., Silva, S.R.P., Lifshitz, Y., Milne, W.I., 1997. Mechanical properties and Raman spectra of tetrahedral amorphous carbon films with high sp^3 fraction deposited using a filtered cathodic arc. *Philosophical Magazine B 76*, 351–361. https://doi.org/10.1080/01418639708241099

Yabuta, H. et al., 2023. Macromolecular organic matter in samples of the asteroid (162173) Ryugu., *Science 379*, eabn9057. https://doi.org/10.1126/science.abn9057

Yan, F., Han, D.-H., 2013. Measurement of elastic properties of kerogen, in: *SEG Technical Program Expanded Abstracts 2013*. Presented at the SEG Technical Program Expanded Abstracts 2013, Society of Exploration Geophysicists, p. SEG-2013. https://doi.org/10.1190/segam2013-1319.1

Yannas, I.V., Luise, R.R., 1982. Distinction between two molecular mechanisms for deformation of glassy amorphous polymers. *Journal of Macromolecular Science, Part B 21*, 443–474. https://doi.org/10.1080/00222348208018794

Yoneda, A., Fukui, H., Xu, F., Nakatsuka, A., Yoshiasa, A., Seto, Y., Ono, K., Tsutsui, S., Uchiyama, H., Baron, A.Q.R., 2014. Elastic anisotropy of experimental analogues of perovskite and post-perovskite help to interpret D″ diversity. *Nat Commun 5*, 3453. https://doi.org/10.1038/ncomms4453

Yu, X., He, C., Zhang, X., Hörst, S.M., Dymont, A.H., McGuiggan, P., Moses, J.I., Lewis, N.K., Fortney, J.J., Gao, P., Kempton, E.M.-R., Moran, S.E., Morley, C.V., Powell, D., Valenti, J.A., Vuitton, V., 2021. Haze evolution in temperate exoplanet atmospheres through surface energy measurements. *Nat Astron 5*, 822–831. https://doi.org/10.1038/s41550-021-01375-3

Yu, X., Hörst, S.M., He, C., McGuiggan, P., Bridges, N.T., 2017. Direct Measurement of Interparticle Forces of Titan Aerosol Analogs ("Tholin") Using Atomic Force Microscopy. *JGR Planets 122*, 2610–2622. https://doi.org/10.1002/2017JE005437

Yu, X., Hörst, S.M., He, C., McGuiggan, P., Crawford, B., 2018. Where Does Titan Sand Come From: Insight From Mechanical Properties of Titan Sand Candidates. *JGR Planets 123*, 2310–2321. https://doi.org/10.1029/2018JE005651

Yu, X., Hörst, S.M., He, C., McGuiggan, P., Kristiansen, K., Zhang, X., 2020. Surface Energy of the Titan Aerosol Analog "Tholin." *ApJ 905*, 88. https://doi.org/10.3847/1538-4357/abc55d

Yu, X., Yu, Y., Garver, J., Li, J., Hawthorn, A., Sciamma-O'Brien, E., Zhang, X., Barth, E., 2023. Material Properties of Organic Liquids, Ices, and Hazes on Titan. *ApJS 266*, 30. https://doi.org/10.3847/1538-4365/acc6cf

Yung, Y.L., Allen, M., Pinto, J.P., 1984. Photochemistry of the atmosphere of Titan - Comparison between model and observations. *ApJS 55*, 465. https://doi.org/10.1086/190963

Zahnle, K.J., Korycansky, D.G., Nixon, C.A., 2014. Transient climate effects of large impacts on Titan. *Icarus 229*, 378–391. https://doi.org/10.1016/j.icarus.2013.11.006

Zhang, W., Zhang, X., Edwards, B.W., Zhong, L., Gao, H., Malaska, M.J., Hodyss, R., Greer, J.R., 2022. Deformation characteristics of solid-state benzene as a step towards understanding planetary geology. *Nat Commun 13*, 7949. https://doi.org/10.1038/s41467-022-35647-x

Zhang, X., Strobel, D.F., Imanaka, H., 2017a. Haze heats Pluto's atmosphere yet explains its cold temperature. *Nature 551*, 352–355. https://doi.org/10.1038/nature24465

Zhang, Xuyao, Li, W., Kou, H., Shao, J., Deng, Y., Zhang, Xianhe, Ma, J., Li, Y., Zhang, Xin, 2019. Temperature and size dependent surface energy of metallic nano-materials. *Journal of Applied Physics 125*, 185105. https://doi.org/10.1063/1.5090301

Zhao, L., Qin, X., Han, D.-H., Geng, J., Yang, Z., Cao, H., 2016. Rock-physics modeling for the elastic properties of organic shale at different maturity stages. *GEOPHYSICS 81*, D527–D541. https://doi.org/10.1190/geo2015-0713.1

Zhao, Q., Liu, Y., Abel, E.W., 2004. Effect of temperature on the surface free energy of amorphous carbon films. *Journal of Colloid and Interface Science 280*, 174–183. https://doi.org/10.1016/j.jcis.2004.07.004

Appendix A. Fitting results of IXS spectra in Chapter 4

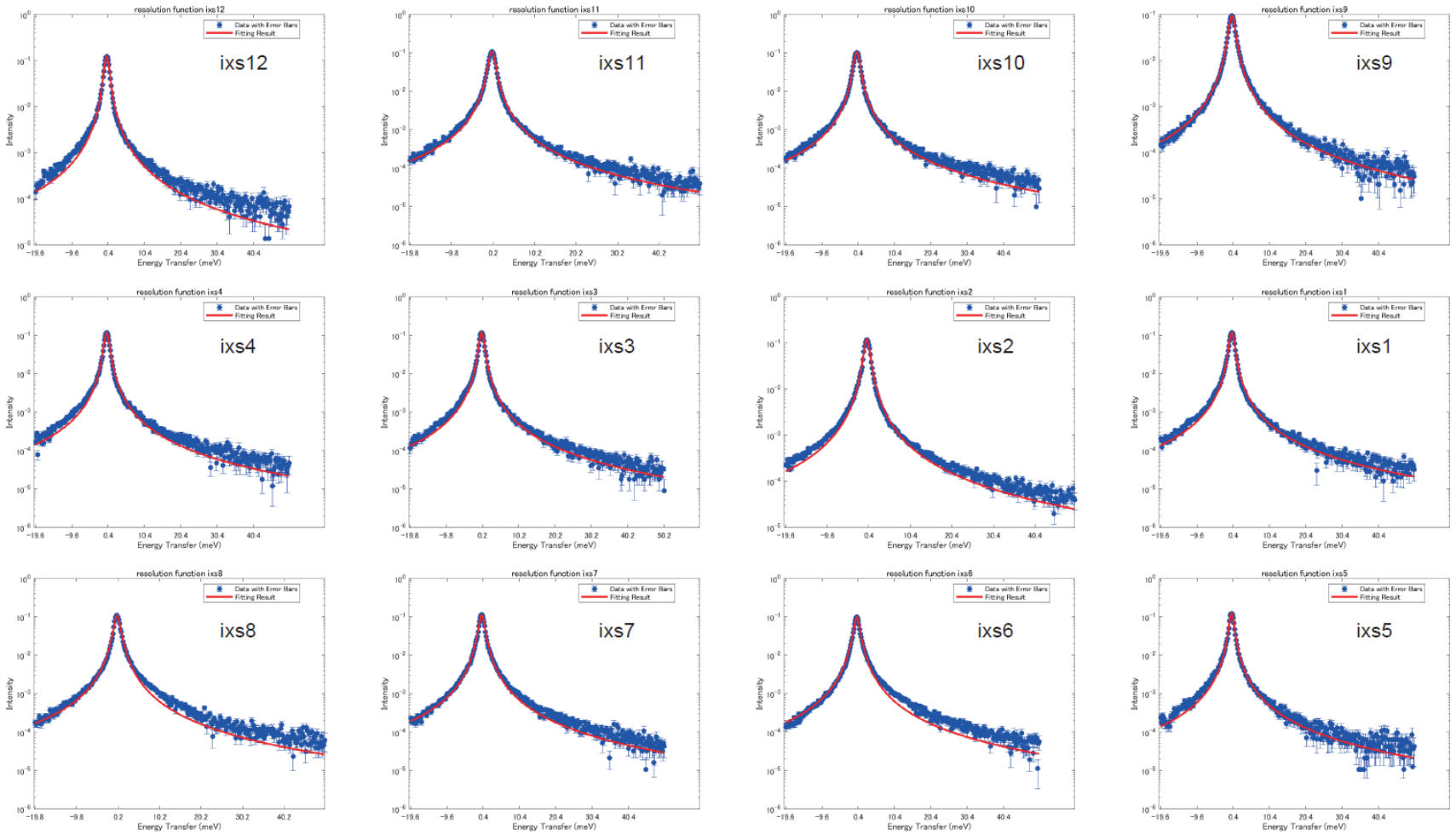

Figure A.1 The fitting results for resolution function measured using scattering from borosilicate glass (Tempax) (Ishikawa & Baron, 2021) in setup B are presented. The red line represents the result of the least-squares fitting of Eq. (4.9), whereas the blue circles with errors show data point.

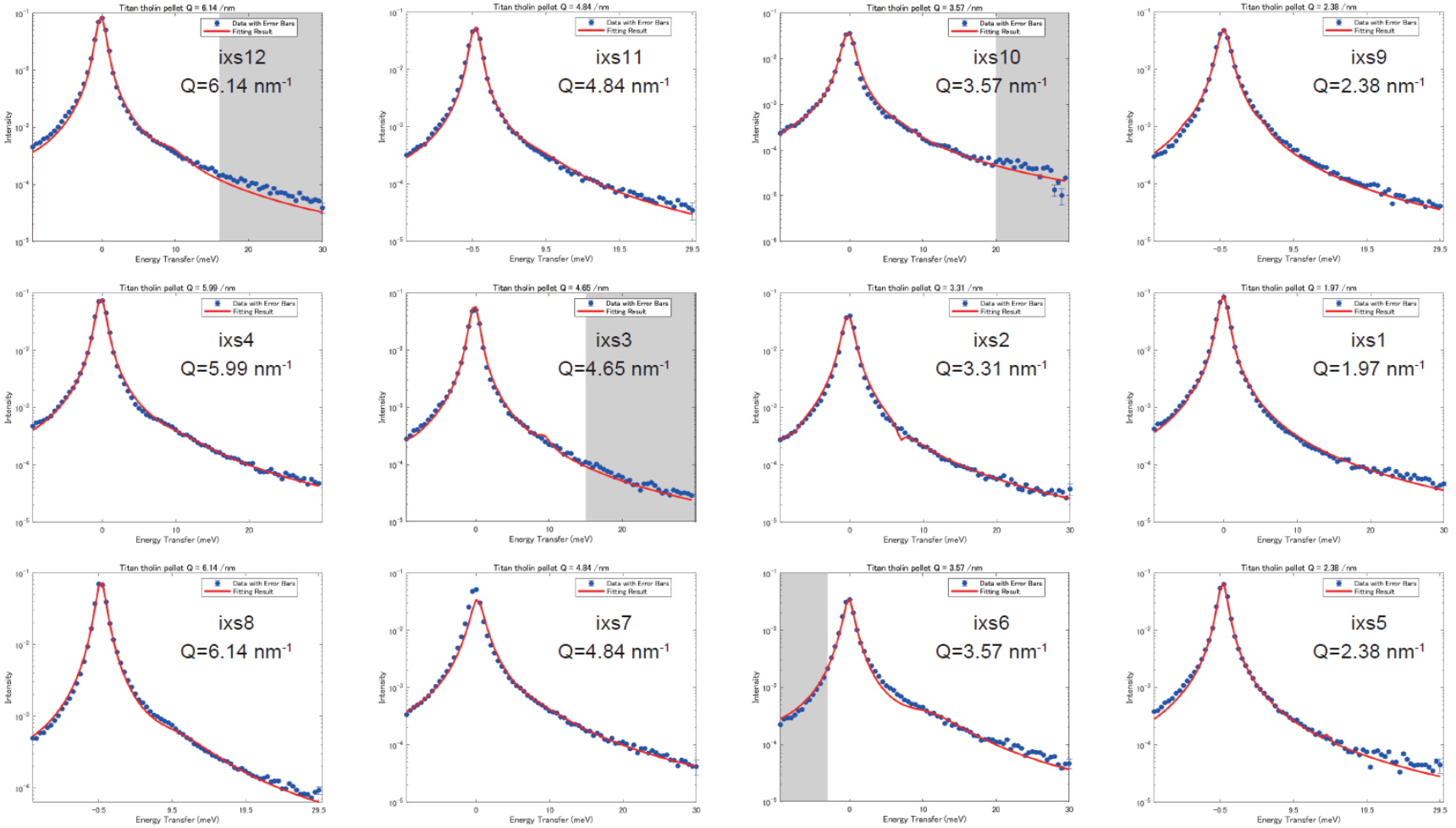

Figure A.2 The fitting results for Run #7 in Chapter 4 (Titan tholin B in setup B, measured at 93 K with a scattering angle of 2θ = 2.062° and an energy scan range from -10 to 30 meV) are presented. The values of the momentum transfer are indicated within each figure. The red line represents the result of least-squares fitting of Eqs. (4.9–12), assuming a finite value of $\Delta\omega$, whereas the blue circles with errors show data point. The spectra of ixs1, ixs2, ixs5, ixs6, ixs7, and ixs8 were excluded from the phonon dispersion data because their results were suspicious or could not be analyzed.

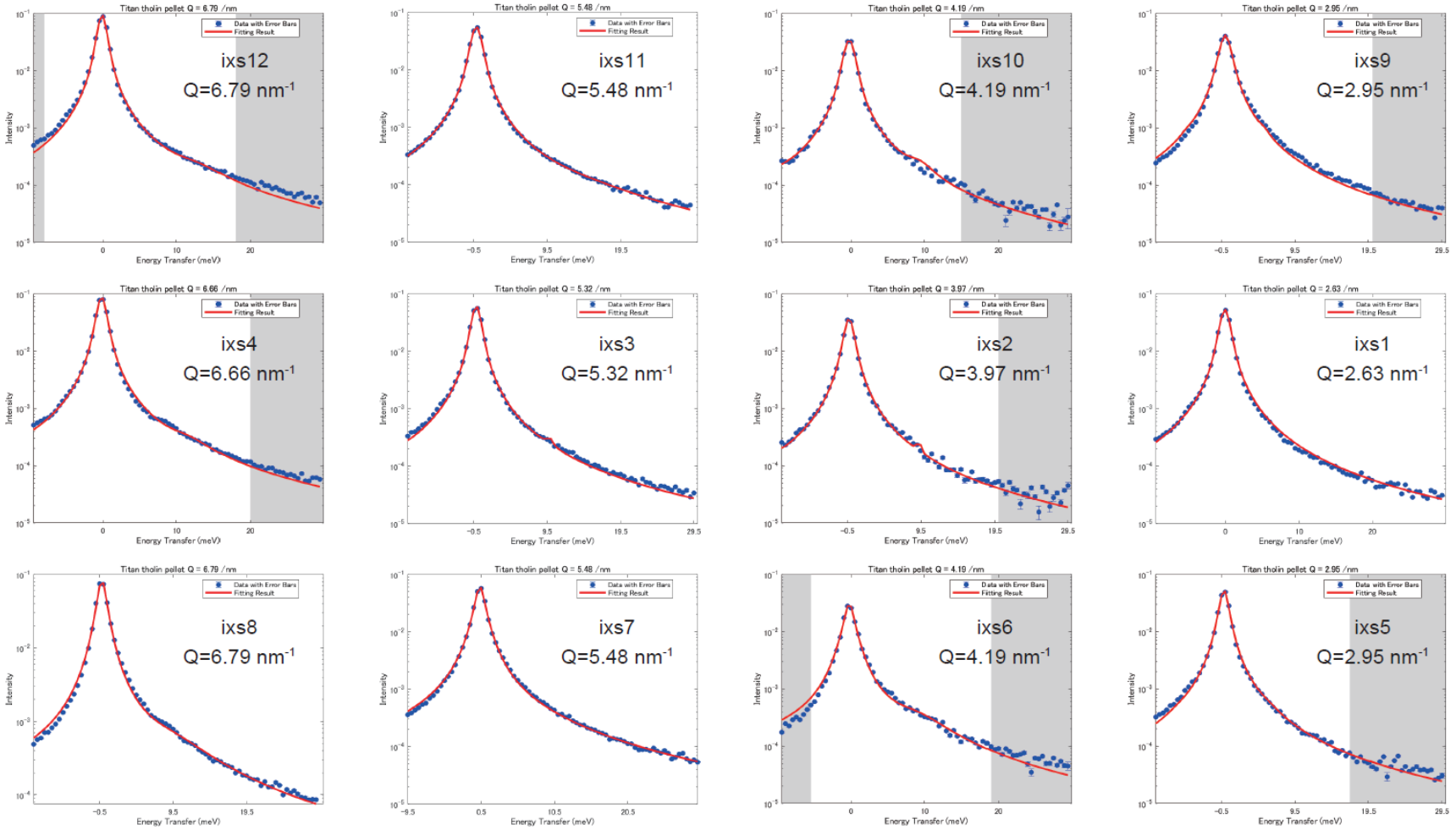

Figure A.3 The fitting results for Run #7 in Chapter 4 (Titan tholin B in setup B, measured at 93 K with a scattering angle of 2θ = 2.409° and an energy scan range from -10 to 30 meV) are presented. The values of the momentum transfer are indicated within each figure. The red line represents the result of least-squares fitting of Eqs. (4.9–12), assuming a finite value of $\Delta\omega$, whereas the blue circles with errors show data point. The spectra of ixs1, ixs2, ixs4, ixs5, ixs6, ixs7, ixs11 and ixs12 were excluded from the phonon dispersion data because their results were suspicious or could not be analyzed.

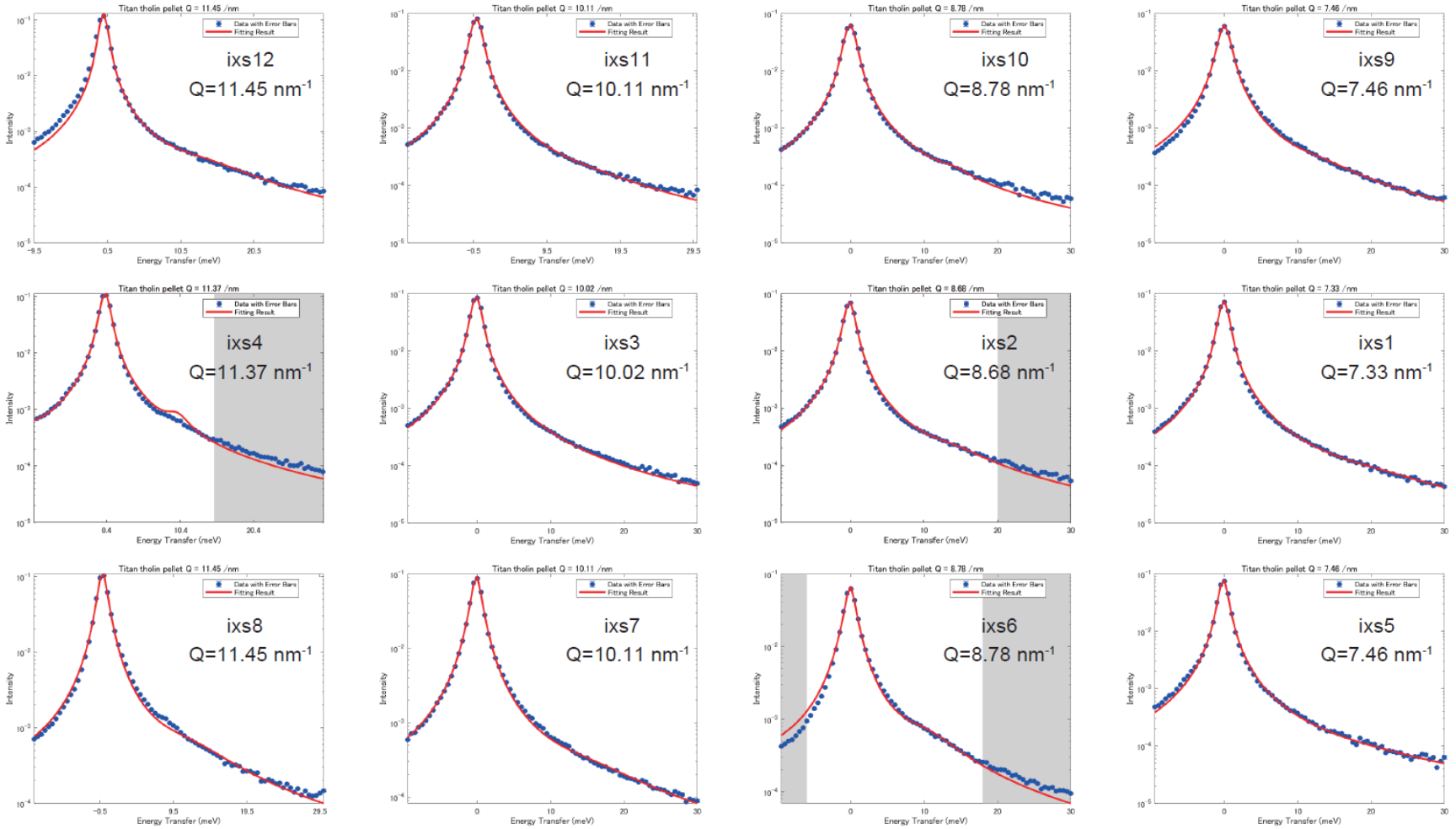

Figure A.4 The fitting results for Run #7 in Chapter 4 (Titan tholin B in setup B, measured at 93 K with a scattering angle of 2θ = 4.861° and an energy scan range from -10 to 40 meV) are presented. The values of the momentum transfer are indicated within each figure. The red line represents the result of least-squares fitting of Eqs. (4.9–12), assuming a finite value of $\Delta\omega$, whereas the blue circles with errors show data point. The spectra of ixs1, ixs5, ixs6, ixs8, ixs9, ixs11 and ixs12 were excluded from the phonon dispersion data because their results were suspicious or could not be analyzed.

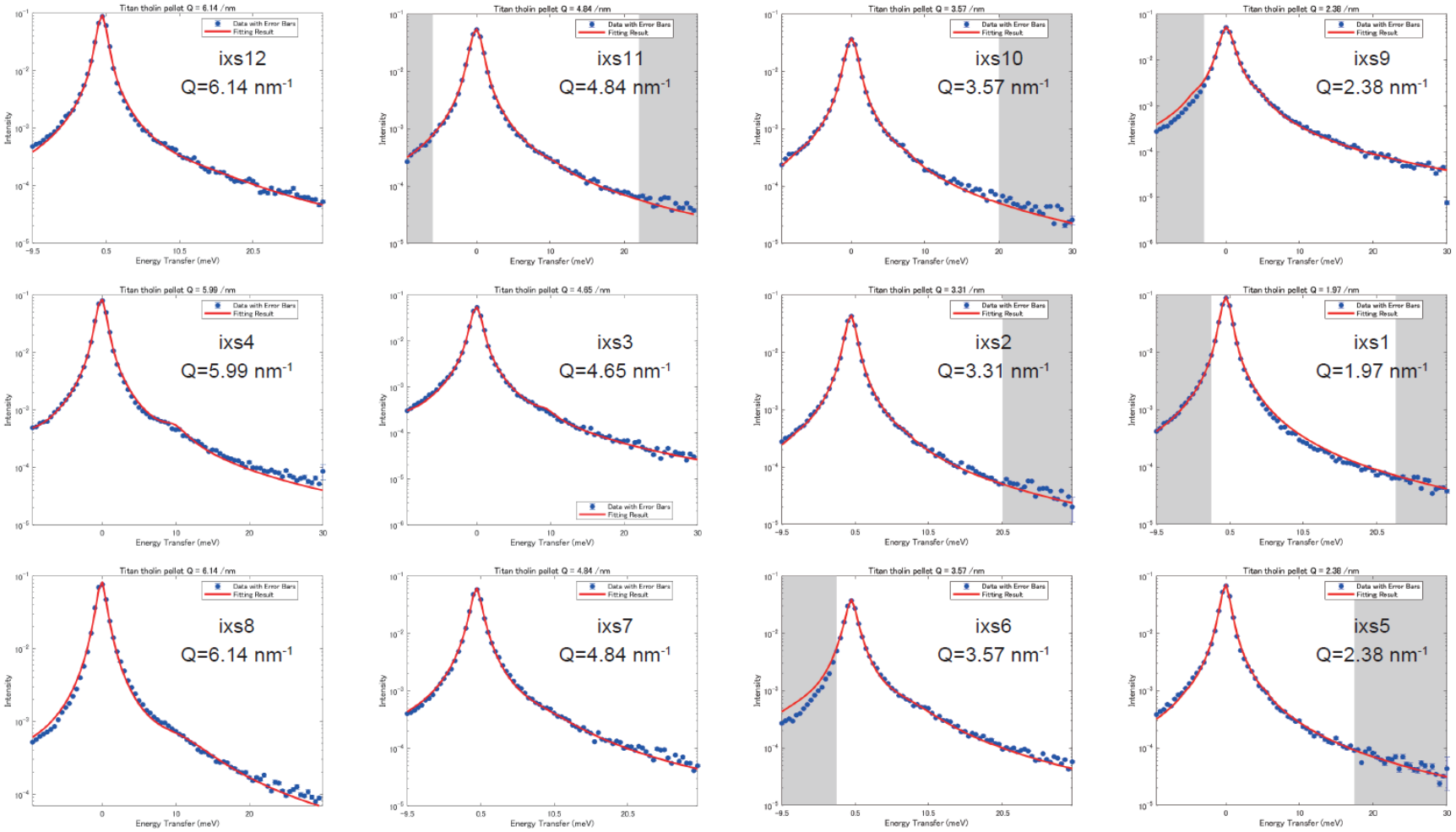

Figure A.5 The fitting results for Run #15 in Chapter 4 (Titan tholin B in setup B, measured at 140 K with a scattering angle of 2θ = 2.062° and an energy scan range from -10 to 30 meV) are presented. The values of the momentum transfer are indicated within each figure. The red line represents the result of least-squares fitting of Eqs. (4.9–12), assuming a finite value of $\Delta\omega$, whereas the blue circles with errors show data point. The spectra of ixs1, ixs6, ixs8, ixs9, ixs11 and ixs12 were excluded from the phonon dispersion data because their results were suspicious or could not be analyzed.

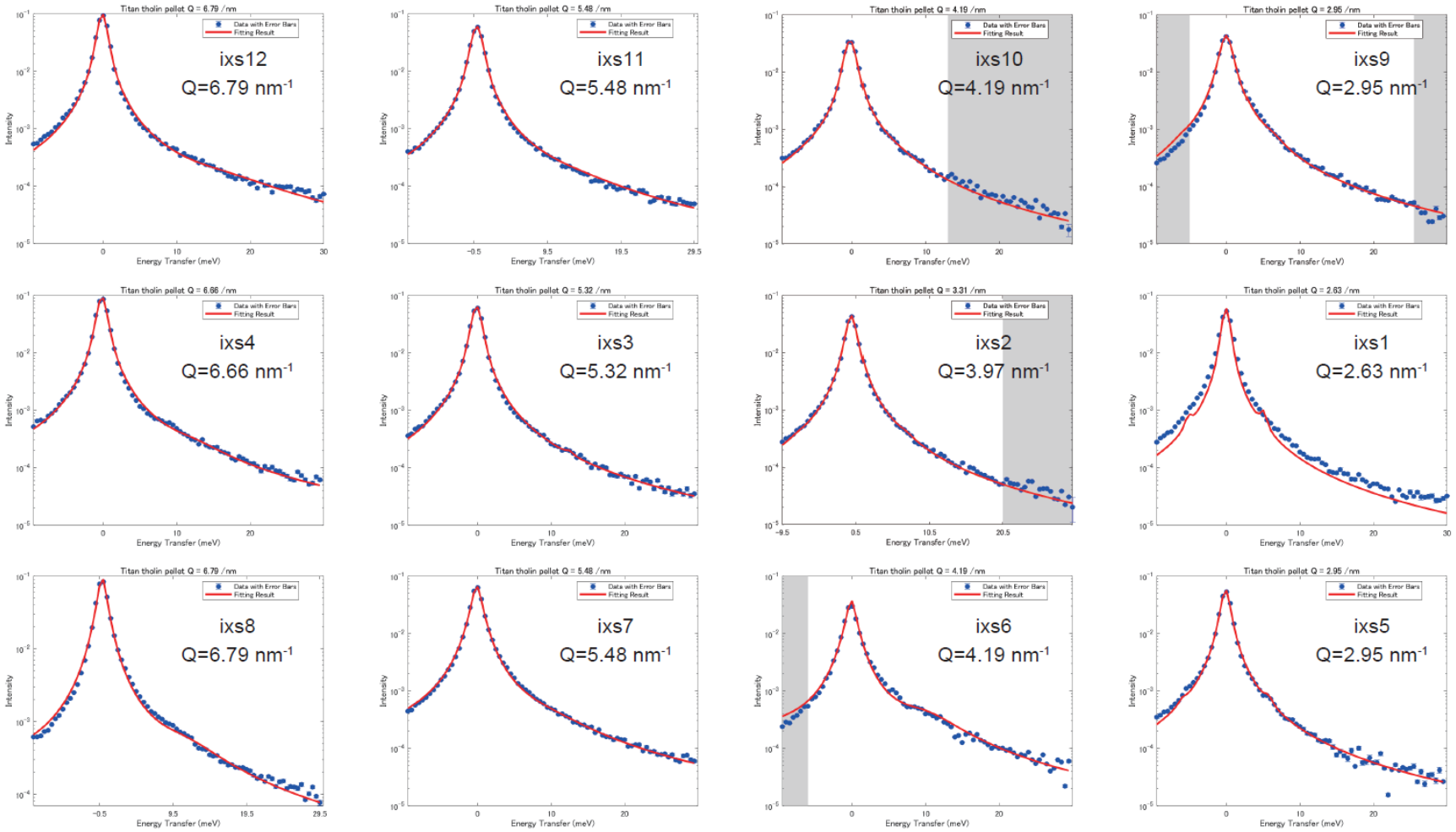

Figure A.6 The fitting results for Run #15 in Chapter 4 (Titan tholin B in setup B, measured at 140 K with a scattering angle of 2θ = 2.409° and an energy scan range from -10 to 30 meV) are presented. The values of the momentum transfer are indicated within each figure. The red line represents the result of least-squares fitting of Eqs. (4.9–12), assuming a finite value of $\Delta\omega$, whereas the blue circles with errors show data point. The spectra of ixs1, ixs2, ixs6, ixs8, and ixs9, were excluded from the phonon dispersion data because their results were suspicious or could not be analyzed.

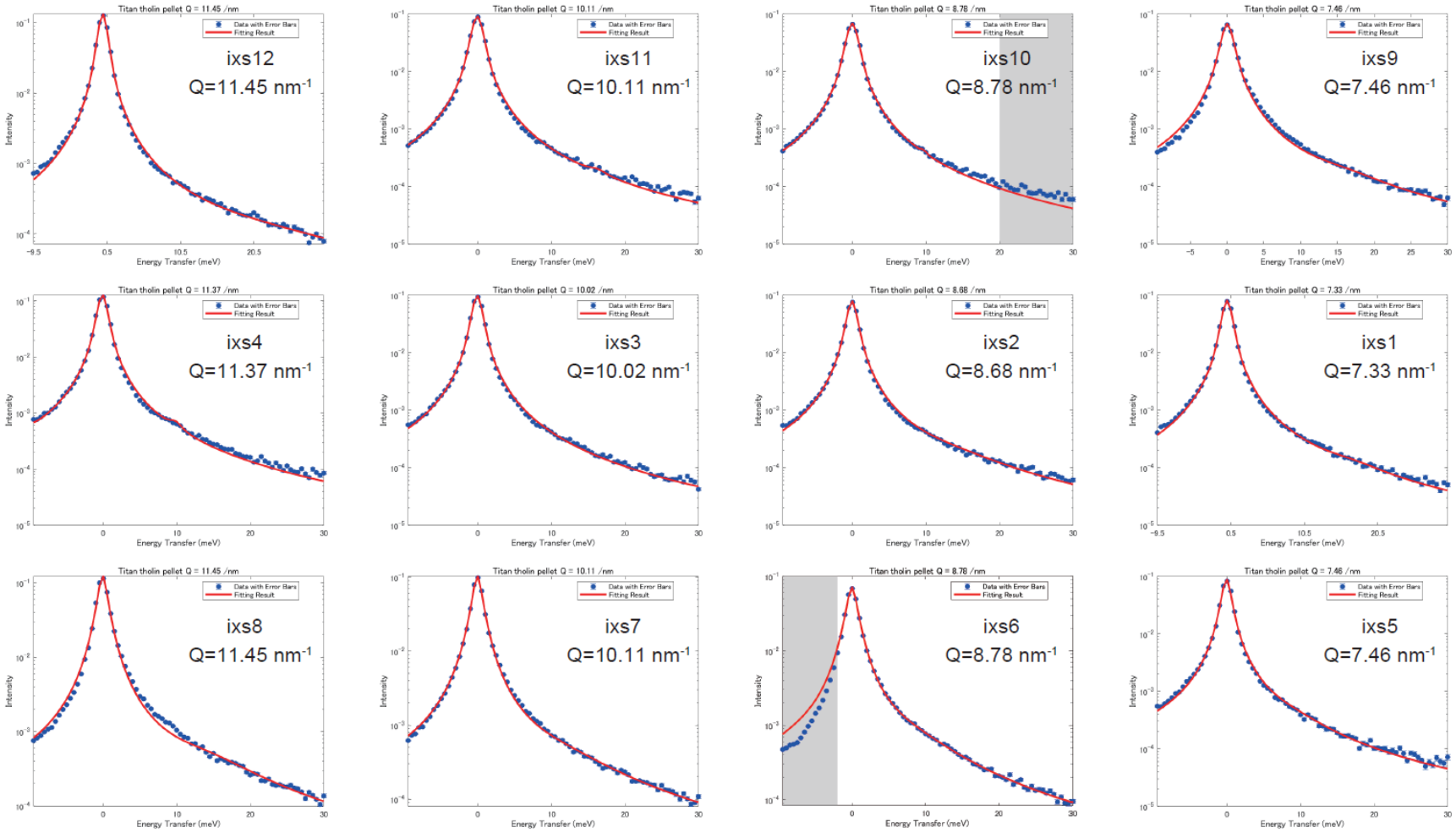

Figure A.7 The fitting results for Run #15 in Chapter 4 (Titan tholin B in setup B, measured at 140 K with a scattering angle of 2θ = 4.861° and an energy scan range from -10 to 40 meV) are presented. The values of the momentum transfer are indicated within each figure. The red line represents the result of least-squares fitting of Eqs. (4.9–12), assuming a finite value of $\Delta\omega$, whereas the blue circles with errors show data point. The spectra of ixs1, ixs2, ixs3, ixs5, ixs6, ixs8, ixs9, ixs10 and ixs12 were excluded from the phonon dispersion data because their results were suspicious or could not be analyzed.

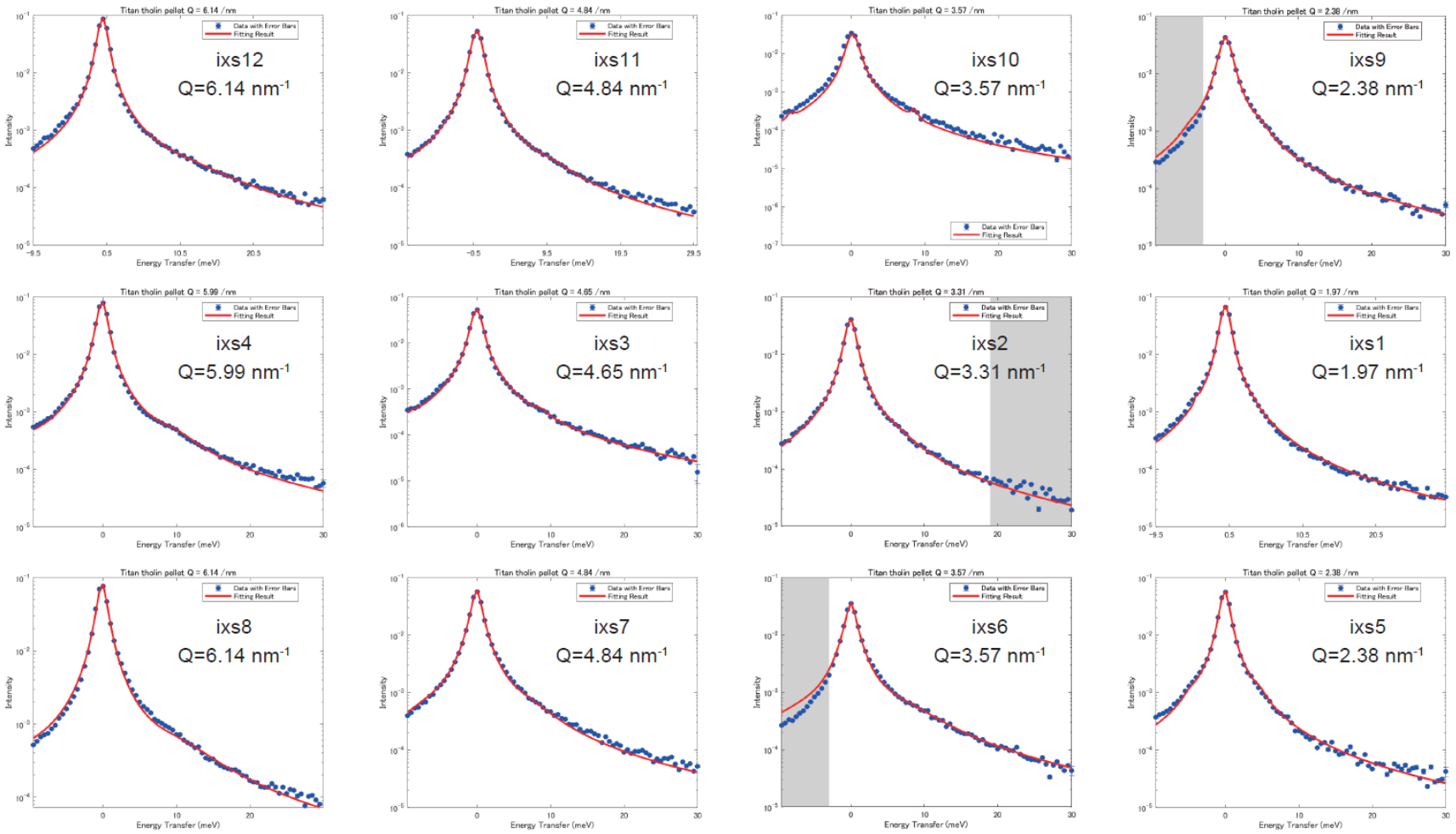

Figure A.8 The fitting results for Run #13 in Chapter 4 (Titan tholin B in setup B, measured at 190 K with a scattering angle of 2θ = 2.062° and an energy scan range from -10 to 30 meV) are presented. The values of the momentum transfer are indicated within each figure. The red line represents the result of least-squares fitting of Eqs. (4.9–12), assuming a finite value of $\Delta\omega$, whereas the blue circles with errors show data point. The spectra of ixs6, ixs8, ixs9, and ixs10 were excluded from the phonon dispersion data because their results were suspicious or could not be analyzed.

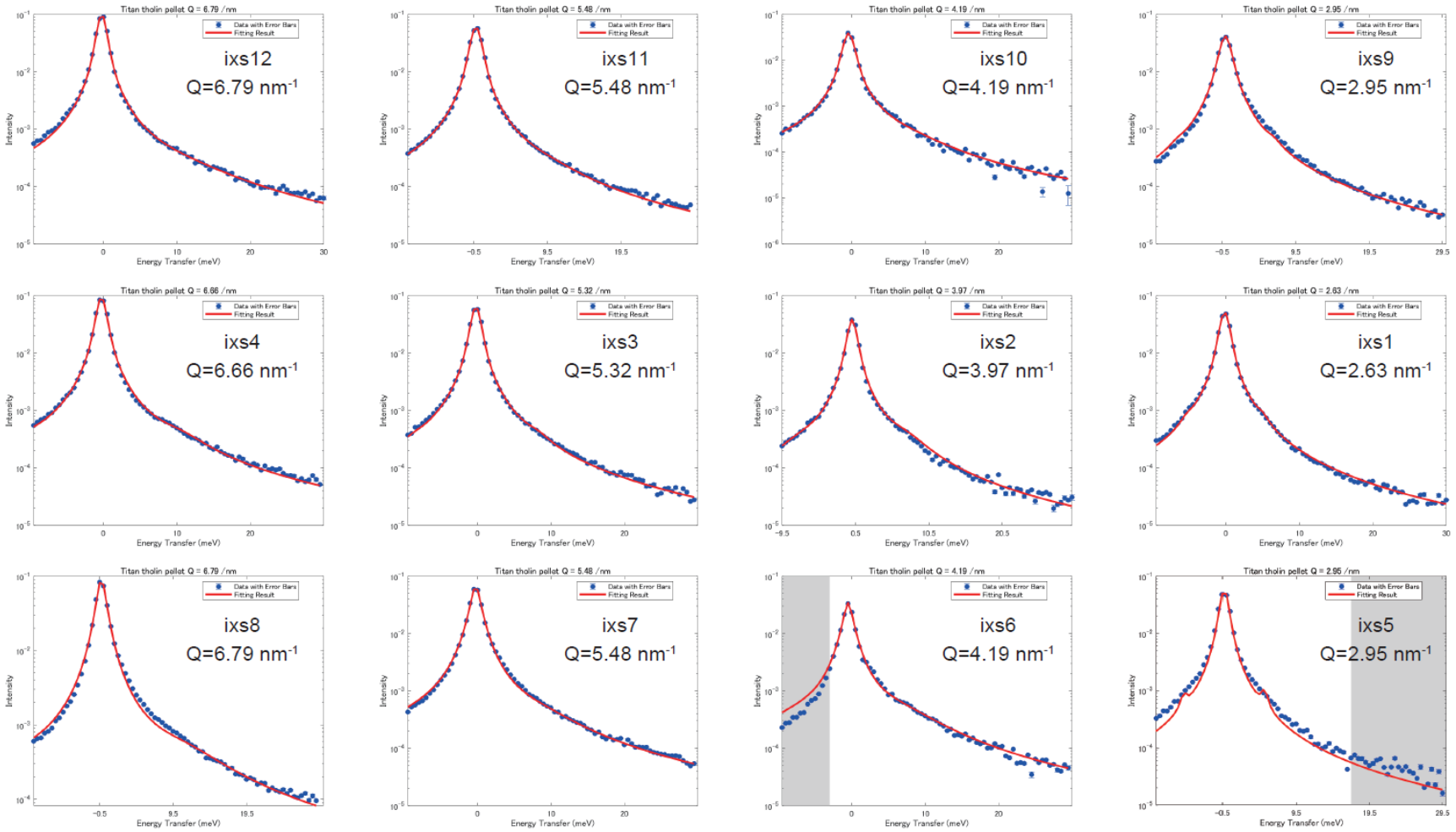

Figure A.9 The fitting results for Run #13 in Chapter 4 (Titan tholin B in setup B, measured at 190 K with a scattering angle of 2θ = 2.409° and an energy scan range from -10 to 30 meV) are presented. The values of the momentum transfer are indicated within each figure. The red line represents the result of least-squares fitting of Eqs. (4.9–12), assuming a finite value of $\Delta\omega$, whereas the blue circles with errors show data point. The spectra of ixs5, ixs6, and ixs8 were excluded from the phonon dispersion data because their results were suspicious or could not be analyzed.

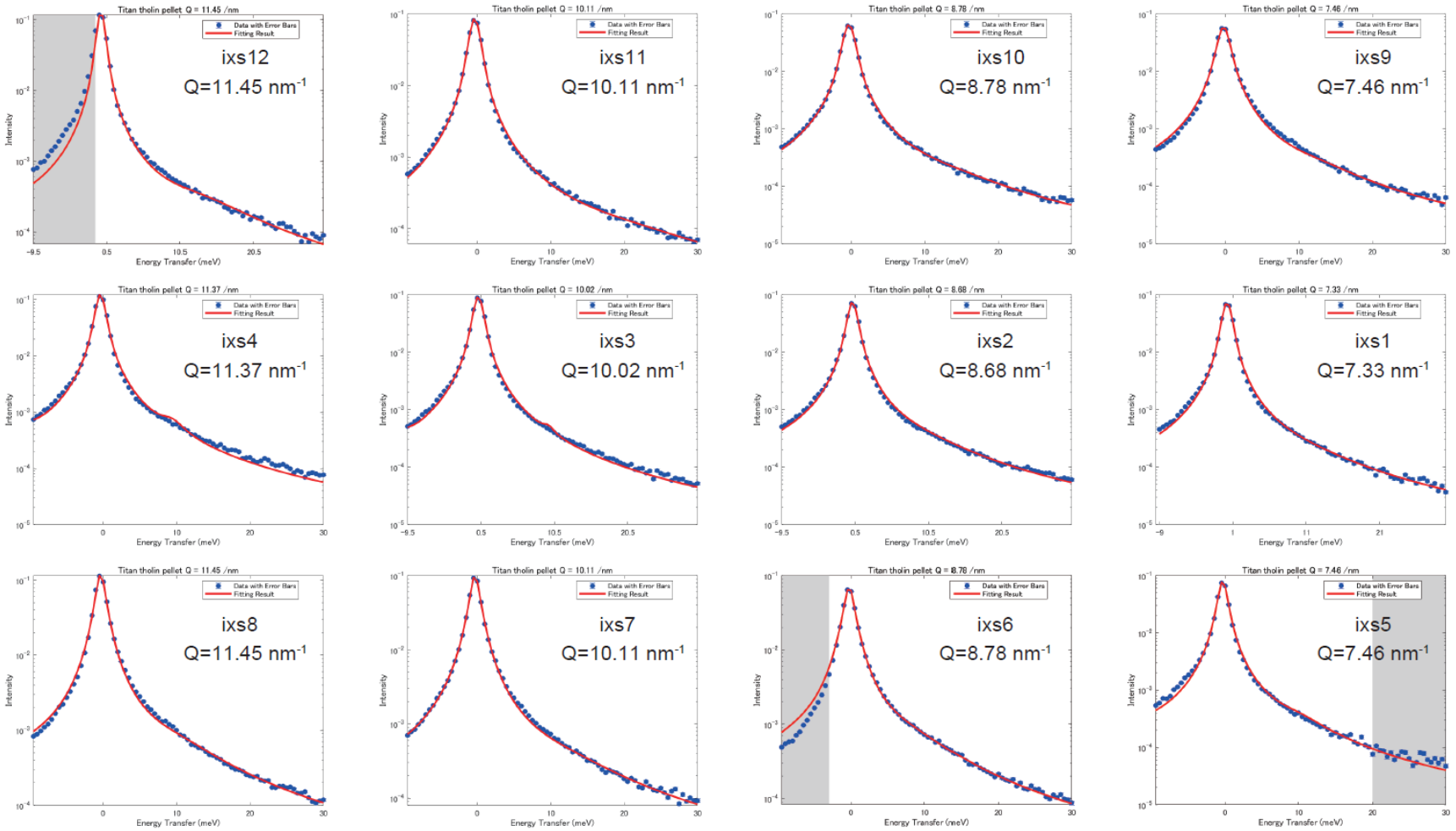

Figure A.10 The fitting results for Run #13 in Chapter 4 (Titan tholin B in setup B, measured at 190 K with a scattering angle of 2θ = 4.861° and an energy scan range from -10 to 40 meV) are presented. The values of the momentum transfer are indicated within each figure. The red line represents the result of least-squares fitting of Eqs. (4.9–12), assuming a finite value of $\Delta\omega$, whereas the blue circles with errors show data point. The spectra of ixs1, ixs2, ixs6, ixs8, ixs11, and ixs12 were excluded from the phonon dispersion data because their results were suspicious or could not be analyzed.

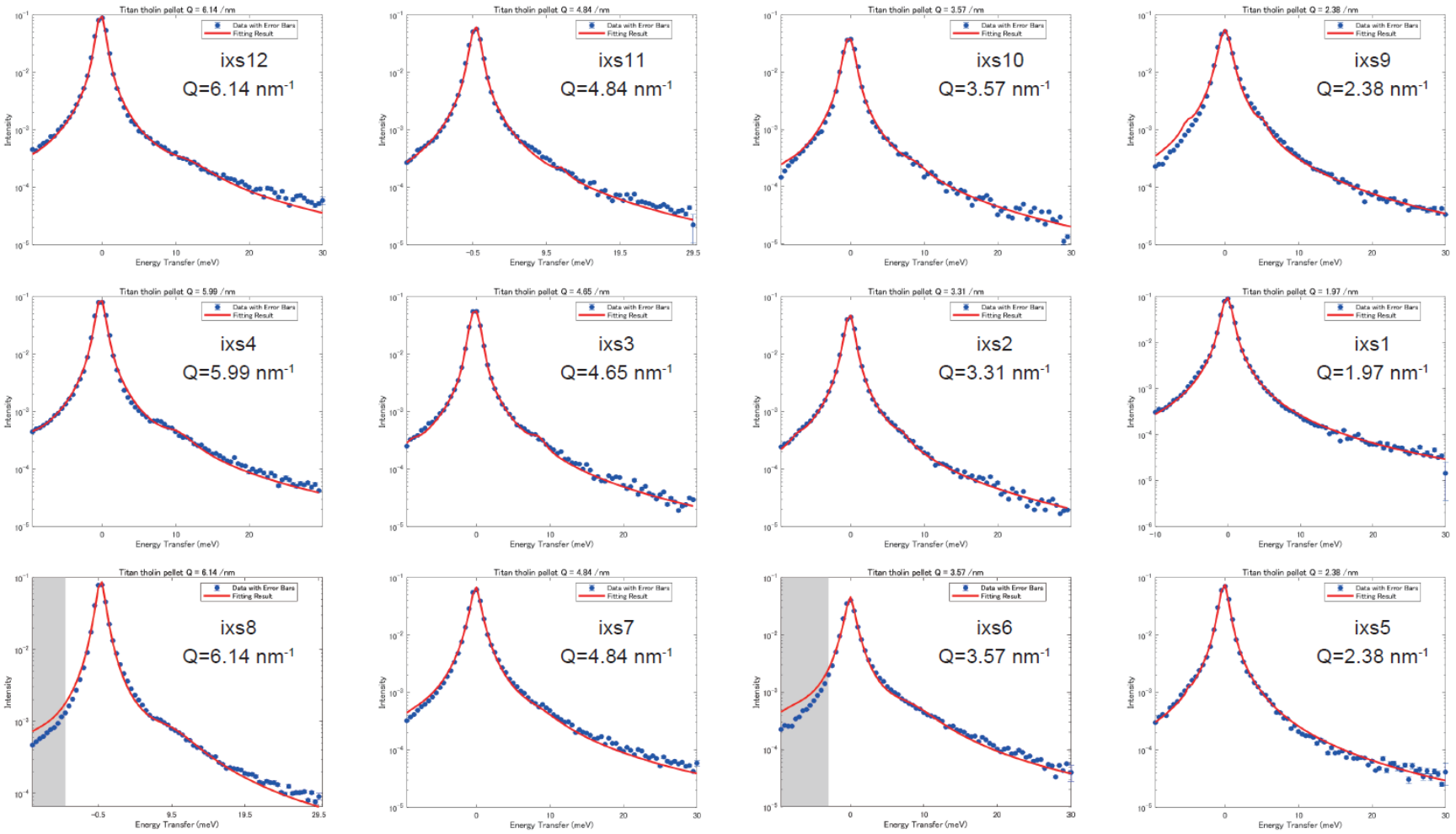

Figure A.11 The fitting results for Run #16 in Chapter 4 (Titan tholin B in setup B, measured at 240 K with a scattering angle of 2θ = 2.062° and an energy scan range from -10 to 30 meV) are presented. The values of the momentum transfer are indicated within each figure. The red line represents the result of least-squares fitting of Eqs. (4.9–12), assuming a finite value of $\Delta\omega$, whereas the blue circles with errors show data point. The spectra of ixs1, ixs6, ixs8, ixs9, and ixs11 were excluded from the phonon dispersion data because their results were suspicious or could not be analyzed.

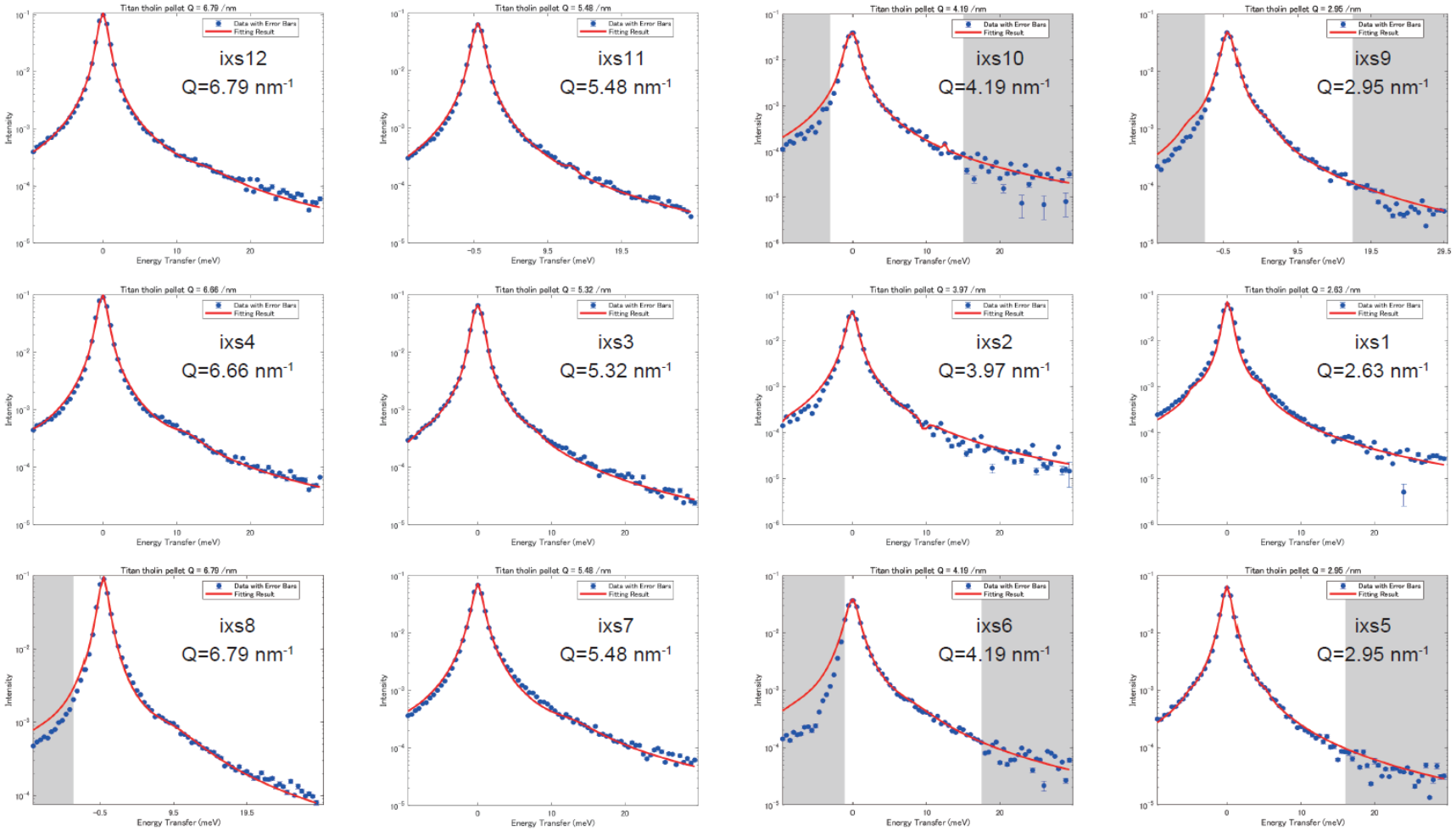

Figure A.12 The fitting results for Run #16 in Chapter 4 (Titan tholin B in setup B, measured at 240 K with a scattering angle of 2θ = 2.409° and an energy scan range from -10 to 30 meV) are presented. The values of the momentum transfer are indicated within each figure. The red line represents the result of least-squares fitting of Eqs. (4.9–12), assuming a finite value of $\Delta\omega$, whereas the blue circles with errors show data point. The spectra of ixs1, ixs2, ixs6, ixs7, ixs8, ixs9, ixs10, ixs11 and ixs12 were excluded from the phonon dispersion data because their results were suspicious or could not be analyzed.

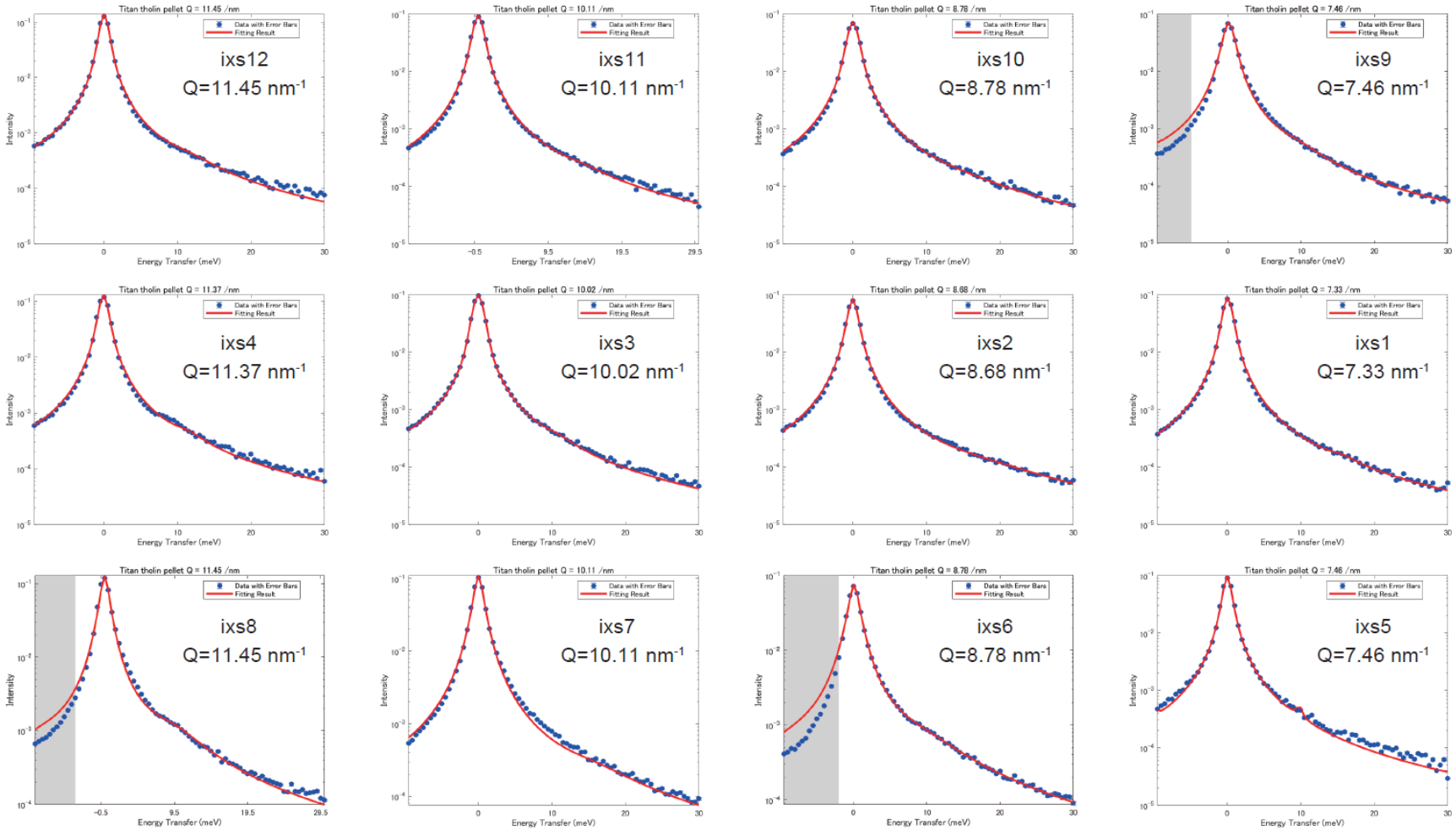

Figure A.13 The fitting results for Run #16 in Chapter 4 (Titan tholin B in setup B, measured at 240 K with a scattering angle of 2θ = 4.861° and an energy scan range from -10 to 40 meV) are presented. The values of the momentum transfer are indicated within each figure. The red line represents the result of least-squares fitting of Eqs. (4.9–12), assuming a finite value of $\Delta\omega$, whereas the blue circles with errors show data point. The spectra of ixs1, ixs2, ixs5, ixs6, ixs7, ixs8, ixs9, ixs10, and ixs11 were excluded from the phonon dispersion data because their results were suspicious or could not be analyzed.

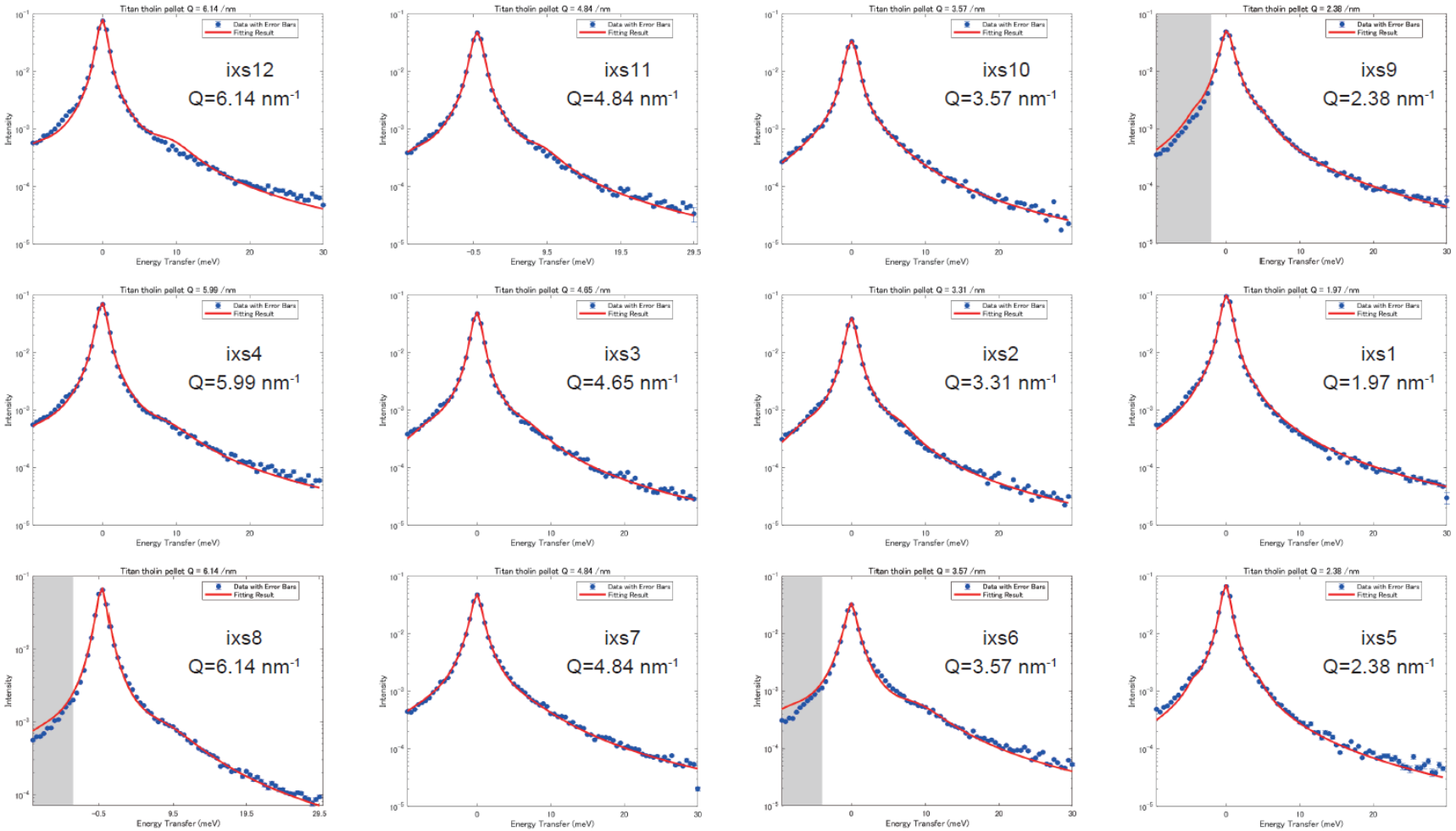

Figure A.14 The fitting results for Run #5 in Chapter 4 (Titan tholin B in setup B, measured at 300 K with a scattering angle of $2\theta =$ 2.062° and an energy scan range from -10 to 30 meV) are presented. The values of the momentum transfer are indicated within each figure. The red line represents the result of least-squares fitting of Eqs. (4.9–12), assuming a finite value of $\Delta\omega$, whereas the blue circles with errors show data point. The spectra of ixs1, ixs6, ixs8, ixs9, ixs10, and ixs12 were excluded from the phonon dispersion data because their results were suspicious or could not be analyzed.

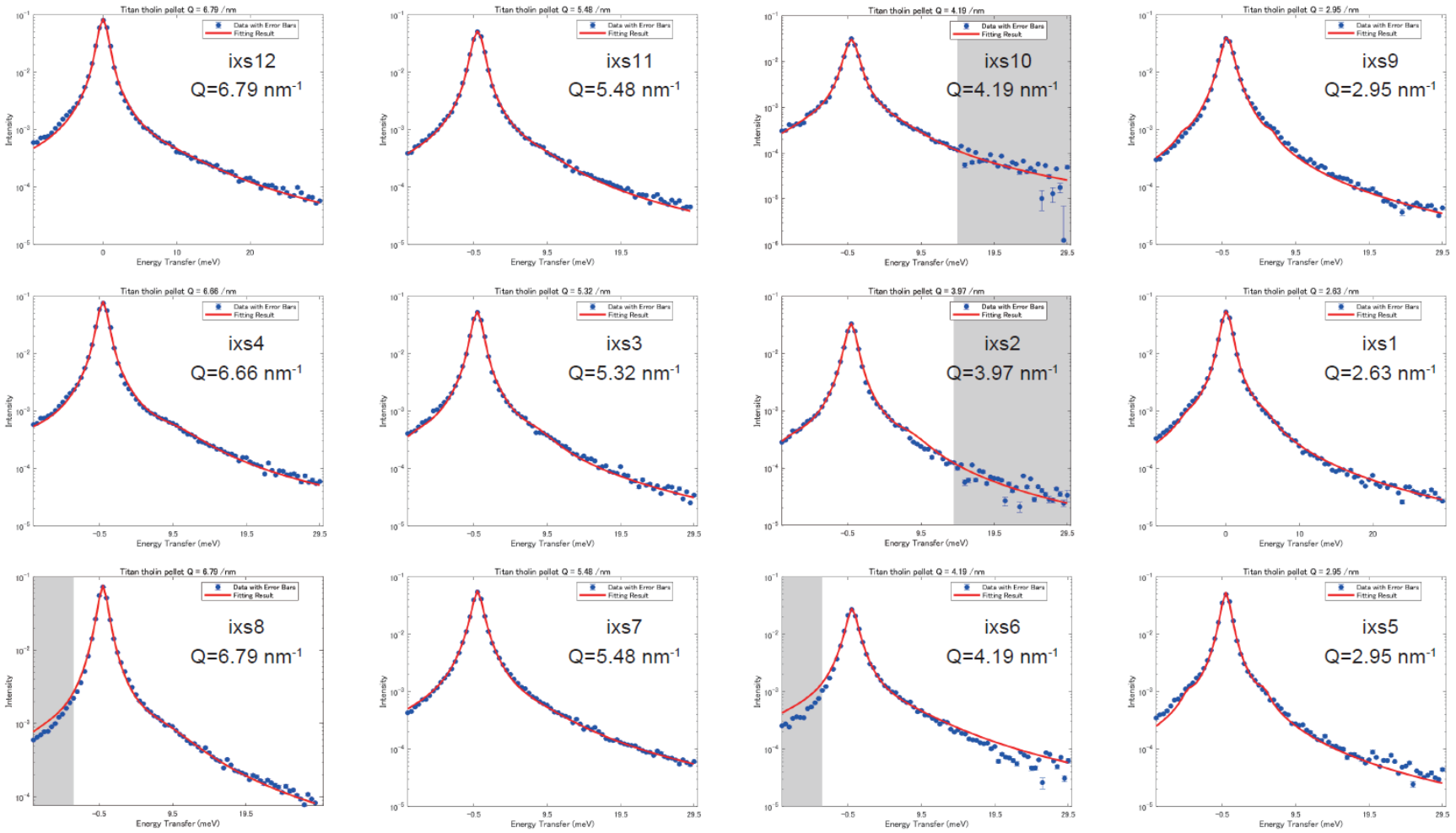

Figure A.15 The fitting results for Run #5 in Chapter 4 (Titan tholin B in setup B, measured at 300 K with a scattering angle of 2θ = 2.409° and an energy scan range from -10 to 30 meV) are presented. The values of the momentum transfer are indicated within each figure. The red line represents the result of least-squares fitting of Eqs. (4.9–12), assuming a finite value of $\Delta\omega$, whereas the blue circles with errors show data point. The spectra of ixs2, ixs6, ixs8, and ixs12 were excluded from the phonon dispersion data because their results were suspicious or could not be analyzed.

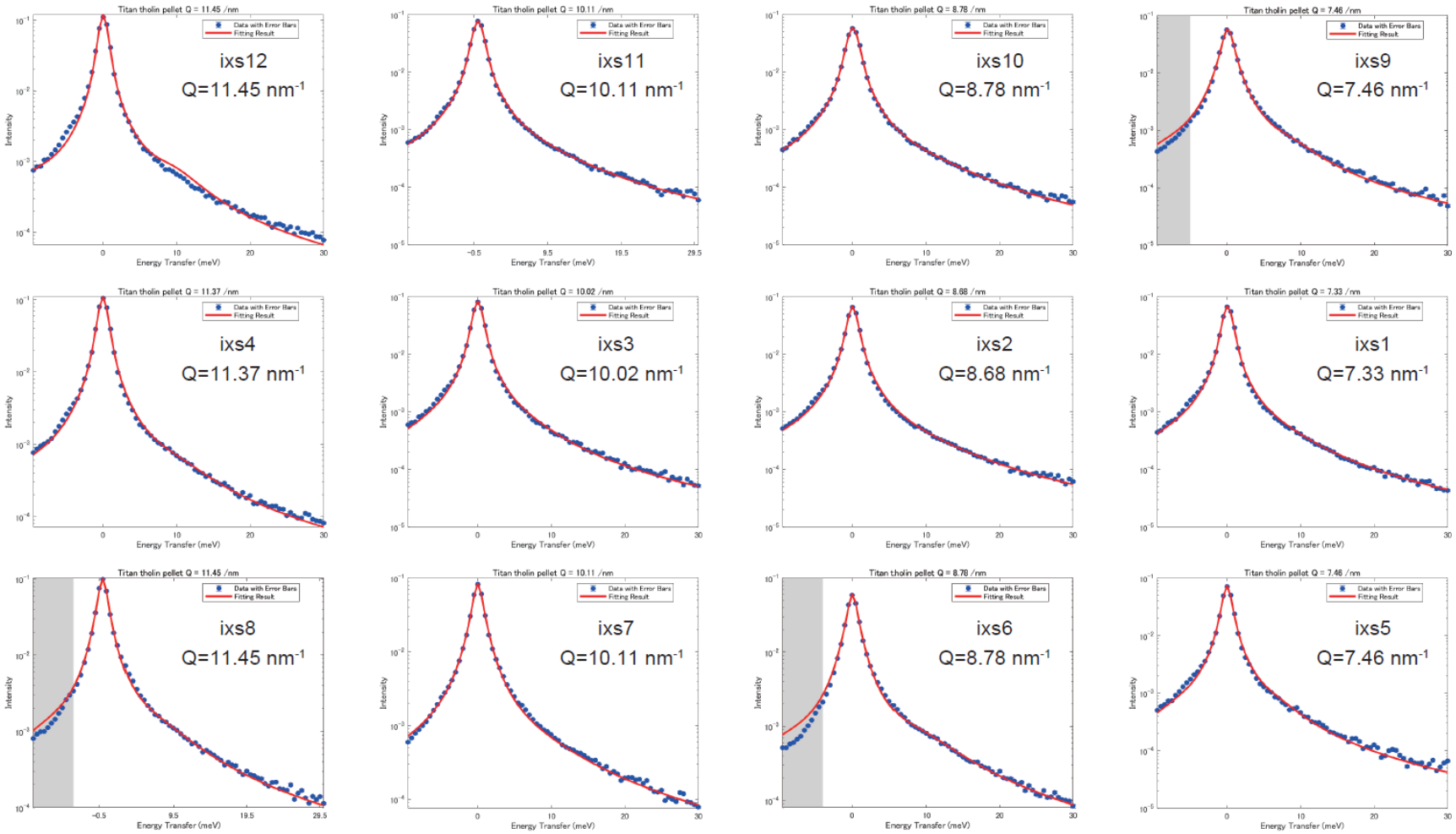

Figure A.16 The fitting results for Run #5 in Chapter 4 (Titan tholin B in setup B, measured at 300 K with a scattering angle of 2θ = 4.861° and an energy scan range from -10 to 40 meV) are presented. The values of the momentum transfer are indicated within each figure. The red line represents the result of least-squares fitting of Eqs. (4.9–12), assuming a finite value of $\Delta\omega$, whereas the blue circles with errors show data point. The spectra of ixs1, ixs2, ixs3, ixs5, ixs6, ixs8, ixs9, and ixs12 were excluded from the phonon dispersion data because their results were suspicious or could not be analyzed.

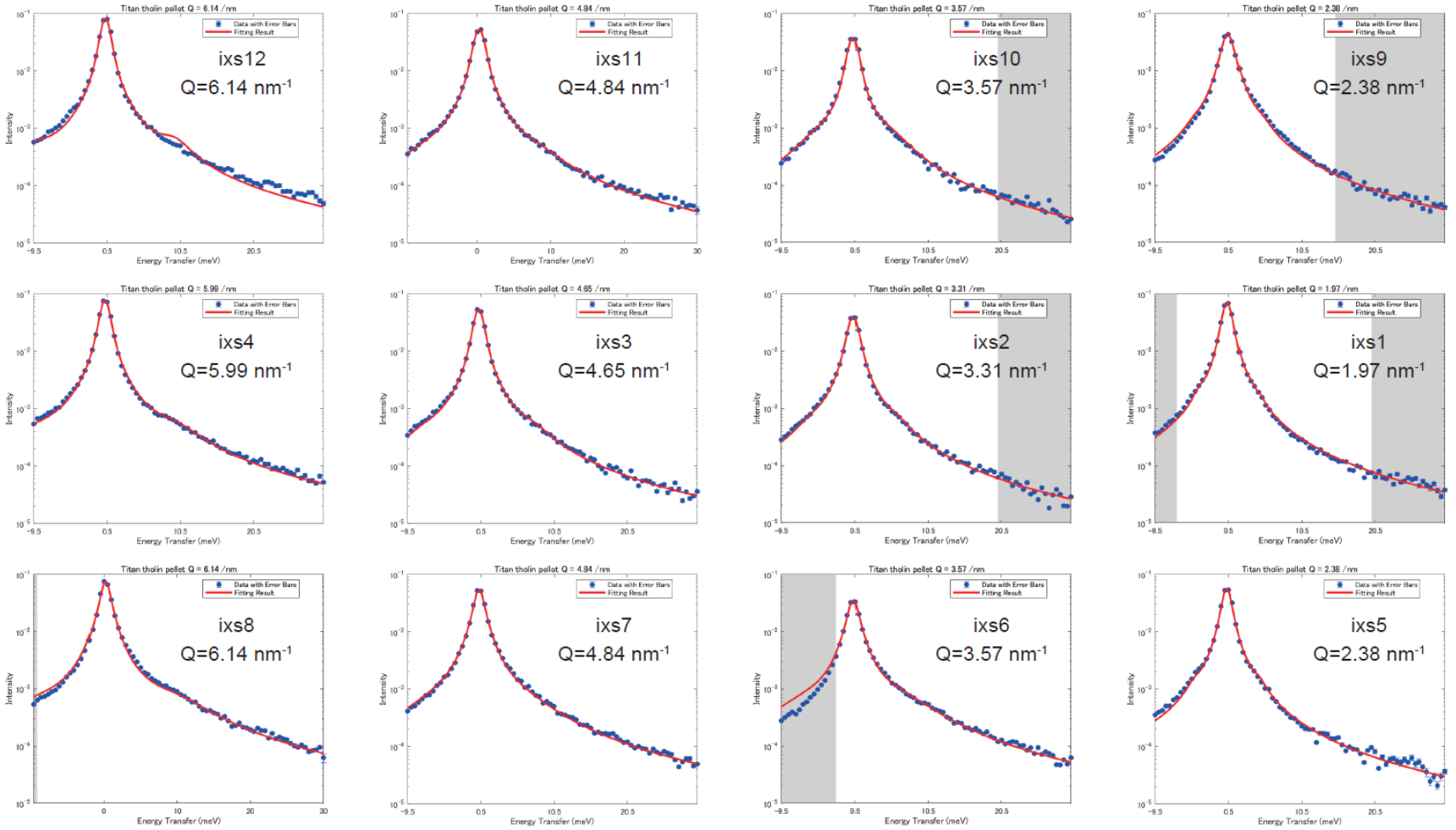

Figure A.17 The fitting results for Run #8 in Chapter 4 (Titan tholin B in setup B, measured at 300 K with a scattering angle of 2θ = 2.062° and an energy scan range from -10 to 30 meV) are presented. The values of the momentum transfer are indicated within each figure. The red line represents the result of least-squares fitting of Eqs. (4.9–12), assuming a finite value of $\Delta\omega$, whereas the blue circles with errors show data point. The spectra of ixs1, ixs6, and ixs12 were excluded from the phonon dispersion data because their results were suspicious or could not be analyzed.

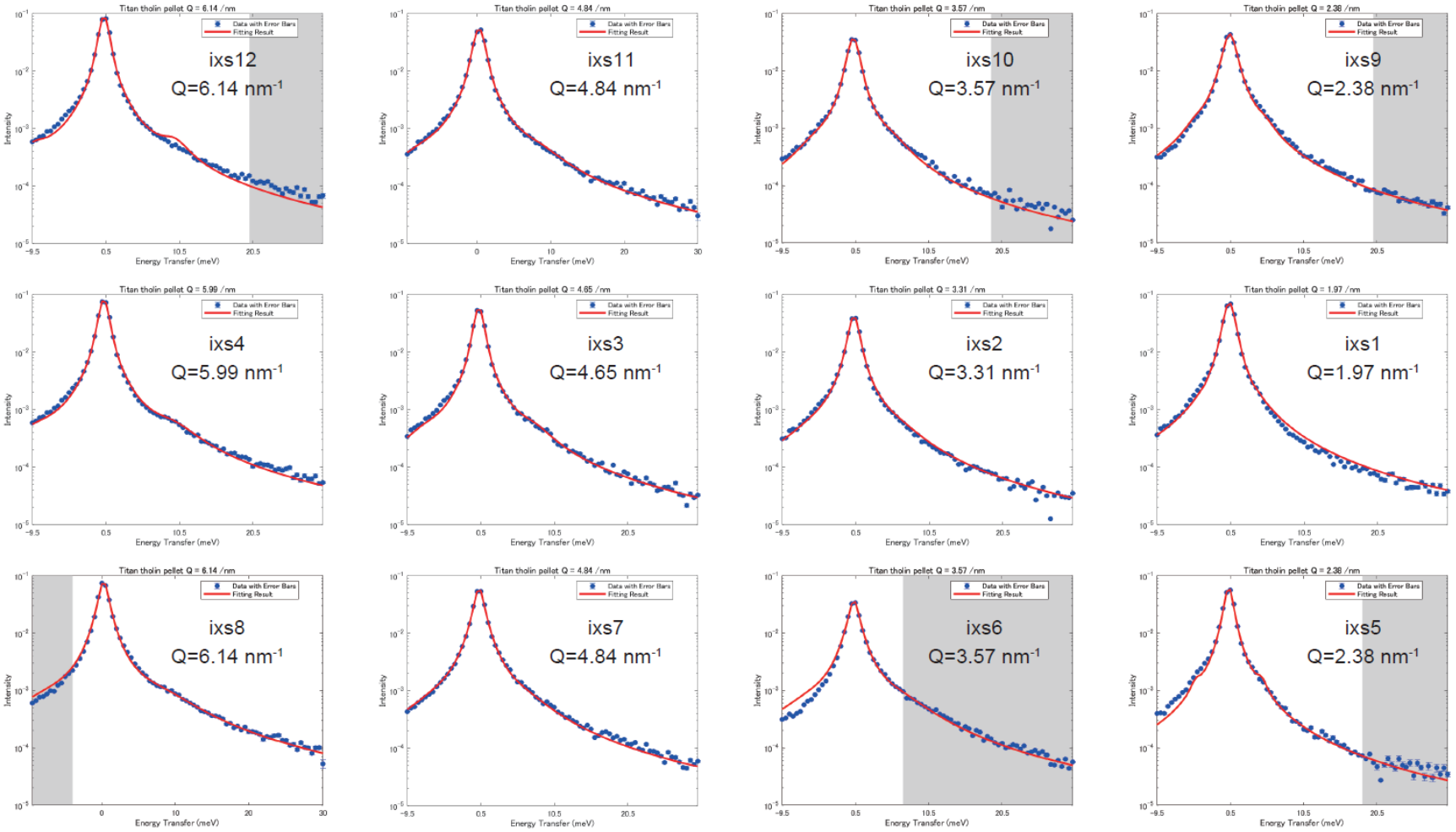

Figure A.18 The fitting results for Run #9 in Chapter 4 (Titan tholin B in setup B, measured at 300 K with a scattering angle of 2θ = 2.062° and an energy scan range from -10 to 30 meV) are presented. The values of the momentum transfer are indicated within each figure. The red line represents the result of least-squares fitting of Eqs. (4.9–12), assuming a finite value of $\Delta\omega$, whereas the blue circles with errors show data point. The spectra of ixs1, ixs6, ixs8, and ixs12 were excluded from the phonon dispersion data because their results were suspicious or could not be analyzed.

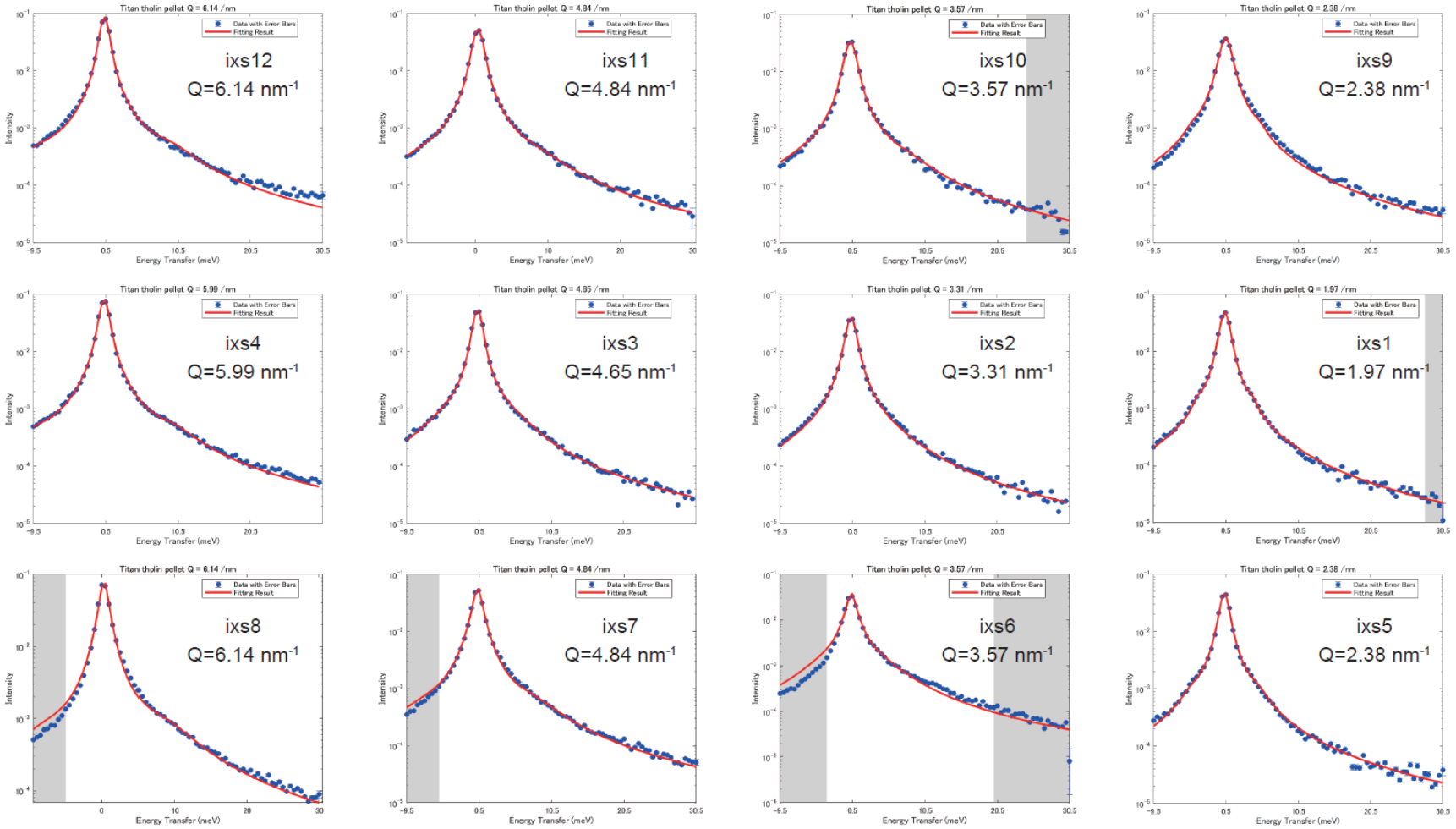

Figure A.19 The fitting results for Run #10 in Chapter 4 (Titan tholin A in setup B, measured at 300 K with a scattering angle of 2θ = 2.062° and an energy scan range from -10 to 30 meV) are presented. The values of the momentum transfer are indicated within each figure. The red line represents the result of least-squares fitting of Eqs. (4.9–12), assuming a finite value of $\Delta\omega$, whereas the blue circles with errors show data point. The spectra of ixs6, ixs7, and ixs8 were excluded from the phonon dispersion data because their results were suspicious or could not be analyzed.

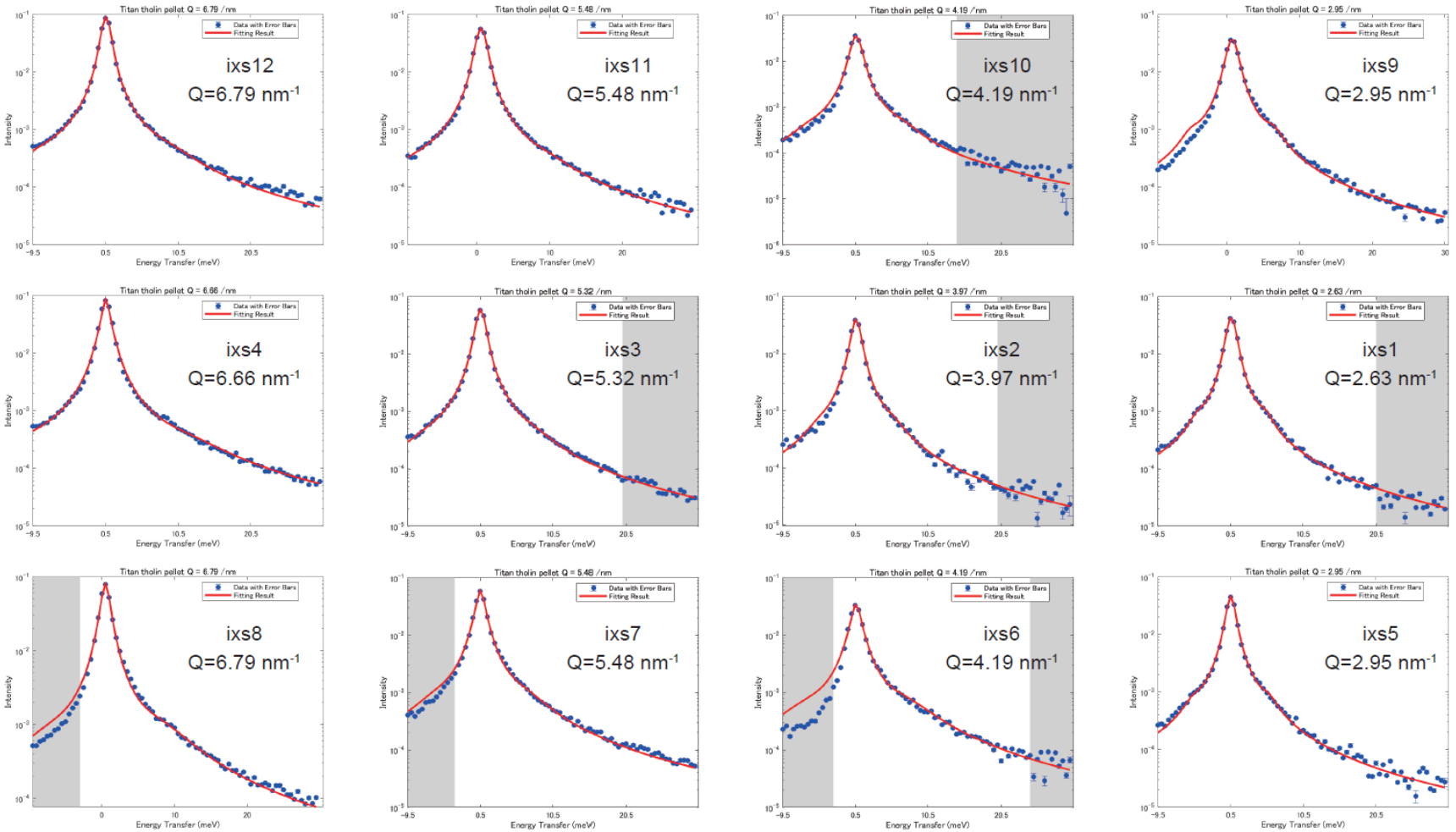

Figure A.20 The fitting results for Run #10 in Chapter 4 (Titan tholin A in setup B, measured at 300 K with a scattering angle of 2θ = 2.409° and an energy scan range from -10 to 30 meV) are presented. The values of the momentum transfer are indicated within each figure. The red line represents the result of least-squares fitting of Eqs. (4.9–12), assuming a finite value of $\Delta\omega$, whereas the blue circles with errors show data point. The spectra of ixs6, ixs7, ixs8, and ixs9 were excluded from the phonon dispersion data because their results were suspicious or could not be analyzed.

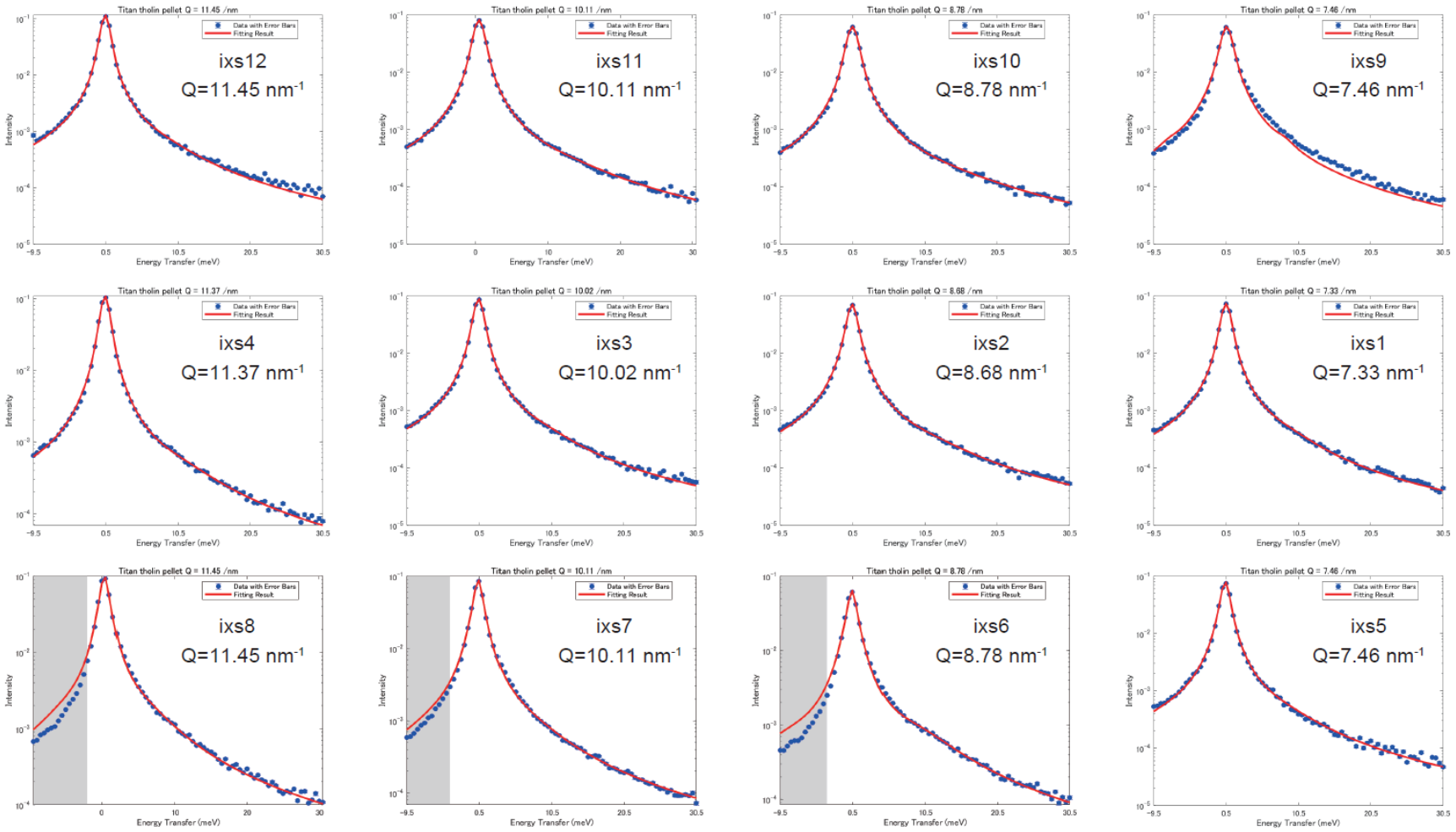

Figure A.21 The fitting results for Run #10 in Chapter 4 (Titan tholin A in setup B, measured at 300 K with a scattering angle of 2θ = 4.861° and an energy scan range from -10 to 40 meV) are presented. The values of the momentum transfer are indicated within each figure. The red line represents the result of least-squares fitting of Eqs. (4.9–12), assuming a finite value of $\Delta\omega$, whereas the blue circles with errors show data point. The spectra of ixs6, ixs7, ixs8, and ixs9 were excluded from the phonon dispersion data because their results were suspicious or could not be analyzed.

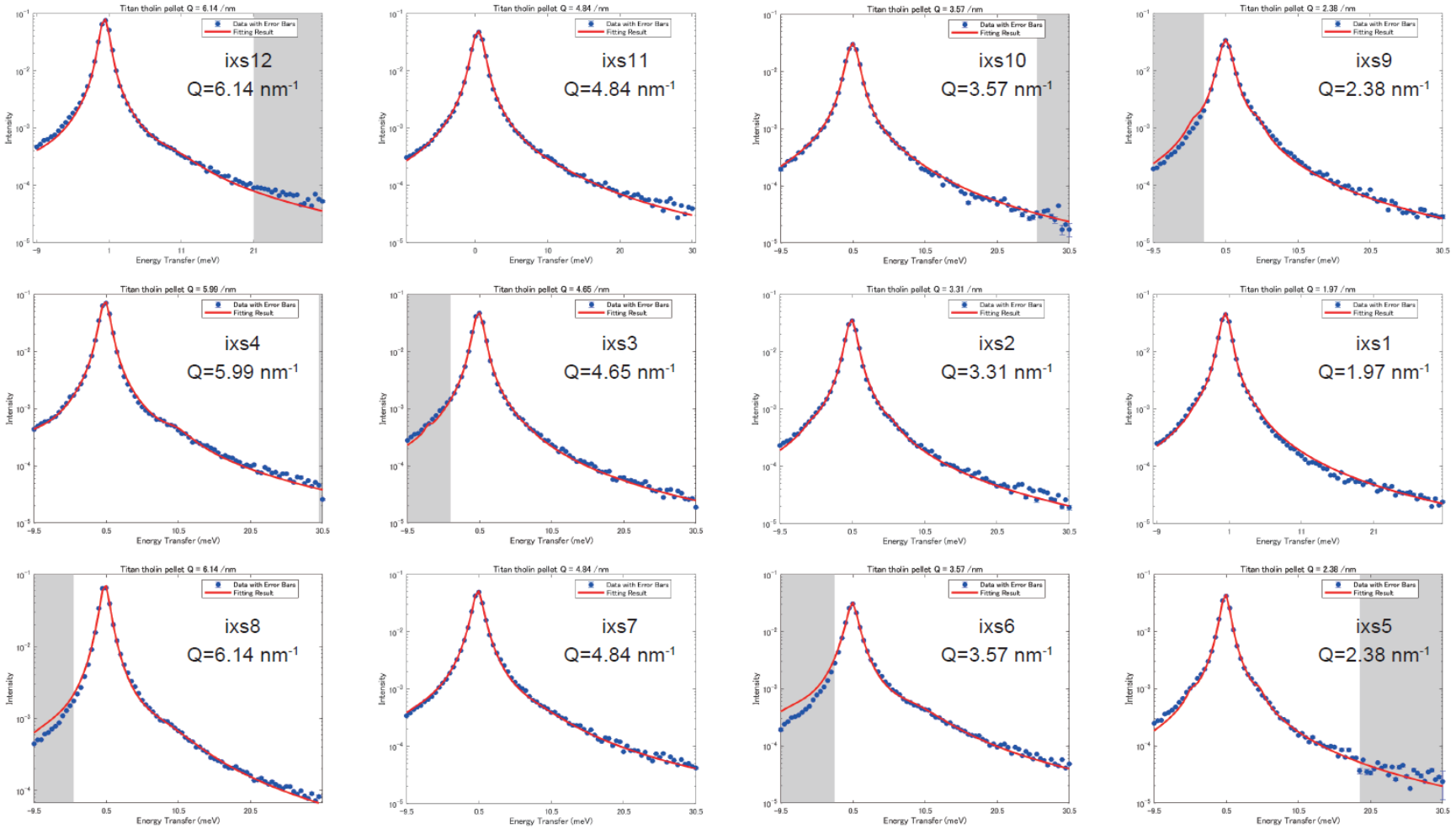

Figure A.22 The fitting results for Run #12 in Chapter 4 (Titan tholin A in setup B, measured at 190 K with a scattering angle of 2θ = 2.062° and an energy scan range from -10 to 30 meV) are presented. The values of the momentum transfer are indicated within each figure. The red line represents the result of least-squares fitting of Eqs. (4.9–12), assuming a finite value of $\Delta\omega$, whereas the blue circles with errors show data point. The spectra of ixs1, ixs3, ixs6, ixs8, ixs9, and ixs10 were excluded from the phonon dispersion data because their results were suspicious or could not be analyzed.

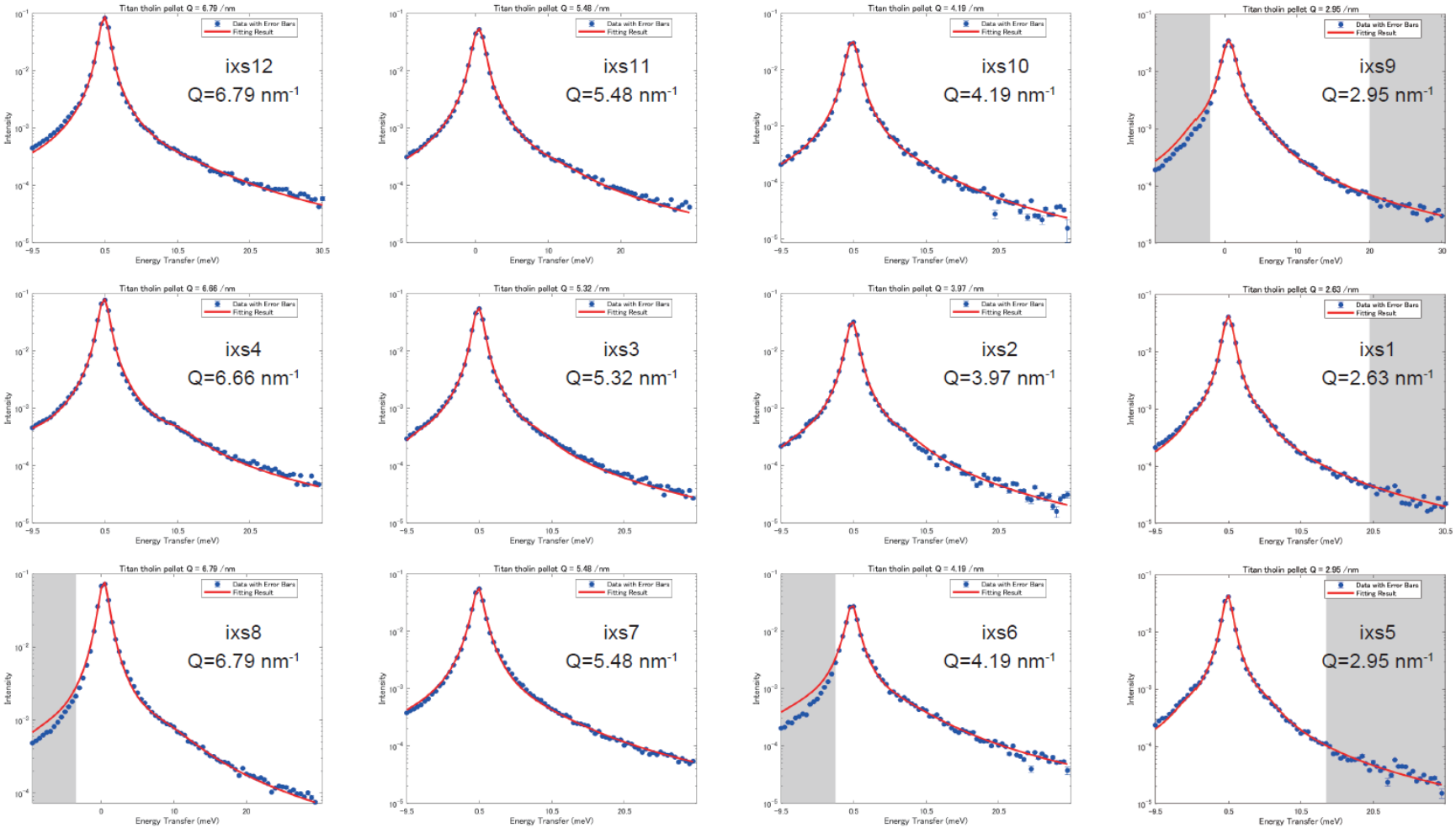

Figure A.23 The fitting results for Run #12 in Chapter 4 (Titan tholin A in setup B, measured at 190 K with a scattering angle of 2θ = 2.409° and an energy scan range from -10 to 30 meV) are presented. The values of the momentum transfer are indicated within each figure. The red line represents the result of least-squares fitting of Eqs. (4.9–12), assuming a finite value of $\Delta\omega$, whereas the blue circles with errors show data point. The spectra of ixs6, ixs8, and ixs9 were excluded from the phonon dispersion data because their results were suspicious or could not be analyzed.

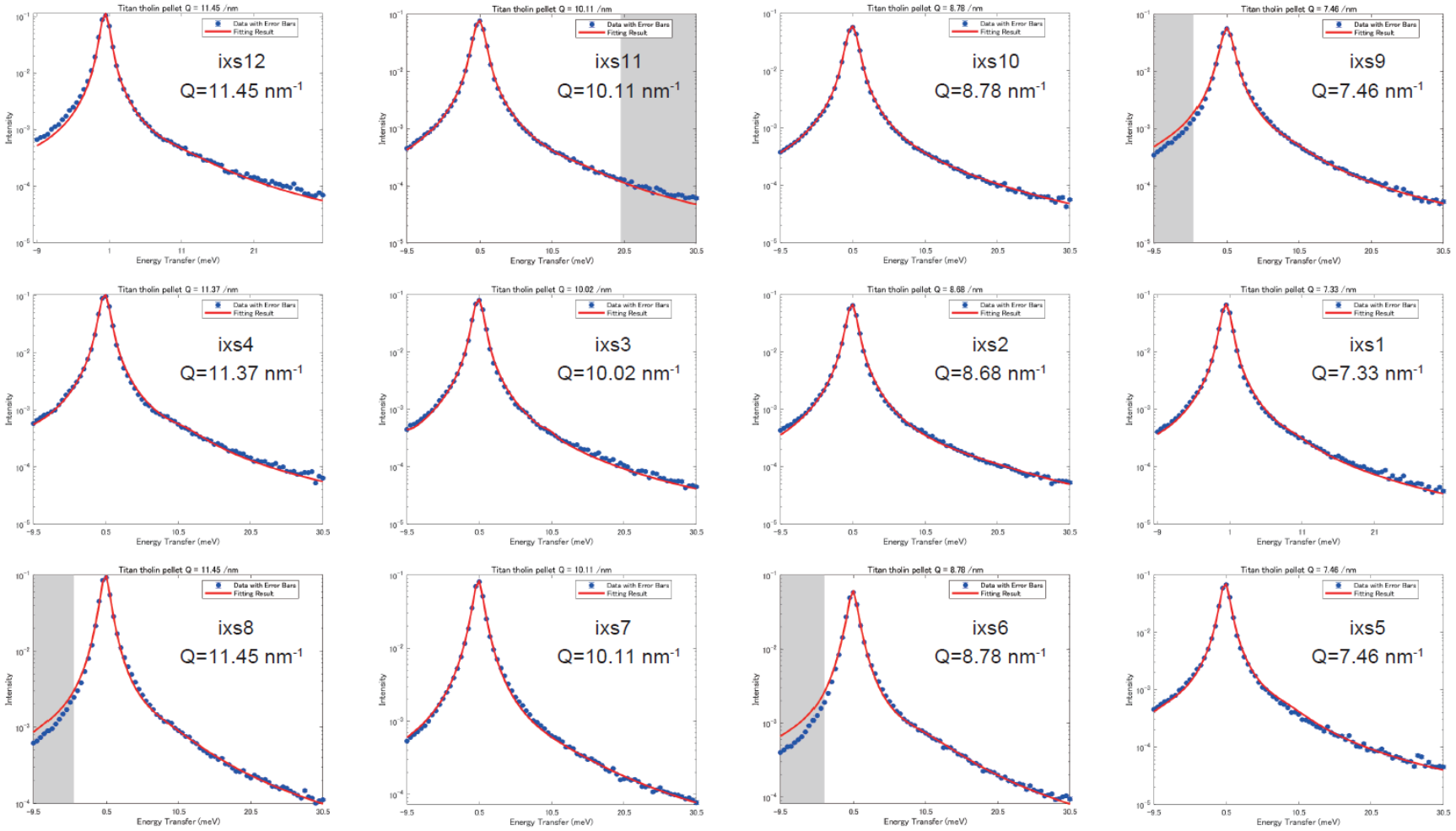

Figure A.24 The fitting results for Run #12 in Chapter 4 (Titan tholin A in setup B, measured at 190 K with a scattering angle of 2θ = 4.861° and an energy scan range from -10 to 40 meV) are presented. The values of the momentum transfer are indicated within each figure. The red line represents the result of least-squares fitting of Eqs. (4.9–12), assuming a finite value of $\Delta\omega$, whereas the blue circles with errors show data point. The spectra of ixs6, ixs7, ixs8, ixs9, ixs11, and ixs12 were excluded from the phonon dispersion data because their results were suspicious or could not be analyzed.

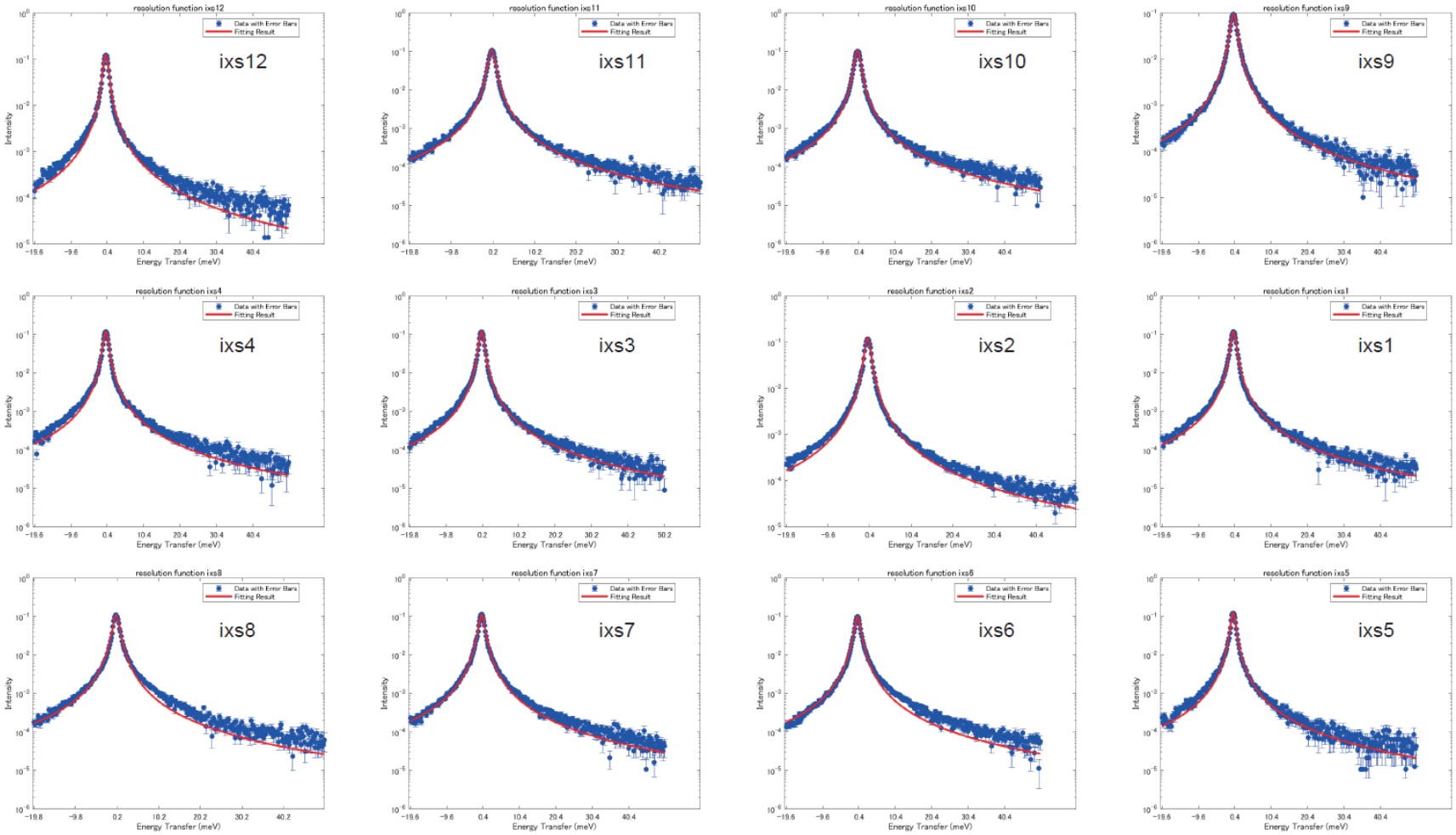

Figure A.25 The fitting results for resolution function measured using scattering from borosilicate glass (Tempax) (Ishikawa & Baron, 2021) in setup A are presented. The red line represents the result of the least-squares fitting of Eq. (4.9), whereas the blue circles with errors show data point.

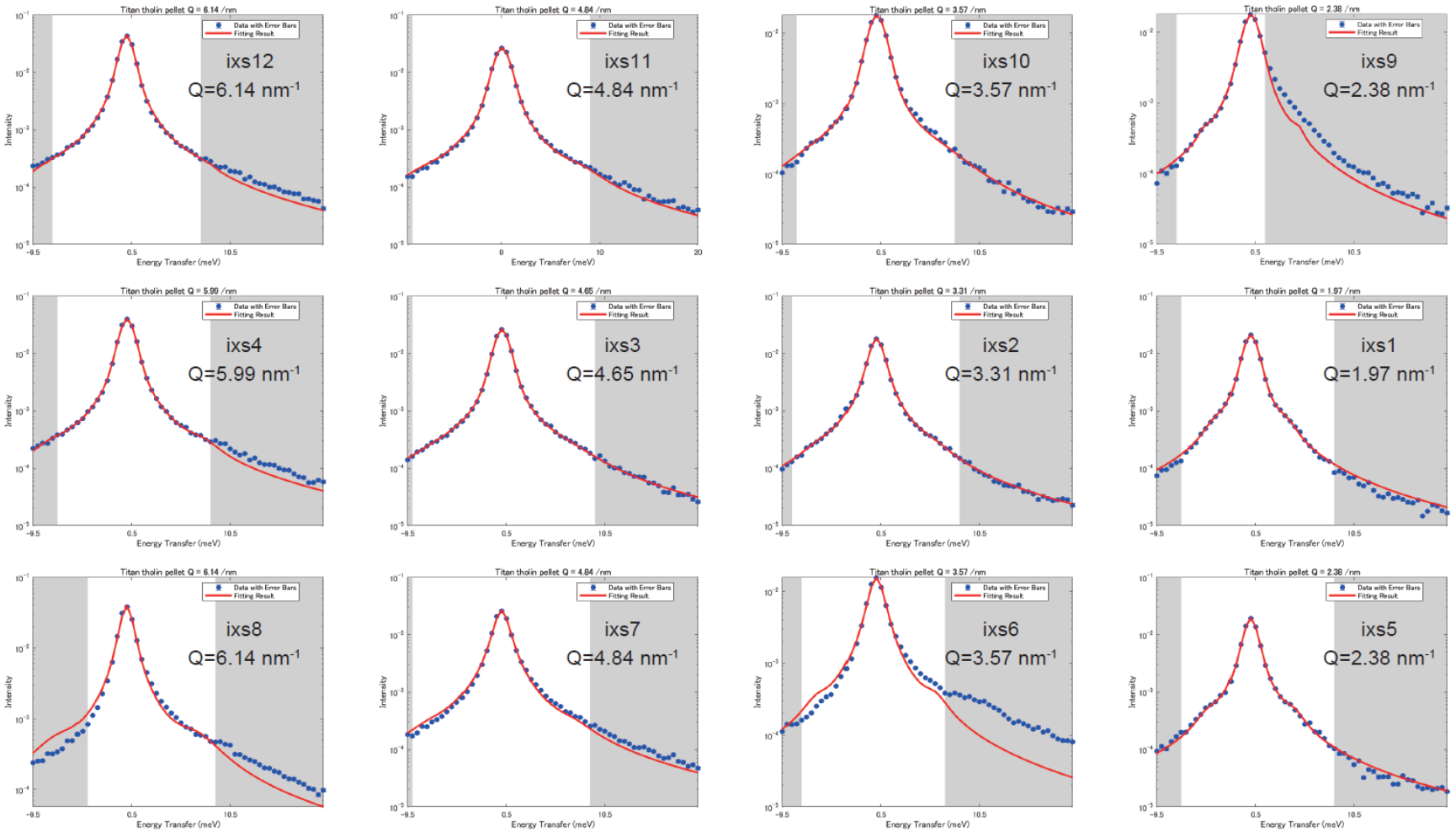

Figure A.26 The fitting results for Run #2 in Chapter 4 (Titan tholin A in setup A, measured at 300 K with a scattering angle of 2θ = 2.062° and an energy scan range from -10 to 25 meV) are presented. The values of the momentum transfer are indicated within each figure. The red line represents the result of least-squares fitting of Eqs. (4.9–12), assuming a finite value of $\Delta\omega$, whereas the blue circles with errors show data point. The spectra of ixs6, ixs8, and ixs9 were excluded from the phonon dispersion data because their results were suspicious or could not be analyzed.

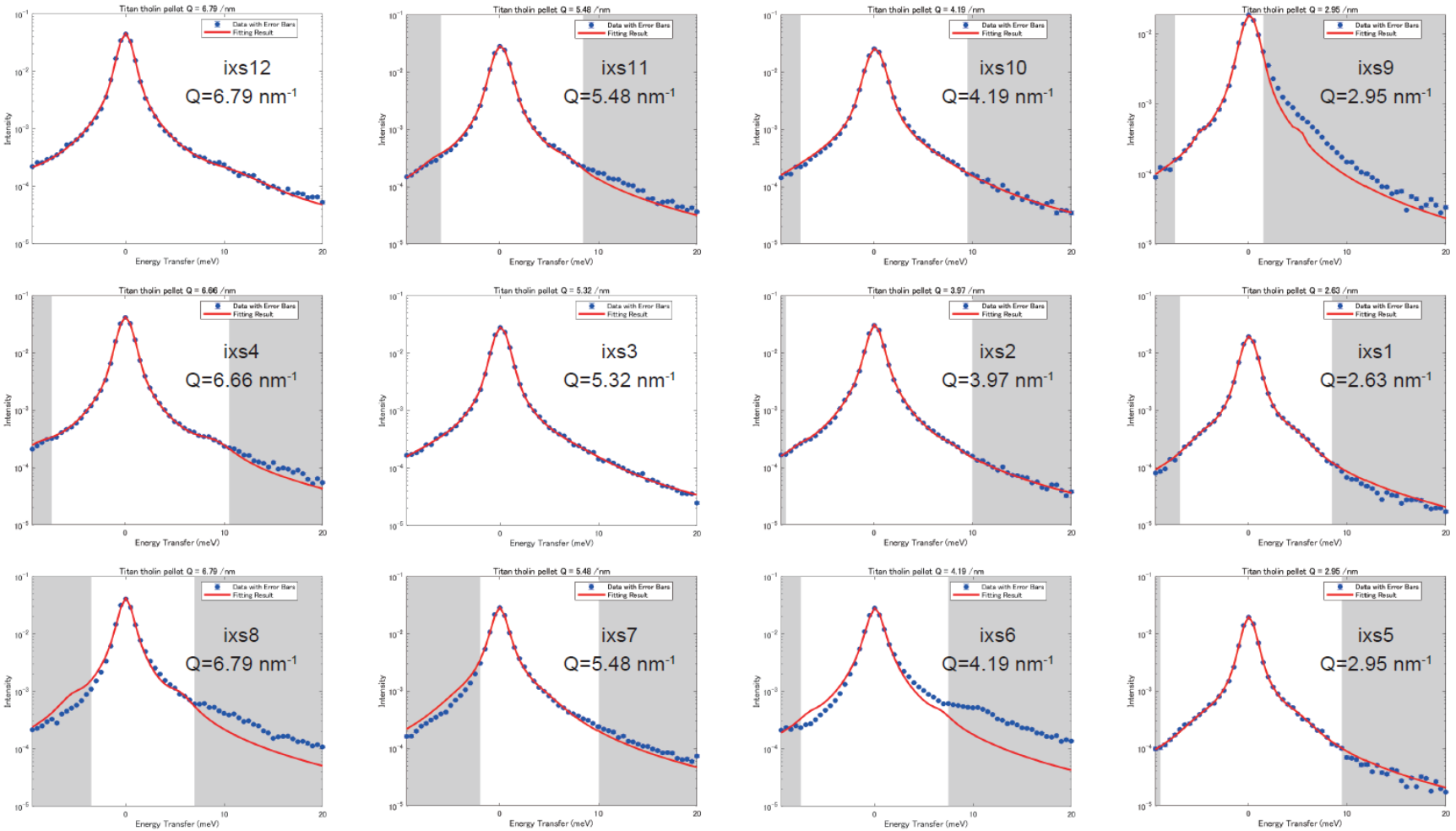

Figure A.27 The fitting results for Run #2 in Chapter 4 (Titan tholin A in setup A, measured at 300 K with a scattering angle of 2θ = 2.409° and an energy scan range from -10 to 30 meV) are presented. The values of the momentum transfer are indicated within each figure. The red line represents the result of least-squares fitting of Eqs. (4.9–12), assuming a finite value of $\Delta\omega$, whereas the blue circles with errors show data point. The spectra of ixs6, ixs7, ixs8, ixs9, and ixs10 were excluded from the phonon dispersion data because their results were suspicious or could not be analyzed.

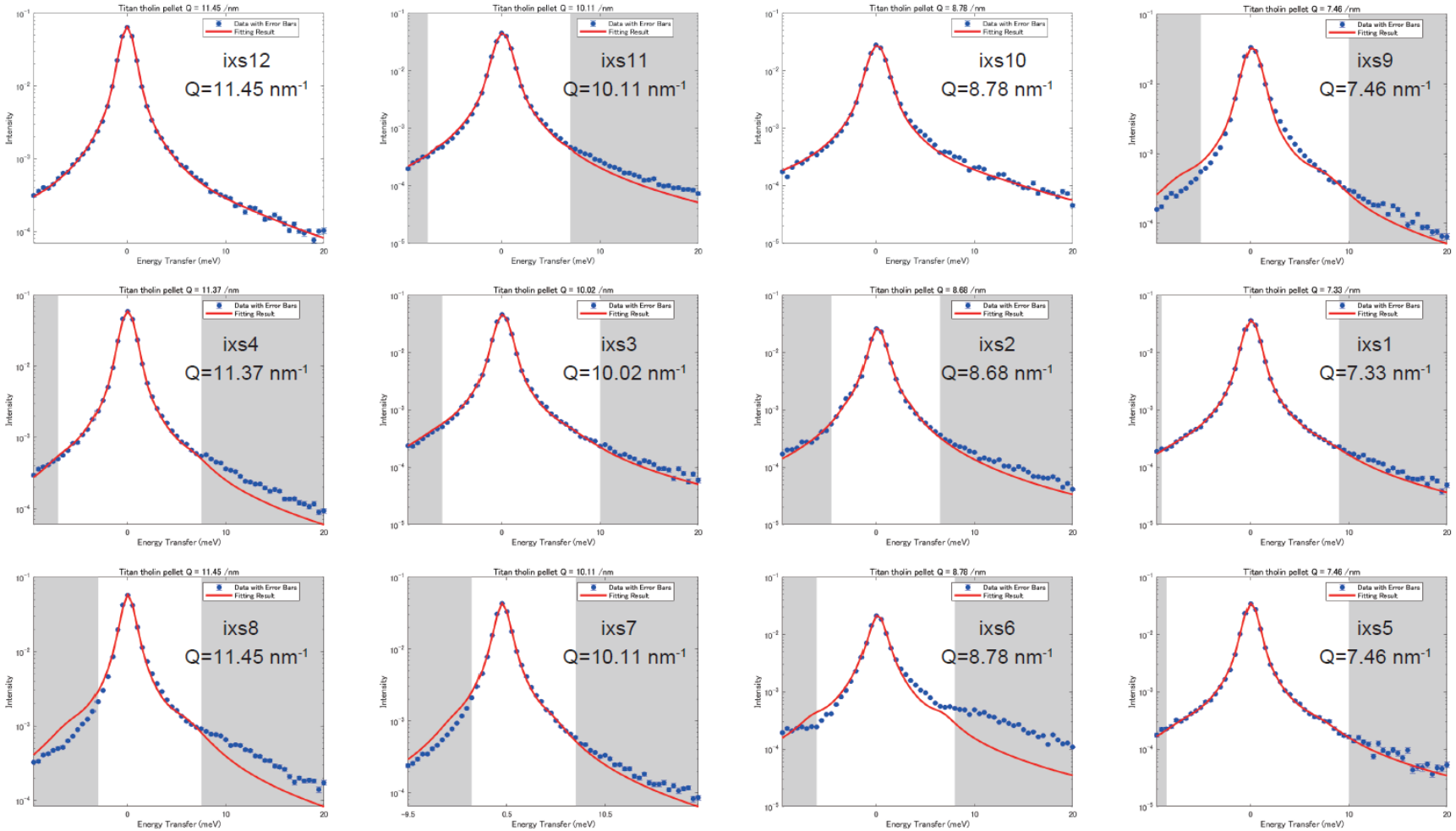

Figure A.28 The fitting results for Run #2 in Chapter 4 (Titan tholin A in setup A, measured at 300 K with a scattering angle of $2\theta = 4.861°$ and an energy scan range from -10 to 30 meV) are presented. The values of the momentum transfer are indicated within each figure. The red line represents the result of least-squares fitting of Eqs. (4.9–12), assuming a finite value of $\Delta\omega$, whereas the blue circles with errors show data point. The spectra of ixs6, ixs7, ixs8, ixs9, ixs10, and ixs11 were excluded from the phonon dispersion data because their results were suspicious or could not be analyzed.

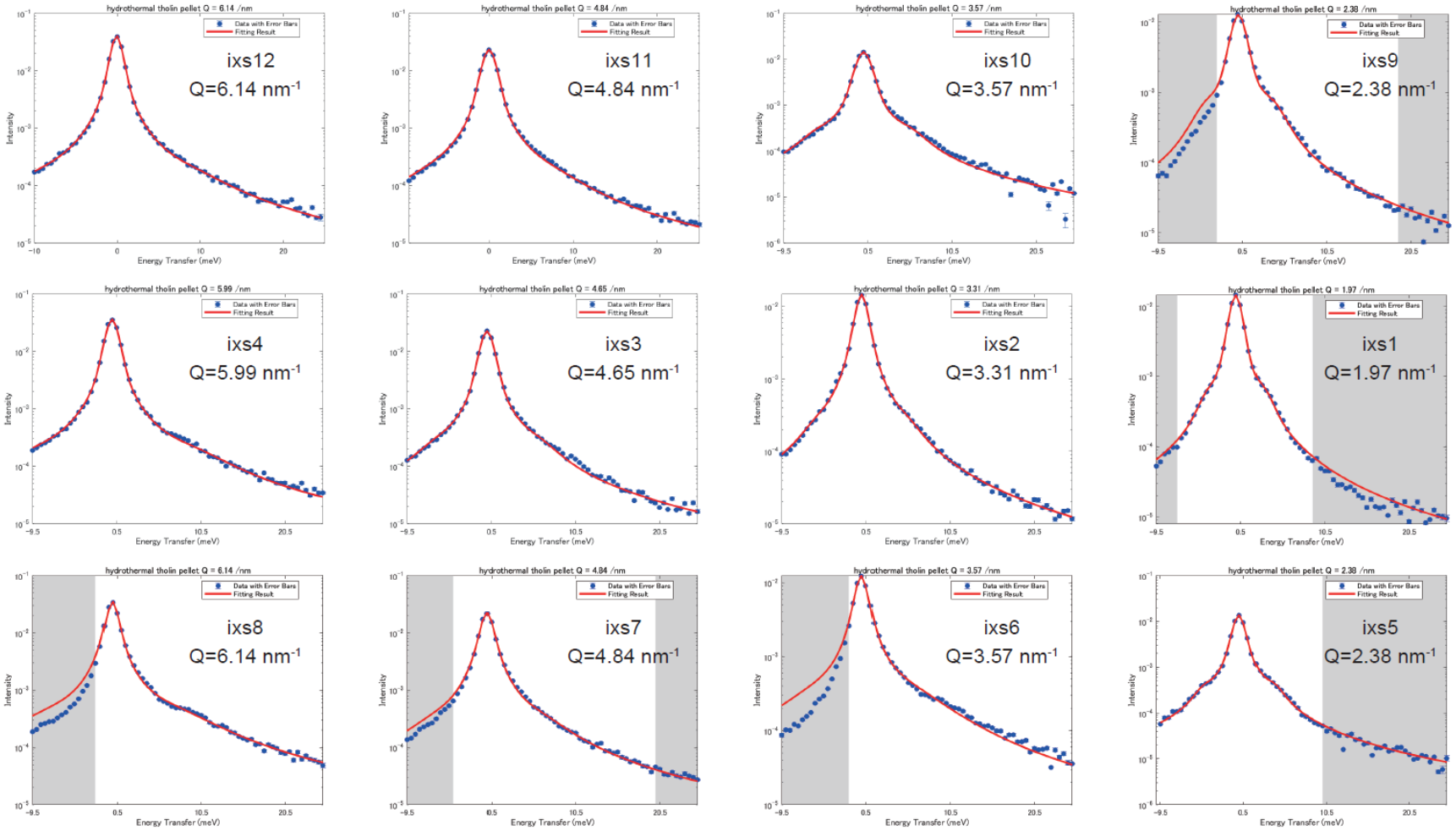

Figure A.29 The fitting results for Run #3 in Chapter 4 (hydrothermal organics in setup A, measured at 300 K with a scattering angle of $2\theta = 2.062°$ and an energy scan range from -10 to 25 meV) are presented. The values of the momentum transfer are indicated within each figure. The red line represents the result of least-squares fitting of Eqs. (4.9–12), assuming a finite value of $\Delta\omega$, whereas the blue circles with errors show data point. The spectra of ixs6, ixs7, ixs8, and ixs9 were excluded from the phonon dispersion data because their results were suspicious or could not be analyzed.

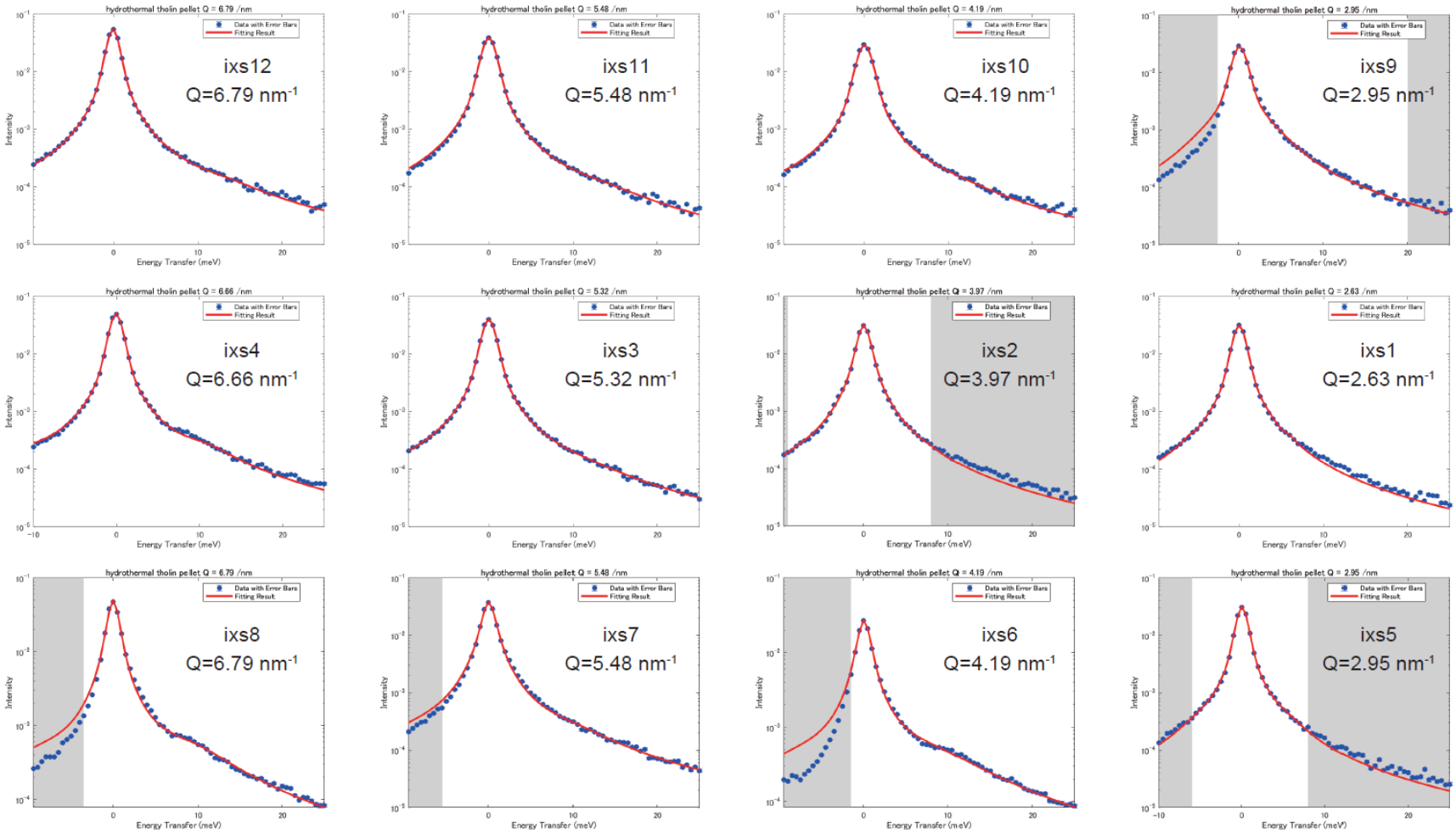

Figure A.30 The fitting results for Run #3 in Chapter 4 (hydrothermal organics in setup A, measured at 300 K with a scattering angle of $2\theta = 2.409°$ and an energy scan range from -10 to 30 meV) are presented. The values of the momentum transfer are indicated within each figure. The red line represents the result of least-squares fitting of Eqs. (4.9–12), assuming a finite value of $\Delta\omega$, whereas the blue circles with errors show data point. The spectra of ixs6, ixs7, ixs8, and ixs9 were excluded from the phonon dispersion data because their results were suspicious or could not be analyzed.

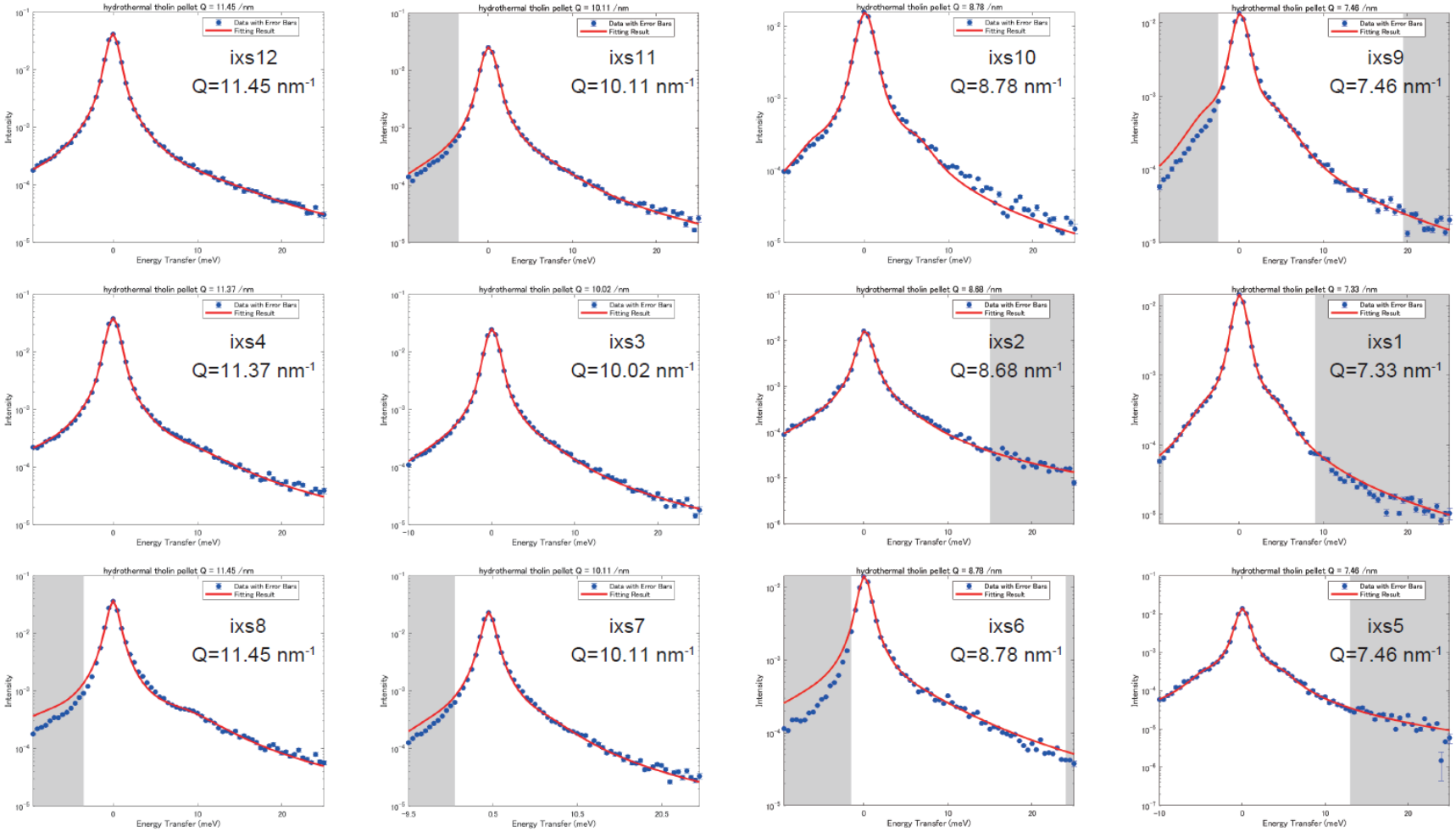

Figure A.31 The fitting results for Run #3 in Chapter 4 (hydrothermal organics in setup A, measured at 300 K with a scattering angle of $2\theta = 4.861°$ and an energy scan range from -10 to 30 meV) are presented. The values of the momentum transfer are indicated within each figure. The red line represents the result of least-squares fitting of Eqs. (4.9–12), assuming a finite value of $\Delta\omega$, whereas the blue circles with errors show data point. The spectra of ixs6, ixs7, ixs8, ixs9, and ixs11 were excluded from the phonon dispersion data because their results were suspicious or could not be analyzed.

Appendix B. Results of analyses of ultrasonic pulse echos in Chapter 4

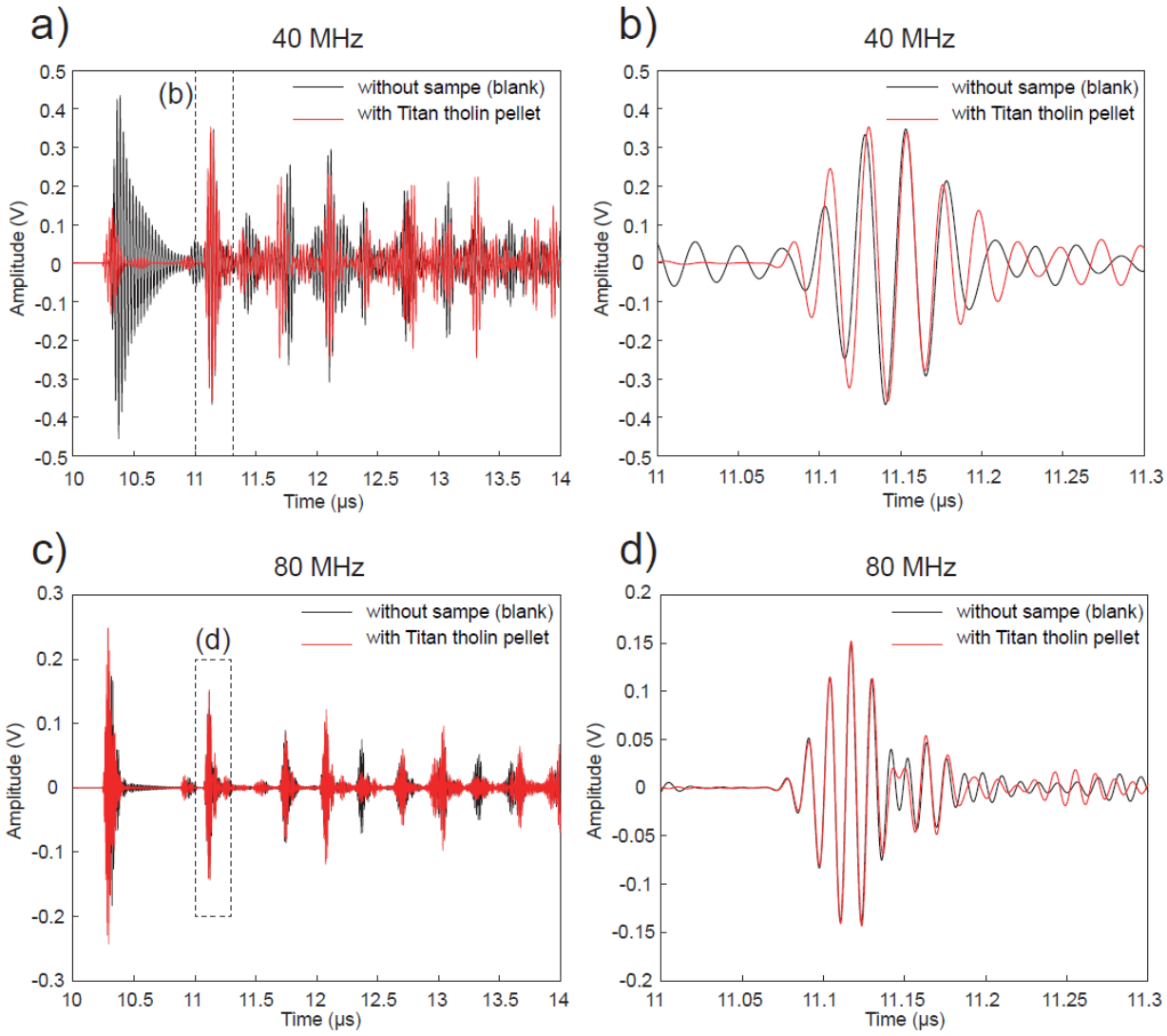

Figure B.1 Results of the analyses of the ultrasonic pulse echo of P-wave in (a,b) 40 MHz and (c,d) in 80 MHz. Red line shows the ultrasonic pulse transmittance wave with Titan tholin pellet. Black line shows the ultrasonic pulse transmittance wave without sample (blank).

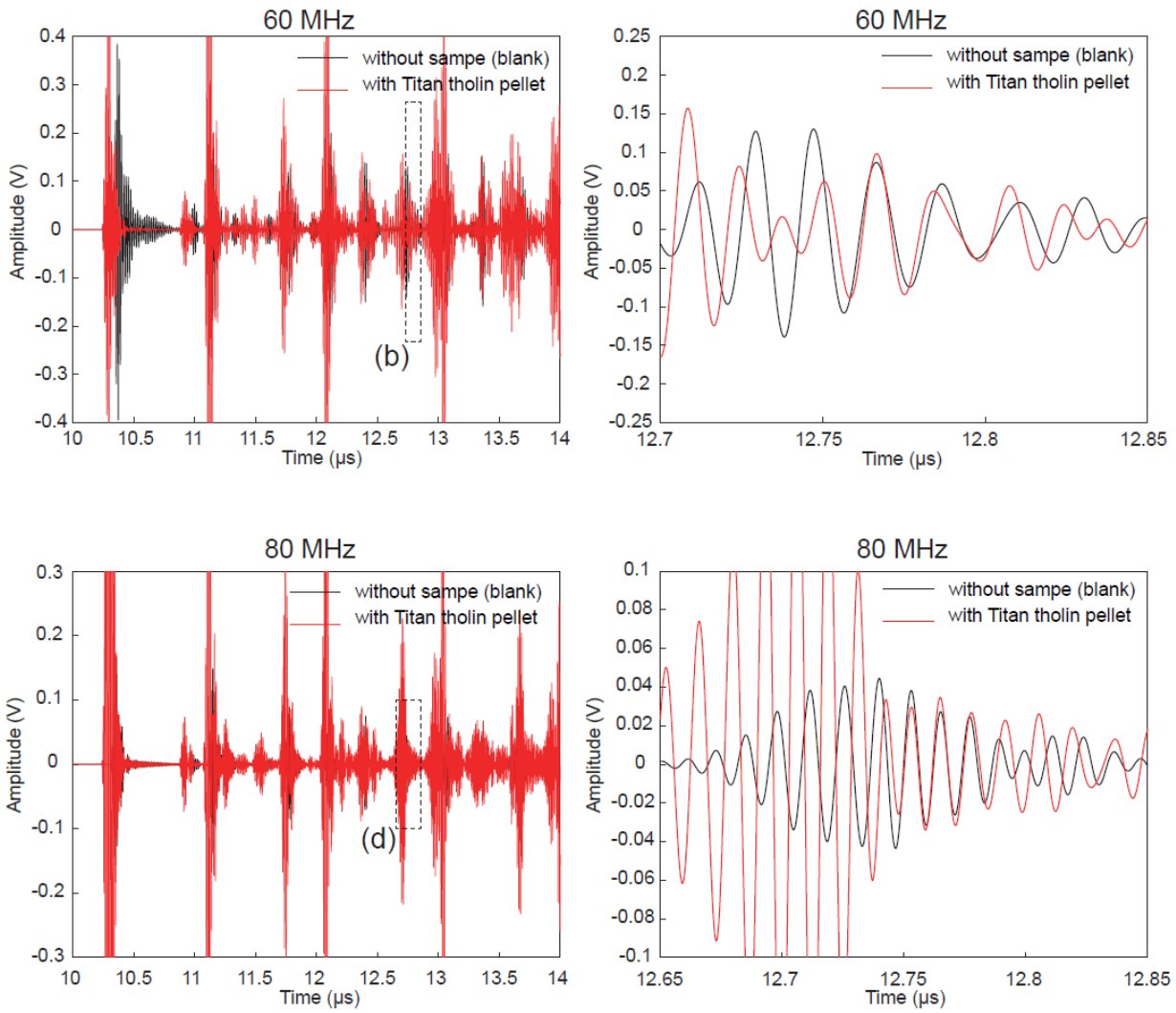

Figure B.2 Results of the analyses of the ultrasonic pulse echo of S-wave in (a,b) 60 MHz and (c,d) in 80 MHz. Red line shows the ultrasonic pulse transmittance wave with Titan tholin pellet. Black line shows the ultrasonic pulse transmittance wave without sample (blank).

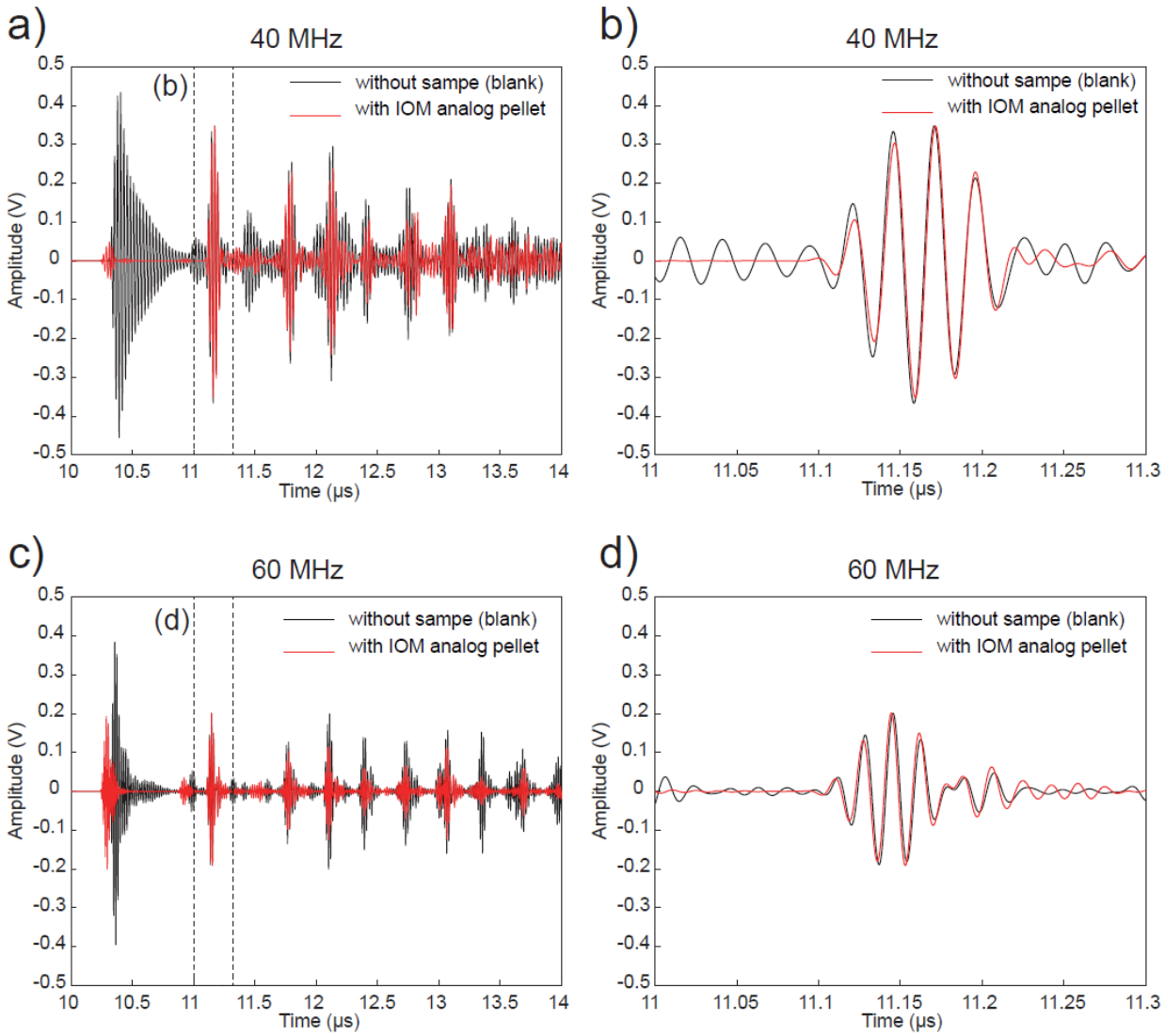

Figure B.3 Results of the analyses of the ultrasonic pulse echo of P-wave in (a,b) 40 MHz and (c,d) in 60 MHz. Red line shows the ultrasonic pulse transmittance wave with hydrothermal organic pellet. Black line shows the ultrasonic pulse transmittance wave without sample (blank).

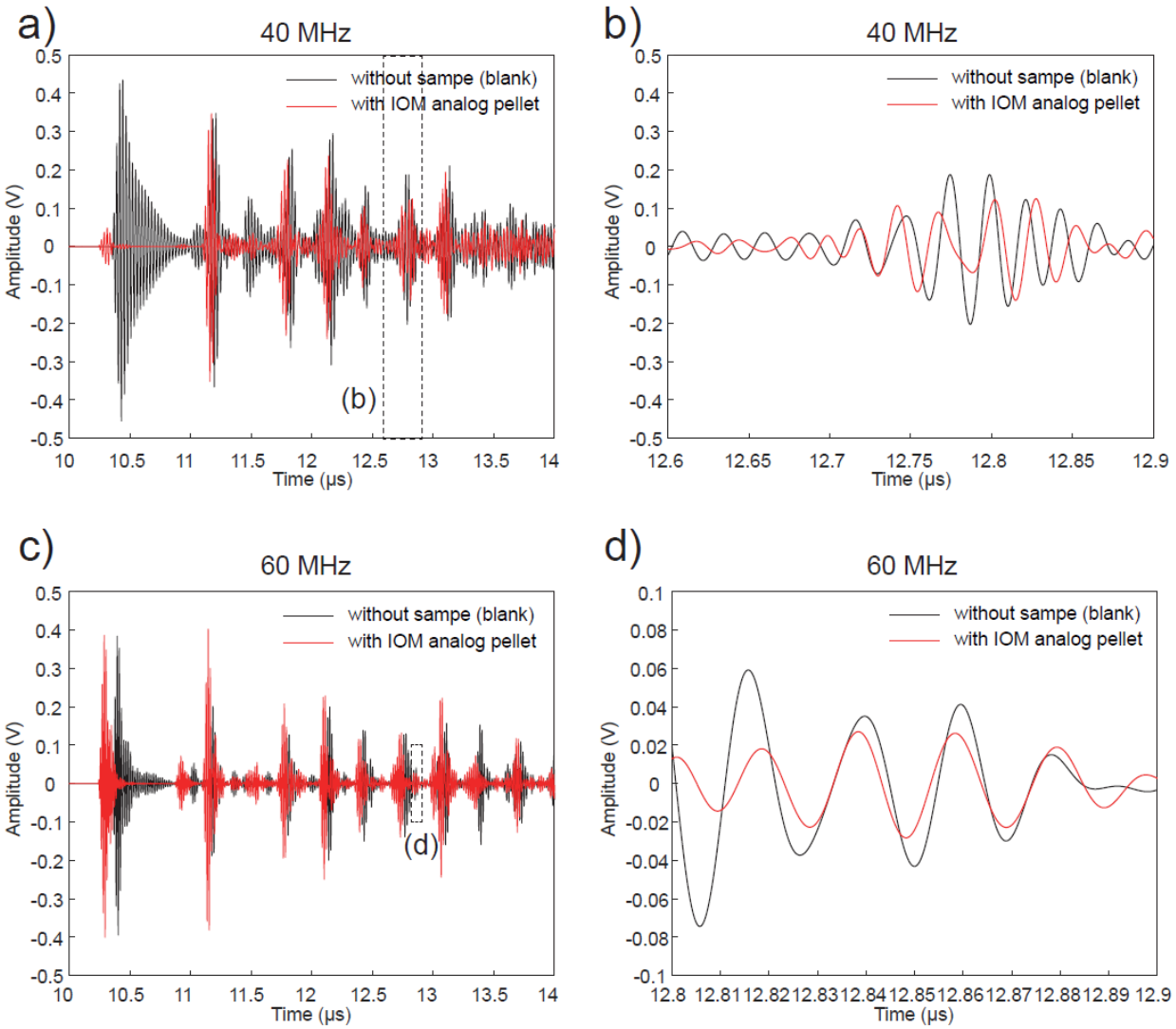

Figure B.4 Results of the analyses of the ultrasonic pulse echo of S-wave in (a,b) 40 MHz and (c,d) in 60 MHz. Red line shows the ultrasonic pulse transmittance wave with hydrothermal organic pellet. Black line shows the ultrasonic pulse transmittance wave without sample (blank).

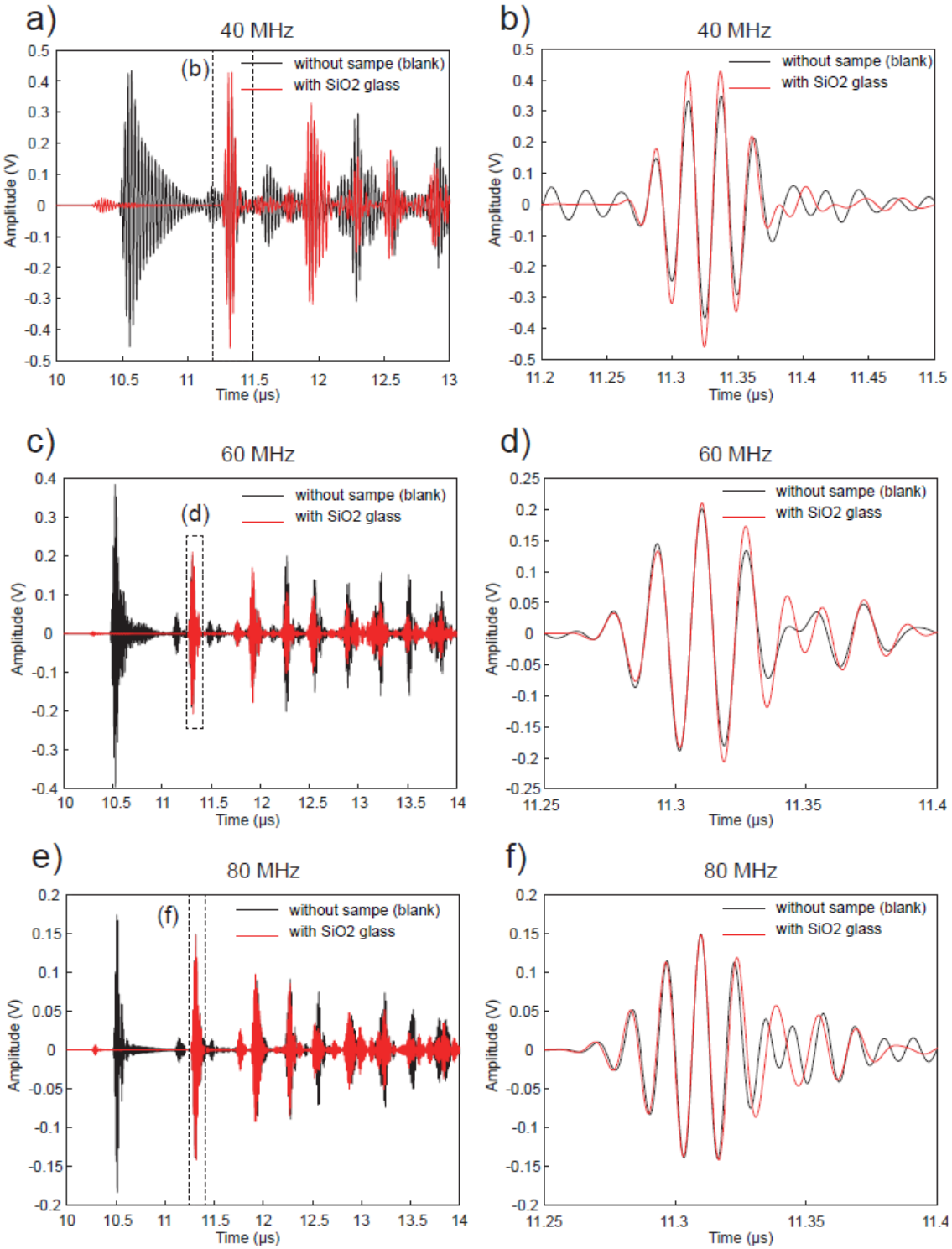

Figure B.5 Results of the analyses of the ultrasonic pulse echo of P-wave (a,b) in 40 MHz, (c,d) in 60 MHz, and (e,f) in 80 MHz. Red line shows the ultrasonic pulse transmittance wave with SiO_2 slide glass. Black line shows the ultrasonic pulse transmittance wave without sample (blank).

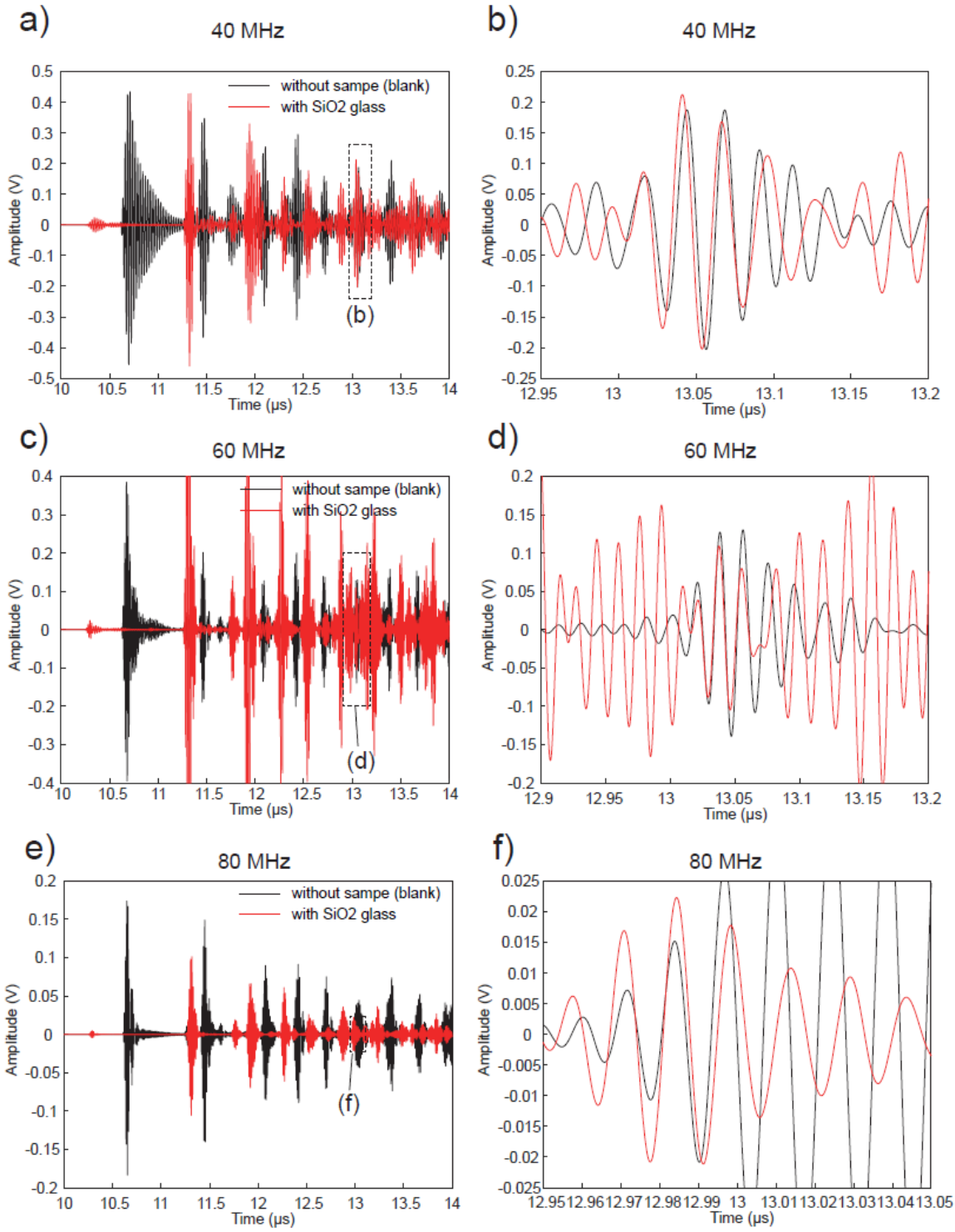

Figure B.6 Results of the analyses of the ultrasonic pulse echo of S-wave (a,b) in 40 MHz, (c,d) in 60 MHz, and (e,f) in 80 MHz. Red line shows the ultrasonic pulse transmittance wave with SiO_2 slide glass. Black line shows the ultrasonic pulse transmittance wave without sample (blank).

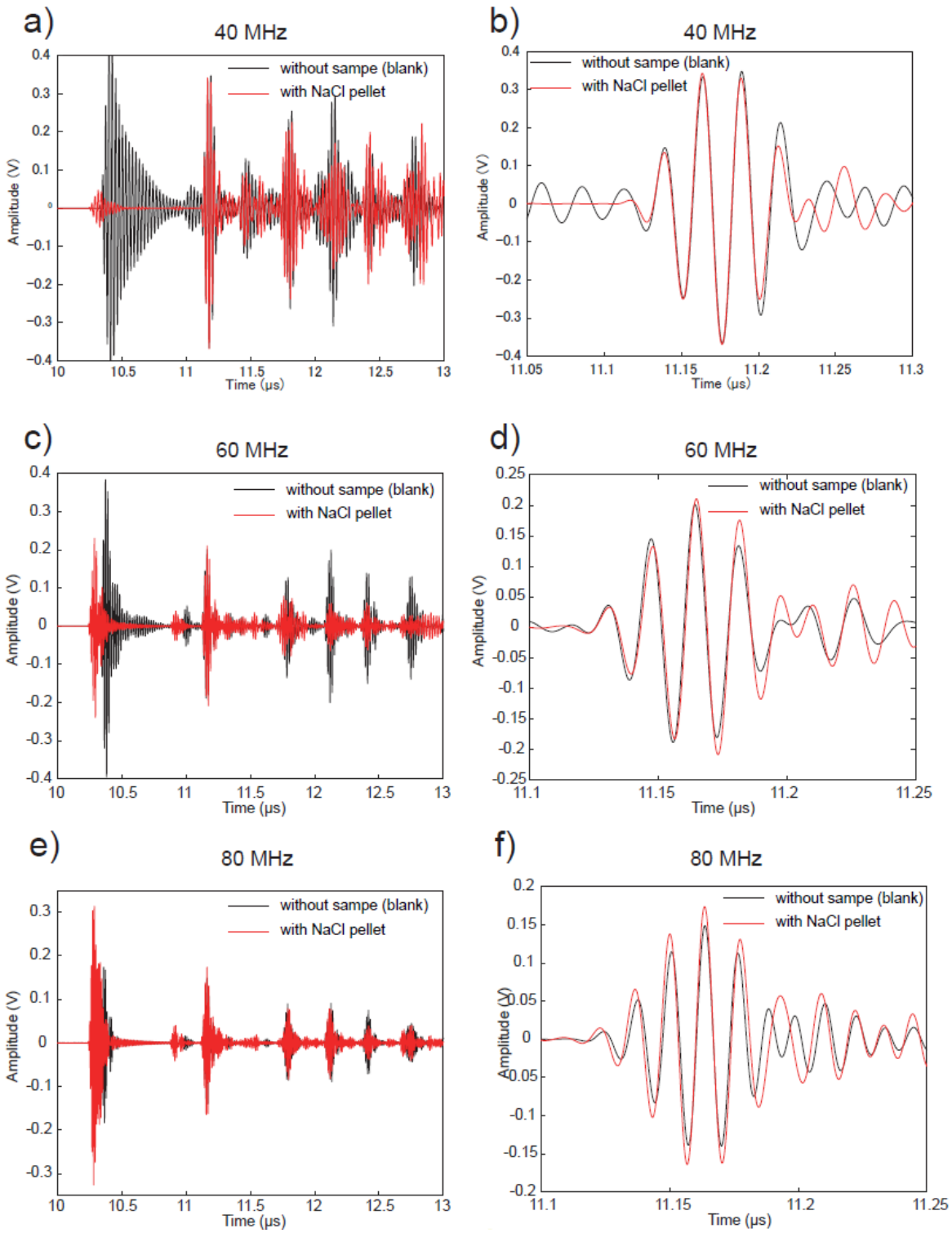

Figure B.7 Results of the analyses of the ultrasonic pulse echo of P-wave (a,b) in 40 MHz, (c,d) in 60 MHz, and (e,f) in 80 MHz. Red line shows the ultrasonic pulse transmittance wave with NaCl pellet. Black line shows the ultrasonic pulse transmittance wave without sample (blank).

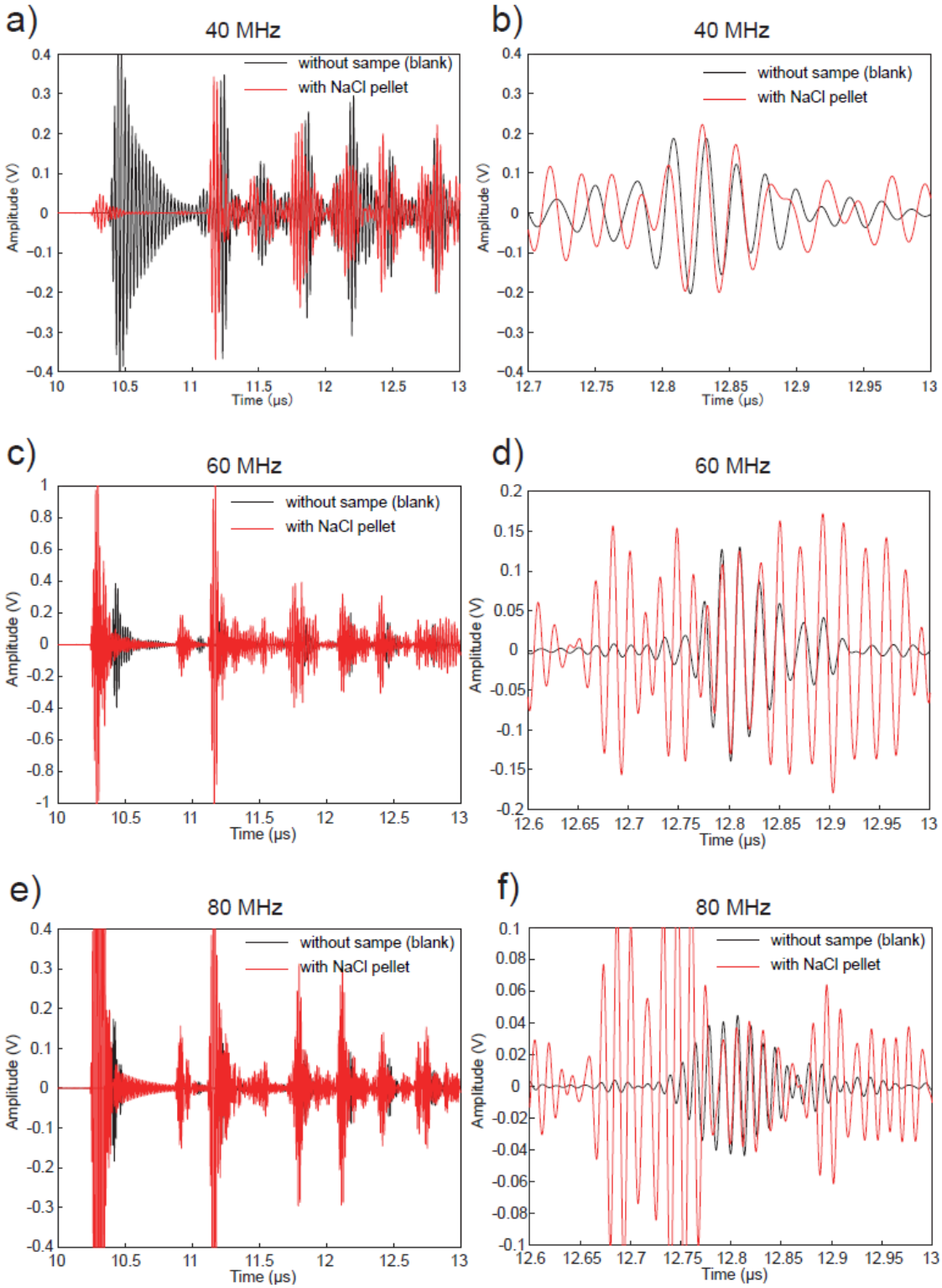

Figure B.8 Results of the analyses of the ultrasonic pulse echo of S-wave (a,b) in 40 MHz, (c,d) in 60 MHz, and (e,f) in 80 MHz. Red line shows the ultrasonic pulse transmittance wave with NaCl pellet. Black line shows the ultrasonic pulse transmittance wave without sample (blank).